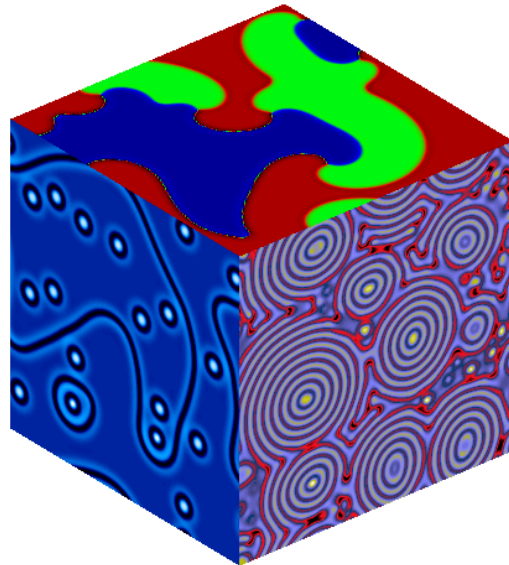
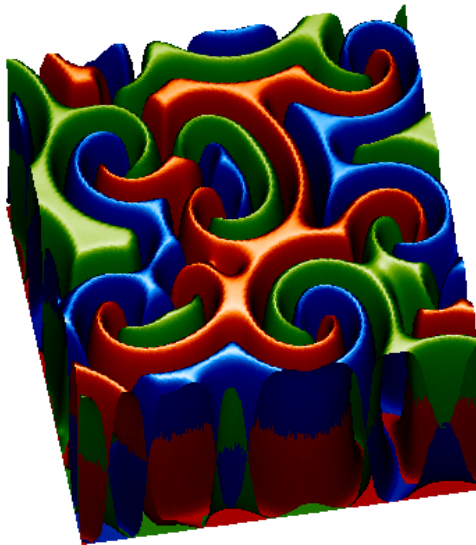




UNIVERSITAT DE LES ILLES BALEARS
DEPARTAMENT DE FISICA

Domain Growth and Topological Defects in Some Nonpotential Problems



*Memoria presentada por Rafael
Gallego Amez para optar al Grado
de Doctor en Ciencias Físicas por la
Universitat de les Illes Balears*

CERTIFICAN

que la presente memoria, titulada "*Domain Growth and Topological Defects in Some Nonpotential Problems*", ha sido realizada por **Rafael Gallego Amez** bajo su dirección, y que concluye la Tesis que presenta para optar al grado de Doctor en Ciencias Físicas.

Y, para que así conste, firman la presente en Palma de Mallorca a 16 de diciembre de 1999.

Maximino San Miguel

Raúl Toral

*A mis padres
Luis y Carmina*

Agradecimientos

Tras casi cuatro años en la Universitat de les Illes Balears, son muchas las personas que en mayor o menor medida han hecho posible que la singladura de esta tesis doctoral haya llegado a buen puerto.

En primer lugar y con mayúsculas, quiero agradecer a mis directores de tesis, Maxi San Miguel y Raúl Toral, la ayuda altruista que siempre me han brindado, y sin la cual la realización de este trabajo no hubiera sido posible. Desde una dirección diligente y responsable, me han orientado en todo momento en la labor científica, ayudándome a vencer todas las dificultades que me he ido encontrando. Realmente no me habéis decepcionado. También quiero dar las gracias a otros miembros del Departamento de Física y a otros colegas científicos por la ayuda prestada en momentos puntuales de la tesis.

En segundo lugar, no me puedo olvidar de mis compañeros de la agencia EFE, que sin duda alguna han contribuido a que mi estancia en la isla fuera más placentera ¡Cuánto os voy a echar de menos! Por un lado Cristóbal ("C++ superstar"), mi compañero de piso, quien a pesar de nuestros gustos musicales, cinematográficos, mujeriles y radiofónicos antagonistas (¡viva García, Schwarzenegger y Roxette!), me ha demostrado ser una persona en la que se puede confiar. Espero que sigas poniendo "el grito" cuando yo me vaya. Lo mismo digo de Benja, mi ex-compañero de despacho (te perdono incluso que me hayas abandonado) y su "mujercita" Chente ("Es Miner de Sa Llotja"), que me introdujeron en el ambiente nocturno mallorquín y casi nunca me han dejado tirado. Tampoco me puedo olvidar de mi colega onatiarra Inigo, gracias a quien aprendí que una "arcada a l'ast" no es ningún tipo de carne asada (esto te lo escribo pa ti y pa mí). Mención especial también para mi otro compañero vasco Víctor Martínez ¡Quién te iba a decir cuando viniste a Mallorca que ahora te encontrarías felizmente casado y con un "peaso" deorro! Qué decir de mi encantadora amiga italiana Rober, carinosa y amable donde las haya. Ti voglio molto bene, Rober. Para su fidanzato Damià también un recuerdo muy especial. Y para Cati, mi compañera mallorquina de "Sex Salines", una forta abraçada. Al resto de efesios, gracias por vuestra amistad y por los buenos momentos vividos.

Para terminar, quería agradecer a mis padres con todo mi corazón su apoyo, sus sabios y útiles consejos y el continuo interés que han mostrado por mi trabajo. A vosotros, porque con vuestro amor y cariño infinitos siempre os habéis desvivido por mí, os dedico esta tesis.

Contents

Resumen	xvii
Summary	xxiii
1 Interface Dynamics, Domain Growth and Dynamical Scaling	1
1.1 Introduction	1
1.2 Potential and Nonpotential Systems	5
1.3 Interface Dynamics	8
1.3.1 Relaxational Gradient Flow Systems	8
1.3.2 Nonrelaxational Potential Flow Systems	14
1.3.3 Nonpotential Systems	18
1.3.4 Oscillatory tails in front profiles	20
1.4 Growth Laws	23
1.4.1 Relaxational systems	23
1.4.1.a Kinetic Glauber-Ising model	23
1.4.1.b Model A dynamics	24
1.4.1.c Model B dynamics	25
1.4.1.d q -state Potts models	26
1.4.1.e Swift-Hohenberg equation	27
1.4.2 Nonrelaxational Systems	29
1.4.2.a Nonlinear Schrödinger equation	30
1.4.2.b One-dimensional cyclic Lotka-Volterra models	32
1.4.2.c Nonpotential Swift-Hohenberg equation	34
1.4.2.d Nonlinear optical systems	36
1.5 Dynamical Scaling	36
1.5.1 Porod's Law	38
1.5.2 Scaling Solution in the One-dimensional Glauber-Ising Model	39
1.5.3 Scaling Function Theories	40
2 Domain Growth in the Busse-Heikes Model for Three Competing Amplitudes	43
2.1 Introduction	43
2.2 Theoretical Model	46
2.3 Zero-dimensional Systems	48

2.3.1	The Case $\mu = 0$	51
2.3.2	The Case $\mu > 0$	56
2.3.3	Busse-Heikes Model in the Presence of Noise	58
2.4	One-dimensional Systems	61
2.4.1	Front Solutions	62
2.4.1.a	<i>Isolated fronts</i>	62
2.4.1.b	<i>Multifront configurations</i>	65
2.4.2	Domain Growth and Dynamical Scaling	68
2.4.2.a	<i>Growth law</i>	69
2.4.2.b	<i>Scaling function</i>	72
2.5	Two-dimensional Systems	73
2.5.1	Vertex Dynamics	75
2.5.1.a	<i>Dynamics of an isolated spiral</i>	76
2.5.1.b	<i>Critical distance for vertex annihilation</i>	77
2.5.1.c	<i>Multivertex configurations</i>	78
2.5.2	Domain Growth and Dynamical Scaling	79
2.5.3	The Role of the Spatial Derivatives	82
2.6	Conclusions	85
3	Parametrically Forced Complex Ginzburg-Landau Equation: Forcing at Three Times the Natural Frequency	87
3.1	Introduction	87
3.2	Uniform Solutions	91
3.3	Phase Approximation	95
3.3.1	The Oscillatory Regime	95
3.3.2	The Excitable Regime	95
3.4	Fronts and Spirals	96
3.4.1	One-dimensional systems	96
3.4.2	Two-dimensional systems	98
3.5	Numerical Results	99
3.6	Conclusions	107
4	Domain Growth, Localized Structures and Labyrinthine Pat- terns in Vectorial Kerr Resonators	109
4.1	Introduction: Domain Growth in Optical Systems	109
4.2	Description of the Model and Asymptotic Steady States	115
4.3	Interface Dynamics	118
4.3.1	One-dimensional systems	118
4.3.2	Two-dimensional systems	120
4.4	Conclusions	128
5	Conclusions	129
Appendix A:	Analytical Approach of the Mean Energy for the Busse- Heikes Model in the Presence of Noise	133

Appendix B: Time Evolution of the Size of an Isolated Domain for the One-dimensional Busse-Heikes Model	137
Appendix C: Eikonal Equation for the Busse-Heikes Model	141
Appendix D: Computation of the Angular Velocity of a Vertex	145
D.1 Geometrical Approach	145
D.2 Free Boundary Formulations	149
BIBLIOGRAPHY	151
CURRICULUM VITAE	161
INDEX	165

List of Figures

1.1	Snapshots of model A dynamics.	4
1.2	Sketch of a potential function with two minima.	9
1.3	Spherical domain.	10
1.4	Time evolution of the radius of a spherical domain in 2D.	14
1.5	Diagram of Ising and Bloch fronts.	20
1.6	Profile of monotonic and nonmonotonic fronts.	21
1.7	Two frozen configurations.	22
1.8	A time sequence of the coalescence of gas bubbles for the NLSE. . .	32
1.9	Stripe structure for Swift-Hohenberg models.	35
1.10	Scaling function for the model A in 2D.	37
2.1	Time sequence of Küppers-Lortz unstable domains.	44
2.2	Linear stability diagram of the homogeneous solutions of (2.1). . .	50
2.3	Sketch of the Küppers-Lortz instability.	51
2.4	Orbits in the 3D space for $\mu = 0$ and amplitudes vs time.	54
2.5	Orbits in the 3D space for $\mu > 0$ amplitudes vs time.	57
2.6	Time evolution of the period without noise.	58
2.7	Time evolution of the amplitudes with noise.	59
2.8	Average value of the period versus theoretical expression.	60
2.9	Alternating period with noise as a function of $\delta^{-1} \log(\mu/\varepsilon)$	61
2.10	Kinds of fronts and their direction of motion for $\delta > 0$	64
2.11	1D Busse-Heikes model: solitary kink velocity as a function of δ . .	64
2.12	Time evolution of the system below the Küppers-Lortz threshold. .	66
2.13	Time evolution of system above the Küppers-Lortz threshold. . . .	67
2.14	Time evolution of the characteristic domain size for $\delta = 0$	69
2.15	Scaling function for $\delta = 0$	69
2.16	Characteristic domain size for $\eta = 3.5$, $\delta = 0.001$	70
2.17	Characteristic domain size for $\eta = 3.5$, $\delta = 0.1$	71
2.18	Equal-time correlation function for $\eta = 3.5$, $\delta = 0.001$	73

2.19	Snapshots with isotropic diffusion terms.	74
2.20	Several stages of the formation of a single spiral.	75
2.21	κ_0 and v_p vs $v_p^2 \kappa_0^{3/2}$ and v_p^2	76
2.22	Annihilation of two counter-rotating vertices.	77
2.23	Critical distance for vertex annihilation.	78
2.24	Vertex configurations for pbc and nbc.	79
2.25	Characteristic domain size for $\eta = 3.5$, $\delta = \{0.001, 0.010\}$	80
2.26	Equal-time correlation function for $\eta = 3.5$, $\delta = 0$	81
2.27	Equal-time correlation function for $\eta = 3.5$, $\delta = 0.01$	81
2.28	Snapshots with isotropic and directional derivatives for $\mu = 0.1$	82
2.29	Snapshots with isotropic and directional derivatives for $\mu = 2.5$	83
2.30	Alternating mean period with isotropic and anisotropic terms.	84
3.1	Frequency locked regimes observed in an experiment.	89
3.2	$\text{Re } A$ for different values of the forcing amplitude.	91
3.3	Nullclines and fixed points of the forced CGLE.	93
3.4	Uniform solutions of Eqs. (3.7a–b).	94
3.5	Plot of the phase field in the excitable regime in 1D.	98
3.6	Example of motion of pairs of inclined fronts.	99
3.7	$ A $ and $\arg(A)$ in the <i>frozen states</i> regime (case I).	102
3.8	Same as in Fig. 3.7 in the <i>frozen states</i> regime (case II)	103
3.9	Same as in Fig. 3.7 in the <i>phase turbulence</i> regime.	104
3.10	Same as in Fig. 3.7 in the <i>defect turbulence</i> regime (case I).	105
3.11	Same as in Fig. 3.7 in the <i>defect turbulence</i> regime (case II).	106
3.12	Oscillatory instability at zero wave number.	107
4.1	Time sequence of domain growth in a DOPO.	112
4.2	Configuration of the nonlinear cavity in a Fabry-Pérot geometry.	115
4.3	Steady state homogeneous solutions for system (4.9).	116
4.4	Marginal stability curves of the homogeneous solutions of (4.9).	117
4.5	Velocity of an isolated kink in 1D.	118
4.6	1D intensity profiles of a polarization domain wall.	119
4.7	Snapshots of the intensities I_+ and I_- at long times in 1D.	119
4.8	Coefficient $\gamma(E_0)$ as defined in the text.	121
4.9	Spherical averaged pair correlation function.	122
4.10	Total field intensity and diameter of a localized structure.	122
4.11	Diagram of the modulational instability gain for a planar front.	123

4.12	Snapshots in the <i>coarsening regime</i>	125
4.13	Snapshots in the regime of formation of <i>localized structures</i>	126
4.14	Snapshots in the regime of <i>labyrinthine patterns</i>	127
A.1	Domain of integration of the integrals in Eqs. (A.3a–b).	134
B.1	Sketch of an isolated domain.	137
C.1	Schematic of the change of coordinates defined by Eq. (C.2).	142
D.1	Geometrical representation of a front with a free end.	146

Resumen

Contexto del trabajo

La evolución interna de la Física ha dado lugar a un interés creciente en la investigación de estructuras espaciales fuera de equilibrio. Estas estructuras pueden aparecer fuera del equilibrio termodinámico como estados estacionarios independientes del tiempo o como estados dinámicos [1, 2]. Los estados dinámicos pueden ser persistentes (incluido el caos espaciotemporal), y transitorios en los que podemos estudiar los procesos de crecimiento y evolución de una estructura espacial [3]. Entre los sistemas en los que se han estudiado procesos de crecimiento cabe destacar: fluidos simples y binarios, aleaciones binarias, superfluidos y superconductores, mezclas poliméricas, geles, láseres, condensación electrón-hueco en semiconductores, sistemas geológicos (minerales), sistemas reactantes químicos, metales, vidrios y cerámicas cristalinas, transiciones orden-desorden, sistemas magnéticos, crecimiento de colonias de bacterias, crecimiento dendrítico, segregación de especies y crecimiento de poblaciones en sistemas predador-presa. Existen esencialmente dos tipos de crecimiento en sistemas físicos: crecimiento interfacial o de dominios [4, 5] y el crecimiento por agregación de partículas similares [6]. Sólo se hablará en esta memoria del primero, el cual se refiere a las etapas de la evolución durante el proceso transitorio hacia un estado final de un sistema en el que coexisten varias fases. Ejemplo prototipo de esta situación es la dinámica de separación de fases cuando una aleación binaria se enfría rápidamente por debajo de una temperatura crítica [4]. El proceso dinámico está gobernado por la creación de defectos topológicos y el movimiento de interfases. En la literatura anglosajona, el proceso de crecimiento de los dominios se suele llamar *coarsening*, un término de origen en el vocabulario metalúrgico que podríamos traducir por *embastecer*. Una cantidad relevante es el tamaño de dominio medio, cuya dependencia temporal proporciona una ley de crecimiento característica.

Los procesos de crecimiento en la aproximación hacia un estado final de equilibrio termodinámico son generalmente bien conocidos [4]. Sólo en los últimos años se han empezado a estudiar dinámicas transitorias cuando el estado final no es de equilibrio termodinámico [7, 8, 9]. Estas dinámicas son a menudo no potenciales. El significado del término “no potencial” se explica con detalle en el capítulo 1. Brevemente, indica que la dinámica no minimiza un potencial o energía libre conocidos. Ello da lugar a un comportamiento y movi-

miento cualitativamente distintos de defectos topológicos e interfases. En un sistema potencial, la estabilidad relativa de las diversas fases permite caracterizar con exactitud el movimiento de las interfases que las delimitan [10]. Por contra, no hay en general un criterio claro que permita dirimir qué fase es más estable que otra en un sistema no potencial. Es difícil hacer una caracterización global de dinámicas no potenciales y cada caso debe estudiarse en general separadamente. Algunos trabajos sobre movimiento de frentes en sistemas no potenciales pueden encontrarse en [11, 12, 13, 14, 15]. El objetivo central de la presente memoria es el estudio de los procesos mediante los cuales un sistema con una dinámica no potencial, que puede albergar varias fases estables, se aproxima a un estado final. El estudio está centrado en sistemas cuyas propiedades pueden expresarse en términos de parámetros de orden escalares no conservados.

En sistemas no potenciales puede haber ocasiones en las que, a pesar de coexistir varias fases estables en el sistema, se inhiba el proceso de crecimiento de dominios y no se llegue a un estado final independiente del tiempo. Por ejemplo, la ausencia de *coarsening* puede ser debida a la aproximación a estados dinámicos persistentes. Un ejemplo es la convección de Rayleigh-Bénard de un fluido sometido a rotación [16, 17, 18]. Por encima de una velocidad de rotación crítica, el sistema se encuentra en una situación de caos espacio-temporal de forma que el tamaño medio de los dominios satura a un valor estadísticamente constante. En este trabajo se estudian sistemas que incorporan dinámicas no potenciales que pueden dar lugar a estados finales de no equilibrio no estacionarios. En otras ocasiones, el proceso de crecimiento puede verse frenado por la aparición de estructuras congeladas (patrones laberínticos, estructuras localizadas, etc.). A menudo, estas estructuras están asociadas a perfiles no monótonos de las interfases, los cuales pueden dar lugar a fuerzas de interacción repulsivas entre frentes. La existencia de *coarsening* depende de la importancia relativa de esta interacción repulsiva en relación con los efectos coadyuvantes al crecimiento. Un ejemplo, ampliamente desarrollado en el capítulo 4, lo constituyen los dominios de polarización formados en el plano transversal de una cavidad óptica que contiene un medio Kerr no lineal cuando se ilumina con luz linealmente polarizada. En el régimen donde hay coexistencia de dos estados homogéneos de polarización linealmente estables (biestabilidad óptica), y dependiendo de la intensidad de la luz incidente, puede haber *coarsening*, formación de estructuras localizadas o creación de patrones laberínticos.

Para sistemas que se aproximan a un estado final de equilibrio termodinámico, se ha observado que el proceso de crecimiento de dominios es autosimilar [4, 19]. Esto significa que la estructura de dominios es, en un sentido estadístico, independiente del tiempo salvo un factor global de escala; se dice entonces que el sistema exhibe escala dinámica. Hay otros sistemas que no poseen en absoluto una escala de longitud característica, pero que sin embargo son autosimilares sobre muchas escalas de longitud. Tales sistemas

se denominan fractales y han cobrado una gran importancia en los últimos años [20]. Ejemplos de crecimiento fractal son la solidificación dendrítica en un medio sobreenfriado, digitaciones viscosas y electrodeposición iónica sobre un electrodo. Los estudios de escala dinámica resultaron de gran ayuda para entender la escala en sistemas fractales (escala multifractal) que es una generalización de la escala simple.

Una pregunta que surge de forma natural es si un sistema con una dinámica no potencial exhibe escala dinámica durante procesos de crecimiento de dominios. Sin embargo, apenas hay trabajos publicados en esta área (una excepción la constituye la referencia [8]). Con el trabajo desarrollado en esta memoria se pretende dar un primer paso para llenar el vacío existente en el estudio de procesos de crecimiento y escala dinámica en sistemas no potenciales. En los sistemas estudiados en esta memoria damos evidencia de una evolución dinámica autosimilar en un régimen de crecimiento de dominios, con leyes de crecimiento diferentes de las correspondientes al límite de dinámica potencial. Por otra parte, explicamos cómo la presencia de defectos topológicos creados en la evolución dinámica transitoria, y efectos no potenciales, pueden frenar el proceso de crecimiento, dando lugar en algunas ocasiones a estados dinámicos persistentes.

Resumen de la memoria

En el capítulo 1 se hace un resumen de algunos de los resultados más destacados que se conocen sobre dinámica de interfases, tanto en sistemas potenciales como no potenciales. Antes, se hace una clasificación de los sistemas dinámicos, con una explicación detallada y concisa del término “no potencial”, que a menudo se utiliza a través de este trabajo. La segunda parte del capítulo está dedicada al resumen de conceptos básicos sobre crecimiento de dominios y escala dinámica. Se presentan los resultados fundamentales sobre leyes de crecimiento para diferentes sistemas importantes. Paralelamente, se hace una comparación entre ellos en un intento de determinar los mecanismos dominantes de los diversos procesos de crecimiento. En cuanto a la escala dinámica, se explica cómo estudiarla y se introduce el concepto de función de escala.

En el capítulo 2 se considera un modelo de tres campos acoplados (modelo de Busse-Heikes [21]), que fue propuesto para estudiar la convección de Rayleigh-Bénard de un fluido sometido a rotación. Cada campo representa la amplitud de un conjunto de rollos de convección paralelos con una orientación de 60° respecto de los otros dos campos. En general, la dinámica es no potencial y hay tres fases estables que coexisten asociadas a cada una de esas orientaciones. La velocidad angular de rotación de la celda del fluido está vinculada a efectos no potenciales en el modelo. Por encima de una velocidad de rotación crítica, tiene lugar una inestabilidad [inestabilidad de Küppers-Lortz (KL)] que da lugar a una alternancia cíclica entre los tres modos. En la

versión original del modelo en que no hay dependencia espacial ni términos de ruido, el sistema oscila entre las tres fases de tal manera que el periodo de alternancia diverge con el tiempo, contrariamente a lo observado experimentalmente. Mostramos como este problema puede ser solventado con la presencia de fluctuaciones, que son modeladas mediante la adición de ruido blanco a las ecuaciones. Asimismo, damos un procedimiento para el cálculo analítico del periodo de alternancia en cierto régimen de parámetros. En dos dimensiones, la inestabilidad de KL se analiza utilizando diferentes tipos de operadores de difusión. Se observa que operadores con derivadas anisótropas dan lugar a un periodo *intrínseco* de la inestabilidad esencialmente constante con el tiempo, mientras que derivadas isotropas dan lugar a la divergencia temporal de este periodo, al igual que sucede en el modelo original sin dependencia espacial. Fuera de la región de la inestabilidad de KL, hay un régimen de coexistencia de tres estados *estables* en competición. En una dimensión espacial se produce crecimiento de dominios hasta llegar a un estado homogéneo que ocupa todo el sistema. Encontramos que el proceso de crecimiento es autosimilar, con una ley de escala que posee dos comportamientos dominantes claramente definidos. En dos dimensiones, el límite de dinámica potencial da lugar a un proceso transitorio de crecimiento de dominios que es autosimilar. Por contra, la dinámica no potencial puede frenar el proceso de crecimiento para sistemas suficientemente grandes. Estudiamos la influencia de efectos no potenciales en el movimiento de frentes así como la formación de defectos formados por espirales de tres brazos. La presencia de estos defectos y el movimiento no potencial de frentes son la causa de que el proceso de crecimiento de dominios no tenga lugar en sistemas grandes. Cuando se elimina una amplitud del modelo, no es posible la formación de espirales y se produce *coarsening*. Este proceso de crecimiento, al igual que en una dimensión, es autosimilar, con una ley de crecimiento distinta de la bien conocida del límite potencial.

El estudio que se realiza en el capítulo 3 se enmarca en el contexto general de formación de estructuras espaciotemporales en sistemas con una simetría rota. En particular, estudiamos el efecto de una modulación temporal a una frecuencia tres veces la crítica sobre una bifurcación de Hopf. El sistema se modela con una ecuación de Ginzburg-Landau compleja con un término cuadrático extra, que proviene del acoplamiento entre el campo externo y los modos inestables. La ruptura de la simetría de fase que provoca el forzamiento externo da lugar, por encima de una intensidad del forzamiento crítica, a tres estados de fase estables. Para forzamientos grandes, el régimen excitable posee las mismas propiedades dinámicas genéricas que el modelo de Busse-Heikes estudiado en el capítulo 2. Por otra parte mostramos, tanto analítica como numéricamente, la existencia de una transición entre espirales de fase de un brazo y espirales de amplitud excitables de tres brazos cuando se incrementa la intensidad del forzamiento.

Los sistemas ópticos no lineales ofrecen un cúmulo de oportunidades para

el estudio de formación de estructuras y otros procesos de no equilibrio en los que el acoplamiento espacial está producido por difracción en vez de difusión. Sólo recientemente se han considerado estudios de crecimiento de dominios para estos sistemas, y se han mostrado algunas leyes de crecimiento obtenidas de simulaciones numéricas [9, 22, 23, 24]. No obstante, no se han descrito mecanismos claros de crecimiento y no se ha considerado, en general, la validez de leyes de escala dinámica. Como ejemplo de un sistema óptico no lineal en el que se pueden examinar los fenómenos de crecimiento de dominios y escala dinámica, consideramos en el capítulo 4 la formación de estructuras transversales en un medio kerr no lineal [25, 26]. Cuando se ilumina una cavidad óptica de dicho medio con un campo externo, aparecen dominios de dos estados estables de polarización en cierto régimen de parámetros. En esta situación de biestabilidad óptica, encontramos tres regímenes correspondientes a la evolución dinámica de tales dominios, a saber: estructuras laberínticas, formación de estructuras localizadas y *coarsening*. Para este último, damos evidencia de la existencia de escala dinámica con una ley de crecimiento resultante de un movimiento interfacial gobernado por efectos de curvatura.

Finalmente, las conclusiones más relevantes de este trabajo se presentan en el capítulo 5.

Summary

Context of the work

The internal evolution of Physics has given rise to an increasing interest in the study of pattern formation out of equilibrium. Patterns may appear out of thermodynamic equilibrium either as time-independent stationary states or as dynamical states [1, 2]. Among the dynamical states, some of them are persistent (including those with spatio-temporal chaos), and others are transient states where the processes of domain growth and dynamical evolution of a spatial pattern can be studied [3]. Systems for which growth processes have been studied include: simple and binary fluids, binary alloys, superfluids and superconductors, polymer blends, gels, lasers, geological systems (minerals), chemically reacting systems, metals, glasses and crystalline ceramics, order-disorder systems, magnetic systems, species segregation, and population growth in predator-prey systems. There are basically two types of growth in physical systems: interfacial or domain growth [4, 5] and growth by aggregation of similar particles [6]. In this thesis we will consider the former, that refers to the dynamical evolution of a system having various stable phases that coexist during the transient process towards a final state. The phase separation dynamics of a binary alloy following a quench below a critical temperature constitutes a prototypical example of this situation. The dynamical evolution is governed by interface motion and the creation of topological defects. A relevant quantity in the coarsening process is the average domain size, whose time-dependence gives a characteristic growth law.

Growth processes in the approximation to a final state of thermodynamic equilibrium are generally well-known [4]. Only recently, however, transient dynamics when the final state is not of thermodynamic equilibrium have been studied [7, 8, 9]. These dynamics are often nonpotential. The meaning of the term “nonpotential” is explained in detail in chapter 1. Briefly, it indicates that the dynamics does not minimize any known potential or free energy. It gives rise to qualitatively different behavior and motion of defects and interfaces. In a potential system, the relative stability of the various phases allows to characterize interface motion [10]. On the contrary, there is not an equivalent criterion of general validity for nonpotential systems. As a consequence, it is difficult to characterize nonpotential dynamics, since every situation must in general be studied separately. Some works on front motion in

nonpotential systems can be found in [11, 12, 13, 14, 15]. The main objective of this thesis is the study of the processes involved in the approximation towards a final state of a nonpotential system holding several stable states that coexist in the transient dynamics. We will focus on systems whose properties can be described in terms of nonconserved scalar order parameters.

In nonpotential systems it may happen that, despite the fact that several stable phases coexist in the system, domain growth is inhibited and a time-independent state is never reached. For example, the absence of coarsening can be due to the appearance of persistent dynamical states. Rotating Rayleigh-Bénard convection is a well-known example [16, 17, 18]. Above a critical rotation angular velocity, the system breaks up into a spatio-temporal dynamical state in which the average domain size saturates to a statistically constant value. In this work, we study nonpotential systems that may lead to nonstationary final states out of equilibrium. In other situations, coarsening can be stopped by the appearance of frozen spatial structures (labyrinthine patterns, localized structures, etc.). Often, these structures are associated with nonmonotonic front profiles, which can give rise to repulsive interaction forces between domain walls. The existence of coarsening depends upon the relative importance of this repulsive interaction and the effects that help domain growth. An example, developed widely in chapter 4, is the formation of polarization domains in the transversal plane of an optical cavity when a nonlinear kerr medium is illuminated with a linearly polarized input field. In the regime where two linearly stable polarization homogeneous states coexist (optical bistability), and depending on the input field intensity, there may be coarsening, formation of localized structures, or creation of labyrinthine patterns.

For systems that approach a final state of thermodynamic equilibrium, domain growth has been seen to be self-similar [4, 19]. This means that the domain structure is, in a statistical sense, independent of time up to a global scale factor: the systems exhibit dynamical scaling. There are other systems that, while not possessing at all a characteristic length, still they are self-similar over many length scales. Such systems are called fractals and have become very important in the last years [20]. Dendritic solidification in a undercooled medium, viscous fingering and ionic electrodeposition, are all examples of fractal growth. Dynamical scaling studies were very important to understand scaling in fractal systems (multifractal scaling) which is a generalization of the single scaling.

A natural question, which we address in this thesis, is the existence of dynamical scaling for a nonpotential problem during the domain growth process. However, very little work has been done previously in this area (ref. [8] is an exception). This thesis intends to give a first step towards understanding domain growth and dynamical scaling in nonpotential systems. For the nonpotential systems studied in this thesis, we give clear evidence of self-similar dynamical evolution in a domain growth regime, with growth laws different

from the ones corresponding to the limit of potential dynamics. Moreover, we explain how the presence of topological defects, created along the transient dynamics, and the nonpotential effects, may inhibit the coarsening process, and sometimes give rise to persistent dynamical states.

Summary of the thesis

In chapter 1 we present some important known results about interface dynamics, both in potential and nonpotential systems. Firstly, we present a classification of dynamical systems, including a detailed explanation of the term “nonpotential”, frequently used throughout this thesis. The second part of the chapter reviews the basic concepts regarding domain growth and dynamical scaling. Basic results about growth laws for different relevant systems are presented. We also compare several systems in order to determine which are the dominant growth mechanisms. Finally, we introduce the concept of scaling function and explain how it can be used to characterize dynamical scaling.

In chapter 2 we consider a model with three coupled fields (Busse-Heikes model [21]), which was proposed to study rotating Rayleigh-Bénard convection. Each field represents the amplitude of a set of parallel convective rolls with a relative orientation of 60° with respect to each other. In general, the dynamics is nonpotential and there are three stable phases that coexist, each one associated with one of the three orientations. The rotation angular velocity of the fluid cell is related to nonpotential effects in the model. Above a critical rotation angular velocity, an instability that leads to a cyclic alternation between the modes takes place [Küppers-Lortz (KL) instability]. In the original version of the model without spatial dependence or noise terms, the system alternates between the three phases. Contrary to what is observed in the experiments, the alternating period diverges with time. We show how this problem can be circumvented with the presence of fluctuations, that are modeled by adding white noise to the equations. Moreover, we give a procedure to calculate the alternating period analytically in a certain range of parameters. In two spatial dimensions, the KL instability is studied by using different kinds of diffusion-like operators. It is observed that operators with anisotropic derivatives lead to an essentially constant *intrinsic* period of the KL instability, whereas isotropic derivatives lead to the temporal divergence of this period, as happens in the original model without spatial dependence. Outside the unstable KL region, there is a regime in which three competing stable states coexist. In one spatial dimension there is domain growth, and the final state is an homogeneous solution filling up the whole system. We find that this coarsening process is self-similar, with a growth law that possesses two clearly defined dominant behaviors. In two dimensions, the limit of potential dynamics is such that there is domain growth with self-similar evolution. On the contrary, the nonpotential dynamics may inhibit coarsening for large enough system sizes. We study the influence of nonpotential effects

on front motion as well as the formation of defects formed by three-armed spirals. These defects, together with the nonpotential dynamics, are responsible for coarsening inhibition in large systems. When only two amplitudes are excited during the growth process, spiral formation is not possible and coarsening takes place. This growth process, as in the case of one dimension, is self-similar, with a growth law different from that of the potential dynamics limit.

The study performed in chapter 3 belongs to the general framework of pattern formation in systems with broken symmetries. In particular, we study the effect of a temporal modulation at three times the critical frequency on a Hopf bifurcation. The system is modeled with a complex Ginzburg-Landau equation with an extra quadratic term, resulting from the strong coupling between the external field and unstable modes. The forcing breaks the phase symmetry, and three stable phase locked states appear above a critical forcing intensity. For large forcings, the excitable regime exhibits the same generic properties of the Busse-Heikes model studied in chapter 2. On the other hand we show, both analytically and numerically, the existence of a transition between one-armed phase spirals and three-armed excitable amplitude spirals when the forcing intensity is increased.

Driven nonlinear optical systems offer a wealth of opportunities for the study of pattern formation and other nonequilibrium processes in which the spatial coupling is caused by diffraction instead of diffusion. Only very recently domain growth has been considered in some of these systems and some growth laws obtained from numerical simulations have been reported [9, 22, 23, 24]. Nevertheless, clear mechanisms for the growth laws have often not yet been identified. In addition, the question of dynamical scaling has, in general, not been addressed so far. As a clear example of a nonlinear optical system in which the issues of domain growth and dynamical scaling can be addressed and for which detailed clear results can be obtained, we consider in chapter 4 the formation of transversal structures in a optical cavity filled with a nonlinear kerr medium [25, 26]. In a certain range of parameters, when the cavity is illuminated with a linearly polarized input field, domains of stable polarization states emerge. In this situation of optical bistability, we find three different regimes corresponding to the dynamical evolution of such domains, namely, labyrinthine patterns, formation of localized structures and domain coarsening. For the latter we give evidence of the existence of dynamical scaling, with a growth law similar to that resulting from a curvature driven interface motion.

Finally, the main conclusions of the thesis are presented in chapter 5.

Chapter 1

Interface Dynamics, Domain Growth and Dynamical Scaling

1.1 Introduction

This chapter is devoted to the discussion of the fundamental laws that govern interface motion in spatially extended systems as well as to the problem of domain growth. We will restrict the discussion to interfaces connecting linearly stable asymptotic states in systems described by scalar order parameters. The propagation of fronts into unstable states has been studied elsewhere [14, 27, 28].

For potential systems, a measure of the relative stability between asymptotic states is guaranteed by the existence of a Lyapunov potential [10], which plays the role of a free energy. In one dimension, the direction of motion of an isolated front is determined through the relative stability of the two linearly stable solutions. Specifically, the front velocity is proportional to the Lyapunov potential difference between the asymptotic states. In higher dimensions, and in the case of equivalent states (that is, states with the same value of the potential), the system tends to reduce the excess of energy located on the interfaces by decreasing their length. As a consequence, small domains shrink and the system coarsens. The driving force of this process is the curvature of the interfaces [29]. This simple description is modified when conservation laws restrict the dynamics [4, 30].

For systems without a Lyapunov potential (to be called *nonpotential* systems), the situation changes significantly. The study of front propagation can no longer be done in terms of a free energy. It is known that a domain wall between two dynamical equivalent states may move in $d = 1$ in either direction due to nonpotential dynamics [11, 13]. In $d > 1$ more complicated effects may appear. In general we must study each case separately because of the absence of a universal characterization of the dynamics.

The problem of the growth of spatial domains of different phases has been thoroughly studied in the context of the dynamics of phase transitions: a sys-

tem is placed in an unstable state and one considers its relaxation to the state of thermodynamic equilibrium [4, 31]. This process is dominated by the motion of domain walls and other defects. Part of the fascination of the field is that it constitutes a dynamical problem out of equilibrium. Specifically, it corresponds to a transition between two stationary states. On the other hand, in the thermodynamic limit, final equilibrium is never achieved. The reason is that the longest relaxation time diverges with the size of the ordered phase. Instead, the system tries to achieve local equilibrium in increasing length scales. As a consequence, domains of the different ordered phases in equilibrium are formed and they grow in time (coarsening process). Asymptotic domain growth laws, with their underlying physical mechanisms, have been well established. In particular interface dynamics and domain growth depend on whether or not the dynamics is conserved. This in turn affects the coarse-grained equation for the order parameter. A growth law $L(t) \sim t^{1/2}$ holds for dynamics with no conservation law and domains made of equivalent phases. This law follows from the minimization of surface energy, and it has been shown to be robust against the appearance of point defects in systems with a discrete number of phases, three dimensional vortices or chiral domain walls [32, 33, 34]. Other well known growth laws [4] are $L(t) \sim t^{1/3}$ for systems with conserved order parameter [30] and $L(t) \sim t$ for nonconserved dynamics with a metastable phase [35], and also for hydrodynamic systems in spatial dimension $d > 2$ [36].

Domain growth in systems that do not approach a final state of thermodynamic equilibrium is much less understood. For example, the mechanisms underlying a growth law $L(t) \sim t^{1/5}$ in pattern forming systems in which the spatial coupling is non purely diffusive (Swift-Hohenberg equation) [7, 37] have not been clearly identified (see section 1.4.2.c). Other general issues that need to be considered are the role of Hamiltonian vs. dissipative dynamics [8], the effects of nonrelaxational dynamics such as one-dimensional motion of fronts between equivalent states [11], the emergence of localized structures [38, 39, 40, 41], or transverse instabilities of domain walls leading to labyrinthine patterns [42].

Historically there have been two routes in the study of coarsening processes. One route is oriented towards the study of spin discrete models such as the stochastic Ising model; often the Glauber dynamics [43] is studied for the nonconserved case, and the Kawasaki dynamics of spin exchange [44] for the conserved one. The second route is based on the study of time-dependent Ginzburg-Landau equations, which describe the relaxational dynamics of a coarse-grained order parameter. In the classification of Hohenberg and Halperin [45], these equations are called model A (nonconserved) and model B (conserved); case C corresponds to the coupling of a conserved order parameter with a nonconserved one. In general these models contain a noise term that accounts for thermal fluctuations. However, as the thermal noise is irrelevant for quenches well below T_c (critical temperature), the

stochastic terms can be put aside of the equations. In this case the Ginzburg-Landau equations are deterministic and the only randomness is in the initial conditions. This is different from the situation that takes place in some kinetic Ising models, which are stochastic by definition (even at $T = 0$), so the average of any thermodynamic variable is realized not only over initial conditions but also along the dynamical trajectories.

It is often believed that in spatial dimension $d \geq 2$, stochastic and deterministic models belong to the same class of universality (at late times). However, in 1D at $T = 0$, the results are known to be different. We will see in section 1.3.1 that in the one-dimensional Ginzburg-Landau model fronts mutually interact via attractive forces giving rise to a growth law $L(t) \sim \log t$. On the other hand, in the stochastic 1D models, where fronts diffuse and annihilate on collision, the growth law is $L(t) \sim t^{1/2}$ (nonconserved case). In reference [46] the exponents that characterize correlations are studied for both stochastic and deterministic models.

Systems that hold very different dynamics may exhibit the same growth law. One example concerns the classical law $L(t) \sim t^{1/2}$ observed in thermodynamic systems such as order-disorder transitions. The dynamics is purely relaxational and the mechanism for domain coarsening is the minimization of surface tension, which implies a force per unit area, proportional to the mean curvature, acting at each point of the walls. This same growth law applies for the coarsening process of polarization domains in a nonlinear Kerr media [47] (see chapter 4). The system can be modeled by damped and driven coupled nonlinear Schrödinger equations which involve a nonrelaxational dynamics. In this case interface dynamics is also curvature driven like in many thermodynamic systems with nonconserved order parameter. However, the dynamics does not follow the minimization of any obvious energy and the concept of surface tension does not seem to be appropriate to explain interface dynamics in this optical system with diffractive spatial coupling. The Cahn-Hilliard dynamics or model B (see section 1.4.1.c) constitutes another example for which the domain growth mechanism is well-known. This corresponds to a conserved scalar order parameter. The observed growth law $L(t) \sim t^{1/3}$ also appears in optical models such as the Degenerate Optical Parametric Oscillator (DOPO) [9]; the associated dynamics is nonrelaxational and it does not possess a conservation law. For this same system a growth law $t^{1/2}$ has also been reported in a different regime of parameters [48]. It seems that the specific form of the spatial-dependent terms as well as the existence of conservation laws both affect crucially the mechanisms responsible for interface motion, and therefore the growth laws. Other factors that might have influence on domain growth processes are: dimension of defects, whether the model is discrete or continuous, and whether it is deterministic or stochastic.

In Fig. 1.1 we show several stages of the time evolution of domain growth for the model A in 2D. This corresponds to a Ginzburg-Landau equation for a

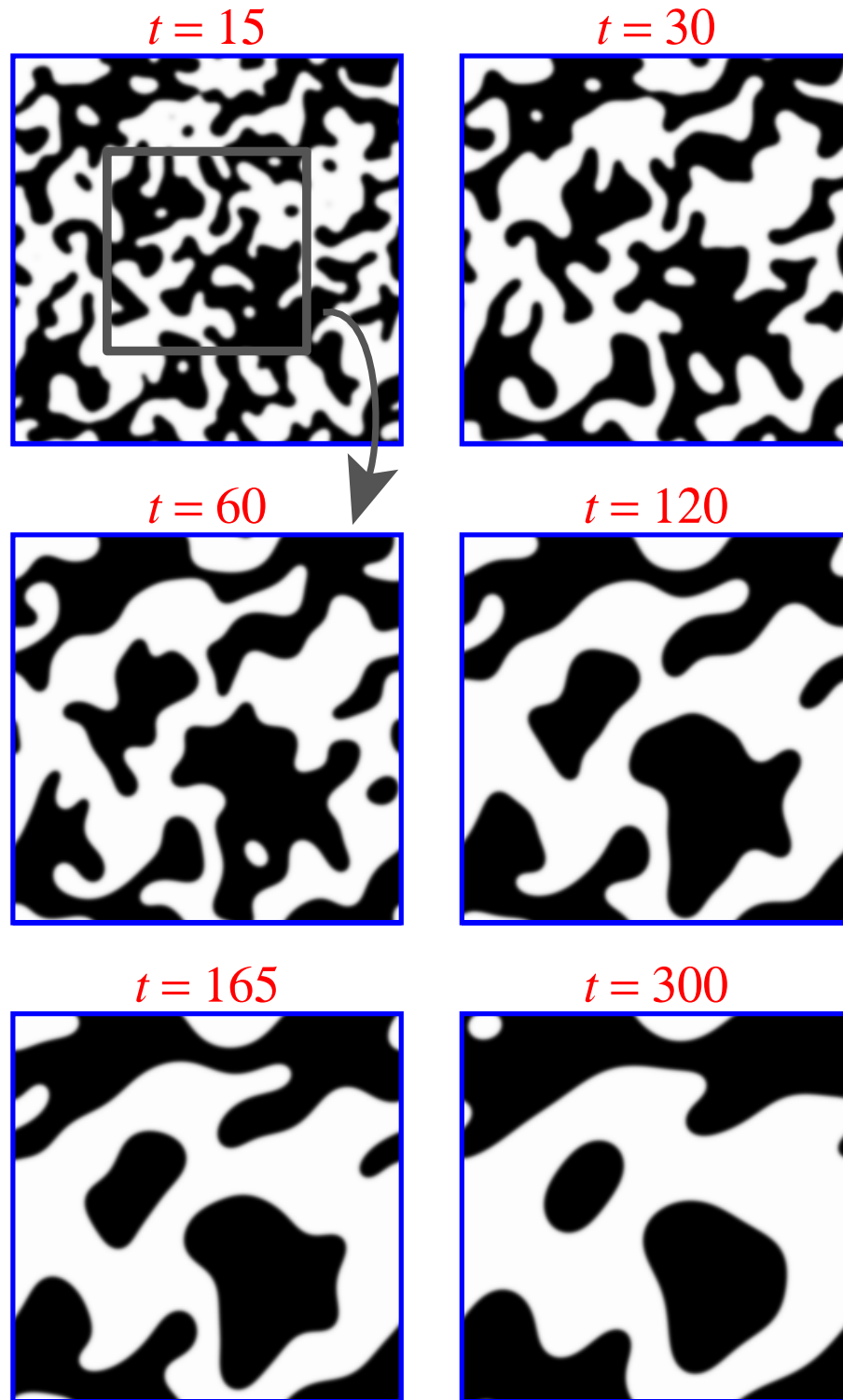


Figure 1.1: Several snapshots corresponding to a numerical simulation of model A dynamics (see section 1.3.1). In the bulk of white (black) regions the field is $+1$ (-1). The structure of domains seems to evolve self-similarly. Since the growth law for this system is $L(t) \sim t^{1/2}$, the structure of domains in a region of size A at time t will be dynamically equivalent to that of a region of size $2A$ at time $4t$ as illustrated in the figure.

nonconserved real order parameter ψ and real coefficients:

$$\partial_t \psi(\mathbf{r}, t) = \nabla^2 \psi + \psi - \psi^3. \quad (1.1)$$

If one looks at the images, it is seen that the domains at long times are statistically similar to those at earlier times, up to a global change of scale. In other words, the coarsening of domains obeys *dynamical scaling*. Other physical systems with self-similar domain growth are spinodal decomposition of binary alloys and phase separation in fluid mixtures.

Briefly, the scaling hypothesis states that, at long times, there exists a characteristic length $L(t)$ such that the domain structure is, in a statistical sense, independent of time when lengths are scaled by $L(t)$. In other words, the dynamical evolution is self-similar and domain structure does not change statistically up to a global scale factor. We will only consider growth processes in the asymptotic dynamics, when well-defined domains have developed in the system. There are some studies of growth phenomena for the early dynamics (p.e. [49]), that correspond to the process of domain creation. It must be stressed that the existence of dynamical scaling has only been proven rigorously for a few models, for instance the one-dimensional Ising model with Glauber dynamics [50]. Nevertheless, there is a clear numerical and experimental evidence of dynamical scaling for many other systems [19, 51, 52].

The chapter is organized as follows. In section 1.2 the term *nonpotential* is explained and a short classification of dissipative dynamical systems is made. In section 1.3 interface dynamics is studied by means of paradigmatic models for both potential and nonpotential systems. In section 1.4 we present some studies on domain growth for systems with different dynamics. Finally we discuss in section 1.5 the issue of dynamical scaling; fundamental ideas are explained and some relevant results for potential systems are presented.

1.2 Potential and Nonpotential Systems

Potential systems are characterized by the existence of a potential function or Lyapunov potential, whose minima characterize the asymptotic state of the system. The system evolves in time approaching the minima of the potential, and once it reaches one of such minima, it remains nearby as long as perturbations on the system are not too large. If \mathcal{F} is a Lyapunov functional (in general, the Lyapunov potential will act on a space of dynamical functions A), it must satisfy the relation:

$$\frac{d\mathcal{F}[A]}{dt} \leq 0, \quad \text{and } \mathcal{F} \text{ bounded from below,} \quad (1.2)$$

which guarantees that the (nondegenerate) minima of \mathcal{F} are stable fixed points of the dynamics. The absolute minimum of \mathcal{F} is often called the *stable* state, while the other minima are referred as *metastable* states. It might occur

that the dynamics is not purely relaxational and a residual dynamics comes into play once the relaxational part has taken the system to a minimum of \mathcal{F} .

In a quite general way, we can write the time evolution equation of dynamical variables describing a dynamical system as [53, 54]

$$\partial_t \mathbf{A}(x, t; \{\alpha\}) = -S \frac{\delta \mathcal{F}}{\delta \mathbf{A}^*} + \mathbf{v}[\mathbf{A}], \quad (1.3)$$

where $\mathbf{A}(x, t; \{\alpha\})$ is the vector of dynamical variables (in general, functions or complex fields of the space coordinates, time and a set of parameters) defined in a Hilbert space \mathcal{H} , \mathcal{F} is a real scalar functional $\mathcal{F}: D \subseteq \mathcal{H} \rightarrow \mathbb{R}$, and $S(\mathbf{A}(x, t; \{\alpha\}))$ is a positive operator¹.

Basing on the decomposition (1.3) we can make a classification of the potential systems as follows [53]:

A) When $\mathbf{v} = 0$, the dynamics is purely relaxational and \mathcal{F} is a Lyapunov functional. The way the system relaxes towards the minima of \mathcal{F} depends on the peculiarities of the self-adjoint operator S . We can distinguish two cases:

A.1) Relaxational gradient potential flow. We include in this class those systems for which the operator S is a multiple of the identity. The system evolves following the lines of maximum slope (steepest descent) of \mathcal{F} , which plays the role of a free energy. A well-known example is the time-dependent Ginzburg-Landau equation (TDGL) for a real field $\psi(\mathbf{x}, t)$ or model A dynamics (without noise):

$$\partial_t \psi = \nabla^2 \psi - V'(\psi), \quad (1.4)$$

where $V(\psi)$ is a function with double-well structure, e.g. $V(\psi) = (1 - \psi^2)^2$. This equation gives the dynamical evolution of a system described by a nonconserved scalar order parameter. It provides a suitable coarse-grained description of the Ising model (continuous version), as well as of binary alloys that undergo an order-disorder transition on cooling through a critical temperature.

It is straightforward to see that eq. (1.4) can be rewritten in the form:

$$\partial_t \psi = -\frac{\delta \mathcal{F}_{\text{GL}}}{\delta \psi}, \quad (1.5)$$

$$\mathcal{F}_{\text{GL}}[\psi] = \int d\mathbf{x} \left[\frac{1}{2} (\nabla \psi)^2 + V(\psi) \right]. \quad (1.6)$$

¹An operator \mathcal{L} defined in a Hilbert space \mathcal{H} (on \mathbb{C}) is said to be positive when $\langle v, \mathcal{L}v \rangle \geq 0$, $\forall v \in \mathcal{H}$, being $\langle \cdot, \cdot \rangle$ the scalar product in \mathcal{H} . Moreover, this definition tacitly demands the hermiticity of \mathcal{L} .

A.2) **Relaxational nongradient potential flow.** In this case the operator S is not multiple of the identity and the dynamics does not follow the lines of maximum slope of \mathcal{F} . The Cahn-Hilliard equation or model B dynamics (without noise) constitutes a well-known example:

$$\partial_t \psi = -\nabla^2 [\nabla^2 \psi - V'(\psi)] = -\nabla^2 \left(-\frac{\delta \mathcal{F}_{\text{GL}}}{\delta \psi} \right). \quad (1.7)$$

This system corresponds to a conserved scalar order parameter and it models, for instance, phase separation in a binary alloy.

B) **Nonrelaxational potential flow.** Now $v \neq 0$ but \mathcal{F} is still a Lyapunov potential. The first term on the rhs of (1.3) represents the relaxational part of the dynamics and the functional $v[A]$ corresponds to the residual dynamics. Most of the models used in equilibrium critical dynamics follow this dynamics. An example for a complex field ψ is:

$$\partial_t \psi = -(1+i) \frac{\delta \mathcal{F}_{\text{GL}}}{\delta \psi^*}. \quad (1.8)$$

It is easy to check that \mathcal{F}_{GL} is a Lyapunov functional:

$$\begin{aligned} \frac{d\mathcal{F}_{\text{GL}}}{dt} &= \int d\mathbf{x} \frac{\delta \mathcal{F}_{\text{GL}}}{\delta \psi^*} \partial_t \psi^* + \text{c.c.} = -(1-i) \int d\mathbf{x} \frac{\delta \mathcal{F}_{\text{GL}}}{\delta \psi^*} \frac{\delta \mathcal{F}_{\text{GL}}}{\delta \psi} + \text{c.c.} \\ &= -2 \int d\mathbf{x} \left| \frac{\delta \mathcal{F}_{\text{GL}}}{\delta \psi} \right|^2 \leq 0. \end{aligned} \quad (1.9)$$

This case corresponds to $S = 1$, $v = -i(\delta \mathcal{F}_{\text{GL}}/\delta \psi^*)$; the dynamics can be decomposed into a relaxational gradient flow plus a term corresponding to a conservative Hamiltonian dynamics.

For the general case (1.3) we have:

$$\begin{aligned} \frac{d\mathcal{F}}{dt} &= \int d\mathbf{x} \frac{\delta \mathcal{F}}{\delta \mathbf{A}^*} \cdot \partial_t \mathbf{A}^* + \text{c.c.} \\ &= - \int d\mathbf{x} \left(\frac{\delta \mathcal{F}}{\delta \mathbf{A}} \right)^* S \left(\frac{\delta \mathcal{F}}{\delta \mathbf{A}} \right) + \int d\mathbf{x} \left(\frac{\delta \mathcal{F}}{\delta \mathbf{A}} \right)^* \cdot v[\mathbf{A}]^* + \text{c.c.} \\ &= -2 \langle \delta_{\mathbf{A}} \mathcal{F}, S \delta_{\mathbf{A}} \mathcal{F} \rangle + 2 \text{Re} \left(\langle v[\mathbf{A}]^*, \delta_{\mathbf{A}} \mathcal{F} \rangle \right), \end{aligned} \quad (1.10)$$

$\langle \cdot, \cdot \rangle$ being a scalar product defined in \mathcal{H} as $\langle \mathbf{f}, \mathbf{g} \rangle = \int d\mathbf{x} \mathbf{f}^* \cdot \mathbf{g}$ and $\delta_{\mathbf{A}} \mathcal{F} \equiv \delta \mathcal{F}/\delta \mathbf{A}$; "c.c." stands for the complex conjugate. Since S is positive self-adjoint, the first term of the last part of (1.10) is less or equal than zero. Hence, a *sufficient* condition for \mathcal{F} to be a Lyapunov functional is

$$\begin{aligned} \text{Re} \left(\langle v[\mathbf{A}]^*, \delta_{\mathbf{A}} \mathcal{F} \rangle \right) &= \int d\mathbf{x} \frac{\delta \mathcal{F}}{\delta \mathbf{A}^*} \cdot v[\mathbf{A}]^* + \text{c.c.} \\ &= \int d\mathbf{x} \frac{\delta \mathcal{F}}{\delta \mathbf{A}^*} \cdot \left[\partial_t \mathbf{A}^* + S \frac{\delta \mathcal{F}}{\delta \mathbf{A}} \right] + \text{c.c.} = 0. \end{aligned} \quad (1.11)$$

The *orthogonality condition* (1.11) can be proved to be equivalent to a Hamilton-Jacobi equation [55]. Its solution is in general cumbersome, although it can be obtained in some cases [56, 57, 58]. If nontrivial solutions for \mathcal{F} of (1.11) are found, we can say that the system is potential. Otherwise, nothing can be guaranteed. In practice, we will say that a system is **nonpotential** when a decomposition of the dynamics in the form (1.3) cannot be found with a nontrivial \mathcal{F} (that is, nonconstant) that decreases in time, although we do not prove that a Lyapunov does not exist. An illustrative example is the complex Ginzburg-Landau equation

$$\partial_t A = (\mu_R + i\mu_I)A + (\gamma_R + i\gamma_I)\nabla^2 A - (\beta_R + i\beta_I)|A|^2 A, \quad (1.12)$$

whose dynamics was classified as nonpotential for a long time (up to limiting cases) until Graham and coworkers, at least in a range of parameters, were able to find an approximate nontrivial solution for (1.11), hence showing that in the aforementioned regime the system dynamics may be characterized in terms of a Lyapunov potential [59, 60]. In reference [53] a detailed discussion about the numerical validity of such approximation can be found.

In potential systems, the Lyapunov functional gives information about global stability. If two fixed points $\bar{\phi}_i(x, t; \{\alpha\})$, $\bar{\phi}_j(x, t; \{\alpha\})$ are such that $\mathcal{F}[\bar{\phi}_i] \leq \mathcal{F}[\bar{\phi}_j]$, we say that $\bar{\phi}_i$ is “more stable” than $\bar{\phi}_j$. This means that if the system is in the state $\bar{\phi}_j$, we can make it switch to the state $\bar{\phi}_i$ by means of a large enough perturbation (e.g. with noise). In a nonpotential system, on the contrary, there are different criteria to determine the relative stability of the asymptotic states. The motion of an interface between two linearly stable solutions of a dynamical system was long ago proposed as a measure of relative stability for a nonpotential system [13]. It might be said then that the most stable state will be the one that tends to overrun the other. However, this is somewhat artificial, and the nonpotential effects must in general be studied for every particular system.

1.3 Interface Dynamics

1.3.1 Relaxational Gradient Flow Systems

Interface dynamics in gradient systems is well-known [4, 10, 29, 61]. By way of illustration, a study of interface motion in the context of the time-dependent Ginzburg-Landau equation (model A dynamics), paradigm of the order-disorder phase transitions, will be presented.

If $\psi(\mathbf{r}, t)$ is the coarse-grained order parameter (concentration, magnetization, etc.) describing the system, its dynamical evolution is given by the equation (1.4):

$$\partial_t \psi = \nabla^2 \psi - V'(\psi), \quad (1.13)$$

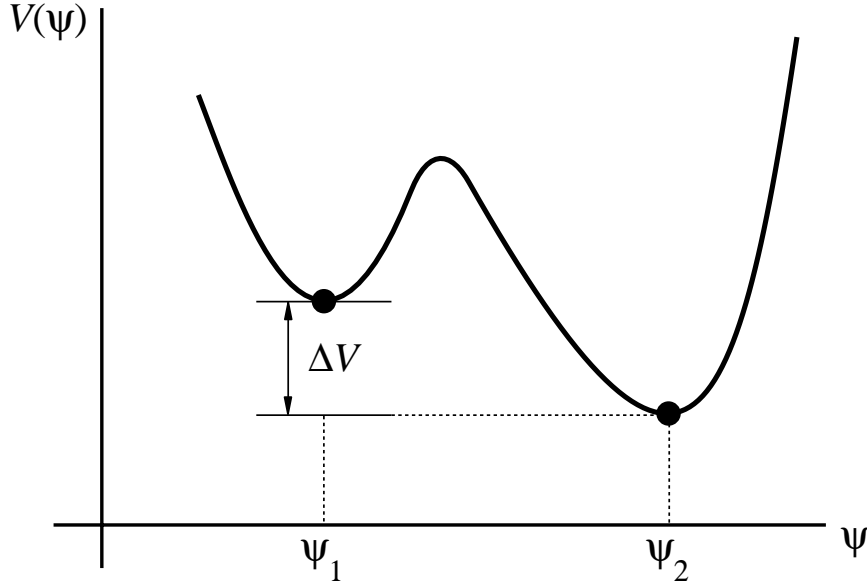


Figure 1.2: Sketch of a potential function with two minima corresponding to the states ψ_1 and ψ_2 .

where $V(\psi)$ is a function with double-well structure as shown in Fig. 1.2. In the following we will accept the possibility of a potential difference between the minima of V due to some external field.

When the system evolves from a random perturbation out of the metastable state ψ_1 , formation of stable droplets of the stable state ψ_2 may be expected. The physical context corresponds to a single transformed region surrounded by the parent phase from which it has nucleated. Assuming that the order parameter does not depend on the orientation, equation (1.13) can be written as:

$$\left(\frac{\partial^2}{\partial r^2} + \frac{d-1}{r} \frac{\partial}{\partial r} \right) \psi(r) - \frac{\partial}{\partial t} \psi = V'(\psi). \quad (1.14)$$

Here $d (\geq 1)$ is the dimensionality. It is useful to make a change of coordinates to a reference system that moves with the interface. Thus, if $R(t)$ is the position of a reference fixed point measured from the origin at time t , we define a new coordinate ξ as:

$$\xi \equiv r - R(t). \quad (1.15)$$

In Fig. 1.3 we show a diagram of an interface with spherical symmetry as well as its profile along the radial direction. Taking into account the equivalences

$$\frac{\partial}{\partial r} \rightarrow \frac{d}{d\xi}, \quad \frac{\partial^2}{\partial r^2} \rightarrow \frac{d^2}{d\xi^2}, \quad \frac{\partial}{\partial t} \rightarrow -\dot{R} \frac{d}{d\xi}, \quad (1.16)$$

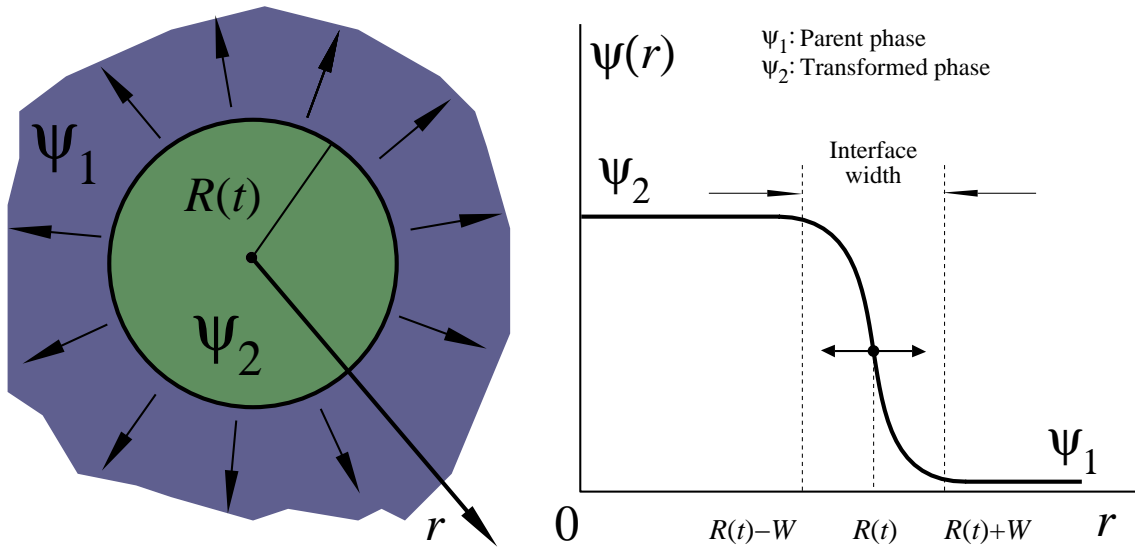


Figure 1.3: Spherical domain and profile along the radial direction of the associated interface, which connects the stable homogeneous states ψ_1 (parent phase) and ψ_2 (transformed phase), and varies significantly in a region of width $2W$. $R(t)$ is the position of a reference fixed point on the interface taken from the origin, and it measures the radius of the domain. Notice that for the nucleation of the phase ψ_2 to occur, it is necessary that $V(\psi_2) < V(\psi_1)$.

the time evolution equation for the interface profile in the moving reference system becomes:

$$\tilde{\psi}'' + \left(\frac{d-1}{\xi+R} + \dot{R} \right) \tilde{\psi}' - V'(\tilde{\psi}) = 0, \quad (1.17)$$

where $\tilde{\psi} = \tilde{\psi}(\xi) \equiv \psi(r, t)$. The primes indicate derivative of the function with respect to its argument. Multiplying (1.17) by $\tilde{\psi}'$ and integrating along the interface, we are left with:

$$0 = \underbrace{\int_{-\infty}^{\infty} d\xi \frac{1}{2} (\tilde{\psi}'(\xi)^2)'}_{I_1} + \underbrace{\int_{-\infty}^{\infty} d\xi \left(\frac{d-1}{\xi+R} + \dot{R} \right) \tilde{\psi}'(\xi)^2}_{I_2} - \underbrace{\int_{-\infty}^{\infty} d\xi V'(\tilde{\psi}) \tilde{\psi}'(\xi)}_{I_3}. \quad (1.18)$$

The integrals I_1 , I_2 and I_3 will be computed next separately. On the one hand, we have

$$I_1 = \frac{1}{2} \left[\tilde{\psi}'(+\infty)^2 - \tilde{\psi}'(-\infty)^2 \right] = 0, \quad (1.19)$$

because $\tilde{\psi}' = 0$ far away from the interface. On the other hand:

$$I_3 = V(\psi_1) - V(\psi_2) \equiv \Delta V, \quad (1.20)$$

where ΔV is the potential difference between the two asymptotic homogeneous states of the interface. Finally, we have

$$I_2 = \int_{-\infty}^{\infty} d\xi \left(\frac{d-1}{\xi+R} + \dot{R} \right) \tilde{\psi}'(\xi)^2 = \lim_{W \rightarrow \infty} \int_{-W}^W d\xi \left(\frac{d-1}{\xi+R} + \dot{R} \right) \tilde{\psi}'(\xi)^2 \quad (1.21)$$

$$\underset{\substack{\approx \\ \downarrow \\ R \gg W}}{\approx} \left(\frac{d-1}{R} + \dot{R} \right) \lim_{W \rightarrow \infty} \int_{-W}^W d\xi \tilde{\psi}'(\xi)^2 = \left(\frac{d-1}{R} + \dot{R} \right) \int_{-\infty}^{\infty} d\xi \tilde{\psi}'(\xi)^2.$$

Gathering all the calculations, we arrive at the equation that gives the time evolution of the radius of the stable phase (transformed phase):

$$\frac{d-1}{R} + \dot{R} = \frac{\Delta V}{\int_{-\infty}^{\infty} d\xi \tilde{\psi}'(\xi)^2} \equiv v_p. \quad (1.22)$$

Hence, the quantity $(d-1)/R + \dot{R}$ is a constant of motion and it is equal to the *asymptotic velocity* of the interface $v_p = \dot{R}(t \rightarrow \infty)$. According to equation (1.22), this velocity is proportional to the *potential difference* between the asymptotic states, which correspond to the minima of V .

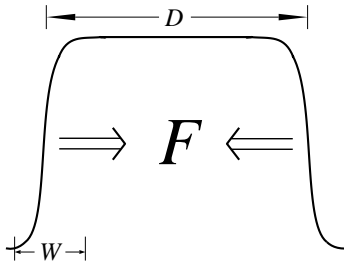
At this point, it is convenient to make a distinction between one- and multidimensional systems, since the underlying physics is different depending on the dimensionality.

d=1

In this case, the interface velocity is given by

$$v_{d=1} \equiv \dot{R} = v_p \propto \Delta V, \quad (1.23)$$

and, as consequence, if the two minima are equivalent ($\Delta V = 0$), the (isolated) front remains at rest. Otherwise it propagates at a constant velocity, proportional to the potential difference between the asymptotic states. When several fronts are present in the system and $\Delta V = 0$, they move due to mutual interactions. A domain delimited by two fronts tends to contract because of short-range *attractive* forces.



The interaction force between two one-dimensional fronts (kinks) of opposite topological charge is given by [38, 62]

$$F \propto \exp\left(-\frac{D}{W}\right), \quad (1.24)$$

where D is the interkink distance, and W is the kink width, as shown in the previous figure. Expression (1.24) is only valid in the limit $D \gg W$ (“dilute-defects gas” approximation), that is, when the interkink distance is much

greater than their width. This kind of interaction leads to a logarithmic variation with time of the domain size [38].

Let us consider a flat domain wall $\psi_0(x)$ connecting two equivalent states $\psi = \psi_1$ and $\psi = \psi_2$. Then the excess of free energy per unit area associated to the presence of the wall, which is nothing but the *surface tension*, is

$$\sigma = \mathcal{F}_{\text{GL}}[\psi_0] - \mathcal{F}_{\text{GL}}[\psi_1] = \int dx \left[\frac{1}{2} \left(\frac{\partial \psi_0}{\partial x} \right)^2 + V(\psi_0) - V(\psi_1) \right], \quad (1.25)$$

where x is the normal coordinate to the interface, and ψ_0 its profile in equilibrium. The energy conservation (kinetic + “potential”, in the one particle scheme) is written as $\frac{1}{2}(\partial\psi_0/\partial x)^2 - V(\psi_0) = -V(\psi_1)$. Consequently

$$\sigma = \int dx \left(\frac{\partial \psi_0}{\partial x} \right)^2. \quad (1.26)$$

If the states are not equivalent, the planar front velocity [see (1.22)] can be written as

$$v_p = \frac{\Delta V}{\int d\xi \psi'(\xi)^2} \approx \sigma^{-1} \Delta V, \quad (1.27)$$

where the field profile ψ has been replaced by its value at $v_p = 0$ to the lowest order in v_p . Therefore, the surface tension plays the role of an *inverse mobility*. Notice that in this case of nonequivalence the asymptotic velocity depends on the interface profile and therefore on the details of the potential. A study of front motion based on energetic arguments can be found in reference [19].

$d \geq 2$

The interface velocity is now:

$$v_{d \geq 2} \equiv \dot{R} = -\frac{d-1}{R} + v_p = -\frac{d-1}{R} + v_{d=1}. \quad (1.28)$$

If the states are equivalent ($\Delta V = 0$), then the time evolution of the domain radius becomes:

$$\dot{R}(t) = -\frac{d-1}{R(t)}. \quad (1.29)$$

Actually, equation (1.29) is a particular case of a more general law found by Allen and Cahn [29]. This law states that interfaces move following the normal direction to each point with a velocity proportional to the mean local curvature (sum of the principal curvatures):

$$v_n(\mathbf{r}, t) = -\kappa(\mathbf{r}, t), \quad \forall \mathbf{r} \text{ on the interface.} \quad (1.30)$$

Hence, when the asymptotic states are equivalent, front motion is determined (for nonconserved fields) purely by the local curvature. The detailed shape of the potential has influence on the front profiles, but it has no effect on their dynamics (at long times). For spherical domains, the curvature is $(d-1)/R$ and (1.30) reduces to (1.29). In contrast to what happens in one dimension, an interface may move in $d > 1$ despite joining equivalent states. Just as in one dimension, there also exist interaction forces between domain walls, but their effect is negligible as compared with the curvature effect.

One of the consequences of (1.30) is that a closed domain always tends to collapse, since it evolves by reducing the curvature of the surrounding interface. In the case with spherical symmetry, integration of (1.29) gives

$$R(t) = [2(t_0 - t) + R_0^2]^{1/2}, \quad R_0 = R(t_0). \quad (1.31)$$

Notice that $R(t)^2 \sim t$, which gives the domain growth law for this sort of systems. We will elaborate on this in section 1.4.1.b.

It is easy to see that the order parameter saturates exponentially far away from the walls. It follows then that the excess of energy is located on the interfaces themselves, and that the driving force for domain growth is the curvature, since the system energy can only diminish through a reduction in the total wall area. As a consequence of this area reduction, the average domain size grows with time and coarsening takes place. The existence of a surface tension entails a force per unit area, proportional to the mean curvature, acting at each point of the interface. For model A dynamics, this force induces front motion with a velocity proportional to the local curvature.

When the planar front velocity is greater than zero, the bulk driving force due to a nonzero potential difference tends to expand a drop, contrary to the shrinking effect of the curvature. It turns out that there exists a *critical radius* of the drop R_c (for spherical domains) such that any drop with a greater radius will grow, whereas any smaller drop will contract until extinction. In the light of the equation (1.22), it is clear that the critical radius is given by

$$R_c = (d-1)v_p^{-1}. \quad (1.32)$$

In general, we will talk of a critical curvature $\kappa_c = v_p$ above which the front does not propagate (outwards). When $v_p \leq 0$, the planar front velocity helps to contract the drop, in the same way as the curvature effect. In this case, any drop will decrease regardless of its initial radius (actually this is true for any closed domain not necessarily spherical). In relation to Fig. 1.2, the case $v_p < 0$ corresponds to a domain of ψ_1 embedded in a sea of ψ_2 , and $v_p > 0$ to the reciprocal situation. In Fig. 1.4 we present plots of the time evolution of the radius and interface velocity for a spherical domain in 2D, as result of the integration of (1.22) with $v_p \geq 0$. Plot (a) shows the radius as a function of time when $v_p > 0$ for an initial radius greater and smaller than the critical one $R_c = v_p^{-1}$; a third curve corresponds to the case without drifting ($v_p = 0$).

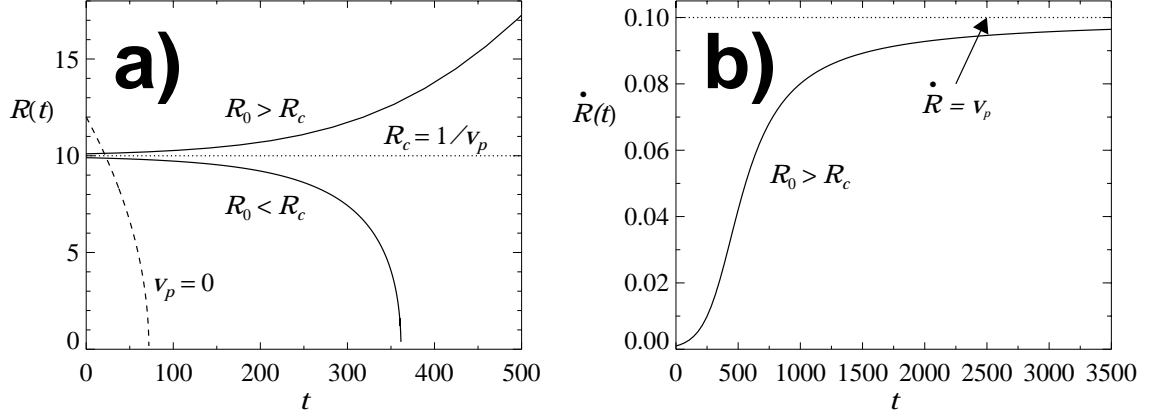


Figure 1.4: (a) Time evolution of the radius of a spherical domain in 2D. Two cases are considered: 1) $v_p = 0.1$, for $R_0 > R_c$ and $R_0 < R_c$, and 2) $v_p = 0$. (b) Interface velocity profile for $R_0 > R_c$.

When $R_0 > R_c$, the domain grows with an increasing interface velocity tending to v_p asymptotically [plot (b)]. Otherwise, if $R_0 < R_c$, the drop contracts with increasing velocity, since the curvature grows with time. In the case of nonequivalent states ($\Delta V \neq 0$), domain growth is dominated at long times by the contribution of the planar front velocity v_p leading to a growth law $L(t) \sim t$ [35].

1.3.2 Nonrelaxational Potential Flow Systems

Following reference [63], we present in this section some aspects concerning interface motion for *nonrelaxational potential flow systems* (see page 7). Some of the methods we will explain are directly applicable to nonpotential systems, as it will be made clear later.

The authors of [63] consider fronts that connect symmetric states in a *one-dimensional* system. They show that the problem can be analyzed in terms of a free energy that takes the same value at the asymptotic states ($x \rightarrow \pm\infty$). Then front motion can be understood as a residual dynamics in an extended attractor on which the free energy takes a constant value.

We first consider a gradient system:

$$\partial_t A_\mu(x, t) = B_\mu^{(0)}(\mathbf{A}, \partial_x) = -\frac{1}{2} \frac{\delta \mathcal{F}_0}{\delta A_\mu}, \quad \mu = 1, \dots, n, \quad (1.33)$$

where \mathcal{F}_0 is a functional of the real field $A(x, t)$. The system described by (1.33) is assumed to have stable front solutions of the form $A_0(x)$ that join two stable homogeneous solutions. Therefore, we have $\delta \mathcal{F}_0 / \delta A_\mu|_{A_0} = 0$. Let us perturb the system (1.33)

$$\partial_t A_\mu(x, t) = B_\mu^{(0)}(\mathbf{A}, \partial_x) + \varepsilon B_\mu^{(1)}(\mathbf{A}, \partial_x). \quad (1.34)$$

Equations (1.33) and (1.34) are supposed to have the following symmetry properties:

(SP1) Invariance under a certain group of symmetry G , and the symmetries S , that connect stable homogeneous solutions of (1.33), are elements of G .

(SP2) Spatio-temporal translation symmetry: $x \rightarrow x + x_0, t \rightarrow t + t_0$.

(SP3) Invariance under parity: $x \rightarrow -x$.

It is clear that (1.34) is not a gradient system anymore, but it can be recast as

$$\partial_t A_\mu(x, t) = -\frac{1}{2} \frac{\delta \mathcal{F}}{\delta A_\mu} + R_\mu, \quad (1.35)$$

$$R_\mu = \frac{1}{2} \frac{\delta \mathcal{F}}{\delta A_\mu} + B_\mu^{(0)}(\mathbf{A}, \partial_x) + \varepsilon B_\mu^{(1)}(\mathbf{A}, \partial_x). \quad (1.36)$$

Imposing the orthogonality condition

$$\int dx R_\mu \frac{\delta \mathcal{F}}{\delta A_\mu} = 0, \quad (1.37)$$

the functional \mathcal{F} is a Lyapunov potential and the dynamics of system (1.34) is a nonrelaxational potential flow, where R_μ is now the residual part. It can be proved that, to first order in ε , the potential \mathcal{F} can be written as $\mathcal{F} = \mathcal{F}_0 + \varepsilon \mathcal{F}_1$, where \mathcal{F}_0 is that of equation (1.33).

Let $A_1(x) = A_0(x) + \varepsilon \delta A_0(x)$ be a stationary solution of (1.34), which is in turn an extremum of \mathcal{F} ; A_0 will be assumed to be an extremum of \mathcal{F}_0 . Then we have:

$$0 = \left. \frac{\delta \mathcal{F}}{\delta A_\mu} \right|_{A_1} = \left. \frac{\delta \mathcal{F}_0}{\delta A_\mu} \right|_{A_1} + \varepsilon \left. \frac{\delta \mathcal{F}_1}{\delta A_\mu} \right|_{A_1}. \quad (1.38)$$

To leading order in ε , we have the expansions:

$$\left. \frac{\delta \mathcal{F}_0}{\delta A_\mu} \right|_{A_1} = \underbrace{\left. \frac{\delta \mathcal{F}_0}{\delta A_\mu} \right|_{A_0}}_{=0} + \sum_\nu \frac{\delta}{\delta A_\nu} \left(\left. \frac{\delta \mathcal{F}_0}{\delta A_\mu} \right|_{A_0} \right) \delta A_{0\nu} + O(\varepsilon^2), \quad (1.39)$$

$$\left. \frac{\delta \mathcal{F}_1}{\delta A_\mu} \right|_{A_1} = \left. \frac{\delta \mathcal{F}_1}{\delta A_\mu} \right|_{A_0} + O(\varepsilon). \quad (1.40)$$

Hence, to first order in ε , (1.38) leads to the following linear equation for δA_0 :

$$\varepsilon (\mathcal{L} \delta A_0)_\mu = \left. \frac{\delta \mathcal{F}_0}{\delta A_\mu} \right|_{A_1} = -\varepsilon \left. \frac{\delta \mathcal{F}_1}{\delta A_\mu} \right|_{A_1} = -\varepsilon \left. \frac{\delta \mathcal{F}_1}{\delta A_\mu} \right|_{A_0}, \quad (1.41)$$

with $\mathcal{L}_{\mu\nu} = (\delta/\delta A_\nu)(\delta\mathcal{F}_0/\delta A_\mu)|_{\mathbf{A}_0}$.

First, we point out that the operator \mathcal{L} is self-adjoint and, because of the translational invariance property (SP2), its kernel is the set of functions $\{\partial_x A_{0\mu}\}$. On the other hand, it can be shown that the solvability condition for (1.41) is always satisfied. Therefore $A_1(x)$ always exists and once again, due to the translational invariance, if $A_1(x)$ is an extremum of the potential, the function $A_1(x-s)$, where s is a parameter, will be also an extremum [the family of functions $\{A_1(x-s), s \in \mathbb{R}\}$ constitutes an extended attractor of the perturbed problem]. It follows that the functions A_1 are tied to the residual dynamics through the relation:

$$\partial_t A_{1\mu}(x-s(t)) = R_\mu[A_1(x-s(t))]. \quad (1.42)$$

If $R_\mu[A_1(x-s(t))]$ is different from zero, eq. (1.42) has sense only if s is a function of time and the wall moves. As $R_\mu = O(\varepsilon)$, it is expected that $\dot{s}(t) = O(\varepsilon)$. If we call $y \equiv x-s$, we get

$$\begin{aligned} -\dot{s} \partial_y A_{1\mu}(y) &= R_\mu(\mathbf{A}_0(y) + \varepsilon \delta \mathbf{A}_0(y)), \\ -\dot{s}(\partial_y A_{0\mu} + \varepsilon \partial_y \delta A_{0\mu}) &= R_\mu(\mathbf{A}_0(\mu)) + \varepsilon \frac{\delta R_\mu}{\delta A_\nu} \delta A_{0\nu} + \dots, \end{aligned}$$

and to first order, it turns out:

$$\dot{s} \partial_y A_{0\mu} = R_\mu(\mathbf{A}_0(y)), \quad (1.43)$$

where, by virtue of (1.33) and (1.36)

$$R_\mu(\mathbf{A}_0(y)) = \varepsilon \left[\frac{1}{2} \frac{\delta \mathcal{F}_1}{\delta A_\mu} \Big|_{\mathbf{A}_0} + B_\mu^{(1)}(\mathbf{A}_0) \right]. \quad (1.44)$$

Following the method of reference [64], it is possible to calculate \mathcal{F}_1 near the attractor and with it the front velocity:

$$\dot{s}(t) = -\varepsilon \frac{\langle \mathbf{B}^{(1)}(\mathbf{A}_0), \partial_y \mathbf{A}_0 \rangle}{\langle \partial_y \mathbf{A}_0, \partial_y \mathbf{A}_0 \rangle} + O(\varepsilon^2). \quad (1.45)$$

An important consequence of what we have said so far is that if the residual part R_μ is zero on the attractor, an interface will not move; the dynamics of the system is purely relaxational and the role of the potential is just the formation of the interfaces. A nonzero residual dynamics will cause a front to move, up to a symmetry that cancels the numerator of (1.45).

The above derivation of (1.45) is interesting because it makes clear the role of residual dynamics in front motion. However, a more general derivation that does not rely on the form (1.35) of the equation of motion can be given. If $A_0(x)$ is the front solution to the lowest order in ε , we assume that a front

solution of the perturbed system (1.34) is given by $A_1(y) = A_0(y) + \varepsilon \delta A_0(y)$ with $y = x - ct$, $c = O(\varepsilon)$. Upon insertion of this solution into (1.34), it yields, to order $O(\varepsilon^0)$:

$$0 = B_\mu^{(0)}(\mathbf{A}_0), \quad (1.46)$$

and to order $O(\varepsilon^1)$:

$$-c \partial_y A_{0\mu} = \varepsilon \frac{\delta B_\mu^{(0)}}{\delta \mathbf{A}} \Big|_{\mathbf{A}_0} \delta \mathbf{A}_0 + \varepsilon B_\mu^{(1)}(\mathbf{A}_0). \quad (1.47)$$

Equation (1.47) can be rewritten as:

$$\frac{\delta B_\mu^{(0)}}{\delta \mathbf{A}} \Big|_{\mathbf{A}_0} \delta \mathbf{A}_0 = -\frac{c}{\varepsilon} \partial_y A_{0\mu} - B_\mu^{(1)}(\mathbf{A}_0). \quad (1.48)$$

The condition for the previous linear equation to be solvable, or in other words, the condition for the perturbed system (1.34) to have a front solution of the form $A_1(y)$, is that the rhs on (1.48) must be orthogonal to the nullspace of the adjoint of the linear operator $\mathcal{L} \equiv \delta B_\mu^{(0)} / \delta \mathbf{A} \Big|_{\mathbf{A}_0}$. If \mathcal{L} is self-adjoint, then it turns out that

$$\ker(\mathcal{L}) = \{\partial_y \mathbf{A}_0\}, \quad (1.49)$$

as it is clear just by taking the derivative of (1.46) with respect to y . Hence:

$$\left\langle -\frac{c}{\varepsilon} \partial_y \mathbf{A}_0 - \mathbf{B}^{(1)}(\mathbf{A}_0), \partial_y \mathbf{A}_0 \right\rangle = 0. \quad (1.50)$$

Finally finding c from (1.50) we obtain (1.45). We want to stress the fact that the method just explained does not depend on whether or not $R_{\nu\mu}$ satisfies the orthogonality condition (1.37). Even if the orthogonality condition is not satisfied, we can take a perturbed gradient system and apply the previous method to obtain the interface velocity. This will be used in the next section, where the front velocity for a nonpotential system will be obtained.

A final remark on symmetry properties is important. Let $A_0^{(1)}$ be a stable front solution of (1.33) and let $A_0^{(2)} = S A_0^{(1)}$ be the new solution obtained by transforming the former by the symmetry S belonging to the group of symmetry G , which leaves the dynamical evolution equation invariant. Since

$$S_{\mu\nu} B_\nu^{(1)}(\mathbf{A}_0) = B_\mu^{(1)}(\mathbf{A}_0), \quad (1.51)$$

both front move at the same velocity according to (1.45) (S preserves scalar products). On the other hand, the invariance under parity generates a new front solution $A_0^{(3)}(x) = A_0^{(1)}(-x)$ moving in opposite direction. Summing up:

$$\dot{s}(\mathbf{A}_0^{(1)}) = \dot{s}(\mathbf{A}_0^{(2)}) = -\dot{s}(\mathbf{A}_0^{(3)}). \quad (1.52)$$

If $A_0^{(2)} = A_0^{(3)}$, then $\dot{s}(A_0^{(1)}) = 0$, that is, the front does not move. In other words, if a symmetry such that $SA_0^{(1)}(x) = A_0^{(1)}(-x)$ exists, then the front is static, even if the residual part is different from zero.

It is interesting to observe that the wall motion may appear as the counterpart of the motion in a limit cycle after a Hopf bifurcation. Let us consider an equation of the form

$$\partial_t A = (\alpha + i\beta)A - A|A|^2, \quad (1.53)$$

which is a gradient flow if $\beta = 0$. When $\beta \neq 0$ it is possible to cast the system into the form:

$$\dot{X} = -\frac{1}{2} \frac{\partial \mathcal{F}_0}{\partial X} + R_X, \quad (1.54)$$

$$\dot{Y} = -\frac{1}{2} \frac{\partial \mathcal{F}_0}{\partial Y} + R_Y, \quad (1.55)$$

with $A \equiv X + iY$, $\mathcal{F}_0 = -\alpha(X^2 + Y^2) + \frac{1}{2}(X^2 + Y^2)^2$, $R_X = -\beta Y$, $R_Y = \beta X$. The orthogonality condition $R_X(\partial \mathcal{F}_0 / \partial X) + R_Y(\partial \mathcal{F}_0 / \partial Y) = 0$ is automatically satisfied in this case, so $\mathcal{F}_1 = 0$. Using polar coordinates $A = re^{i\theta}$, it turns out that $r = \sqrt{\alpha}$ on the attractor ($\partial \mathcal{F}_0 / \partial X = \partial \mathcal{F}_0 / \partial Y = 0$), and the velocity is $\dot{s} = \dot{\theta} = \beta$. Notice that R_X and R_Y can be eliminated by means of a change to a reference system $A \rightarrow Ae^{-i\beta t}$ that incorporates the motion in the attractor.

1.3.3 Nonpotential Systems

The complex Ginzburg-Landau equation (CGLE), one of the paradigms of spatio-temporal chaos, constitutes an example of nonpotential system where front motion has been studied [11, 14, 15]. The CGLE is an equation for the spatio-temporal evolution of the envelope amplitude (slowly varying in space and time) of the oscillations of a system near a Hopf bifurcation. We will restrict ourselves to the CGLE in 1D parametrically forced at twice the natural frequency. This situation gives a particularly clear example of nonpotential motion of a domain wall between equivalent states. We stress, however, as already said in section 1.2, that an approximate Lyapunov functional for the CGLE without forcing has been found in a certain range of parameters [53, 59, 60].

The evolution equation for the complex order parameter A of the Hopf bifurcation is:

$$\partial_t A = (\mu + i\nu)A + (1 + i\alpha)\nabla^2 A - (1 + i\beta)|A|^2 A + \gamma A^*. \quad (1.56)$$

All the parameters are real and $\gamma > 0$ is the forcing amplitude. When the parameters α , β and ν are zero, equation (1.56) can be written in gradient

form:

$$\partial_t A = -\frac{\delta \mathcal{F}}{\delta A^*}, \quad (1.57)$$

$$\mathcal{F} = \int dx \left\{ -\mu |A|^2 + |\nabla A|^2 + \frac{1}{2} |A|^4 - \frac{1}{2} \gamma (A^2 + A^{*2}) \right\}. \quad (1.58)$$

In this limit, equation (1.56) possesses stable front like stable solutions that connect linearly stable homogeneous solutions ($\text{Re } A = \pm(\mu + \gamma)^{1/2}$, $\text{Im } A = 0$). These are:

Ising wall:

$$X_I = \pm(\mu + \gamma)^{1/2} \tanh \left\{ \left[\frac{1}{2}(\mu + \gamma) \right]^{1/2} x \right\}, \quad Y_I = 0, \quad (1.59)$$

Bloch wall:

$$X_B = \pm(\mu + \gamma)^{1/2} \tanh [(2\gamma)^{1/2} x], \quad Y_B = \pm \frac{(\mu - 3\gamma)^{1/2}}{\cosh [(2\gamma)^{1/2} x]}, \quad (1.60)$$

with $X \equiv \text{Re } A$ and $Y \equiv \text{Im } A$. Notice that both solutions have well-defined parity. The Ising wall is stable for $\gamma > \gamma_c = \mu/3$, and the Bloch one for $\gamma < \gamma_c$. Therefore, for $\gamma = \gamma_c$ an interchange of stability between both solutions occurs. On the other hand, the phase $\phi = \arctan(Y/X)$ changes continuously from $-\pi$ to π across a Bloch front, while it changes abruptly in the case of an Ising front.

In the potential limit ($\alpha = \beta = \nu = 0$), both fronts are stationary since the asymptotic states are equally stable. But, what happens in the nonpotential situation? A perturbative approach can be carried out when the parameters ν , α and β are small. One then looks for a front solution in the form:

$$A(x - s(t)) = A_0(x - s(t)) + \varepsilon \delta A_0(x - s(t)) + O(\varepsilon^2), \quad (1.61)$$

where A_0 is the front solution of the potential problem. The first solvability condition for the existence of a stationary solution $A_1(x - s(t))$ of (1.56) leads, in the case of Bloch walls, to obtain the *interface velocity* $\dot{s}(t)$. To leading order in perturbation we are led to expression (1.45) with the identifications:

$$\mathbf{B}^{(1)}(\mathbf{A}_0) \rightarrow \begin{bmatrix} -\tilde{\nu} Y_0' - \tilde{\alpha} Y_0'' + (X_0^2 + Y_0^2) \tilde{\beta} Y_0' \\ \tilde{\nu} X_0' + \tilde{\alpha} X_0'' - (X_0^2 + Y_0^2) \tilde{\beta} X_0' \end{bmatrix}, \quad \mathbf{A}_0 \rightarrow \begin{bmatrix} X_0 \\ Y_0 \end{bmatrix},$$

where $\{\alpha, \beta, \nu\} = O(\varepsilon)$ and $\tilde{\alpha} = \alpha/\varepsilon$, $\tilde{\beta} = \beta/\varepsilon$, $\tilde{\nu} = \nu/\varepsilon$. The primes indicate derivative of the function with respect to its argument $y \equiv x - s(t)$. In the case of Ising walls, $Y_0 = 0$ ($\Rightarrow \mathbf{B}^{(1)}(\mathbf{A}_0) = \mathbf{0}$) and $\dot{s} = 0$. Hence, there exists

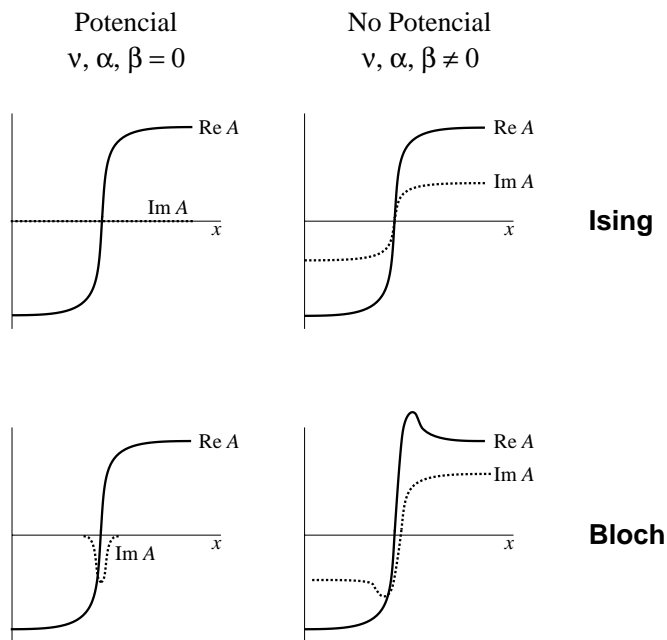


Figure 1.5: Diagram of the Ising and Bloch fronts in the potential and nonpotential cases. Notice the parity symmetry breaking in the Bloch solution due to nonpotential effects. This symmetry breaking is responsible for the motion of the front.

a nonequilibrium analog of the static Ising wall. For the Bloch walls, the interface velocity turns out to be:

$$\dot{s}(t) = \chi \left(\frac{\mu + \gamma}{2\gamma} \right)^{1/2} \frac{3\pi}{2(3\mu - \gamma)} [-\nu + \beta\mu + (\alpha - \beta)\gamma], \quad (1.62)$$

where $\chi = \pm\sqrt{\mu - 3\gamma}$, the extremal value of $Y = \text{Im } A$ [$\chi = Y(0)$], is the “chiral parameter”. To leading order, the wall velocity (1.62) is proportional to the nonpotential coefficients $\{\alpha, \beta, \nu\}$ and its sign depends on that of the chiral parameter. A localized breaking of parity, due to that of chirality, occurs at the interface and leads to its motion (see Fig. 1.5).

When ε is small and $\gamma > \gamma_c$, there are Ising walls between states of opposite phase. For $\gamma < \gamma_c$, these domain walls convert into Bloch walls. The transition occurs at the forcing value for which the wall starts moving. For α, β and ν small, the value of γ_c is close to $\mu/3$.

Bloch-wall motion is rather surprising since the interface separates symmetric states, which would correspond to states of the same free energy in an equilibrium problem. This motion is due to nonpotential effects, which show up at the core of the wall.

1.3.4 Oscillatory tails in front profiles

Up to now, we have dealt with monotonic front profiles. We want to study in this section the influence on interface dynamics of fronts whose profiles show damped oscillatory tails. The contents of this section apply to both potential and nonpotential systems. When we studied interface dynamics in the context of the model A in section 1.3, we said that the detailed shape of the interfaces

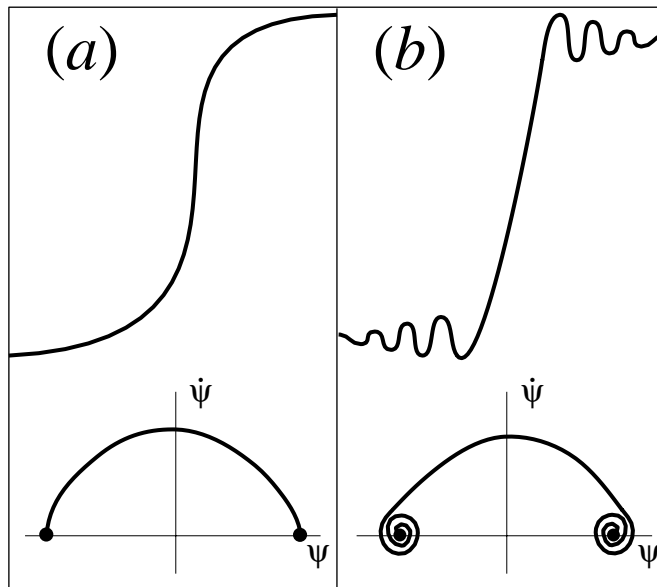


Figure 1.6: (a) Profile of a monotonic front and corresponding heteroclinic orbit in phase space, and (b) *idem* for a front showing spatial oscillations.

does not affect the dynamics of domains at long times in a situation of bistability. This may be no longer true when the front profiles show spatial oscillations (see Fig. 1.6). It is known that the interaction between nonmonotonic fronts can involve both attractive and *repulsive* forces [38]. Some physical systems holding oscillating interfaces are studied in [22, 47, 65].

In 1D, oscillating domain walls with opposite topological charge may not annihilate each other, but they may locate at a certain distance when an equilibrium of forces occurs. In the case of multifront configurations, the system may lock in an array of alternating kink and antikink solutions. These frozen states are in general different for each particular realization of the dynamics (initial conditions). This is a manifestation of spatial chaos. The nature of this spatial chaos may be associated with the random pinning of defects with exponentially damped oscillatory interactions. Therefore, unlike what happens with monotonic front profiles (e.g., for model A), coarsening in 1D can be inhibited by this effect.

In higher dimensions, and for systems with short-range interactions, the interaction force between walls is negligible as compared with other effects, for instance the curvature driving force. However, when the interfaces are very close to each other, the oscillatory tails might cause them to be mutually repelling, thus stopping the shrinking of a small domain. The repulsive forces induced by spatial oscillations may lead to the stabilization of a closed domain of a stable phase at a certain radius. The result is a *localized structure*. The oscillatory tails have been seen to be a necessary ingredient (but not sufficient) for the formation of localized structures in bistable systems [22]. The localized structure is formed when the force that tends to shrink the domain (e.g., a curvature driving force) is counterbalanced by the self-interaction repulsive forces of the wall that surrounds the domain. The oscillatory tails also play an important role in the formation of labyrinthine

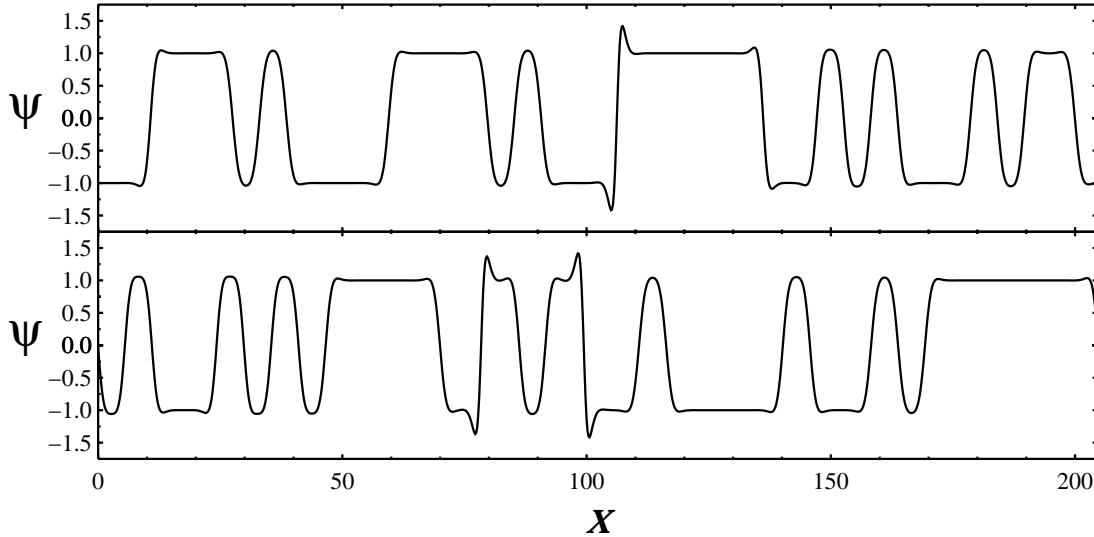


Figure 1.7: Two frozen configurations corresponding to system (1.66). The initial conditions were a random perturbation of the unstable state $\psi = 0$.

patterns [42, 47, 66, 67]. In chapter 4 a nonlinear optical system that supports localized structures and labyrinthine patterns in a regime of bistability is studied.

The existence of oscillatory tails can be determined by means of a spatial linear stability analysis of the homogeneous asymptotic solutions. A nonvanishing imaginary part of any of the resulting eigenvalues reveals the existence of oscillatory tails in the front profiles; the real part has to do with the damping rate of the oscillations. Let us see an example.

For model A, the stationary solutions satisfy

$$\partial_{xx}\psi - V'(\psi) = 0. \quad (1.63)$$

Let us call ψ_1 and ψ_2 the minima of the potential V . Writing $\psi = \psi_i + \varepsilon e^{\lambda x}$, we get, upon insertion into (1.63),

$$\lambda^2 = V''(\psi_i), \quad i = 1, 2. \quad (1.64)$$

Since the ψ_i are minima of V , $V''(\psi_i) > 0$, $i = 1, 2$, so that the eigenvalues λ given by (1.64) are real. Therefore, the fronts are monotonic. For the potential $V(\psi) = (1 - \psi^2)^2$, the explicit expression for the domain walls is:

$$\psi(x) = \pm \tanh[\sqrt{2}(x - x_0)], \quad (1.65)$$

where x_0 is any real number; this reflects the translational invariance of the system. Let us consider now a generalization of model A, the extended Fisher-Kolmogorov equation [68]:

$$\partial_t \psi = \partial_{xx}\psi - \partial_{xxx}\psi - V'(\psi). \quad (1.66)$$

This equation is frequently used as a model system for the study of pattern formation from an unstable spatially homogeneous state [38]. The same analysis as before yields four complex spatial eigenvalues, so that the fronts have oscillatory tails. As said before, there may be a number of possible frozen steady state configurations due to the random pinning of interfaces (see Fig. 1.7).

1.4 Growth Laws

Next, we give some examples of systems, relaxational and nonrelaxational, for which the time evolution of the characteristic domain size is known during domain growth process.

1.4.1 Relaxational systems

A summary of growth laws for relaxational systems with purely dissipative dynamics is shown in the next table (restricted to the constraint $n \leq d$) [19]:

$$n = 1 : \quad L(t) \sim \begin{cases} t^{1/2} & \text{if } \mu = 0, \\ t^{1/3} & \text{if } \mu = 2, \end{cases} \quad (1.67)$$

$$n = 2 : \quad L(t) \sim \begin{cases} t^{1/2} & \text{if } \mu = 0, \\ (t \log t)^{1/4} & \text{if } \mu = 2, \end{cases} \quad (1.68)$$

$$n > 2 : \quad L(t) \sim t^{1/(2+\mu)}, \quad (1.69)$$

where n is the number of components of the order parameter ($n = 1$ is the scalar case), $\mu = 0$ is the nonconserved case and $\mu = 2$ the conserved one. Exceptional cases are excluded. This is the case of the two-dimensional XY model for which numerical simulations of the conserved case are consistent with $L(t) \sim t^{1/4}$ [69].

There have been much work devoted to domain coarsening and dynamical scaling in potential dynamics. Next, we present some prototype systems which have been studied in detail.

1.4.1.a Kinetic Glauber-Ising model

The Ising model is the basic model of phase transitions and it was first used to explain ferromagnetic properties. Its main virtue stems from the fact that it leads to a exact treatment in Statistical Mechanics. In 2D, it constitutes a nontrivial example of a phase transition that can be studied with all mathematical rigor. From its introduction in 1925 by Lenz, the Ising model has served as paradigm in Statistical Mechanics, providing an inestimable tool towards a better understanding of equilibrium and nonequilibrium systems

(kinetic model). Although its microscopic bases are rather simple, it has the necessary ingredients to explain a nontrivial behavior, in this case a critical phenomenon associated with a second order phase transition (in dimension two or greater).

The model is discrete and it is defined by the Ising Hamiltonian

$$\mathcal{H} = -J \sum_{\text{nn}} S_i S_j, \quad (1.70)$$

where J is a coupling constant and the S_i are spin variables, which can take values 1 or -1 ; “nn” indicates that the sum is performed over pairs of nearest neighbors. The kinetic Ising model is defined by equations for the spin configuration probabilities P which are constructed from the Hamiltonian \mathcal{H} (see [50, 70] for the details). In the case of Glauber dynamics these equations are [43]:

$$\begin{aligned} \frac{d}{dt} P(S_1, \dots, S_N, t) = & -P(S_1, \dots, S_N, t) \sum_i \frac{1 - S_i \tanh \beta h_i}{2} \\ & + \sum_i P(S_1, \dots, -S_i, \dots, S_N, t) \frac{1 + S_i \tanh \beta h_i}{2}. \end{aligned} \quad (1.71)$$

Here $\beta = 1/T$, $h_i = J \sum_{\text{nn of } i} S_j$ is the local field at site i , and for convenience periodic boundary conditions $S_{i+N} = S_i$ have been adopted. The dynamics (1.71) leads to the final equilibrium state with a configuration probability given by the Boltzmann distribution $P \sim e^{-\beta \mathcal{H}}$. Since the correlation length is finite at any nonzero temperature, this system is particularly interesting at $T = 0$, where equilibrium cannot be achieved in finite time: domain growth proceeds indefinitely, yielding universal nonequilibrium behavior at long times. The Glauber dynamics gives a residual noise at $T = 0$ that causes interfaces to move randomly. If two adjacent interfaces meet, then they annihilate. This process gives rise to a reduction in the number of walls, and therefore to domain growth.

The characteristic domain size turns out to be $L(t) \sim t^{1/2}$, *independently of the dimensionality*. The domain structure is universal, in the sense that it is independent of the nature of the random initial conditions, as long as $L(t)$ is large compared to any length scale characterizing the initial conditions.

It is surprising that the growth law does not depend on the spatial dimension, since the physics is different in 1D. In 2D there is a phase transition and domain growth is curvature driven. In 1D there is neither a phase transition nor curvature effects.

1.4.1.b Model A dynamics

This is a continuous model in terms of a coarse-grained order parameter $\psi(\mathbf{r}, t)$ (e.g., the magnetization density) [eq. (1.4)]. Equation (1.4) provides a

suitable coarse-grained description for the Ising model (continuous version). It also describes alloys undergoing an order-disorder transition after cooling through a critical temperature.

We already saw in section 1.3.1 that for this model the normal interface velocity in $d \geq 2$ is proportional to the local curvature (Allen-Cahn law):

$$v(\mathbf{r}, t) = -\kappa(\mathbf{r}, t), \quad \forall \mathbf{r} \text{ on the interface.} \quad (1.72)$$

If there is a single characteristic scale L , then the wall velocity is $v \sim dL/dt$, and the curvature $\kappa \sim 1/L$. Equating and integrating gives $L(t) \sim t^{1/2}$. Therefore, in this case, the dynamical evolution of the order parameter can be completely described by interface motion driven by curvature (surface tension). The form of the potential V only fixes the form of the front profile.

These growth laws can also be obtained using naive arguments based on the results obtained in section 1.3.1 for spherical domains. We know that a domain of radius R collapses in a time of order R^2 . Therefore, crudely speaking, after time t there will be no domains smaller than $t^{1/2}$, so the characteristic domain size is $L(t) \sim t^{1/2}$. These arguments capture the essential physics and yield the exact growth law (see for example [4]). The growth law for this model has also been obtained using renormalization group techniques [71].

In 1D, at variance with the Glauber discrete model, the growth law is different. Besides being deterministic, in the 1D model curvature effects are absent and coarsening takes place by means of short-range attractive forces between adjacent fronts. If two contiguous fronts are separated a distance D , they attract each other with a force given by (1.24):

$$F \sim \exp(-D/W), \quad (1.73)$$

where W is the front width. The force F is proportional to the front velocity, so if L is the characteristic domain size, we have

$$\dot{L} \sim e^{-L/W} \quad \Rightarrow \quad L(t) \sim \log t. \quad (1.74)$$

This result coincides with the one obtained by means of more elaborate statistical calculations [72, 73].

1.4.1.c Model B dynamics

When the order parameter is conserved, as in phase separation, a different dynamics occurs. In binary alloy, for example, it is physically clear that atoms of the two phases are locally exchanged. This leads to diffusive transport of the order parameter, and an equation of motion of the form (1.7), known as Cahn-Hilliard equation or model B dynamics (without noise). A detailed discussion of this model can be found in the lectures by Langer [61].

In terms of the chemical potential $\mu \equiv \delta\mathcal{F}_{\text{GL}}/\delta\psi$, eq. (1.7) can be written as a continuity equation

$$\partial_t\psi = -\nabla \cdot \mathbf{j} \quad \text{mass conservation,} \quad (1.75a)$$

$$\mathbf{j} = -\nabla\mu \quad \text{Fick's law (phenomenological).} \quad (1.75b)$$

A detailed analysis shows that the chemical potential μ verifies the relations [19]:

$$\nabla^2\mu \cong 0 \quad \text{in the bulk of a phase,} \quad (1.76a)$$

$$\mu \cong -\frac{\sigma\kappa}{2} \quad \text{close to an interface.} \quad (1.76b)$$

Here σ is the surface tension, κ the local curvature and $V(\psi)$ is assumed to have two equivalent minima at $\psi = \pm 1$.

In order to study interface dynamics, equation (1.75b) is used. An interface propagates with a velocity given by the imbalance between the current flowing into and out of it, that is:

$$v \Delta\psi = j_{\text{out}} - j_{\text{in}} = -\left[\frac{\partial\mu}{\partial x}\right] = -[\mathbf{x} \cdot \nabla\mu], \quad (1.77)$$

where v is the interface velocity in the direction of increasing ψ , x is the normal coordinate to interface, and $[\cdot \cdot \cdot]$ indicates the discontinuity across the interface.

As it was done for the nonconserved case, we can give an intuitive argument to determine the growth law of this model. From (1.76b), it follows that the chemical potential has a typical value $\mu \sim \sigma/L$ on the interfaces and it varies in a length scale of order L . The current, and therefore the velocity, scale as $|\nabla\mu| \sim \sigma/L^2$, giving $dL/dt \sim \sigma/L^2$ and $L(t) \sim t^{1/3}$. This result has been made evident by means of numerical simulations [74] as well as renormalization group treatment [75].

In the limit that one phase occupies an infinitesimal volume fraction, the original Lifshitz-Slyozov-Wagner theory [76] convincingly demonstrates a $t^{1/3}$ growth law. The physical mechanism is the evaporation of material (or magnetization) from small droplets and condensation onto larger droplets.

1.4.1.d *q-state Potts models*

Potts models are a class of (discrete) models of Statistical Mechanics used to study phase transitions [77]. They are a generalization of the Ising model (section 1.4.1.a). Their dynamics describes the coarsening of domains of q different equilibrium ordered phases following a quench from an homogeneous phase. Potts models have been used to describe many physical systems such as binary alloys, liquid crystals, magnetic bubbles, Langmuir films, and soap bubbles. After the quench, domains of different ordered phases form and grow

with time as the systems attains local equilibrium on larger and larger length scales.

The system is considered on a lattice, and at each point of it, a variable or spin s_i is defined. This variable can be thought as an indicator of the local microscopic state of the physical system and it might represent the orientation of some kind of magnetic dipole located in a crystal lattice. In the q -state Potts model, each spin variable can take q possible values: $1, 2, \dots, q$. The model is built by taking a Hamiltonian that favors the situation in which neighboring variables are oriented in the same way. In the kinetic model, the system follows a gradient relaxational dynamics in the landscape determined by this Hamiltonian.

The number of states of the Potts model affects different aspects of the growth process. The case $q = 2$ corresponds to the Ising model, and there are experimental realizations also for $q = 3, 4, \infty$. The limit $q \rightarrow \infty$ is known to describe the evolution of a dry soap froth, or the growth of metallic grains. Both for q finite and infinite numerical studies of domain growth [78, 79, 80] give a $L(t) \sim t^{1/2}$ growth law (in dimension greater than one). Its important to notice that for $q \geq 3$ the system can hold vertices, that are point defects at which several interfaces (at least three) coexist. The $t^{1/2}$ law has been shown to be robust against the presence of these vertices.

A suitable continuous version of the q -state Potts model is based on q coarse-grained occupation density fields $\{\phi_i(\mathbf{r}, t), i = 1, \dots, q\}$, such that ϕ_i assumes the value 1 in the bulk of the i th ordered phase and decays continuously to 0 outside. An suitable free-energy functional is [81]:

$$\mathcal{F}[\{\phi_i\}] = \int d^d x \left\{ \sum_{i=1}^q \left[\frac{1}{2} (\nabla \phi_i)^2 + V(\{\phi_i\}) \right] - \lambda_1 \left(\sum_{i=1}^q \phi_i - 1 \right) + \lambda_2 \left[\sum_{i=1}^q \left(\phi_i - \frac{1}{q} \right)^2 - \frac{q-1}{q} \right]^2 \right\}, \quad (1.78)$$

where V is a potential with q equivalent minima in $(1, 0, \dots, 0), (0, 1, \dots, 0), \dots, (0, 0, \dots, 1)$; this prevents two different phases from sharing the same position in space. On the other hand, $\lambda_1(\mathbf{r}, t)$ is a Lagrange multiplier enforcing the constraint $\sum_i \phi_i = 1$, and $\lambda_2 \sim O(1)$ is such that the state $(1/q, \dots, 1/q)$ is unstable.

The growth law $L(t) \sim t^{1/2}$ is observed numerically $\forall q$ (in $d \geq 2$). In reference [78] an analytical procedure to find the scaling functions is given, as well as the exponents describing the time dependence of autocorrelations.

1.4.1.e Swift-Hohenberg equation

The Swift-Hohenberg (SHE) equation was first introduced to model the onset of a convective instability in simple fluids. It describes the time evolution of a

real dynamical variable $\psi(\mathbf{r}, t)$ in the form:

$$\partial_t \psi(\mathbf{r}, t) = [\varepsilon - (1 + \nabla^2)^2] \psi(\mathbf{r}, t) - \psi(\mathbf{r}, t)^3. \quad (1.79)$$

Equation (1.79) can be recast as:

$$\frac{\partial \psi(\mathbf{r}, t)}{\partial t} = - \frac{\delta \mathcal{F}_{\text{SH}}[\psi]}{\delta \psi(\mathbf{r}, t)}, \quad (1.80)$$

where the (real) functional \mathcal{F} is:

$$\mathcal{F}_{\text{SH}}[\psi] = \int d\mathbf{r} \left[-\frac{\varepsilon - 1}{2} \psi^2 + \frac{1}{4} \psi^4 - (\nabla \psi)^2 + \frac{1}{2} (\nabla^2 \psi)^2 \right]. \quad (1.81)$$

The stationary solution $\psi = 0$ corresponds to a conductive state below the instability. This occurs at $\varepsilon = 0$ and gives rise to a convective steady state with rolls of certain wavelength. Now, we distinguish between one- and two-dimensional systems in the process of decay of the metastable state $\psi = 0$ for $\varepsilon > 0$. In $d = 1$ essentially a single domain of a preferred wavenumber emerges, whereas in $d = 2$ domains of different orientation of a selected wavevector grow in time.

d=1

In reference [82] a numerical study of pattern formation in the one-dimensional SHE is made. Special emphasis is put on the selected wavevector of the emerging patterns.

In (1.79), the stationary state $\psi(x) = 0$ is unstable against perturbations of wavenumber q such that $\omega(q) = \varepsilon - (q^2 - 1)^2 > 0$. The fastest growing mode is determined by $\partial_q \omega|_{q=q_0} = 0$ and it corresponds to $q_0 = 1$. For $\varepsilon \gtrsim 0$ there exist stationary periodic solutions characterized by a wavevector $q \in [q_{-L}, q_L]$, $q_{\pm L} = \sqrt{1 \pm \varepsilon^{1/2}}$, L being the system size. On the other hand, only the solutions with $q_{-E} \leq q \leq q_E$ are stable; out of this interval, solutions are unstable against long wavelength perturbations (Eckhaus instability). The value q_E can be computed analytically for ε small and numerically for any ε [83].

For long enough times, $\psi(x, t)$ is seen to converge to a periodic stationary solution that depends on the initial random perturbation. The selected wavenumber lies within a well-defined range centered around the fastest growing mode during the linear regime after the instability.

Some works [84] suggest that the selection process follows a variational principle and that the selected wavenumber is the one that minimizes the functional (1.81) for any initial condition. In the numerical simulations it is observed that the number of nodes of the field at long times is conserved. This indicates that a wavenumber is selected. Actually the wavenumber field distribution is centered around $q = q_0$. In the study done in [82] the difference between the wavenumber q_0 of the fastest growing mode and the one

that minimizes \mathcal{F}_{SH} , q_m , is within the numerical accuracy, so it is not possible to make a clear conclusion. However, a later work [85] makes evident that, under quite general initial conditions, the selected wavenumber is the one of maximum linear growth q'_0 . The authors analyze pattern formation growing from initial conditions whose wavenumber is out of the stable band $[q_{-E}, q_E]$. A linear analysis shows that in this case q'_0 and q_m are clearly different, which allows to resolve which one is selected.

The addition to (1.79) of a stochastic term (e.g., Gaussian white noise) considerably modifies the pattern selection process. Random fluctuations are important during the initial stages after the instability, for a time interval that depends on the relative amplitude of the fluctuations of the solution itself. Now, in contrast to the deterministic case, the final stationary solution is not determined by the initial condition nor it shows a definite periodicity. The stationary power spectrum is broad, indicating that stationary configurations cannot be characterized by a unique wavevector, although there is still a preferential wavevector. The spectrum gets wider with the amplitude of fluctuations, and if these are not too large, the number of nodes is approximately constant for each individual realization (at long times).

$d=2$

In references [37, 86] a study of coarsening and dynamical scaling of the SHE in two spatial dimensions was made.

A notable feature of (1.81) is that it is minimized by a one-dimensional periodic function corresponding to a configuration of straight and parallel stripes. Although other systems select a characteristic finite wavelength, this model differs from them in that the roll structure is rotationally invariant.

In the deterministic case, the presence of defects prevents that a solution of parallel rolls minimizing \mathcal{F}_{SH} is reached. In a large enough system, the stationary solutions are made of domains of rolls with different orientation that change with noise intensity. Stationary states are strongly influenced by any source of random noise, so that, above a critical noise intensity, an isotropic state emerges, and it is characterized by a diffusive peak in the structure factor. Below this critical value, phases with much larger translational correlation lengths emerge. A growth law $L(t) \sim t^{1/5}$ is obtained with and without noise (see [7] and references therein).

1.4.2 Nonrelaxational Systems

Little work has been devoted to the study of coarsening processes in nonrelaxational systems. Next we summarize some recent work on this direction.

1.4.2.a Nonlinear Schrödinger equation

The formation of singularities at finite time in nonlinear wave phenomena (for example optics) is generically described by the (focusing) nonlinear Schrödinger equation (NLSE):

$$i \partial_t \psi = -\nabla^2 \psi - |\psi|^2 \psi, \quad (1.82)$$

where ψ is a complex quantity that represents the amplitude of the wave, i.e., the electric field in optics. The nonlinear terms represents the action of a refraction index that depends on the field intensity. The electric field diverges at finite time for spatial dimension $d \geq 2$ and a large set of initial conditions. Equation (1.82) cannot account for the formation of stable and intense light pulses observed experimentally. For very large electric fields higher orders in the expansion of the nonlinear refraction index must be included. In references [8, 12] the formation of these localized structures when higher order terms are added to (1.82) is studied. The starting point is the so-called subcritical NLSE:

$$i \partial_t \psi = -\frac{1}{2} \nabla^2 \psi - 2\rho_c |\psi|^2 \psi + |\psi|^4 \psi. \quad (1.83)$$

Here $\rho_c > 0$ is a constant. This equation also appears in other contexts such as the study of quantum solids and liquids, dynamics of magnetic and molecular chains, nuclear hydrodynamics and nonlinear optics. It models for instance (in the Hartree approximation) a bosonic system with two body attractive interactions and three body repulsive interactions. In general the inverse of ρ_c represents the small expansion parameter of the nonlinear terms: for $|\psi|^2 \ll \rho_c$ the cubic term is sufficient to describe the evolution of the system; however, when $|\psi|^2 \approx \rho_c$, one must add the quintic term. For superfluid He II, ρ_c is physically related to the critical density for cavitation, that is, the density at which the sound velocity vanishes².

The subcritical NLSE describes a Hamiltonian system where the energy has two local minima. The dynamics of formation of droplets takes place out of equilibrium. In addition, there is no explicit relaxation process: the dynamics is completely reversible (and Hamiltonian). We point out that the NLSE can be obtained as a limiting case of the complex Ginzburg-Landau equation when the real parts of the coefficients are zero. Equation (1.83) can be rewritten in the form:

$$\partial_t \psi = -i \frac{\delta \mathcal{F}_{\text{NLSE}}}{\delta \psi^*}, \quad (1.84)$$

$$\mathcal{F}_{\text{NLSE}} = \int d^d x \left\{ \frac{1}{2} |\nabla \psi|^2 - \rho_c |\psi|^4 + \frac{1}{3} |\psi|^6 \right\}.$$

²If we define $\rho = |\psi|^2$ as the local “density of the liquid”) (“density of light” in nonlinear optics), ρ satisfies a wave equation $\partial_{tt} \rho = c^2 \nabla^2 \rho$, where $c = \sqrt{2\rho(\rho - \rho_c)}$ is the sound velocity; therefore c vanishes for $\rho = \rho_c$.

We have that $d\mathcal{F}_{\text{NLSE}}/dt = 0$ and $\mathcal{F}_{\text{NLSE}}$ is a conserved quantity. Also the total number of particles $N = \int d^d x |\psi|^2$ is conserved. Moreover, (1.83) is invariant under spatio-temporal translations and global phase changes.

The dynamics described by the subcritical NLSE provides for the formation of droplets that stabilize thanks to nonrelaxational dynamics [12, 87]. However, we stress that a nonrelaxational dynamics is not necessary (in a nonconservative system) for the formation of localized structures. For instance, the existence of oscillatory tails in the profiles of the fronts separating the various phases may lead to the stabilization of droplets (see section 1.3.4).

In [8] the issues of domain growth and dynamical scaling are studied in the Hamiltonian kinetics of a first order phase transition described by (1.83). Starting from an uniform initial density $\rho_0 = |\psi_0|^2$ slightly less than ρ_c , a long wavelength instability develops. Along the evolution three main stages may be distinguished:

- (S1) Exponential growth in time of density variations. Drops with the length scale of the fastest growing mode are created.
- (S2) Creation of well-defined domains with large ($\sim \rho_c$) and small (~ 0) stable densities.
- (S3) Coalescence of stable droplets and bubbles. This causes a decrease in the number of domains and therefore the coarsening of the structure.

Between stages (S1) and (S2) an intermediate short stage takes place. During this period the pressure difference between the low density (gas) and the large density (liquid) phases contracts the liquid phase, until the liquid density reaches $\frac{3}{2}\rho_c$, the point where pressure equilibrium is established. In Fig. 1.8 four snapshots of the time evolution of the system are shown. We can notice the coalescence phenomenon of gas bubbles.

Numerically the number of domains $n(t)$ and their characteristic size $L(t)$ are observed to vary as:

Spatial dimension	$n(t)$	$L(t)$
1	$t^{-1/4}$	$t^{1/4}$
2	t^{-1}	$t^{1/2}$
3	t^{-1}	$t^{1/3}$

Because of the slow coalescence or condensation of the small oscillating droplets, the final state of the system is a single isolated droplet. The excess energy transforms into vibrations of the droplet and small scale oscillations.

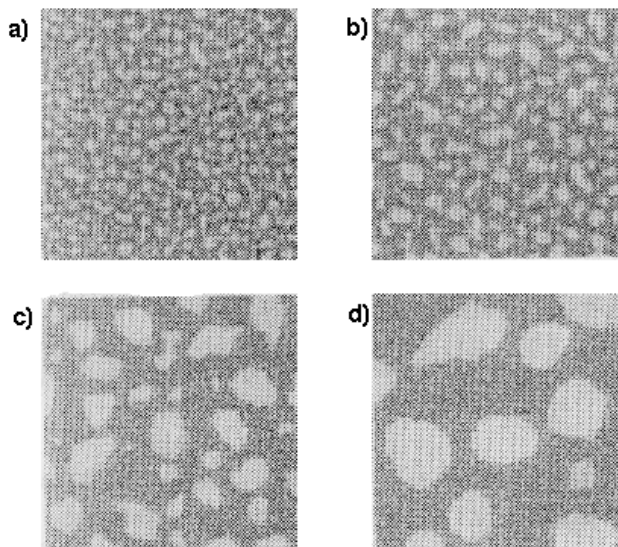


Figure 1.8: A time sequence of the coalescence of gas bubbles. The gray scale represents the vapor phase by a light gray and the liquid by a dark gray. The images are taken at (a) $t = 36.2$, (b) $t = 61.1$, (c) $t = 203.35$, (d) $t = 634.7$ time units. Taken from [8].

1.4.2.b One-dimensional cyclic Lotka-Volterra models

The classic Lotka-Volterra (LV) equations mimic the dynamics of interacting species such as predator-prey systems. They predict successfully population oscillations which are known to exist in nature. The competing dynamics of these equations has been reproduced and controlled experimentally through an optical system [88].

The cyclic N -species LV model is implemented in the following way. We consider a one-dimensional lattice of size \mathcal{N} with periodic boundary conditions. Each site of the lattice is in a given state N_i with $N_i = A, B, C, \dots$. Every species plays the role of prey and predator simultaneously. The food chain is thus assumed to be cyclic; e.g., in the three-species system, A eats B , B eats C , and C eats A . Every “eating” event leads to duplication of the winner and elimination of the loser. An exhaustive study of this model is done in [89]. Two kinds of dynamics are analyzed, namely

Sequential dynamics. We choose randomly a site and then one of its two nearest neighbors. If the neighbor is a predator of the chosen site, the state of the latter changes to the state of the predator.

Parallel dynamics. All sites are updated simultaneously and change their state if one of their nearest neighbors is their predator. Interfaces move ballistically in such a way that two of them moving in the same direction do not interact.

The coarsening behavior of the system depends on spatial fluctuations present in the initial state as well as on the number of species. Only symmetric initial conditions are considered, that is, those for which the density of each species is $1/N$.

In the case of *two species*, interfaces perform a random walk and annihilate upon collision. This exactly soluble model is equivalent to the one-dimensional kinetic Glauber-Ising model at zero temperature (page 23). The system separates into single species domains whose characteristic size grows as $L(t) \sim t^{1/2}$. In contrast, mean-field theory predicts $L(t) \sim t$, result that, although correct in the $t \rightarrow 0$ limit where correlations are absent, it is not asymptotically correct because correlations are important at long times.

For *three species*, growth laws depend on the dynamics acting on the system. In the case of parallel dynamics, the system organizes into large ballistically growing superdomains. Each superdomain contains interfaces moving in the same direction, neighboring superdomains contain interfaces moving in the opposite direction. The superdomain characteristic size grows as t and that of subdomains separated by interfaces moving in the same direction grows as $t^{1/2}$. When the dynamics is sequential, interfaces perform a random walk supplemented by superimposed diffusion. Unlike the parallel case, two interfaces moving in the same direction may annihilate by a diffusive process and give rise to an interface moving in opposite direction. The system organizes in domains that contain interfaces moving to the left and right. The subdomain size grows as $t^{3/4}$, whereas the larger scale domains evolve as in the parallel case ($\sim t$).

Cases with *four and five species* are also studied in [89]. We stress that in the case $N \geq 5$, the system quickly reaches a frozen state with noninteracting neighboring species [90]; however, the approach towards saturation has not been established, though. In [91] frozen structures of arbitrary dimension in LV models are studied. In the realm of a Kirkwood approximation, a critical number of species above which the system freezes is predicted analytically in all spatial dimensions.

It is straightforward to generalize these models to reaction-diffusion equations, which have been widely applied to more complex ecological processes. For example, in the three species system A, B, C , with reaction scheme



the extension to a reaction-diffusion model supplemented by reproduction and self-regulation is expressed by the equations [89]:

$$\begin{aligned} \partial_t a &= \partial_{xx} a + a(1 - a) + \lambda a(b - c), \\ \partial_t b &= \partial_{xx} b + b(1 - b) + \lambda b(c - a), \\ \partial_t c &= \partial_{xx} c + c(1 - c) + \lambda c(a - b). \end{aligned} \quad (1.86)$$

The previous system of equations is nonpotential and equivalent to the theoretical model studied in chapter 2 [eq. (2.53)] with the identifications $a_i \rightarrow A_i^2$, $\eta = 0$, $\delta = -\lambda$. Equations (1.86) describe, for $\lambda \neq 0$, a coarsening process in which interfaces connect linearly *unstable* asymptotic states. The interface velocity can be found through the “marginal stability principle”, which

is a theorem for the Fisher-Kolmogorov equation [92] while for many other reaction-diffusion equations the marginal stability principle has been verified numerically [1, 93]. In chapter 2 only coarsening processes with stable domains are studied.

1.4.2.c Nonpotential Swift-Hohenberg equation

The SHE, as introduced in section 1.4.1.e, was introduced to look at the effect of fluctuations on the transition to the convective roll state. It is an equation for a *real* order parameter $\psi(\mathbf{r}, t)$, function of the horizontal coordinates $\mathbf{r} = (x, y)$ and time t . The SHE and various generalizations of it have proven to be quite successful in explaining many of the features of convective flow in Rayleigh-Bénard convection. In particular Swift-Hohenberg models describe the spontaneous formation of spiral patterns in some fluid systems [94]. The original SHE [eq. (1.79)] is potential and is the simplest one consistent with the symmetries of the problem and the existence of a stripe pattern. However, potential dynamics is not always appropriate for this kind of systems far from equilibrium, and so various modifications have been proposed. In particular, a modification of the nonlinear terms is suggested in [95]. The resulting equation is:

$$\partial_t \psi = \varepsilon \psi - (\nabla^2 + 1)^2 \psi + 3(\nabla \psi)^2 \nabla^2 \psi. \quad (1.87)$$

The previous equation is nonpotential and gives a better representation of the stability of the stripe phase as the wavevector and control parameter are varied for convection. A further model, also nonpotential, incorporates a mean flow varying with the horizontal coordinates [96, 97]:

$$\begin{aligned} \partial_t \psi + \mathbf{U} \cdot \nabla \psi &= \varepsilon \psi - (\nabla^2 + 1)^2 \psi + \text{NL}, \\ \nabla \times \mathbf{U} &= \Omega \hat{\mathbf{z}}, \\ \tau_\nu \partial_t \Omega - \sigma(\nabla^2 - c^2)\Omega &= g_m \hat{\mathbf{z}} \cdot \nabla(\nabla^2 \psi) \times \nabla \psi, \end{aligned} \quad (1.88)$$

where $\mathbf{U}(x, y, t)$ is the divergence-free horizontal velocity that advects the field ψ in the first equation [the symbol NL refers to the nonlinearity choices either of (1.79) or (1.87)]. The velocity \mathbf{U} is defined in terms of the vertical vorticity Ω , which is in turn driven by distortions of the stripe pattern through the third equation. Here g_m gives the coupling between the mean flow and the stripes, and increases as the Prandtl number decreases. The remaining parameters are associated with several fluid properties. Rotating Rayleigh-Bénard convection has also been studied in the realm of Swift-Hohenberg models, both with [98] and without [17, 99, 100] the inclusion of mean flow effects.

Domain growth in two-dimensional Swift-Hohenberg models has been addressed in reference [7]. The cases studied are the original SHE [eq. (1.79)] and the two nonpotential generalizations (1.87) and (1.88). The authors investigate the formation of a “stripe” state in two dimensions, with rotational

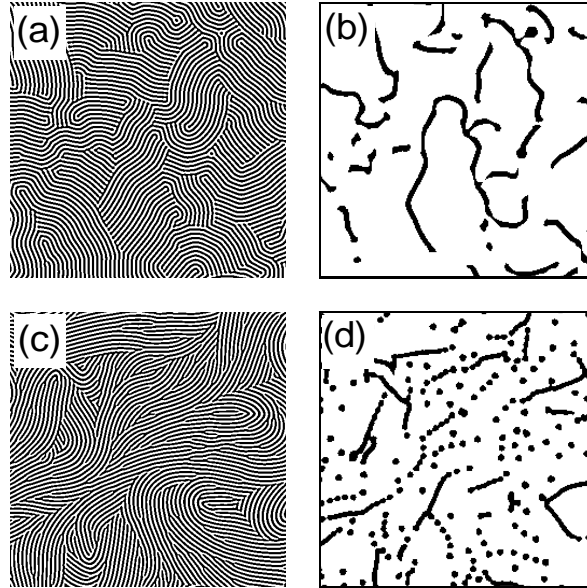


Figure 1.9: Stripe structure for (a) potential and (c) nonpotential models of convection during the coarsening process. Black and white denote positive and negative values of the field respectively. Panels (b) and (d) show the corresponding defect structure which concern the regions where the amplitude of the stripe pattern falls below 75% of the maximum value. Taken from [7].

invariance in the plane. This situation models Rayleigh-Bénard convection, with the stripes corresponding to the familiar convection rolls. After a quench into the ordered region, given by stepping the Rayleigh number, regions of differently oriented stripes grow from random initial fluctuations as the dynamics rapidly drives the system locally to a state with the characteristic length scale of the stripes. It is interesting to know how the length scale over which the stripes are ordered grows and what is the asymptotic wavelength of the structure (that is, what is the selected wavevector). The numerical results of [7] reveal a slow evolution of a length scale ξ_q , defined as the width of the wavevector distribution in Fourier space, consistent with $\xi_q \sim t^{1/5}$ for *all three* cases studied: potential, nonpotential, and with the inclusion of mean flow (also nonpotential). For the nonpotential cases, they found a second length scale ξ_r defined from the correlations of the orientation of the stripes in real space, and it appears to show a different behavior consistent with $\xi_r \sim t^{1/2}$. The appearance of a second length scale may be due to the fact that correlations along the stripes are stronger than perpendicular to the stripes. It seems that the selected wavevector is that at which isolated dislocations are stationary.

The morphology of the system turns out to be quite different for the potential and nonpotential cases, as shown in Fig. 1.9. For the potential equation the pattern may be roughly described as consisting of domains of straight stripes with sharp boundaries between the domains, although there are also some regions where a smoother variation of the stripes is seen. Two kinds of domains may be identified: lines where one set of stripes ends and a second set starts, and lines where there is a sharp kink in the stripe orientation, but a smaller perturbation of the amplitude (this is the reason why these kinks are not observed in panel (b) of Fig. 1.9). For the nonpotential equations stripes

smoothly curved over the characteristic scale are evident; also isolated dislocation defects are more apparent.

The defect structure of stripe phases is complicated, and understanding the role of the various defects in the coarsening process remains a challenge for the future. For example, it is not understood yet why the addition of noise causes an increase in the growth rate of the characteristic length scale, because noise is expected not to be relevant at long scales. Elder, Viñals and Grant [37] find a $t^{1/4}$ law with noise, whereas a $t^{1/5}$ dependence is found in [7, 37] in the absence of noise.

1.4.2.d *Nonlinear optical systems*

Optical bistable systems provide examples of nonequilibrium systems undergoing instabilities leading to pattern dynamics [101]. Transverse pattern dynamics is often studied by means of models involving a nonrelaxational dynamics, and the issue of domain growth has been studied in a number of these systems. We postpone the discussion until chapter 4, where we give a summary of the most outstanding results concerning domain growth in optical systems. We will study in detail the kinetics of pattern formation in an optical cavity filled with an isotropic Kerr medium pumped with an external input field.

1.5 Dynamical Scaling

Two functions frequently used to explore the domain structure are the equal-time correlation function

$$C(\mathbf{r}, t) = \langle \phi(\mathbf{x} + \mathbf{r}, t) \phi(\mathbf{x}, t) \rangle_{\text{i.c.}}, \quad (1.89)$$

and its Fourier transform, the equal-time structure factor,

$$S(\mathbf{k}, t) = \langle \hat{\phi}(\mathbf{k}, t) \hat{\phi}(-\mathbf{k}, t) \rangle_{\text{i.c.}} = \hat{C}(\mathbf{k}, t). \quad (1.90)$$

The angular brackets indicate an ensemble average. The structure factor is a fundamental measure of the nonequilibrium properties of the system. The existence of a single characteristic length scale implies, according to the scaling hypothesis, that the pair correlation function and the structure factor have the scaling forms:

$$C(\mathbf{r}, t) = f(r/L(t)), \quad (1.91a)$$

$$S(\mathbf{k}, t) = L(t)^d \hat{f}(kL(t)), \quad (1.91b)$$

where d is the spatial dimensionality, and $\hat{f}(k)$ is the Fourier transform of $f(x)$. The scaling limit is defined by $r \gg \xi$, $L \gg \xi$, with r/L arbitrary, where

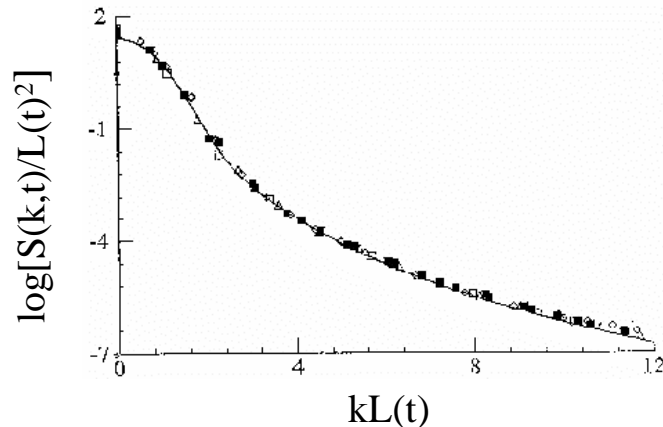


Figure 1.10: Scaling function for the model A in two dimensions. The continuous line corresponds to the theoretical prediction by Ohta, Kawasaki and Jasnow. Symbols are \diamond $t = 100$, \blacksquare $t = 200$, \triangle $t = 300$, \square $t = 500$. Taken from [102].

ξ is the equilibrium correlation length. In a system evolving selfsimilarly, when plotting $C(r, t)$ against $r/L(t)$ for different times, all the curves follow the same profile, the profile of the *scaling function* $f(x)$. The scaling forms (1.91a–b) are well supported by simulation [51] data and experiments [52]. In Fig. 1.10 the scaling function profile for model A is shown.

There are several ways to find the characteristic length $L(t) = K(t)^{-1}$. For example $K(t)$ could be defined as $K_1(t)$, the first moment of $S(k, t)$. Alternatively, $K(t)$ might be chosen as the position $K_m(t)$ of the maximum of $S(k, t)$. If there exists a unique time-dependent characteristic length, any choice must be valid. In Monte Carlo studies it is convenient to use $K_1(t)$, partly because it is difficult to determine K_m accurately. In other cases, such as binary fluids experiments, it is common to use $K_m(t)$ since its position can be determined quite accurately. For systems with nonconserved order parameter, as ferromagnetic materials and order-disorder transitions, it turns out that $K_1 = K_m = 0$, but it is possible to take $K(t) = \sqrt{K_2(t)}$, where K_2 is the second moment of $S(k, t)$. In all the cases, $K(t)^{-1}$ is supposed to be a measure of the size of the ordered regions developing in the system.

The scaling forms (1.91a–b) are certainly plausible. However, it should be noted that the existence of a dominant length scale does not imply necessarily that $f(x)$ is independent of time. Corrections to dynamical scaling such that f is weakly time-dependent may be expected. The scaling function f is not a universal function in the sense that it can depend on thermodynamic variables that characterize the cooling point. For example, the scaling functions for binary alloys and fluids depend on temperature and concentration, although weakly. Other aspect to keep in mind is that if (1.91b) is correct, a number of magnitudes are related, for example the position of the peak of the structure factor $K_m(t)$ and its height $S(K_m(t), t)$. So, if we take $k = K_m(t)$,

(1.91b) implies

$$S(K_m(t), t) = K_m^{-d} \hat{f}(1). \quad (1.92)$$

If we assume that the height of the peak and its position follow a power law behavior with exponents α and β , then from (1.92) we infer

$$C_1 t^\alpha = C_2 t^{\beta d} \hat{f}(1) \Rightarrow C_1 C_2^{-d} t^{\alpha - \beta d} = \hat{f}(1) \Rightarrow \alpha = \beta d. \quad (1.93)$$

Fisher and Huse [103] indicated that the two-time correlation function $C(\mathbf{r}, t, t') = \langle \phi(\mathbf{x}, t') \phi(\mathbf{r} + \mathbf{x}, t) \rangle$ also possesses nontrivial scaling properties. A simple generalization of (1.91a) gives

$$C(\mathbf{r}, t, t') = f\left(\frac{r}{L}, \frac{r}{L'}\right), \quad (1.94)$$

where $L = L(t)$ and $L' = L(t')$. Specially interesting is the limit $L \gg L'$ for which equation (1.94) adopts the form

$$C(\mathbf{r}, t, t') \rightarrow \left(\frac{L'}{L}\right)^{\bar{\lambda}} h\left(\frac{r}{L}\right), \quad L \gg L', \quad (1.95)$$

where $\bar{\lambda}$ is a nontrivial exponent related to the phase order kinetics; it has been measured in an experiment with nematic liquid crystal films [104]. The *autocorrelation function* $A(t) = C(\mathbf{0}, t, t')$ is therefore a function only of the quotient L'/L , with $A(t) \approx (L'/L)^{\bar{\lambda}}$ for $L \gg L'$.

1.5.1 Porod's Law

The presence of topological defects, seeded by the initial conditions, in a system undergoing phase ordering has an important effect on the form of the pair correlation function at short distances, and therefore on the structure factor at long wavenumbers.

Let us consider a system governed by a scalar order parameter ϕ such that the homogeneous states $\phi = \pm 1$ are stable. Consider two points \mathbf{x} and $\mathbf{x} + \mathbf{r}$, with $\xi \ll r \ll L$. The product $\phi(\mathbf{x})\phi(\mathbf{x} + \mathbf{r})$ will be -1 if an interface passes between them, and $+1$ if there is no interface. Since $r \ll L$, the probability to find more than one interface can be neglected. The calculation of the correlation function at short distances amounts to find the probability that a randomly placed rod of length r cuts a domain wall. This probability is of order r/L , so we estimate

$$C(\mathbf{r}, t) \approx (-1)\frac{r}{L} + (+1)\left(1 - \frac{r}{L}\right) = 1 - \frac{2r}{L}, \quad r \ll L. \quad (1.96)$$

The factor 2 in this result should not be taken into account seriously. We are interested in the scaling limit defined by $r, L \gg \xi$, with $x = r/L$ arbitrary.

The form (1.96) implies a power law tail in the structure factor, which can be obtained by simple power-counting

$$S(\mathbf{k}, t) \sim \frac{1}{L k^{d+1}}, \quad kL \gg 1. \quad (1.97)$$

Equation (1.97) expresses a result known universally as *Porod's law*. It was first written down in the general context of scattering from two-phase media. The factor $1/L$ is simply (up to constants) the total area of interface per unit volume. Taking this into account, structure factor measurements may be used to find this area.

If Porod's law applies, it means that the interfaces are abrupt. The large field gradients near defects give rise to a nonanalytic behavior of the scaling function $f(x)$ at the origin for pair correlations.

1.5.2 Scaling Solution in the One-dimensional Glauber-Ising Model

There are few exactly solved models of phase-ordering dynamics, and although they are quite far from describing systems of physical interest, some qualitative features survive in more physically relevant models.

We will only consider here the kinetic Ising model in 1D [50]. This and other examples can be found in [19] and references therein.

As said in section 1.4.1.a, the one-dimensional Ising model with Glauber dynamics is a discrete model with a nonconserved order parameter. The model is defined by equations (1.70) and (1.71).

From (1.71) it is not difficult to find the equation of motion for the pair correlation function $C_{ij} = \langle S_i(t)S_j(t) \rangle$, where the brackets represent an average over the distribution P . If the set of initial conditions is invariant under translations, C_{ij} depends only on the separation $r = |i - j|$ after averaging. Thus

$$\dot{C}(r, t) = C(r + 1, t) - 2C(r, t) + C(r - 1, t), \quad r \neq 0. \quad (1.98)$$

For $r = 0$, $C(0, t) = 1$, $\forall t$ trivially. The simplest way to obtain $C(r, t)$ in the scaling limit is to take the continuous limit of (1.98). This leads to the diffusion equation $\partial_t C = \partial_{rr} C$, with constraint $C(0, t) = 1$. A scaling solution obviously requires $L(t) \sim t^{1/2}$. Upon insertion of $C(r, t) = f(r/t^{1/2})$ in the diffusion equation, it yields $f'' = -\frac{x}{2}f'$. The integration of this equation with boundary conditions $f(0) = 1$, $f(\infty) = 0$ gives $f(x) = \text{erfc}(x/2)$, where erfc is the complementary error function. Thus the scaling solution is

$$C(r, t) = \text{erfc} \left(\frac{r}{2t^{1/2}} \right). \quad (1.99)$$

In particular, at short distances

$$C(r, t) = 1 - \frac{r}{(\pi t)^{1/2}} + O(r^3/t^{3/2}), \quad (1.100)$$

so that Porod's law is satisfied.

1.5.3 Scaling Function Theories

There is no doubt that the calculation of scaling functions is a much more arduous task than the determination of growth laws. In fact, it has been a long-standing challenge. In spite of this, scaling functions can be calculated in a number of soluble models. A number of approximate scaling functions have been proposed for nonconserved fields. The most physically appealing approach for scalar fields (governed by a potential dynamics) is that of Ohta, Jasnow and Kawasaki (OJK) [105], which starts from the Allen-Cahn equation (1.72) for the normal velocity of the interfaces.

In their work, OJK replace the physical field $\phi(\mathbf{r}, t)$, which takes the values ± 1 everywhere except at domain walls, where it varies rapidly, by an auxiliary field $A(\mathbf{r}, t)$ smoothly varying in space. This is achieved by using a nonlinear function $\phi(A)$ with a “sigmoid” shape (such as $\tanh A$). The OJK theory includes interface dynamics defined by the zeroes of A . As a starting point, the normal velocity of a domain wall is considered. This is given by the Allen-Cahn law $v = -\kappa = -\nabla \cdot \mathbf{n}$, where κ is the local curvature and $\mathbf{n} = \nabla A / |\nabla A|$ is a unit vector normal to the wall. This gives

$$v = \frac{-\nabla^2 A + \sum_{i,j} n_i n_j \nabla_{x_i} \cdot \nabla_{x_j} A}{|\nabla A|}, \quad (1.101)$$

where $\{x_i\}$ are the Cartesian coordinates. In a frame of reference comoving with the interface

$$\frac{dA}{dt} = 0 = \frac{\partial A}{\partial t} + \mathbf{v} \cdot \nabla A \quad \Longrightarrow \quad v = -\frac{1}{|\nabla A|} \frac{\partial A}{\partial t}. \quad (1.102)$$

Eliminating v between equations (1.101) and (1.102), we obtain a closed equation for the auxiliary field A :

$$\frac{\partial A}{\partial t} = \nabla^2 A - \sum_{i,j} n_i n_j \nabla_{x_i} \cdot \nabla_{x_j} A. \quad (1.103)$$

The next step of OJK was to replace $n_i n_j$ by its spherical average δ_{ij}/d [This is equivalent to linearize eq. (1.103)], obtaining the diffusion equation

$$\frac{\partial A}{\partial t} = D \nabla^2 A, \quad D \equiv \frac{d-1}{d}. \quad (1.104)$$

A convenient choice for the distribution of initial conditions is a Gaussian distribution for the field $A(\mathbf{r}, 0)$, with mean zero and correlator $\langle A(\mathbf{r}, 0) A(\mathbf{r}', 0) \rangle = \Delta \delta(\mathbf{r} - \mathbf{r}')$. With this, it is straightforward to calculate the

pair correlation function:

$$\begin{aligned}
\langle A(\mathbf{r}, t)A(0, t) \rangle &= \frac{1}{(2\pi)^d} \int d\mathbf{k} d\mathbf{k}' e^{i\mathbf{k}\cdot\mathbf{r}} e^{-D(k^2+k'^2)} \langle \hat{A}(\mathbf{k}, t) \hat{A}(\mathbf{k}', t) \rangle \\
&= \frac{\Delta}{(2\pi)^d} \int d\mathbf{k} e^{i\mathbf{k}\cdot\mathbf{r}} e^{-2Dk^2t} = \frac{\Delta}{(2\pi)^d} \prod_{n=1}^d \int_{-\infty}^{+\infty} dk_n e^{-2Dk_n^2t + ik_n x_n} \\
&= \frac{\Delta}{(2\pi)^d} \prod_{n=1}^d \left(\frac{\pi}{2Dt} \right)^{1/2} \exp\left(-\frac{x_n^2}{8Dt} \right) \\
&= \frac{\Delta}{(8\pi Dt)^{1/2}} \exp\left(-\frac{r^2}{8Dt} \right).
\end{aligned} \tag{1.105}$$

To calculate the pair correlation function of the original field ϕ , we need to know the joint probability distribution for $A(\mathbf{r}, t)$ and $A(0, t)$, which is relatively simple to write down for a Gaussian field satisfying a diffusion equation. In the scaling regime, walls occupy a negligible fraction volume. Thus, the field $\phi(A)$ can be replaced by $\text{sgn}(A)$. With all this considerations, it is not difficult to find the scaling function (after some tedious analytical calculations) which turns out to be

$$\hat{f}(x) = \frac{2}{\pi} \frac{(2\pi)^{d/2}}{x} \int_0^\infty dR R^d (e^{R^2} - 1)^{-1/2} (xR)^{1-d/2} J_{d/2}(xR), \tag{1.106}$$

where $x = kL(t)$ and J is a Bessel function of first class. We remember that (1.106) is in principle only valid for nonconserved scalar order parameters in dimension greater or equal than two. For example, simply substituting $d = 1$ in (1.106) the scaling function for the one-dimensional Ising-Glauber model is not recovered. Expression (1.106) together with the scaling forms (1.91a–b) fit very well data from numerical studies for a number of systems (see for example Fig. 1.10).

There exist other more sophisticated methods to calculate scaling functions, but all of them are elaborated on the basis of the OJK theory. This is the case of the *Mazenko approach* ([19] and references therein). This approach combines a clever choice for the function $\phi(A)$ with the minimal assumption that the field A is Gaussian. Specifically, $\phi(A)$ is chosen to be the equilibrium interface profile function, defined by $\phi'(A) = V'(\phi)$, with boundary conditions $\phi(\pm\infty) = \pm 1$, $\phi(0) = 0$. The field A then has a physical interpretation, near walls, as a coordinate normal to the wall.

The main advantages of the Mazenko approach are

- (A1) Only the assumption that the field A is Gaussian is required.
- (A2) The scaling function has a nontrivial dependence on d . In fact, the scaling function of the one-dimensional Ising-Glauber model is recovered in the limit $d \rightarrow 1$, and for $d \rightarrow \infty$ the OJK function is obtained.

(A3) The nontrivial behavior of different time correlation functions emerges in a natural way.

The Mazenko approach can be used with some modifications for both scalar and vectorial fields.

Another more sophisticated theory has been developed by Bray and Humayun [106], and has the advantage that it can, in principle, be systematically improved. For scalar fields, the time-dependent Ginzburg-Landau equation (1.4) is taken as a point of departure. The idea that the detailed form of the potential is not important in driving interface motion is exploited. We recall that interfaces move only at long times due to local curvature effects. Therefore, the scaling function must be independent of the potential (that is, of the particular profile of the domain walls), which allows to choose a particular $V(\phi)$ such that the partial differential equation for the field $A(r, t)$ is as simple as possible. This approximation recovers scaling functions of precedent theories in leading order.

Chapter 2

Domain Growth in the Busse-Heikes Model for Three Competing Amplitudes

Abstract. *We consider in this work a nonpotential model for three competing amplitudes which has been proposed to study rotating Rayleigh-Bénard convection. When the strength of the nonpotential terms is larger than a critical value, an alternation between three unstable asymptotic states takes place. This corresponds to the so-called Küppers-Lortz instability in the fluid description. In 0D we find, in a certain range of parameters, a Lyapunov potential that allows us to split the dynamics into a relaxational plus a residual part. We give explicit relations for the time variation of the amplitudes and the period of the orbits as a function of the energy. On the other hand, we show how the addition of noise to the equations can stabilize the switching period between the unstable states. In 1D we present a study of dynamical scaling and domain growth below the Küppers-Lortz instability. We find that dynamical scaling holds as in the potential case, but with a crossover between two well defined regimes characterized by a logarithmic and linear domain growth, respectively. In 2D the formation of rotating amplitude spirals may prevent coarsening below the Küppers-Lortz instability region. When a field amplitude is excluded, spiral formation is no longer possible and domain growth takes place. We checked that the dynamics is self-similar, with a modified growth law with respect to the potential limit. The effect of different kinds of spatial-dependent terms on the dynamics is also studied.*

2.1 Introduction

Rotating Rayleigh-Bénard convection constitutes a well-known example of a physical system for which the final state is far from thermodynamic equilibrium. Several equivalent states coexist in the system and they are subjected to a nonpotential dynamics. The study of rotating convection was directly motivated by the dynamics of planetary and stellar atmospheres and the circulation of ocean currents. Rotating convection has been studied in the realm of Swift-Hohenberg models with [98] and without [17, 99, 100] the inclusion of mean flow effects. So far, experiments on rotating convection have only been performed for small Prandtl numbers. Large Prandtl num-

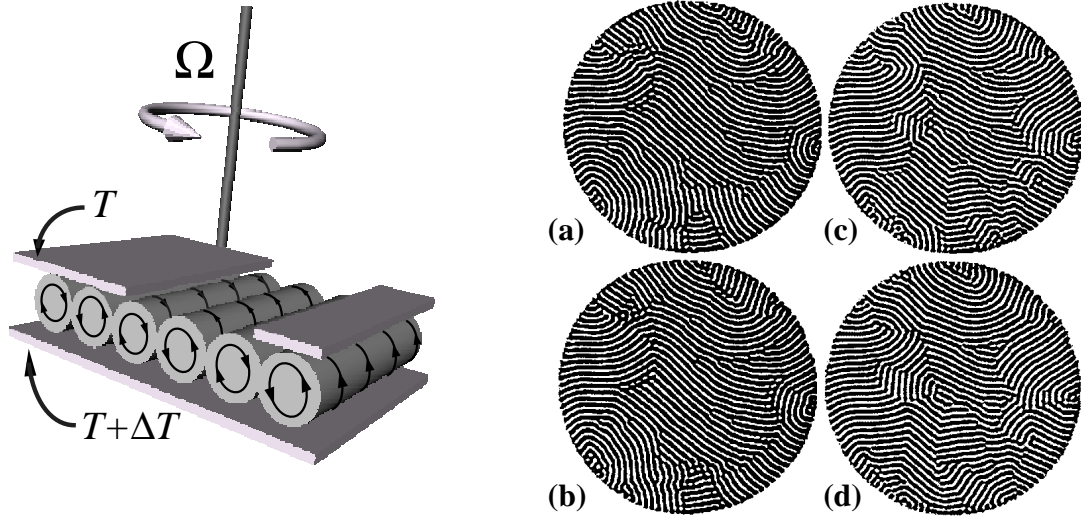


Figure 2.1: (Left) scheme of the convection of a fluid under rotation. When the rotation angular velocity Ω goes beyond a certain threshold, the convective rolls become unstable, giving rise to a self-sustained spatio-temporal chaos regime (KL instability). (Right) time sequence of Küppers-Lortz unstable domains. Taken from [107].

bers lead to more rigid convection rolls so that the mean flow coupling can be neglected. Specially interesting, both experimental and theoretically, is a spatio-temporal regime that takes place above a rotation angular velocity. The system breaks up into a persistent dynamical state such that set of parallel convection rolls are seen to change orientation (in the reference frame that moves with the fluid) with a characteristic period. This phenomenon is known as the Küppers-Lortz (KL) instability [16] (see Fig. 2.1). Experimental characterization of complex spatio-temporal dynamics in the KL unstable region has been reported in some works (see for example [107, 108, 109]). The KL instability has the attractive feature that it appears immediately at the onset of convection for arbitrary small amplitudes as long as the rotation angular velocity is sufficiently large. This feature makes it theoretically more tractable than most other systems with spatio-temporal chaos, since weakly nonlinear theory in the form of amplitude equations is expected to be applicable. In the limit of large Prandtl numbers, three-amplitude models have shown to exhibit the same qualitative features as more sophisticated Swift-Hohenberg models [17] that take into account the full range of possible roll orientations.

In this chapter we study a model proposed by Busse and Heikes to describe the KL instability. It consists of three coupled amplitude equations in the rotating frame, corresponding to three modes with wavevectors advanced 60° with respect to each other in the direction of rotation. As previously done by other authors [99, 110, 111], we incorporate spatial effects to account for the dynamical evolution of spatial domains.

From a dynamical point of view, the Busse-Heikes (BH) model describes the time evolution of three competing equivalent states under a nonpotential dynamics, both below and beyond the KL instability threshold. This model is mathematically equivalent to the May-Leonard biological model of competition between three species [112]. Other three-state models under cyclic dynamics have been studied elsewhere (see for example [89, 113] and references therein). The zero-dimensional version of the model captures certain elements of KL convection. In particular, the alternating period between the modes can be worked out analytically in a certain range of parameters. With the inclusion of noise terms in the model the period of the orbits saturates to a constant statistical value. In the limit of small noise intensities, an analytical approach to the mean period can be given. When spatial-dependent terms are taken into account, and below the KL instability point, where three homogeneous states coexist, the BH equations are a prototype nonpotential model for which the issues of domain growth and dynamical scaling can be explored. In one spatial dimension there is always coarsening out of the KL unstable region. Two-dimensional systems, on the other hand, show different dynamical behavior grossly dominated by vertices where three domain walls meet and which have no parallel in one-dimensional systems. Coarsening is inhibited even below the KL instability point by the appearance of three-armed rotating spirals, each arm associated with a front connecting two homogeneous states. However, nonpotential domain growth can be triggered by exciting the growth of only two of the three modes.

In section 2.2 we introduce the theoretical model and discuss several possible choices for the spatial-dependent diffusion terms. Section 2.3 deals with the zero-dimensional version of the model. We describe the homogeneous solutions and analyze their linear stability. We also compute both analytical and numerically the alternating period of the KL instability in a certain range of parameters, with and without the inclusion of noise terms in the equations. Section 2.4 is devoted to one-dimensional systems. We focus on a region below the KL instability in order to study the issues of domain growth and dynamical scaling. Two-dimensional systems are worked out in section 2.5. We investigate the formation of rotating spiral structures that inhibit coarsening. We also study domain growth and dynamical scaling in the limit of potential dynamics, and in the nonpotential regime when only two modes are excited in the transient dynamics. Moreover, the effect on the dynamics of isotropic and anisotropic spatial-dependent diffusion terms is studied. Finally, in section 2.6 we end with some conclusions and an outlook.

2.2 Theoretical Model

We base our study on the following theoretical model:

$$\begin{aligned}\partial_t A_1 &= \mathcal{L}_1 A_1 + A_1[\nu - |A_1|^2 - (\eta + \delta)|A_2|^2 - (\eta - \delta)|A_3|^2], \\ \partial_t A_2 &= \mathcal{L}_2 A_2 + A_2[\nu - |A_2|^2 - (\eta + \delta)|A_3|^2 - (\eta - \delta)|A_1|^2], \\ \partial_t A_3 &= \mathcal{L}_3 A_3 + A_3[\nu - |A_3|^2 - (\eta + \delta)|A_1|^2 - (\eta - \delta)|A_2|^2].\end{aligned}\tag{2.1}$$

Here $\mathcal{L}_i(\partial^{(n)}; \{\alpha\})$ ($i = 1, 2, 3$) are linear differential operators, and the A_i 's are complex amplitudes. If one neglects the spatial dependence, we recover a model first proposed in the context of fluid dynamics by Busse and Heikes [21], which is mathematically equivalent to a model of three competing biological species [112]. In the Busse-Heikes model, A_1 , A_2 , and A_3 are the amplitudes of the three selected modes corresponding to three different orientations of the convection rolls in the rotating cell. The parameter ν is proportional to the difference between the Rayleigh number and the critical Rayleigh number for convection. We will consider exclusively in this chapter the case of well-developed convection for which ν can be rescaled to 1, i.e. $\nu = 1$ henceforth. The exact relation of η and δ to the fluid properties has been given in [21]. We mention here that η is a parameter related to the temperature gradient and the Taylor number (proportional to the rotation speed Ω) in such a way that it takes a nonzero value in the case of no rotation, $\Omega = 0$, whereas δ is related to the Taylor number in such a way that $\Omega = 0$ implies $\delta = 0$. The analysis of [21] and [112] shows that, in zero-dimensional systems and for a certain range of the parameters η and δ (see section 2.3), there are no stable homogeneous solutions and the dynamics tends asymptotically to a sequence of alternations of the three modes (Küppers-Lortz instability). An unwanted feature of the 0D model is that the alternation time is not constant, but increases with time, contrary to experiments where an approximately constant period is observed. Busse and Heikes proposed that the addition of small noise could stabilize the period [54] (we discuss that in section 2.3.3), but an alternative explanation proposed by Tu and Cross [110] considered the addition of spatial-dependent terms to the equations without the necessity of the inclusion of the noise terms.

Two main classes of operators can be considered: isotropic and anisotropic. Whereas a multiple scale analysis of the convective instability usually leads to anisotropic terms, the isotropic terms are often justified in the sake of mathematical simplicity. The simplest isotropic terms are the Laplacian operators:

$$\mathcal{L}_j^{\text{ID}} = \nabla^2, \quad j = 1, 2, 3.\tag{2.2}$$

They have been considered, for instance, in [89] in the context of population dynamics.

Two types of anisotropic terms have been proposed for similar fluid problems in the literature: (*i*) the Newell-Whitehead-Segel (NWS) terms [114] and (*ii*) the Gunaratne-Ouyang-Swinney (GOS) terms [115, 116].

The NWS theory [114] is based on the observation that close to the onset of patterns, the uniform state is unstable only to perturbations with wavenumber close to q_0 . Their multiple scale analysis yields spatial-dependent terms of the form:

$$\mathcal{L}_j^{\text{NWS}} = \left(\partial_{x_j} - \frac{i}{2q_0} \partial_{y_j y_j} \right)^2, \quad j = 1, 2, 3, \quad (2.3)$$

where $x_j = \mathbf{r} \cdot \hat{\mathbf{n}}_j$, $y_j = (\mathbf{r} \times \hat{\mathbf{n}}_j) \cdot \hat{\mathbf{z}}$, and $\hat{\mathbf{n}}_j$ is the unit vector normal to the j th roll. These terms are considered in [110].

The GOS terms were obtained in [115] by using an analysis identical to the NWS theory to lowest order in perturbation theory and have been reobtained by the use of renormalization group techniques by Graham [116]. The advantage of these terms is that they exactly preserve the Euclidean symmetries of the physical system (invariance under translations, rotations, and reflection). The GOS terms read:

$$\mathcal{L}_j^{\text{GOS}} = \left(\partial_{x_j} - \frac{i}{2q_0} \nabla^2 \right)^2, \quad j = 1, 2, 3. \quad (2.4)$$

Without altering the essentials of the problem the NWS and GOS terms can be further simplified leading to second-order directional derivatives along three directions with a relative orientation of 60° [110]:

$$\mathcal{L}_j^{\text{AD}} = \partial_{x_j x_j}, \quad j = 1, 2, 3. \quad (2.5)$$

The terms (2.5) are more tractable numerically and they are the only anisotropic terms that we will consider. With the inclusion of the isotropic derivatives (2.2) we will take (2.1) as a mathematical model to study scaling properties and growth processes in a nonpotential dynamics. In section 2.5.3 we compare the dynamical evolution corresponding to each one of the isotropic and anisotropic spatial-dependent terms presented before.

Notice that system (2.1) is invariant under the following transformations:

- (a) $x \rightarrow x + x_0, t \rightarrow t + t_0$ (spatio-temporal translation symmetry).
- (b) $\{\mathcal{L}_1, A_1\} \rightarrow \{\mathcal{L}_2, A_2\}, \{\mathcal{L}_2, A_2\} \rightarrow \{\mathcal{L}_3, A_3\}, \{\mathcal{L}_3, A_3\} \rightarrow \{\mathcal{L}_1, A_1\}$ (cyclic permutation symmetry).
- (c) $\{\mathcal{L}_i, A_i\} \rightleftharpoons \{\mathcal{L}_j, A_j\}, \delta \rightarrow -\delta$, where i, j are the indices of any two different amplitudes.

The system (2.1) can be rewritten as

$$A_i(\mathbf{r}, t; \eta, \delta) = -\frac{\delta \mathcal{F}_{\text{BH}}}{\delta A_i^*} + \delta \cdot f_i(A_1, A_2, A_3), \quad i = 1, 2, 3, \quad (2.6)$$

where \mathcal{F}_{BH} is a real functional of the fields whose expression is:

$$\mathcal{F}_{\text{BH}}[A_1, A_2, A_3] = \int d\mathbf{r} \left[\frac{1}{2} \sum_{i=1}^3 |\mathcal{L}_i^{1/2} A_i|^2 - \sum_{i=1}^3 |A_i|^2 + \frac{1}{2} \sum_{i=1}^3 |A_i|^4 + \eta \sum_{\substack{i,j=1 \\ i < j}}^3 |A_i|^2 |A_j|^2 \right], \quad (2.7)$$

and the functions $\{f_i\}_{i=1}^3$ are given by:

$$\begin{aligned} f_1 &= A_1(|A_3|^2 - |A_2|^2), \\ f_2 &= A_2(|A_1|^2 - |A_3|^2), \\ f_3 &= A_3(|A_2|^2 - |A_1|^2). \end{aligned} \quad (2.8)$$

When $\delta = 0$, the dynamical flow is of the *relaxational gradient* type (see section 1.2), that is, the functional \mathcal{F}_{BH} is a Lyapunov functional that decreases monotonically with time. When $\delta \neq 0$, however, one cannot find generally such a functional and we say that the system is *nonpotential*. However, and according to the discussion of section 1.2, \mathcal{F}_{BH} is a Lyapunov potential if the following orthogonality condition is satisfied [see Eq. (1.11)]:

$$\delta \int d\mathbf{r} \frac{\delta \mathcal{F}_{\text{BH}}}{\delta \mathbf{A}^*} \cdot \mathbf{f}(\mathbf{A})^* + \text{c.c.} = 0, \quad (2.9)$$

with $\mathbf{A} = (A_1, A_2, A_3)$, $\mathbf{f} = (f_1, f_2, f_3)$. Without spatial dependence (2.9) is satisfied for $\eta = 1$ as explained in section 2.3.1; in this case the BH dynamics is a nonrelaxational potential flow (see 1.2). Unfortunately, (2.9) is not trivially satisfied when $\eta = 1$ for any of the spatial-dependent terms mentioned before.

2.3 Zero-dimensional Systems

Before extending the study to higher dimensions, it is useful to understand the zero-dimensional case (BH model) which can give us some insight into the dynamical behavior of the system.

Writing $\mathcal{L}_j = 0$, $A_j(t) = \sqrt{R_j(t)} e^{i\theta_j(t)}$, $j = 1, 2, 3$, we obtain from (2.1) equations for the modulus square of the amplitudes:

$$\begin{aligned} \dot{R}_1 &= 2R_1[1 - R_1 - (1 + \mu + \delta)R_2 - (1 + \mu - \delta)R_3], \\ \dot{R}_2 &= 2R_2[1 - R_2 - (1 + \mu + \delta)R_3 - (1 + \mu - \delta)R_1], \\ \dot{R}_3 &= 2R_3[1 - R_3 - (1 + \mu + \delta)R_1 - (1 + \mu - \delta)R_2], \end{aligned} \quad (2.10)$$

and the phases

$$\begin{aligned}
\dot{\theta}_1 &= 0, \\
\dot{\theta}_2 &= 0, \\
\dot{\theta}_3 &= 0,
\end{aligned} \tag{2.11}$$

where $\mu = \eta - 1$. Therefore, the phases are arbitrary constants fixing the location of the rolls. A solution of the form $\Psi(\mathbf{r}) = \sqrt{R_j} e^{iq_0(\hat{n}_j \cdot \mathbf{r} + \theta_j)} + \text{c.c.}$ represents a set of rolls of wavelength $2\pi/q_0$ oriented in a direction perpendicular to the vector \hat{n}_j . Hence, in this 0D model one can simply consider the equations for the *real* variables $\{R_j\}_{j=1}^3$ instead of the equations for the complex variables $\{A_j\}_{j=1}^3$. A similar set of equations has been proposed to study population competition dynamics. For a single biological species, the Verhulst or logistic model assumes that its population $N(t)$ satisfies the evolution equation:

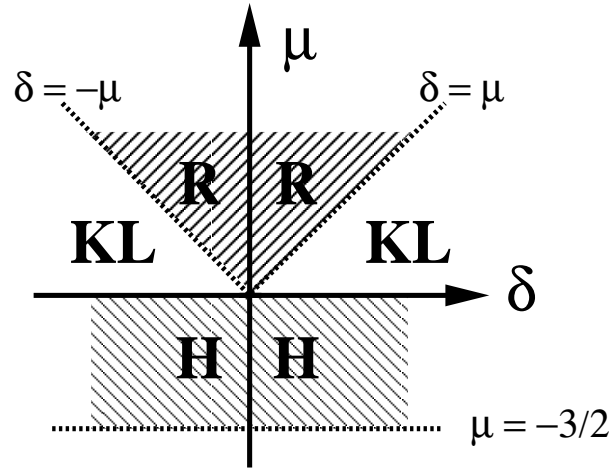
$$\frac{dN}{dt} = rN(1 - \lambda N), \tag{2.12}$$

where r is the reproductive growth rate and λ is a coefficient denoting competition amongst the members of the species. If three species are competing together, it is adequate in some occasions to model this competition by introducing a Gause-Lotka-Volterra type of equations [112]:

$$\begin{aligned}
\dot{N}_1 &= rN_1(1 - \lambda N_1 - \alpha N_2 - \beta N_3), \\
\dot{N}_2 &= rN_2(1 - \lambda N_2 - \alpha N_3 - \beta N_1), \\
\dot{N}_3 &= rN_3(1 - \lambda N_3 - \alpha N_1 - \beta N_2),
\end{aligned} \tag{2.13}$$

which are the same that the BH equations (2.10) with the identifications $r = 2$, $\lambda = 1$, $\alpha = 1 + \mu + \delta$, $\beta = 1 + \mu - \delta$. These equations are the basis of May and Leonard analysis [112]. We also mention the work of Soward [117] which is concerned with the study of the nature of the bifurcations mainly, but not limited to, close to the convective instability for small ν , in a slightly more general model that includes also quadratic nonlinearities in the equations. In the remaining of the section we will analyze some of the properties of the homogeneous solutions of the BH equations (2.1). Although our analysis essentially reobtains the results of May and Leonard, we find it convenient to give it in some detail because, besides obtaining some further analytical expressions for the time variation of the amplitudes, we are able in some cases of rewriting the dynamics in terms of a Lyapunov potential. The existence of this Lyapunov potential allows us to interpret the asymptotic dynamics for $\mu = 0$ as a residual (conservative) Hamiltonian dynamics. For $\mu > 0$ we will use an adiabatic approximation with a time-dependent Hamiltonian. This interpretation will turn out to be very useful in the case that noise terms are added to the dynamical equations, because the found Lyapunov potential governs approximately the stationary probability distribution.

Figure 2.2: Linear stability diagram of the homogeneous solutions of (2.1). Inside the region labeled 'R', rolls are stable whereas in the 'H' region, the stable solution is the hexagon. The 'KL' region corresponds to the Küppers-Lortz instability. Other homogeneous solutions are never stable.



There exist two kinds of homogeneous solutions that are stable in some region of the parameter space spanned by μ and δ . These are:

(a) *Roll solutions.* There are three of these kind, each characterized by one amplitude equal to 1 and the other two equal to zero, that is

$$\text{R: } R_i = 1, R_j = 0, j \neq i, i = 1, 2, 3. \quad (2.14)$$

These solutions are linearly stable whenever $|\delta| < \mu$.

(b) *Hexagon solution.* This solution is such that the three modes are different from zero and take the same value:

$$\text{H: } R_1 = R_2 = R_3 = \frac{1}{3 + 2\mu}. \quad (2.15)$$

This solution requires $\mu > -3/2$ and is linearly stable for $\mu < 0$.

There are other stationary solutions of (2.1), but there are never stable. With all this information, we can construct the stability diagram of the homogeneous solutions (2.14) and (2.15) (see Fig. 2.2). The KL instability occurs when $|\delta| > \eta - 1 = \mu$ and it can be described in the context of this zero-dimensional model as a cyclic alternation between the three unstable roll solutions just as shown in Fig. 2.3. In brief: the KL unstable region is characterized by the presence of three unstable fixed points, and a heteroclinic cycle connecting them.

We will restrict ourselves in this section only to the KL regime, leaving the study of other regimes (which are trivial in the 0D model) for higher dimensions.

If $\delta = 0$ the system is purely relaxational and the corresponding stability

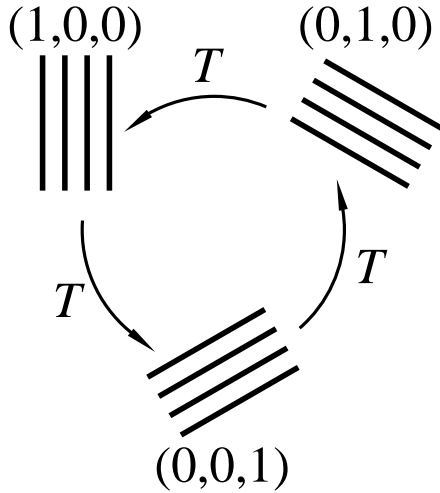


Figure 2.3: Sketch of the KL instability. The system switches alternatively between the three unstable fixed points.

diagram can be obtained also by looking at the minima of the *potential*:

$$\begin{aligned}
 V(A_1, A_2, A_3) &= -\sum_{i=1}^3 |A_i|^2 + \frac{1}{2} \sum_{i=1}^3 |A_i|^4 + (1 + \mu) \sum_{\substack{i,j=1 \\ i < j}}^3 |A_i|^2 |A_j|^2 \\
 &= -(R_1 + R_2 + R_3) + \frac{1}{2}(R_1^2 + R_2^2 + R_3^2) + (1 + \mu)(R_1 R_2 + R_2 R_3 + R_1 R_3). \quad (2.16)
 \end{aligned}$$

Note that V is just the functional \mathcal{F}_{BH} given by Eq. (2.7) in zero spatial dimensions. For the roll and hexagon solutions, the potential takes the values:

$$V_{\text{R}} = -\frac{1}{2} \quad \text{Roll solution,} \quad (2.17)$$

$$V_{\text{H}} = \frac{-3}{6 + 4\mu} \quad \text{Hexagon solution.} \quad (2.18)$$

The study of the potential (for $\delta = 0$) shows that the rolls (hexagons) are maxima (minima) of the potential for $\mu < 0$ and minima (maxima) for $\mu > 0$. Also, the potential for the roll solutions is smaller than the potential for the other solutions whenever $\mu > 0$, indicating that the rolls are the most stable (and indeed the only stable ones) solutions in this case. Unfortunately, this simple criterion does not have an equivalent in the nonpotential case, $\delta \neq 0$, for which one has to perform the full linear stability analysis.

2.3.1 The Case $\mu = 0$

When $\delta = 0$, it is clear that the function V is a Lyapunov function. What is not evident is the fact that V acts also as a potential in the case $\mu = 0$. This is seen by writing the orthogonality condition (2.9) in zero spatial dimensions,

which amounts to:

$$\delta \cdot \mu = 0. \quad (2.19)$$

Hence, in the case $\mu = 0$, V acts as a Lyapunov and the dynamics is driven by a *nonrelaxational potential flow* and, whereas the dynamics still leads to the surface of minima of the Lyapunov function, there is a residual motion [given by the rhs of Eq. (2.6)] in this surface for which $dV/dt = 0$. In other words: the relaxational terms in the dynamics make the system evolve towards the degenerate minimum of the potential (which for $\mu = 0$ occurs at $R_1 + R_2 + R_3 = 1$). The residual motion is governed by the nonpotential part that is proportional to δ and this residual motion disappears for $\delta = 0$, the relaxational gradient case.

According to this reduction of the dynamics as a residual motion in the surface of minima of the potential V , strictly valid only for $\mu = 0$, it turns out that it is possible to solve essentially the equations of motion. By “essentially” we mean that after a transient time in which the system is driven to the minima of V , the residual motion is a conservative one in which it is possible to define a Hamiltonian-like function that allows one to find explicit expressions for the time variation of the dynamical variables. Let us define the variable

$$x(t) = R_1(t) + R_2(t) + R_3(t). \quad (2.20)$$

It is straightforward to see that $x(t)$ satisfies the evolution equation:

$$\dot{x} = 2x(1 - x) - 4\mu y, \quad (2.21)$$

where

$$y(t) = R_1 R_2 + R_2 R_3 + R_3 R_1. \quad (2.22)$$

When $\mu = 0$, the equation for $x(t)$ is closed and its solution is

$$x(t) = \frac{1}{\left(\frac{1}{x_0} - 1\right) e^{-2t} + 1}. \quad (2.23)$$

Here $x_0 \equiv x(t = 0)$. Eq. (2.23) is such that $\lim_{t \rightarrow \infty} x(t) = 1$ regardless of the initial condition. In practice, and due to the exponential decay in the denominator of (2.23), after a transient time $t = O(1)$, $x(t)$ already takes its asymptotic value $x(t) = 1$. We can then eliminate from the evolution equations one of the three variables, taking, for instance, $R_1(t) = 1 - R_2(t) - R_3(t)$. In this way, the original two-variable problem is reduced to a residual dynamics in a two-variable subspace:

$$\begin{aligned} \dot{R}_2 &= 2\delta R_2(1 - R_2 - 2R_3), \\ \dot{R}_3 &= -2\delta R_3(1 - 2R_2 - R_3). \end{aligned} \quad (2.24)$$

These are Hamilton's equations:

$$\begin{aligned}\dot{R}_2 &= 2\delta \frac{\delta \mathcal{H}}{\delta R_3}, \\ \dot{R}_3 &= -2\delta \frac{\delta \mathcal{H}}{\delta R_2},\end{aligned}\tag{2.25}$$

corresponding to the Hamiltonian:

$$\mathcal{H}(R_2, R_3) = R_2 R_3 (1 - R_2 - R_3).\tag{2.26}$$

Since time does not appear explicitly in (2.26), the Hamiltonian $\mathcal{H}(t) = E$ is a constant of motion (which will be called the "energy") in the asymptotic dynamics for which the Hamiltonian description is valid. Although the Hamiltonian dynamics is valid only after a transient time, the value of E depends only on initial conditions at $t = 0$. The dependence of E on the initial conditions can be found by introducing the variable $\hat{\mathcal{H}}$:

$$\hat{\mathcal{H}} = R_1 R_2 R_3,\tag{2.27}$$

which, in the asymptotic limit ($t \rightarrow \infty$) is equivalent to \mathcal{H} . It is easy to show that for arbitrary values of μ and δ , $\hat{\mathcal{H}}$ satisfies the following evolution equation:

$$\hat{\mathcal{H}}^{-1} \frac{d\hat{\mathcal{H}}}{dt} = 6 - (6 + 4\mu)x.\tag{2.28}$$

One can reduce the original dynamical problem to variables $(x, y, \hat{\mathcal{H}})$ but the equation for y turns out to be too complicated (see [117]). Now, substituting the solution for $x(t)$ valid in the $\mu = 0$ case [Eq. (2.23)], we get

$$\hat{\mathcal{H}}(t) = \hat{\mathcal{H}}_0 [(1 - x_0)e^{-2t} + 1]^{-3},\tag{2.29}$$

where $\hat{\mathcal{H}}_0 = \hat{\mathcal{H}}(t = 0)$. The asymptotic value for $\mathcal{H}(t)$ is

$$E = \lim_{t \rightarrow \infty} \mathcal{H}(t) = \lim_{t \rightarrow \infty} \hat{\mathcal{H}}(t) = \hat{\mathcal{H}}_0 x_0^{-3} = \frac{R_1(0)R_2(0)R_3(0)}{(R_1(0) + R_2(0) + R_3(0))^3}.\tag{2.30}$$

Again, this asymptotic value is reached after a transient time of order 1. The previous expression suggests to define the time-dependent variable

$$E(t) = \frac{\hat{\mathcal{H}}}{x^3} = \frac{R_1 R_2 R_3}{(R_1 + R_2 + R_3)^3},\tag{2.31}$$

whose evolution equation (again, for arbitrary μ, δ) is

$$\frac{dE}{dt} = -4\mu \left(x - \frac{3y}{x} \right) E \equiv -4\mu f(t)E.\tag{2.32}$$

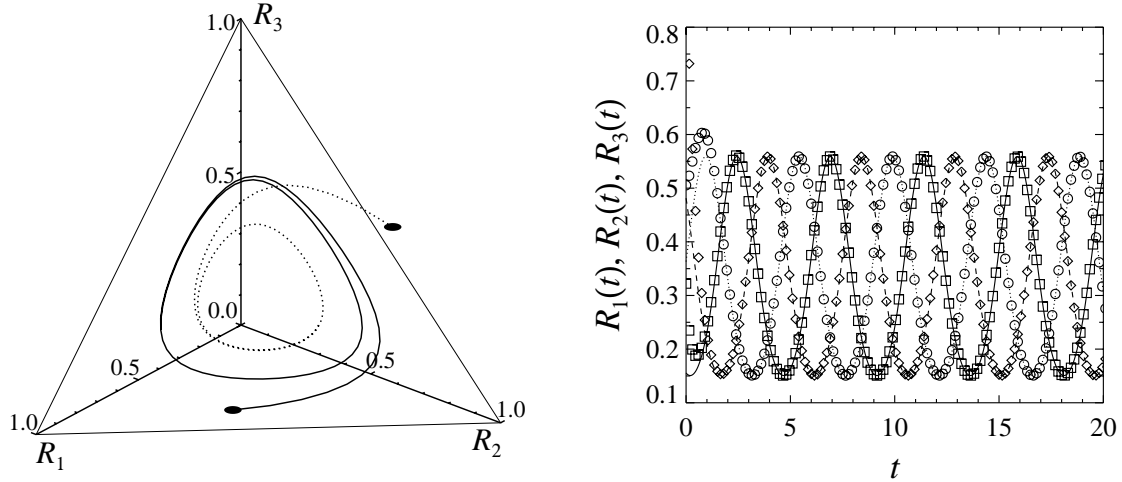


Figure 2.4: (Left) Hamiltonian orbits in the 3D space $\{R_1, R_2, R_3\}$ corresponding to two different initial conditions. After a transient time of order 1, the trajectory is a periodic orbit located on the plane $R_1 + R_2 + R_3 = 1$. (Right) Time evolution of the amplitudes. The lines are the theoretical predictions that come from Eqs. (2.40a–c). Parameter values are $\mu = 0$, $\delta = 1.3$.

Therefore, in the case $\mu = 0$, $E(t) = E$ is a constant of motion that coincides, in the asymptotic limit when $x = 1$, with the numerical value of the Hamiltonian \mathcal{H} . According to their definition, $E(t)$ is a bounded function $0 \leq E(t) \leq 1/27$, and $f(t) \geq 0$ for $\{R_1, R_2, R_3\} \geq 0$.

The problem in the case $\mu = 0$ can now be given an explicit solution [112]. After a transient time (or order 1), the motion occurs on the plane $R_1 + R_2 + R_3 = 1$ (see Fig. 2.4). The motion is periodic because it corresponds to a Hamiltonian orbit with a fixed energy. The exact shape of the trajectory depends on the value of the energy E which, in turn, depends on initial conditions. More interestingly, the period of the orbit can also be computed. We can solve for instance for R_3 by eliminating R_2 from the expression (2.26) for the energy:

$$R_2 = \frac{1}{2} \left(1 - R_3 \pm \sqrt{(1 - R_3)^2 - \frac{4E}{R_3}} \right). \quad (2.33)$$

We obtain a closed equation for R_3 :

$$\dot{R}_3 = \pm 2\delta \sqrt{R_3^2(1 - R_3)^2 - 4ER_3}. \quad (2.34)$$

Let b and c the return points, i.e., the solutions of

$$R_3(1 - R_3)^2 - 4E = 0, \quad (2.35)$$

lying in the interval $(0, 1)^1$. The three roots $\{a, b, c\}$ of the above three-degree equation are real and two of them (the return points b, c) lie in the interval

¹The case $R_3 = 0$ necessarily leads to $E = 0$ and the dynamics stops.

(0, 1). The explicit expression for the roots is:

$$a = \frac{2}{3} \left[1 + \cos \frac{\theta}{3} \right], \quad (2.36a)$$

$$b = \frac{2}{3} \left[1 + \cos \left(\frac{\theta - 2\pi}{3} \right) \right], \quad (2.36b)$$

$$c = \frac{2}{3} \left[1 + \cos \left(\frac{\theta + 2\pi}{3} \right) \right], \quad (2.36c)$$

where $\theta = \arccos(54E - 1)$. Integration of Eq. (2.34) yields the equation of motion for $R_3(t)$:

$$\int_c^{R_3(t)} \frac{dx}{\sqrt{x(x-a)(x-b)(x-c)}} = 2\delta \int_{t_0}^t dt', \quad (2.37)$$

where we have chosen the initial time t_0 to correspond to the minimum value when $R_3(t) = c$. The integral in the left hand side can be expressed in terms of the Jacobi elliptic function $\text{sn}[x|q]$, to yield:

$$R_3(t) = \frac{bc}{b + (c-b) \text{sn}^2[\delta \sqrt{b(a-c)}(t-t_0)|q]}, \quad q = \frac{a(b-c)}{b(a-c)}. \quad (2.38)$$

The period of the orbit T can be expressed in terms of the complete elliptic function of the first kind $K(q)$:

$$T = \frac{2}{\delta \sqrt{b(a-c)}} K(q), \quad (2.39)$$

and the equation for $R_3(t)$ can be written as:

$$R_3(t) = \frac{bc}{b + (c-b) \text{sn}^2[2K(q)T^{-1}(t-t_0)|q]}. \quad (2.40a)$$

Finally, the evolution equations for the other variables are:

$$R_1(t) = R_3(t - T/3), \quad (2.40b)$$

$$R_2(t) = R_3(t - 2T/3). \quad (2.40c)$$

Summarizing, the behavior of the dynamical system in the case $\mu = 0$ can be described as follows: after a transient time (or order 1) the three variables $\{R_j\}_{j=1}^3$ vary periodically in time on the plane $R_1 + R_2 + R_3 = 1$. When R_1 decreases, R_2 increases, etc. The period of the orbit depends only on the initial conditions through a constant of motion E . The explicit expression for the period, $T = T(E)$ [Eq. (2.39)], shows that the period diverges logarithmically when E tends to zero, namely

$$T(E) = -\frac{3}{2\delta} \log E \times (1 + O(E)), \quad (2.41)$$

and the amplitude of the oscillations $\Delta \equiv b - c$ depends also on the constant E . When E tends to 0 the amplitude approaches 1:

$$\Delta = (1 - 2E^{1/2}) \times (1 + O(E)). \quad (2.42)$$

All these relations have been confirmed by a numerical integration of the BH equations. In Fig. 2.4 we plot the time evolution of the amplitudes in the case $\mu = 0$, $\delta = 1.3$. In this figure we can observe that, after an initial transient time, there is a periodic motion (characteristic of the KL instability) well described by the previous analytical expressions.

2.3.2 The Case $\mu > 0$

Once we have understood the case $\mu = 0$, we now turn to $\mu > 0$. In this case, the function V is no longer a Lyapunov potential and we can not restrict the motion to the manifold of minima of V . However, since the main features of the KL dynamics are already present in the case $\mu = 0$, one would like to perform some kind of perturbative analysis valid for small μ in order to characterize the KL instability. We exploit these ideas to develop some heuristic arguments that will allow us to make some quantitative predictions about the evolution of the system.

According to Eq. (2.32), and since the quantity $f(t)$ is always positive, one can infer that $E(t)$ decreases with time in a characteristic time scale of order μ^{-1} . If μ is small, $E(t)$ decreases very slowly and we can extend the picture of the previous section by using an adiabatic approximation. We assume, then, that the dynamics for $\mu > 0$ can be described by a Hamiltonian dynamics with an energy that slowly decreases with time. Hence, in reducing the energy, the system changes (similarly to a damped harmonic oscillator) spiraling from a periodic orbit to another. Assuming this picture of a time-dependent energy $E(t)$, the main features of the case $\mu = 0$ can now be extended. This model has several predictions:

- (P1) After a transient time of order 1, The motion occurs near the plane $R_1 + R_2 + R_3 = 1$. This is checked in the simulations as we can see in Fig. 2.5.
- (P2) The period of the orbits is now a function of time. Since the energy decreases towards zero, it follows from previous arguments that the period diverges with time. Moreover, it is possible to give an approximate expression for the time dependence of the period. Integration of Eq. (2.32) leads to:

$$E(t) = E(0) e^{-4\mu \int_{t_0}^t f(t') dt'} \approx E(t_0) e^{-4\mu(t-t_0)}, \quad (2.43)$$

where we have approximated $f(t)$ by its asymptotic value $f(t) = 1$. Once we have the time evolution of the energy, we can compute the time dependence of the period by using $T(t) = T(E(t))$ as given by (2.39). For

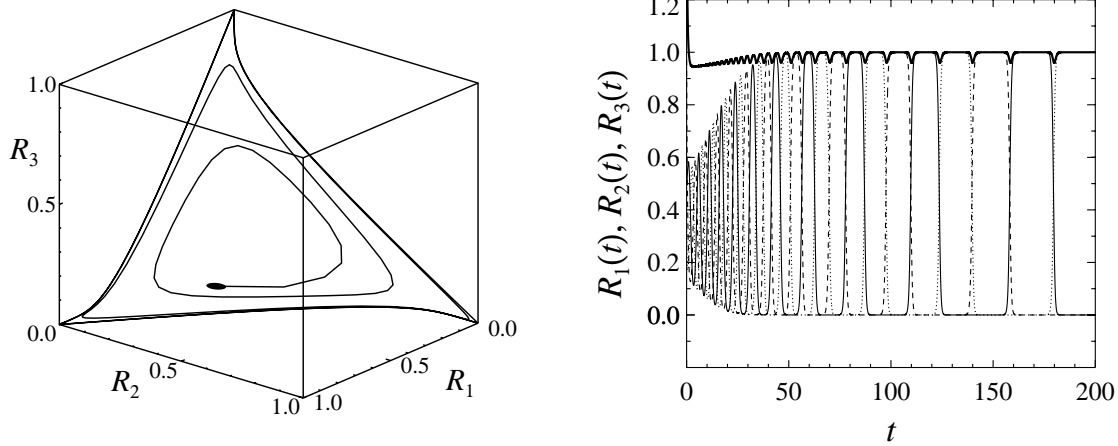


Figure 2.5: (Left) three dimensional trajectory in the 3D space $\{R_1, R_2, R_3\}$ in the KL instability region, and (right) time evolution of the amplitudes; the thick line corresponds two the sum of the three amplitudes which is approximately equal to 1. Notice that the time period between consecutive alternations of the modes increases with time. Parameter values are $\mu = 0.1$ and $\delta = 1.3$.

large times, the energy is small and the asymptotic result (2.41) leads to:

$$T(t) = T_0 + \frac{6\mu}{\delta} t. \quad (2.44)$$

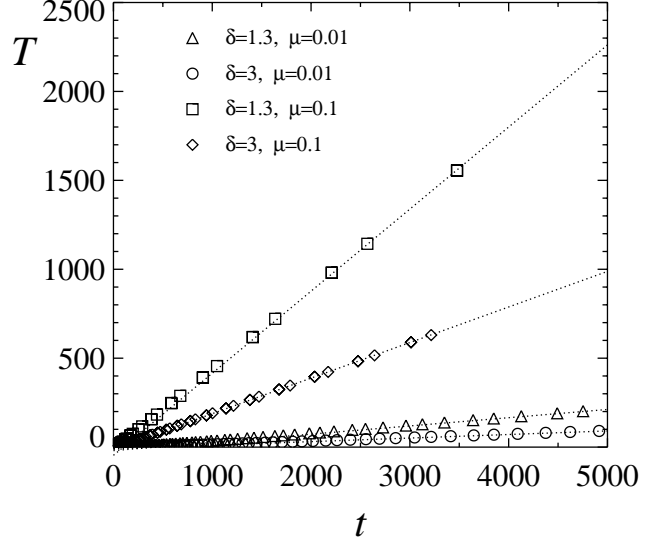
This shows that the period increases linearly with time, in agreement with the results of [112] in which the residence period was shown to behave also linearly with time (although with a different prefactor). In order to check this relation, we have performed a numerical integration of Eqs. (2.10) and computed the period T , defined as the time it takes a given amplitude to reach a reference level (taken arbitrarily as $R_j = 0.5$), as a function of time. The results for $\delta = \{1.3, 3\}$ and $\mu = \{0.01, 0.1\}$, plotted in Fig. 2.6, show that there is a perfect agreement between the theoretical expression and the numerical results.

(P3) The amplitude of the oscillations, as given by the return points $\Delta(t) = b(t) - c(t)$, is now a function of time. Using expression (2.42) with an energy that decreases with time as in (2.43), we obtain that the amplitude of the oscillations increases with time [see Fig. 2.5], and that it approaches 1 in a time of order $t \sim \mu^{-1}$. More specifically, we have:

$$1 - \Delta(t) = (1 - \Delta_0) e^{-2\mu t}. \quad (2.45)$$

In summary, for the case $\mu > 0$, the period of the orbits, which is a function of the energy, increases linearly with time and the amplitude of the oscillations approaches 1. We characterize in this way the increase of the period between successive alternation of the dominating modes [see Fig. 2.5] as an

Figure 2.6: Time evolution of the period, defined as the time between a given amplitude crosses the reference level $R_j = 0.5$, for several values of μ and δ . We also plot lines with slopes $6\mu/\delta$ as predicted by Eq. (2.44).



effect of the Hamiltonian dynamics with a slowly decreasing energy. This prediction of the BH model for the KL instability is unphysical, since the experimental results do not show such an increase of the period. Busse and Heikes were fully aware of this problem and suggested that noise terms (“small amplitude disturbances”), that are present at all times, prevent the amplitudes from decaying to arbitrary small levels and a motion which is essentially periodic but with a fluctuating period is established. In the next section we study the effect of noise in the dynamical equations.

2.3.3 Busse-Heikes Model in the Presence of Noise

In order to account for the effect of the fluctuations, we modify the BH equations by the inclusion of noise terms:

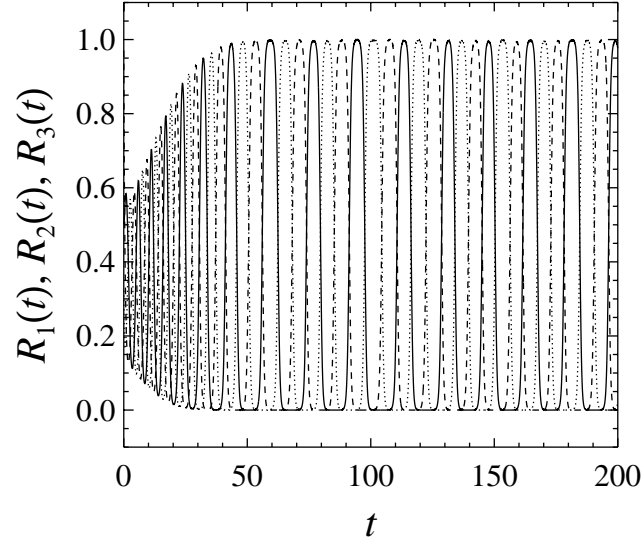
$$\begin{aligned}
 \dot{A}_1 &= A_1[1 - |A_1|^2 - (1 + \mu + \delta)|A_2|^2 - (1 + \mu - \delta)|A_3|^2] + \xi_1(t), \\
 \dot{A}_2 &= A_2[1 - |A_2|^2 - (1 + \mu + \delta)|A_3|^2 - (1 + \mu - \delta)|A_1|^2] + \xi_2(t), \\
 \dot{A}_3 &= A_3[1 - |A_3|^2 - (1 + \mu + \delta)|A_1|^2 - (1 + \mu - \delta)|A_2|^2] + \xi_3(t).
 \end{aligned} \tag{2.46}$$

We take the simplest case in which the $\xi_i(t)$ are complex white-noise processes with correlations:

$$\langle \xi_i(t) \xi_j^*(t') \rangle = 2\varepsilon \delta(t - t') \delta_{ij}. \tag{2.47}$$

As mentioned before, and in the case of parameter values lying inside the KL instability region, noise prevents the system from spending an increasing amount of time near any of the (unstable) fixed points. The mechanism for this is that fluctuations are amplified when the trajectory comes close to one of the (unstable) fixed points of the dynamics and the trajectory is then repelled

Figure 2.7: Time evolution of the amplitudes corresponding to the Busse-Heikes model with noise [Eqs. (2.46)]. In this case the oscillating period fluctuates around a mean value. Parameter values are $\delta = 1.32$, $\mu = 0.10$, $\varepsilon = 10^{-6}$.

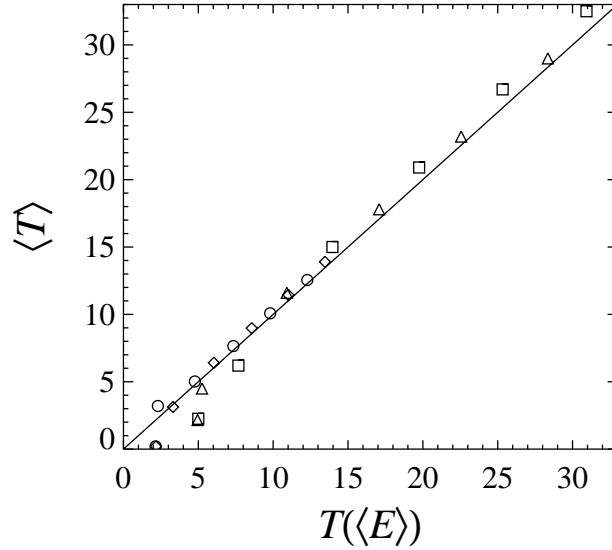


towards another fixed point. Hence, a fluctuating, but periodic on average, trajectory is sustained by noise. Within the general picture developed in the previous sections, the main role of noise for $\mu > 0$ is that of preventing $E(t)$ from decaying to zero. This can be understood in the following qualitative terms: when noise is absent, the dynamics brings the system to the surface of minima of V , where the dissipative terms act by decreasing the energy in a time scale of order μ^{-1} [see Eq. (2.43)]. The inclusion of noise has the effect of counteracting this energy decrease that occurs in the surface of minima of V by “injecting energy” into the system. As a consequence, $E(t)$ no longer decays to zero but it stabilizes around a mean value $\langle E \rangle$. By stabilizing the orbit around that one corresponding to the mean value $\langle E \rangle$, fluctuations in the residual motion stabilize the mean period to a finite value. In order to check this picture, we have performed numerical simulations of Eqs. (2.46) for small noise amplitude ε , using a stochastic Runge-Kutta algorithm [54]. The numerical simulations (see Fig. 2.7), show indeed that the trajectories have a well-defined average period $\langle T \rangle$.

From a more quantitative point of view, we can, according to the previous picture, compute the mean period $\langle T \rangle$, which in the purely Hamiltonian case was a function of E , by using the same function applied to the mean value of E , i.e. $\langle T \rangle = T(\langle E \rangle)$. This relation has been checked in the numerical simulations. In Fig. 2.8 we plot the mean period $\langle T \rangle$ versus the period calculated from the mean energy, $\langle E \rangle$, which has also been evaluated numerically. From this figure it appears that our qualitative argument of a trajectory stabilized around the Hamiltonian orbit, corresponding to the average energy, is well supported by the numerical simulations.

In order to proceed further, we consider the probability distribution for the amplitude variables, $P(A_1, A_2, A_3; t)$. According to well-known theory, this

Figure 2.8: Average value of the period as computed in the numerical simulations of the Busse-Heikes model in the presence of noise plotted versus the theoretical value that follows from application of the relation $T(\langle E \rangle)$, where $\langle E \rangle$ has been obtained numerically. Same symbols meaning than in Fig. 2.6.



distribution follows a Fokker-Planck equation. In the case of a relaxational nongradient dynamics with a potential V , (the case for $\mu = 0$ and $\delta \neq 0$) and when the residual terms (those proportional to δ) satisfy the orthogonality condition and are divergence free:

$$\sum_{j=1}^3 \frac{\partial f_j}{\partial A_j} = 0, \quad (2.48)$$

a condition satisfied in the case of the BH equations, it is possible to show that the stationary probability distribution for the $\{A_j\}_{j=1}^3$ variables is given by [54]:

$$P_{\text{st}}(A_1, A_2, A_3) = Z^{-1} \exp[-V(A_1, A_2, A_3)/\varepsilon]. \quad (2.49)$$

For $\mu > 0$ this is no longer true but we expect that for small μ a similar relation would be valid if we use a potential function Φ that differs from V in terms that vanish for vanishing μ . Using this probability distribution, one can compute the average value of the variable E as:

$$\langle E \rangle = Z^{-1} \int dA_1 dA_1^* dA_2 dA_2^* dA_3 dA_3^* E \exp(-\Phi/\varepsilon). \quad (2.50)$$

We take the crude approximation $\Phi = V$ and, after a change of variables to amplitude and phase, the mean value of the energy can then be computed as:

$$\langle E \rangle = \frac{\int_0^\infty dR_1 \int_0^\infty dR_2 \int_0^\infty dR_3 E \exp[-V/\varepsilon]}{\int_0^\infty dR_1 \int_0^\infty dR_2 \int_0^\infty dR_3 \exp[-V/\varepsilon]}, \quad (2.51)$$

where V and E are given in terms of the variables $\{R_j\}_{j=1}^3$ in Eqs. (2.16) and (2.31) respectively. In the case $\mu = 0$ (for which the above expression is exact) we obtain the value $\langle E \rangle = 1/60$ independent of ε and $T = T(\langle E \rangle = 1/60) \approx 6.4467/\delta$.

In the case $\mu > 0$, the above integral can be performed by means of a steepest descent calculation, valid in the limit $\varepsilon \rightarrow 0$, where it yields the asymptotic behavior $\langle E \rangle \rightarrow (\varepsilon/\mu)^2$ (see appendix A). The mean period can now be computed, in this limit of small ε , using (2.41). The result is that the period, as a function of the system parameters $\{\delta, \mu, \varepsilon\}$, behaves as:

$$T(\varepsilon, \mu, \delta) \approx \frac{3}{\delta} \log(\mu/\varepsilon), \quad (2.52)$$

a relation that is expected to hold in the limit of small ε and for small values of μ . In Fig. 2.9 we show that there is indeed a linear relation between the period computed in the numerical simulations and $\delta^{-1} \log(\mu/\varepsilon)$, as predicted by the above formula, although the exact prefactor 3 is not reproduced. We find it remarkable that, in view of the simplifications involved in our treatment, this linear relation holds for a large range of values for the parameters μ , δ and ε .

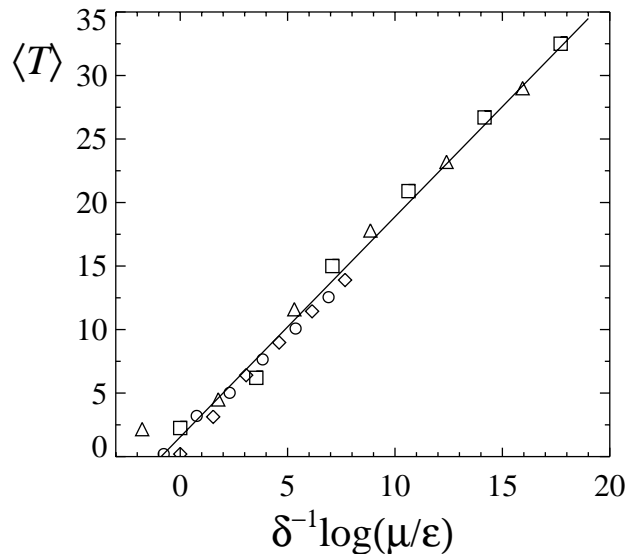


Figure 2.9: Average period, $\langle T \rangle$, plotted as a function of $\delta^{-1} \log(\mu/\varepsilon)$ in order to check the predicted linear relation [Eq. (2.52)]. The straight line is the best fit and has a slope of 1.734. Same symbols meaning than in Fig. 2.6, and values of ε ranging from $\varepsilon = 10^{-2}$ to $\varepsilon = 10^{-7}$.

2.4 One-dimensional Systems

The study of the 1D BH model represents a first step towards understanding the problem of domain growth and dynamical scaling in nonrelaxational systems, which by and large have not been considered. We focus on the region below the KL instability (region ‘R’ of Fig. 2.2), where the roll solutions are stable, and the dynamics is nonpotential except for $\delta = 0$.

For simplicity, we only consider the case of *real* variables. We write the 1D BH model as:

$$\begin{aligned}\partial_t A_1 &= \partial_{xx} A_1 + A_1[1 - A_1^2 - (\eta + \delta)A_2^2 - (\eta - \delta)A_3^2], \\ \partial_t A_2 &= \partial_{xx} A_2 + A_2[1 - A_2^2 - (\eta + \delta)A_3^2 - (\eta - \delta)A_1^2], \\ \partial_t A_3 &= \partial_{xx} A_3 + A_3[1 - A_3^2 - (\eta + \delta)A_1^2 - (\eta - \delta)A_2^2].\end{aligned}\tag{2.53}$$

A similar set of equations is introduced in reference [89] for some particular values of the parameters η and δ in the context of population dynamics [Eqs. (1.86)]. In their case A_i^2 represents the population of a biological species. From the point of view of Statistical Mechanics, system (2.53) describes a general model of three competing, nonconserved real order parameters with short-range interactions.

2.4.1 Front Solutions

2.4.1.a Isolated fronts

In the context of the present study, fronts or domain walls are defects that connect two homogeneous solutions. We observe numerically that the stable kink solutions are such that one of the three amplitudes, say A_k , satisfying the boundary conditions $A_k(x \rightarrow \pm\infty) = 0$ is zero everywhere. In order to study the dynamics of the nonpotential kinks, we first consider the kinks associated with the potential problem (stationary solutions of (2.53) with $\delta = 0$) and then we treat the nonpotential terms as a perturbation. The two nonvanishing stationary amplitudes A_i and A_j are, for $\delta = 0$, solutions of

$$\begin{aligned}\partial_{xx} A_i^0 &= -A_i^0 + (A_i^0)^3 + \eta A_i^0 (A_j^0)^2, \\ \partial_{xx} A_j^0 &= -A_j^0 + (A_j^0)^3 + \eta A_j^0 (A_i^0)^2,\end{aligned}\tag{2.54}$$

with boundary conditions $A_i^0(-\infty) = A_j^0(+\infty) = 0$ and $A_i^0(+\infty) = A_j^0(-\infty) = 1$.

The system (2.54) may be considered to represent the two-dimensional motion of a Newtonian particle of unit mass ($x \rightarrow t$, $A_i^0 \rightarrow X$, $A_j^0 \rightarrow Y$) under the action of a force with potential function $V(X, Y) = \frac{1}{2}(X^2 + Y^2) - \frac{1}{4}(X^4 + Y^4) - \frac{1}{2}\eta X^2 Y^2$. This function has two maxima at $m_0 = \{A_i^0 = 1, A_j^0 = 0\}$ and $m_1 = \{A_i^0 = 0, A_j^0 = 1\}$. It is clear that there exists a unique trajectory (allowed by the dynamics) along which a particle located in m_0 (m_1) can reach m_1 (m_0). The kink profile corresponds to the variation in time of the particle coordinates $(X(t), Y(t))$ when it moves between the two maxima [10].

An explicit analytical solution can be found in two particular cases [118]. First, when $0 < \eta - 1 \ll 1$, we have

$$\begin{aligned}A_i^0(x) &= r(x) \left[1 + \exp\left(2\sqrt{\eta - 1}(x - x_0)\right) \right]^{-1/2}, \\ A_j^0(x) &= r(x) e^x \left[1 + \exp\left(2\sqrt{\eta - 1}(x - x_0)\right) \right]^{-1/2},\end{aligned}\tag{2.55}$$

with $r(x) = 1 + (\eta - 1)R(x)$, $R(x) = O(1)$. Secondly, when $\eta = 3$ it is possible to obtain exact analytical solutions:

$$\begin{aligned} A_i^0(x) &= \frac{1}{1 + e^{\mp\sqrt{2}(x-x_0)}} = \frac{1}{2} \left[1 \pm \tanh\left(\frac{x-x_0}{\sqrt{2}}\right) \right], \\ A_j^0(x) &= \frac{1}{1 + e^{\pm\sqrt{2}(x-x_0)}} = \frac{1}{2} \left[1 \mp \tanh\left(\frac{x-x_0}{\sqrt{2}}\right) \right]. \end{aligned} \quad (2.56)$$

In both cases x_0 is arbitrary but fixed, reflecting the translational invariance of the system. From these solutions it is clear that the spatial scale over which A_i^0 and A_j^0 vary is of order $1/\sqrt{\eta-1}$.

The three roll solutions (2.14) are equivalent and they yield the same value for the Lyapunov functional (2.7). Therefore, we expect isolated kinks not to move in the potential problem ($\delta = 0$). However, when nonpotential terms are present, there is a symmetry breaking and an isolated kink moves at a constant velocity $v(\eta, \delta)$. This can be found by using standard perturbation techniques as done in section 1.3.2. Let us assume δ to be small, say of order ε , and look for a solution of Eqs. (2.53) [with $A_k(x) = 0$] of the form

$$\begin{aligned} A_i(x) &= A_i^0(x - s(t)) + \varepsilon A_i^1(x - s(t)) + O(\varepsilon^2), \\ A_j(x) &= A_j^0(x - s(t)) + \varepsilon A_j^1(x - s(t)) + O(\varepsilon^2), \end{aligned} \quad (2.57)$$

where $A_i^0(x)$ and $A_j^0(x)$ are solutions of (2.54). Substituting into (2.53) and equating terms of equal powers of ε , we find, to order $O(\varepsilon^0)$:

$$\begin{aligned} \partial_x^2 A_i^0 + A_i^0 - (A_i^0)^3 - \eta A_i^0 (A_j^0)^2 &= 0, \\ \partial_x^2 A_j^0 + A_j^0 - (A_j^0)^3 - \eta A_j^0 (A_i^0)^2 &= 0, \end{aligned} \quad (2.58)$$

and to order $O(\varepsilon^1)$:

$$\mathcal{L} \alpha = \alpha', \quad (2.59)$$

where

$$\begin{aligned} \mathcal{L} &= \begin{pmatrix} \partial_{xx} + 1 - \eta[(A_i^0)^2 + (A_j^0)^2] & -2\eta A_i^0 A_j^0 \\ -2\eta A_i^0 A_j^0 & \partial_{xx} + 1 - \eta[(A_i^0)^2 + (A_j^0)^2] \end{pmatrix}, \\ \alpha &= \begin{pmatrix} A_i^1 \\ A_j^1 \end{pmatrix}, \quad \alpha' = \begin{pmatrix} \delta\varepsilon^{-1}(A_i^0)^2 A_j^0 - A_i^0 \partial_t s \\ -\delta\varepsilon^{-1} A_j^0 (A_i^0)^2 - A_j^0 \partial_t s \end{pmatrix}. \end{aligned}$$

The solvability condition for the existence of a solution $(A_i^1(x), A_j^1(x))$ reads

$$(\Phi^\dagger, \alpha') = 0, \quad (2.60)$$

where (\cdot, \cdot) is a scalar product in $L^2(\mathbb{R})$ defined by $(f, g) = \int_{-\infty}^{\infty} dx f(x)^* g(x)$ and Φ^\dagger belongs to the null space of the auto-adjoint operator \mathcal{L} . Because of

the translational invariance, \mathcal{L} has a zero eigenvalue so that its kernel is not empty. The associated eigenvector is

$$\Phi^\dagger = \begin{pmatrix} \partial_x A_i^0 \\ \partial_x A_j^0 \end{pmatrix}. \quad (2.61)$$

This is immediately seen taking, for example, the derivative of (2.58) with respect to x . Eq. (2.60) can now be explicitly evaluated. From this equation, the solitary *kink velocity* $v(\eta, \delta) \equiv \partial_t s$ in the nonpotential case is obtained to leading order:

$$v(\eta, \delta) = \delta \frac{\int_{-\infty}^{\infty} dx A_i^0 A_j^0 (A_j^0 \partial_x A_i^0 - A_i^0 \partial_x A_j^0)}{\int_{-\infty}^{\infty} dx [(\partial_x A_i^0)^2 + (\partial_x A_j^0)^2]} + O(\delta^2) \equiv \delta \cdot h(\eta) + O(\delta^2). \quad (2.62)$$

Hence, in the nonpotential case, the kink moves despite connecting states associated with the same value of the Lyapunov potential of the equilibrium problem. For the particular case of $\eta = 3$ for which an analytical result is available for the kink profile [Eqs. (2.56)], an explicit result is obtained for the solitary kink velocity, namely, $v(3, \delta) = \delta\sqrt{2}/4$.

The expression (2.62) gives not only the magnitude of the velocity but also the direction of motion, which is related to the sign of v . First, we note that the velocity is to leading order proportional to δ , so the direction of the motion depends upon the sign of δ . To illustrate how (2.62) determines the direction, let us consider for example a kink with boundary conditions:

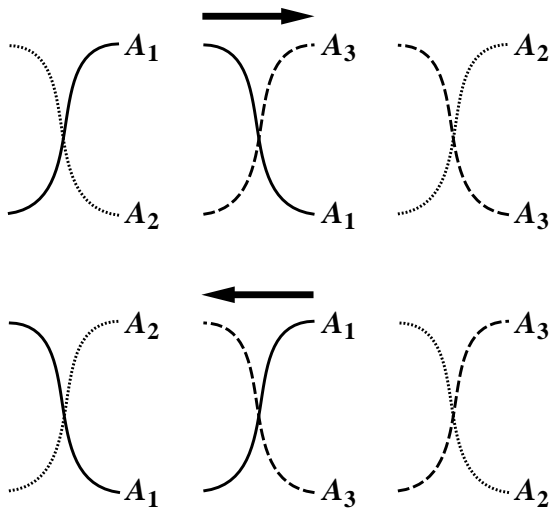


Figure 2.10: Kinds of fronts and their direction of motion for $\delta > 0$. The remaining amplitude for each kink is understood to be zero across the interface. For $\delta < 0$ the picture is the same but with the arrows interchanged.

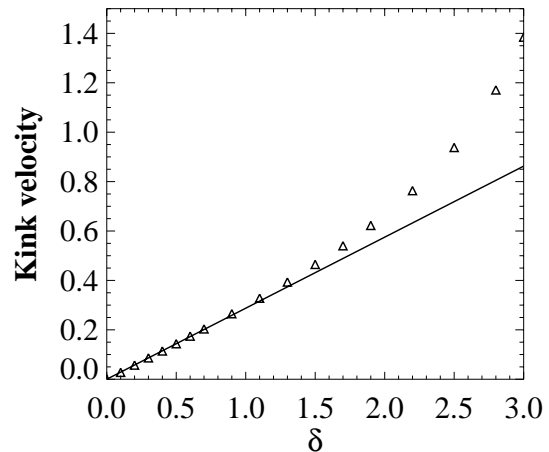


Figure 2.11: Solitary kink velocity as a function of the nonpotential parameter δ for $\eta = 3.5$. The straight line corresponds to the theoretical perturbative approach (2.62) whereas the points come from numerical simulation.

$A_i(-\infty) = A_j(+\infty) = 0$ and $A_i(+\infty) = A_j(-\infty) = 1$; $A_i^0(x)$ and $A_j^0(x)$ are such that $\partial_x A_i^0 > 0$ and $\partial_x A_j^0 < 0$. In this case the numerator of (2.62) is positive and v has the sign of δ . A positive (negative) value of v corresponds to a kink moving to the right (left). In Fig. 2.10 we show a classification of the six possible types of isolated kinks and their direction of motion. Three of them move in one direction and the other three in opposite direction.

We have checked numerically the domain of validity of the perturbative result (2.62). To this end we may either use the analytical result of the kink profiles $A_{i,j}^0$ for $\eta = 3$ or, more generally, the kink profiles $A_{i,j}^0$ obtained numerically. For a value of $\eta = 3.5$, we see that the perturbative result to first order in δ [Eq. (2.62)] turns out to be in good agreement with the numerical results approximately for values $\delta \lesssim 1.5$ (see Fig. 2.11). Of course this upper limit of validity depends on η in such a way that it gets bigger as η is larger. Above this limit the linear relation between v and δ is no longer valid and one needs to compute further corrections in terms of successive powers of δ .

2.4.1.b Multifront configurations

To study transient dynamics and domain growth we consider random initial conditions of small amplitude around the unstable solution $A_1 = A_2 = A_3 = 0$. In this situation a multifront pattern emerges rather than a solitary kink. In order to study dynamical scaling, we are interested in the late stage of this dynamics, once well-defined domains have been formed.

When δ is different from zero, the long stage dynamics can be explained in terms of moving fronts which annihilate each other. Kink annihilation induces domain coarsening, leading to a final state with a homogeneous roll solution filling up the whole system. There are two very distinct competing physical phenomena that affect kink dynamics. On the one hand, there is kink interaction due to short-range attractive forces. This is the only effect that takes place in the potential dynamics limit ($\delta = 0$), and it leads to a growth law logarithmic with time (see section 1.4.1.b). On the other hand, we have the kink motion driven by nonpotential effects. In this case, we do not expect the growth law to be logarithmic, at least in the regime where the nonpotential effects (the strength of which is measured by δ) are important. In Fig. 2.12 we show some snapshots corresponding to a typical run of the temporal evolution of the system (we use periodic boundary conditions). The first snapshot corresponds to an early stage during which domains are forming. Once formed, kinks move in such a way that annihilation of counter-propagating adjacent kinks leads to coarsening. Eventually, as corresponding to the last snapshot, the system may be in a state with a group of kinks moving all in the same direction. These will interact among them (with a interaction force that varies logarithmically with the interkink distance) until extinction.

We have performed a perturbation analysis of domain growth in the simplest example of a single domain bounded by two moving domain walls. A

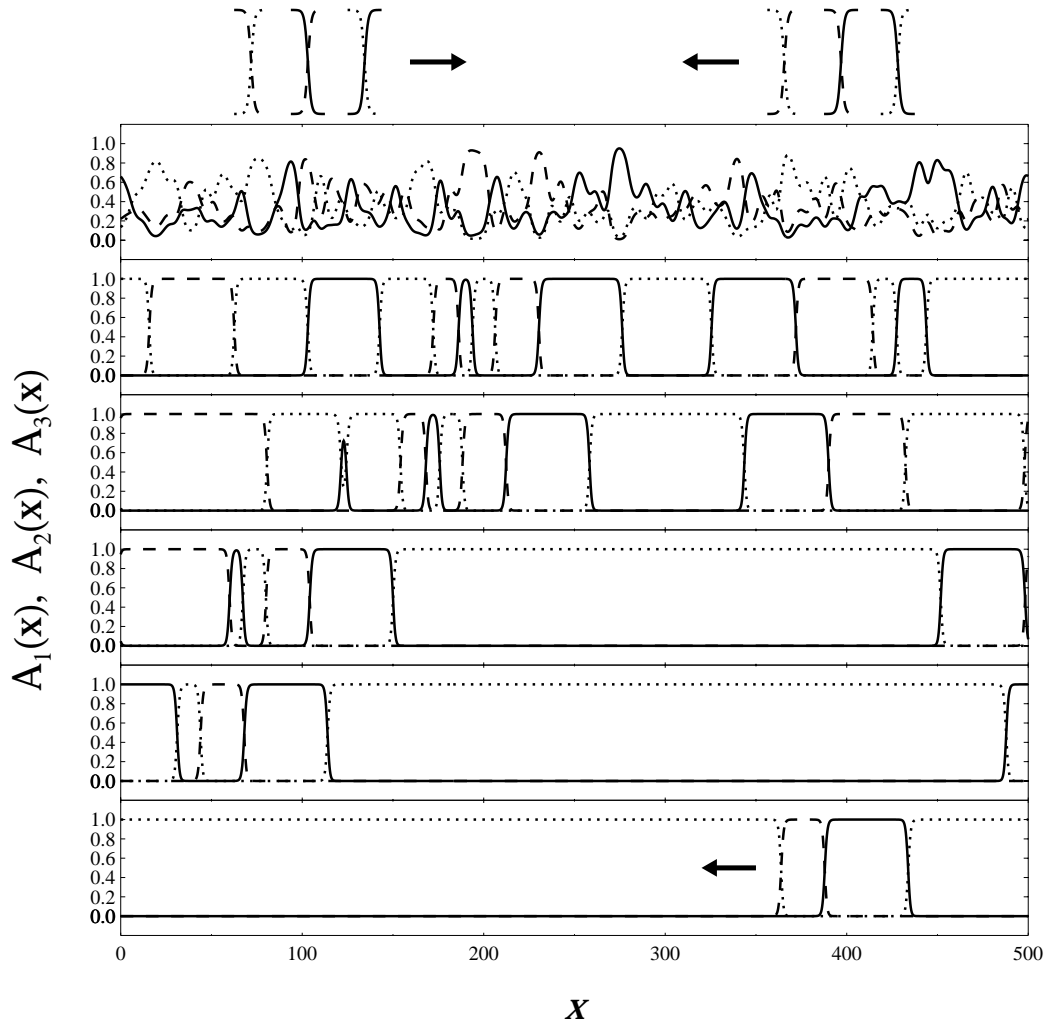


Figure 2.12: Snapshots of the time evolution of system (2.53) out of the KL instability region. In the upper part, the sense of motion of the various kinks is indicated. The last snapshot in the bottom part corresponds to a group of kinks moving to the left. Eventually they will all disappear leaving a roll solution filling up the whole system. Patterns at times (from top to bottom): 5, 125, 250, 1000, 1250, and 2500. Parameter values are: $\eta = 3.5$, $\delta = 2$.

differential equation for the domain size $L(t)$ can be obtained in the general case (see appendix B). For $\eta = 3$ it adopts the simple form:

$$\partial_t L(t) = 2v(3, \delta) - 24\sqrt{2} e^{-\sqrt{2}L(t)} = \pm \frac{\delta}{\sqrt{2}} - 24\sqrt{2} e^{-\sqrt{2}L(t)}, \quad (2.63)$$

where $v(3, \delta)$ is the solitary kink velocity. This expression is obtained in the “dilute-defect gas approximation”, that is, when the width of the fronts is much smaller than the distance between them. The first term in the right hand side of (2.63) can be either negative or positive and represents the contribution to the variation of the domain size owing to nonpotential effects. The second term is related to the interacting force between the kinks and it is always negative (attractive force) so that it always tends to shrink the domain.

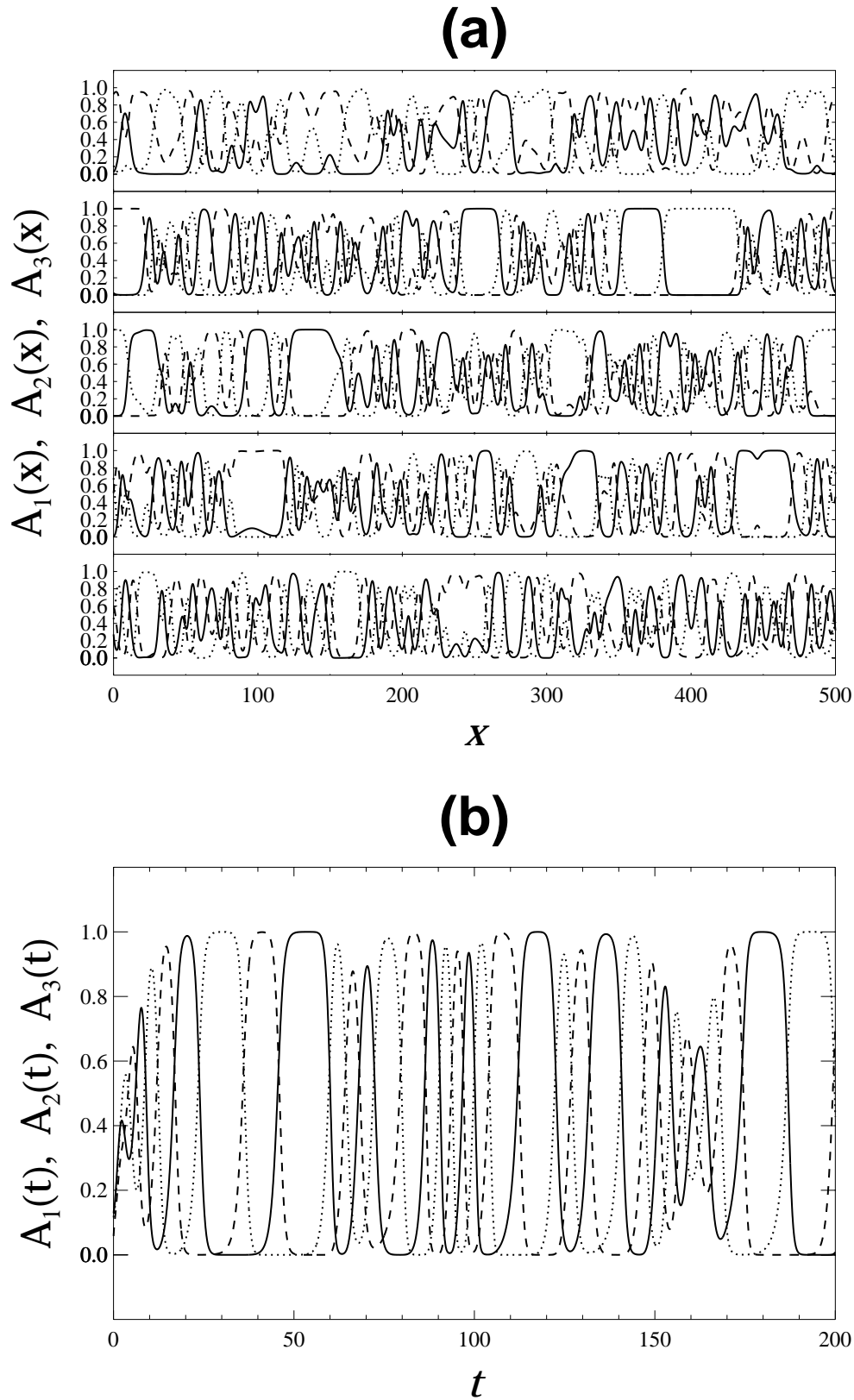


Figure 2.13: (a) Snapshots of the time evolution of system (2.53) inside the KL instability region. Patterns at times (from top to bottom): 12, 52, 92, 132, 172, and (b) amplitudes vs. time in a fixed point of space (taken at the center of the system). Parameter values are: $\eta = 2$, $\delta = 1.5$.

If both terms are negative, the kinks will annihilate each other independent of the initial domain size. Otherwise, when the first term is positive, the two effects act in opposite directions. In fact, given an initial size of the domain L_0 , it is possible to find a value $\delta = \delta_c$ for which the domain neither shrinks nor grows; in this case, the initial domain would not evolve in time being a stationary solution. For values $\delta > \delta_c$ the domain would get wider whereas for $\delta < \delta_c$ it would shrink. Note that in the $\delta = 0$ case (potential regime), the isolated domain always collapses, but this can be stopped with a suitable strength of the nonpotential terms. Furthermore, given a fixed value of δ , if L_0 is large enough, the dominant term responsible of the kink motion is the one associated with $v(\eta, \delta)$. In this case the fronts move at a constant velocity leading to a variation of the domain size linear with time. On the other hand, if L_0 is small enough, kink interaction will be the dominant effect and the single domain size will collapse logarithmically with time. This picture of the size dynamics of a single domain also explains basically what happens when more domains (and a nonvanishing third amplitude) coexist. It gives a useful understanding of the characteristic growth laws obtained from a statistical analysis in the next section.

Inside the KL instability region, the instability manifests itself in the bulk of domains as an alternation between the three amplitudes. In addition, there is a nonpotential front motion. The system switches to a persistent dynamical state so that a stationary state is never reached. In Fig. 2.13 we show typical configurations of the system inside the KL instability region as well as the time evolution of the amplitudes in a fixed point of space. Notice that, in the region where the rolls are stable, the system also oscillates cyclically at each point, but the alternation is only due to front motion.

2.4.2 Domain Growth and Dynamical Scaling

In this section we focus on the scaling properties of the system (2.53) in a late stage of the dynamics, namely when well-defined domains have formed. The system under study here gives us the opportunity of answering the question of whether a nonpotential dynamics satisfies dynamical scaling. To check numerically the validity of the scaling hypothesis, we have integrated the system of equations (2.53) by using a finite difference method for both, the spatial and temporal derivatives. In the simulations we have taken a constant value for η , namely $\eta = 3.5$, and we have varied δ from $\delta = 0$ (potential case) to $\delta = 0.1$ (a value below the KL instability threshold). We have used periodic boundary conditions and have averaged our results over 100–500 runs. To study domain structure, we consider the correlation function of one of the three amplitudes, which is defined as:

$$C_i(x, t) = \langle A_i(x + x', t) A_i(x', t) \rangle_{\text{i.c.}}, \quad (2.64)$$

where angular brackets indicate an average over initial conditions (“runs”). Note that, for symmetry arguments, $C_1 = C_2 = C_3 \equiv C$. We use the correlation

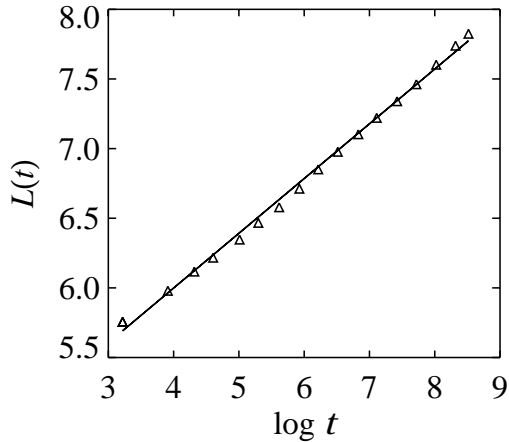


Figure 2.14: Time evolution of the characteristic domain size for the 1D BH model in potential case $\delta = 0$. The system size is $S = 1000$. The straight line is a linear regression fit of the displayed points.

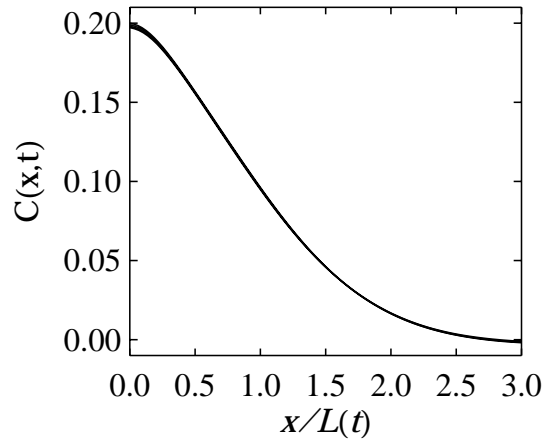


Figure 2.15: Scaling function for the 1D BH model in the potential case $\delta = 0$. The plot has been made by over plotting $C(x, t_i)$ vs $x/L(t_i)$ for several times from $t = 200$ up to $t = 5000$.

function better than the structure factor because of the large fluctuations of the structure factor at small wave numbers. A typical length scale $L(t)$ associated with the average domain size can be defined in several ways. Specifically, we have determined it by computing the value of x for which $C(x, t)$ is half its value at the origin at time t , that is $C(L(t), t) = \frac{1}{2}C(0, t)$. The calculation has been performed by fitting the four points of $C(x, t)$ closest to $C(0, t)$ to a cubic polynomial. Another typical length, $L_1(t)$ can be evaluated directly as the system size divided by the number of kinks. We have verified that the quotient $L_1(t)/L(t)$ remains nearly constant, as expected, when a single characteristic length dominates the problem.

2.4.2.a Growth law

We consider first the potential case $\delta = 0$: in Fig. 2.14 we show that the domain size follows the expected logarithmic behavior. The attractive interaction among the kinks leads to a very long transient before the system reaches its final state which corresponds to one roll solution filling up the whole system.

In the nonpotential case, the averaged domain size $L(t)$ is shown in Fig. 2.16 for a system of size $S = 500$ and $\delta = 10^{-3}$. For the earliest times, when the kinks are very close to each other, and according to the discussion of section 2.4.1.b, we expect the interaction terms to be the dominant ones (as long as δ is small enough). This leads to an initial logarithmic growth of $L(t)$. Due to coarsening the characteristic domain size becomes larger and the domain wall interaction becomes weaker as the time increases. For longer times the nonpotential effects dominate with respect to wall interaction. In

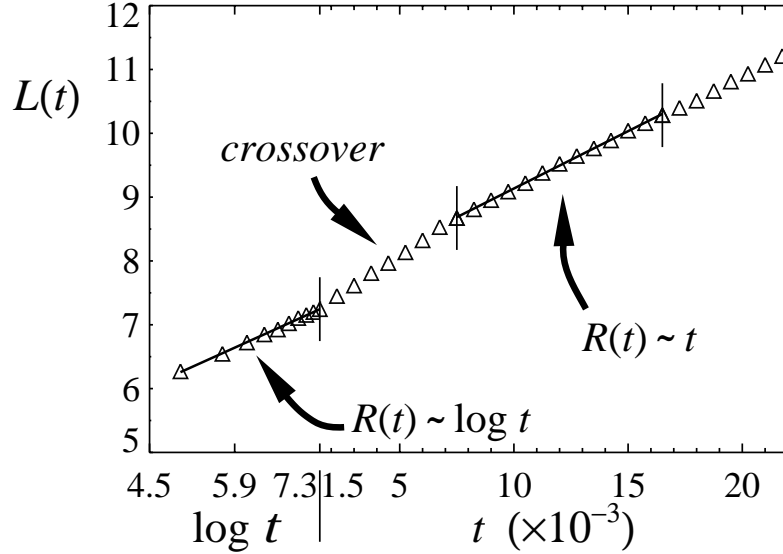


Figure 2.16: Time evolution of the characteristic domain size for $\delta = 0.001$ and $S = 1000$. The initial logarithmic growth law becomes linear after a crossover. For the largest times, finite size effects appear.

this regime we can consider each domain wall to move at a constant velocity. We obtain for this stage a growth consistent with a linear profile with time. Between these two dominant behaviors there exists a crossover for which the weights of both effects (interaction and nonpotential) in driving the domain wall motion are of the same order. Finally, at very late times finite size effects come into play: the domain size saturates to a constant value and the number of domain walls is too small to generate good statistics. When δ is large enough the initial kink annihilation is so fast that the initial logarithmic growth and the crossover stage can hardly be observed in the numerical integration. In this case of large nonpotential effects, a linear growth law is observed from the shortest times as it is shown in Fig. 2.17 for a very large system of size $S = 100000$. For smaller systems finite size effects occur at relatively early times. For example saturation effects appear for $t \gtrsim 200$ for a system of size $S = 500$. The bigger δ , the sooner finite size effects appear.

In the regime for which the nonpotential effects are the dominant ones, we can give a simple explanation of the linear growth law observed based on mean field theory arguments. Statistically speaking, there will be the same number of kinks moving to the right and to the left. As a matter of fact, in an appropriate reference frame, the system can be seen as composed of motionless kinks (type 1) and kinks moving at a velocity of $2v$ in one fixed direction (type 2). If we call $N_1(t)$ and $N_2(t)$ the *average* number of kinks of both types at time t , the number of kinks of, say type 1, at time $t + dt$ will be:

$$N_1(t + dt) = N_1(t) - N_1(t) 2v dt \times \frac{N_2(t)}{S}, \quad (2.65)$$

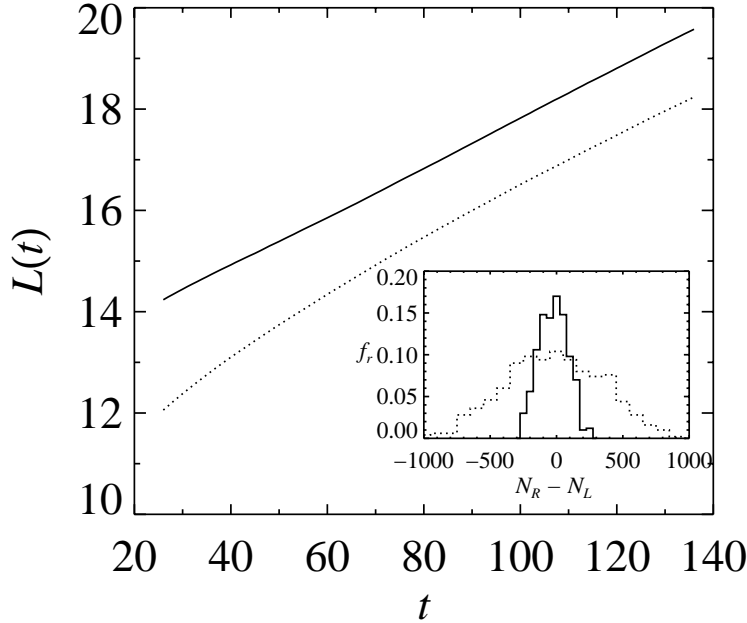


Figure 2.17: Time evolution of the characteristic domain size for the 1D BH model in the nonpotential case for two distributions of the initial conditions with different width of the random variable $\Delta N = N_R - N_L$ which measures the difference between right and left moving interfaces. The inset shows the corresponding histograms in terms of the relative frequency of ΔN . The initial conditions were generated as explained in section 2.4.2.a. The growth exponents obtained numerically are close to 1.0 and 0.7 for the solid and dashed curves respectively. Parameter values are $\eta = 3.5$ and $\delta = 0.1$; the system size is $S = 100000$.

where the second term in the right hand side represents the number of kinks disappeared in dt by annihilation, and S stands for the system size. The important point is that $N_1(t) = N_2(t) = N(t)$ (remember that we are dealing with averaged quantities), so that (2.65) transforms into $\dot{N}(t) = -(2v/L)N(t)^2$. Integration of the previous equation gives $N(t) = [(2v/L)t + N_0^{-1}]^{-1} \sim t^{-1}$, so that the average interkink distance $L(t) \sim N(t)^{-1} \sim t$ is linear with time.

We note that this mean field argument and the linear growth law does not hold for a discrete model with domain walls performing independent random walks; in this case a power law $L(t) \sim t^{1/2}$ can be rigorously demonstrated [89, 119]. This fact is not surprising because it is known that growth laws for discrete and stochastic models may differ from those of the corresponding continuous and deterministic versions [46]. One representative example is the Ising model with Glauber dynamics (section 1.4.1.a) versus the model A dynamics (section 1.4.1.b). In the former, the characteristic domain size grows as $L(t) \sim t^{1/2}$ *independently of the dimensionality*, whereas in the latter the growth law is $L(t) \sim \log t$ for $d = 1$ and $L(t) \sim t^{1/2}$ for $d > 1$. An explanation for the failure of the mean field argument when applied to the discrete model is that the initial fluctuation ΔN in the number of kinks moving in each direction is important. It seems that such fluctuations are not significant enough in the continuous model in which domain walls emerge from a slight pertur-

bation of the unstable state $A_1 = A_2 = A_3 = 0$. To check this idea we have computed the growth law $L(t)$ for the continuous system with modified initial conditions. We have generated initial conditions with a wider distribution of the random variable ΔN as follows: for each point x_j of the discretized mesh, a random number n_j from the set $\{1, 2, 3\}$ is chosen. Then the amplitude values at x_j are $A_k(x_j) = \delta_{kn_j}$, $k = 1, 2, 3$ (δ_{ij} stands for the Kronecker function). This generation of initial domain walls mimics the situation of a discrete model. The histogram of ΔN for the situations considered is shown in Fig. 2.17. For the artificially generated initial distribution of kinks we obtain a growth rate which is no longer linear as shown in Fig. 2.17.

We finally note that at long times the system will consist of an homogeneous roll state or a group of kinks moving either to the right or to the left². Note that the periodic boundary conditions impose constraints about the number of such moving kinks. To be precise, the number of kinks moving in a fixed direction must be a multiple of three. We can form a subgroup of three kinks moving in the same direction by joining those appearing in each row of Fig. 2.10. The moving kinks will continue interacting among them until eventually they all will disappear. In this situation we expect the growth law to be logarithmic with time but one of such groups is composed typically of three, six or rarely nine kinks, a number too small to generate good statistics.

2.4.2.b *Scaling function*

We now address the question of the validity of the dynamical scaling hypothesis (1.91a). For this purpose, we have plotted the equal time correlation function $C(x, t)$ versus the scaled length $x/L(t)$ for several times. Fig. 2.15 shows the scaling function in the potential case. In Fig. 2.18 we show, for a value $\delta = 0.001$, the correlation functions for several times before and after scaling the system length. Our results show that the correlation functions follow a single profile when the length is scaled with the characteristic domain sizes obtained above. We therefore conclude that a scaling description of the system is also valid as in the potential case, but now with a nonpotential dynamics. The upper limit of the time interval during which there is scaling is determined by the appearance of finite size effects. The range of values of δ for which there is scaling in a quite large time interval is rather small. For values of δ of even a few tenths, the finite size effects show up for very short times. Moreover the fluctuations in the scaling function grow as δ increases. For these reasons, we have not been able to obtain a conclusive comparison between scaling functions for different values of δ , although their shapes appear to be rather insensitive to the value of δ .

²We have checked on our numerical simulations, that on average, half the runs lead to a state corresponding to a group of kinks moving to the right and half of them to kinks moving to the left.

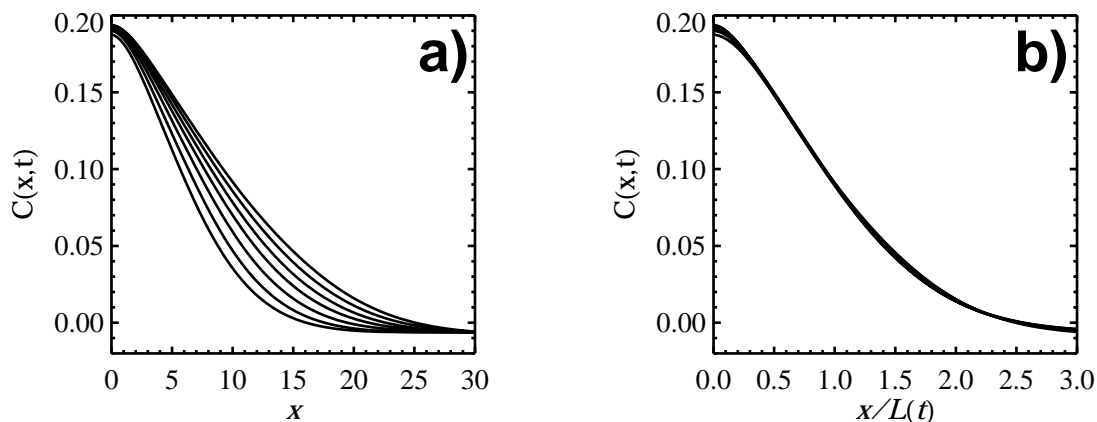


Figure 2.18: (a) Equal-time correlation function vs the nonscaled length for $\delta = 0.001$, $S = 1000$, and several different times from $t = 150$ to $t = 15000$; (b) equal-time correlation function vs the scaled length. The system parameters and the times for each curve are the same as in (a).

2.5 Two-dimensional Systems

In 2D more complicated phenomena may occur. Just like the 1D case, we will take real variables and, except in section 2.5.3, we will restrict ourselves to the ID terms (2.2) and will focus on the region where the rolls are the stable homogeneous solutions.

In Fig. 2.19 we present some snapshots of the dynamical evolution of the system for the potential and nonpotential regimes. When $\delta = 0$ and from the point of view of Statistical Mechanics, the system is described by three coupled nonconserved scalar order parameters with short-range interactions subjected to a relaxational gradient dynamical flow. According to the general discussion of section 1.4.1 for this kind of systems, the dynamical evolution is such that the system coarsens while approaching the minima of the Lyapunov potential \mathcal{F}_{BH} [Eq. (2.7)]. The final stationary state is a roll solution filling up the whole system. For the nonpotential situation it happens that, even below the KL instability region, the system remains in a persistent dynamical state in which no domain grows to fill the whole system. There are two reasons for that:

- (1) having more than two equivalent states, and
- (2) the nonpotential dynamics.

If only two fields were involved, the dynamical evolution drives the system to a state composed of islands of one phase immersed in a sea of the other phase. These closed domains either expand or shrink. However, when a third amplitude comes into play, there exists the possibility of formation of points (to be called *vertices*) where the three fields take the same value. As it will be

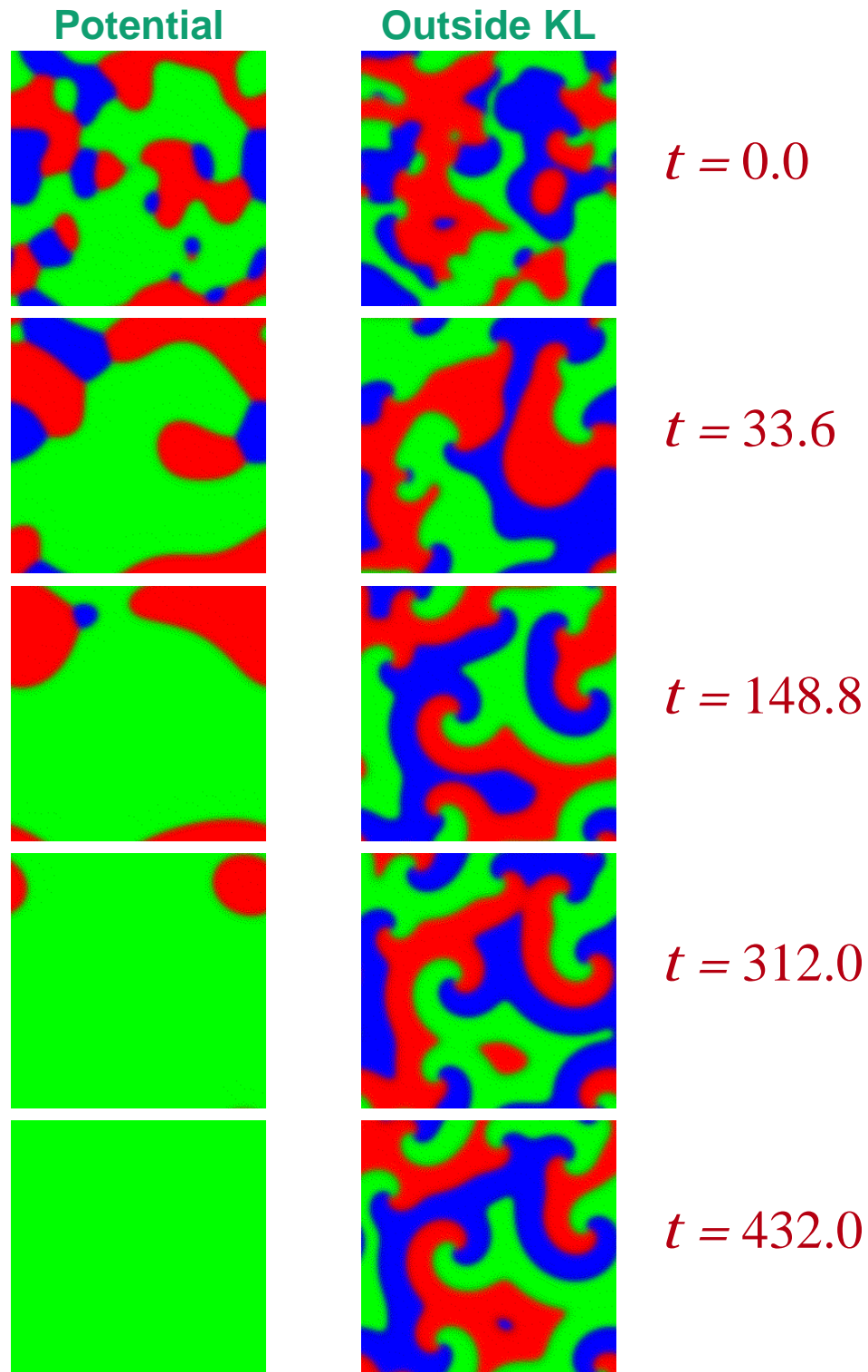


Figure 2.19: Snapshots corresponding to the numerical simulation of system (2.1) in two dimensions with isotropic diffusion terms. The red, green and blue regions represent the regions occupied by the modes A_1 , A_2 , and A_3 respectively. Parameter values are $\eta = 4.0$ and $\delta = 0$ (2) for the potential (nonpotential) regime.

seen later, the nonpotential dynamics prevents the system from coarsening by inducing the rotation of front lines around vertices.

The isotropic nature of the ID terms make fronts, which separate two homogeneous roll states, to move in the normal direction to each point. In appendix C we demonstrate that the normal front velocity (eikonal equation) is given by:

$$v_n(\mathbf{r}, t; \eta, \delta) = -\kappa(\mathbf{r}, t) + v_p(\eta, \delta), \quad (2.66)$$

where κ is the local curvature of the front line and $v_p(\eta, \delta)$ is the planar front velocity. This is just equal to the velocity of a (isolated) one-dimensional front [Eq. (2.62)] and it only depends on the system parameters. For η, δ fixed, there exists a critical value of the curvature, $\kappa_c = v_p$, such that an interface does not propagate (outwards). In the case of a circular drop of radius R , Eq. (2.66) transforms into $v_n = -R^{-1} + v_p$. We conclude that for a radius $R_c = v_p^{-1}$, and as long as $v_p > 0$, the drop neither grows nor shrinks. Any drop with radius $R > R_c$ grows and if $R < R_c$ it shrinks. If $v_p < 0$, both nonpotential and curvature effects act in the same direction leading to the collapse of the droplet. The concept of critical radius was already introduced in section 1.3.1 when we studied the interface dynamics of spherical domains in relaxational gradient flow systems. However, while the critical radius defined there had its origin in the potential difference between the asymptotic states of the interface, in the present case it stems from nonpotential effects.

2.5.1 Vertex Dynamics

Points where the three competing fields A_1, A_2 and A_3 take the same value are called vertices. Once a vertex is formed, and whenever the nonpotential parameter δ is different from zero, the front lines meeting at the vertex start rotating (clockwise or anticlockwise) as they twist. The sense of rotation changes with the sign of δ . When the stationary state is attained, the front lines adopt a spiral shape, their tangent vectors at the vertex form an angle

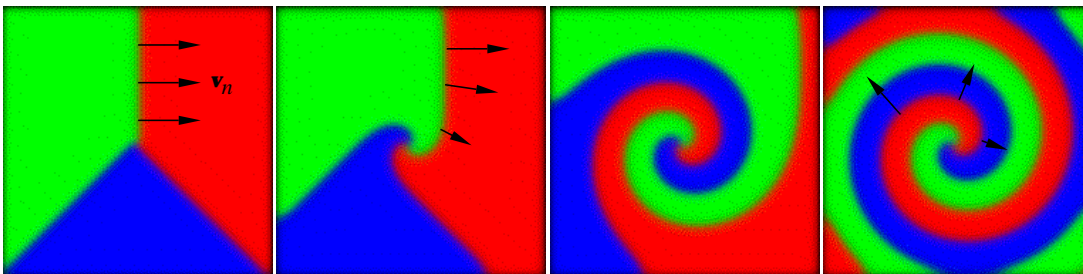


Figure 2.20: Several stages of the formation of a single spiral. Arrows stand for the normal front velocity.

of 120° with each other, and the structure rotates with a constant angular velocity ω . We observed numerically that the shape of a front line is close to an Archimedes' spiral. On the other hand, since the curvature of an spiral decreases with the distance to the center, according to (2.66) the normal front velocity of a rotating front line increases as moving away from the vertex. Fig. 2.20 shows several stages of the formation of a single spiral. The rotation angular velocity ω of a spiral front line around a vertex depends on the non-potential parameter δ . In next section we study the dynamics of an isolated spiral and in particular the dependence of ω on the system parameters.

2.5.1.a Dynamics of an isolated spiral

We follow a geometrical approach that takes as starting point an integro-differential equation for the curvature of a front line with a free end. Another approach starts from the differential equation that gives the points of the rotating front line. In either case, we are led to the result that the rotation angular velocity behaves as (see appendix D):

$$\omega = (8/27)^{1/2} \kappa_0^{3/2} v_p^{1/2} \propto v_p^2, \quad (2.67)$$

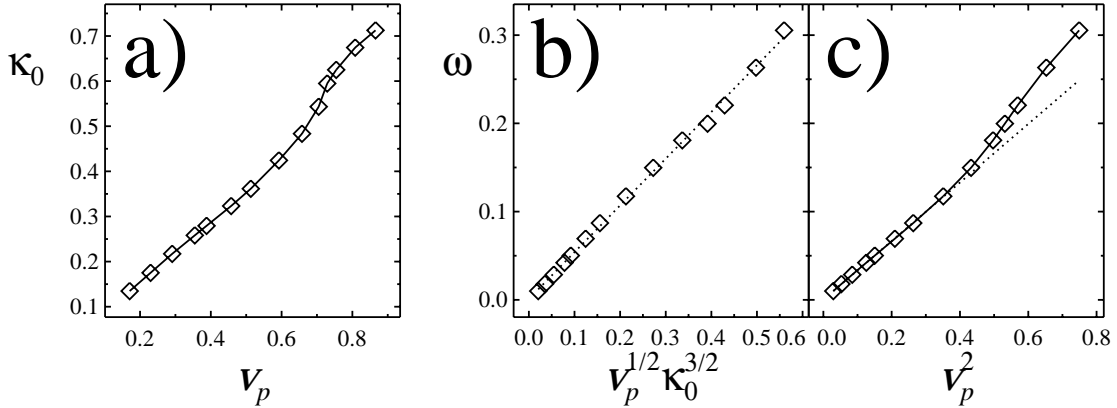


Figure 2.21: (a) Curvature κ_0 of a front line at the vertex position as a function of the planar front velocity v_p ; (b) rotation angular velocity of a vertex as a function of $v_p^2 \kappa_0^{3/2}$, and (c) as a function of v_p^2 . In (b) the dotted straight line is the linear regression fit of the displayed points; its slope is 0.52, a value close to the theoretically predicted value $(8/27)^{1/2} \simeq 0.54$. The straight line in (c) fits the first eight points. The parameter η is equal to 3.5 for the three plots.

where κ_0 is the curvature of the front line at the vertex. Now, since $v_p \sim \delta + O(\delta^2)$ [see Eq. (2.62)], it yields $\omega \sim \delta^2 + O(\delta^3)$. In Fig. 2.21a we see that the linear relation between κ_0 and v_p is well-satisfied for small and intermediate values of v_p , but it breaks down when nonpotential effects are strong (large v_p 's). In Figs. 2.21b–c we represent the rotation angular velocity as a function of $\kappa_0^{3/2} v_p^{1/2}$ and v_p^2 . The relation $\omega \propto \kappa_0^{3/2} v_p^{1/2}$ is well-satisfied in the whole range

of parameters. On the other hand, just like the curvature at the origin κ_0 , ω loses the linear relation with v_p^2 for large v_p 's.

The rotation angular velocity of an isolated vertex is closely related to the period T between the alternating modes in a fixed point of space. A behavior $1/T \propto \omega \sim v_p^2 \sim \delta^2$ is expected for δ small (see section 2.5.3).

2.5.1.b Critical distance for vertex annihilation

When a pattern grows from random initial conditions, a multivertex configuration emerges. For $\delta \neq 0$, large systems do not reach a final homogeneous state because coarsening is inhibited by spiral motion. However, small size systems can reach a final homogeneous state through vertex annihilation. Vertices can disappear from the system in a number of ways, depending on the type of boundary conditions (see next section). In particular, two vertices with opposite sense of rotation annihilate with each other if located closer than a *critical distance* $d_c(\delta)$. On the contrary, if they are separated a distance $d > d_c$, they will never annihilate. In Fig. 2.22 we show several stages of the vertex annihilation process. As a consequence, coarsening will occur for system sizes $S \lesssim d_c$ since in that case any pair of vertices will be closer than the critical distance. When two counter-rotating vertices are closer than d_c they approach each other as the domain between them shrinks. The area of this domain becomes zero upon annihilation. If this domain is assumed to be spherical its radius must be smaller than the critical one R_c [discussed after (2.66)] for the vertices to annihilate. Then it is plausible that $d_c = O(R_c)$. This argument gives a correct order of magnitude for d_c as shown in Fig. 2.23b. In order to get further insight into the magnitude of d_c , let us consider two

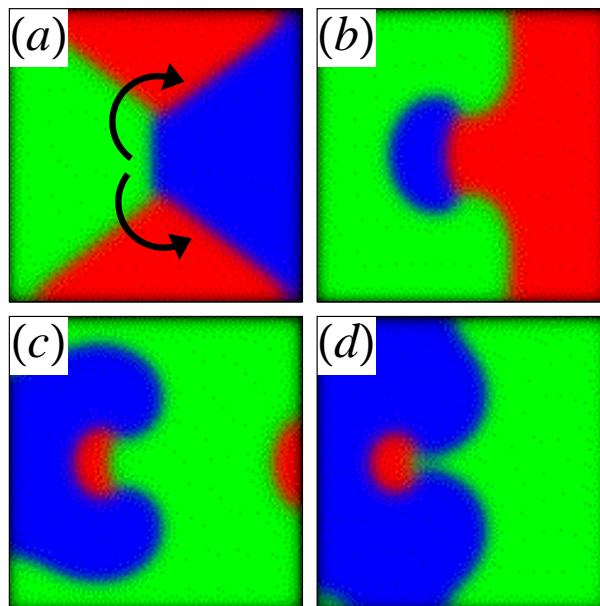


Figure 2.22: Some stages of the annihilation process of two counter-rotating vertices. The sense of rotation for each vertex is indicated.

counter-rotating vertices in a situation such that the tangent vectors at each vertex of two interfaces point at each other (along the line passing through the two vertices). Looking carefully at the numerical simulations we observe that, when the two vertices are separated a distance close to the critical one, the aforementioned interfaces are approximately tangent. The situation is depicted in Fig. 2.23a. Let us consider for instance the left spiral. The parametric equations of the front line whose tangent vector at the left vertex (taken as the origin) points at the right one are, in the approximation of Archimedes' spirals, $\{x(\phi) = a\phi \cos(\phi), y(\phi) = a\phi \sin(\phi)\}$, where ϕ is the polar angle and $a = 2/\kappa_0$, κ_0 being the curvature at the vertex. If we call ϕ_c the angle (measured as indicated in Fig. 2.23a) corresponding to the point at which the front lines are tangent, a straightforward calculation gives

$$d_c = 2 \times a\phi_c \cos \phi_c = \frac{2.24}{\kappa_0} \sim \delta^{-1}, \quad \delta \text{ small.} \quad (2.68)$$

In Fig. 2.23b the intervertex distance as given by (2.68) is compared with data from numerical simulation. The agreement is quite good.

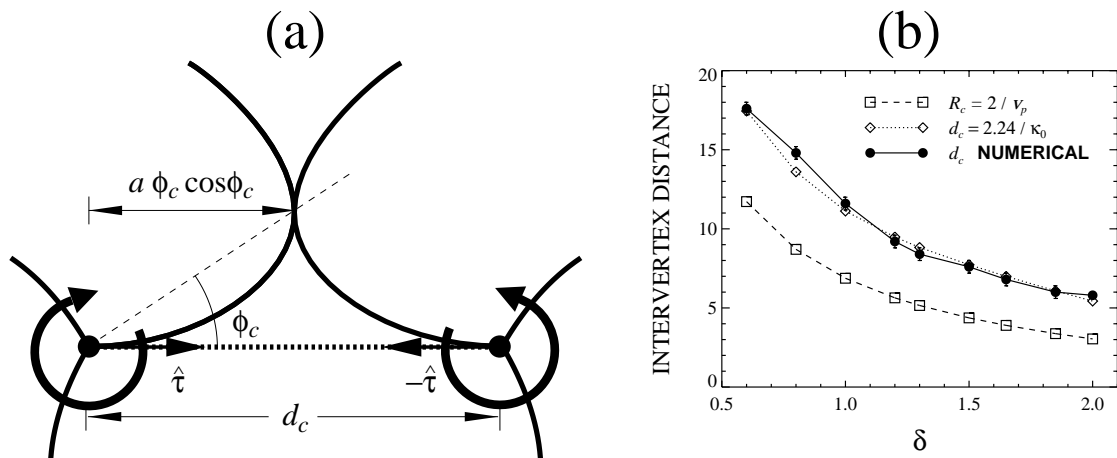


Figure 2.23: (a) Scheme of two counter-rotating vertices separated the critical distance; (b) critical distance for vertex annihilation as a function of the nonpotential parameter δ for $\eta = 3.5$. The critical radius is also included for comparison.

2.5.1.c Multivertex configurations

In a noncoarsening situation vertices are essentially pinned for short time scales. For larger time scales, they diffuse through the system. We have studied vertex motion using both periodic (pbc) and null boundary conditions (nbc).

With pbc, the number of vertices is asymptotically constant and a noncoarsening situation arises. The only way for the vertices to disappear is the annihilation of two vertices with opposite sense of rotation. Furthermore, the

number of vertices is always even, half clockwise and half anticlockwise. Vertex motion is rather erratic at the beginning but eventually it becomes highly correlated: vertices all tend approximately to move in the same direction. This is seen in Fig. 2.24a.

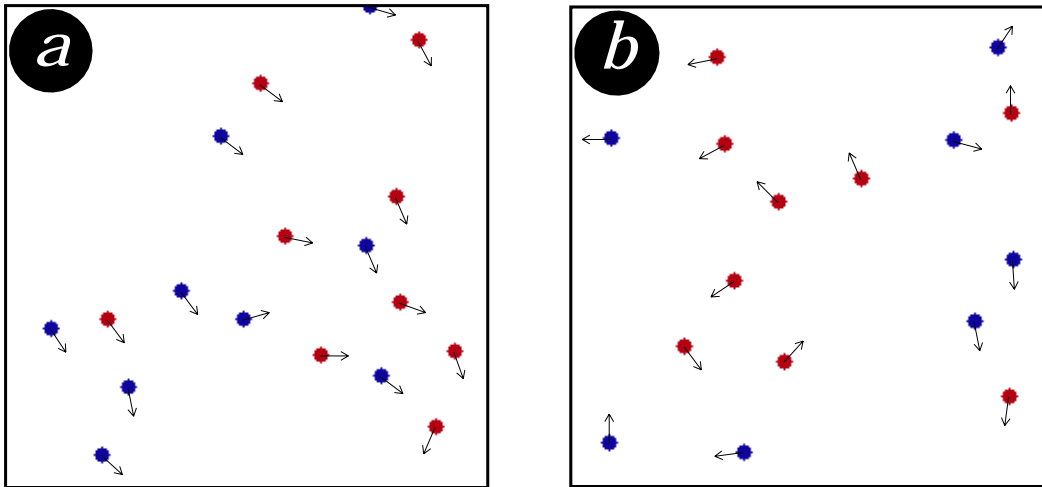


Figure 2.24: Vertex configurations for (a) periodic boundary conditions and (b) null boundary conditions. The arrows indicate the direction of motion of vertices. Blue (red) points represent clockwise (anticlockwise) vertices. Notice that, for periodic boundary conditions, vertices all tend to move in the same direction.

On the other hand, the situation changes significantly when using nbc. Now, there are no constraints neither about the number nor the type of vertices. Moreover, vertices can disappear (but never appear) by an additional mechanism which is the collision against an edge of the lattice. There may be in fact situations in which all the vertices are clockwise or anticlockwise. Unlike what happens with pbc, correlated motions of vertices are not observed (see Fig. 2.24b).

2.5.2 Domain Growth and Dynamical Scaling

We already said that coarsening takes place (for arbitrary large systems) as long as the nonpotential parameter δ is identically zero, that is, in the potential limit. It is well-known that growth processes corresponding to a nonconserved scalar order parameter subjected to a relaxational gradient type dynamics with a curvature driven interface motion are self-similar with a growth law $L(t) \sim t^{1/2}$ [32, 33, 34]. Actually model (2.1) consists of three coupled nonconserved scalar order parameters, but the same results apply in this case.

When $\delta \neq 0$, we force a situation in which one of the three amplitudes vanishes to induce nonpotential domain coarsening. This may be done with

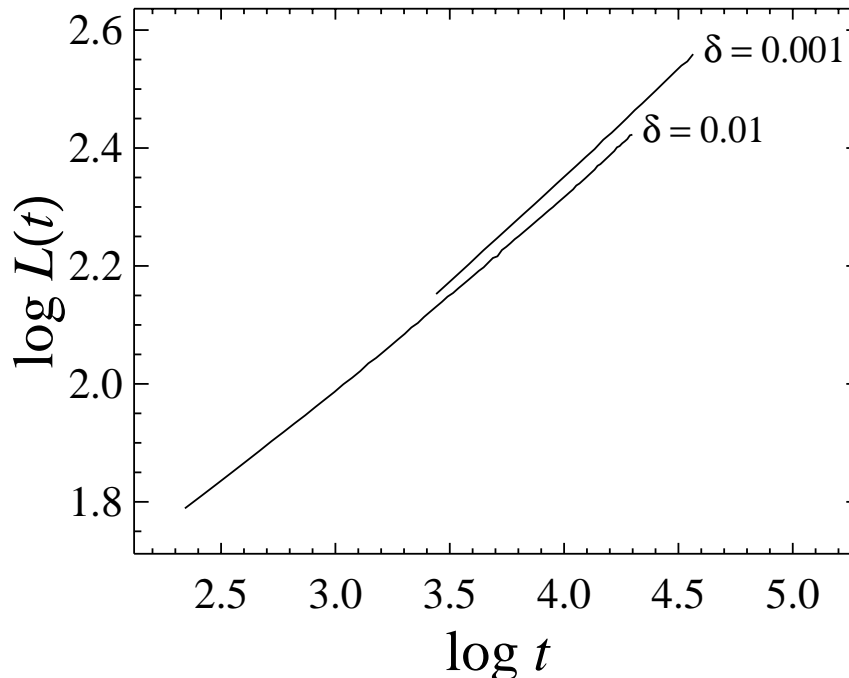


Figure 2.25: Time evolution of the characteristic domain size (with logarithmic axis scales) for $\eta = 3.5$ and $\delta = \{0.001, 0.010\}$. Time extends over the range for which dynamical scaling is observed.

an initial condition of the form $\{A_1(\mathbf{r}, 0) = 0, A_2(\mathbf{r}, 0) = \xi_2(\mathbf{r}), A_3(\mathbf{r}, 0) = \xi_3(\mathbf{r})\}$, where $\xi_{2,3}(\mathbf{r})$ are small random perturbations. In this way, only the amplitudes A_2 and A_3 are excited in the transient dynamics, while A_1 remains zero. When only domains of two of the three amplitudes grow, vertex formation is no longer possible and coarsening takes place. Fig. 2.25 shows, with logarithmic scales, the time evolution of the average domain size $L(t)$ for $\delta = \{0.001, 0.010\}$; the maximum time for each curve indicates the beginning of the appearance of finite size effects. The quantity $L(t)$ has been obtained as the width of the equal time correlation function (spherical averaged) $C(\mathbf{r}, t) = \langle A_i(\mathbf{r} + \mathbf{x}, t) A_i(\mathbf{x}, t) \rangle$. The curve for $\delta = 0.001$ is nearly linear with a slope of 0.36 ± 0.01 . This value is smaller than the value 0.5 corresponding to the potential limit. The value $\delta = 0.01$ leads to a nonlinear curve for the log-log plot of $L(t)$. This indicates that the time evolution of the characteristic domain size does not follow a power law. From the eikonal equation (2.66) it follows that $\dot{L} \sim v_p$ asymptotically, so that one would expect a behavior $L(t) \sim t$. However, very large systems could be needed in order to observe this asymptotic behavior.

Dynamical scaling can be proved by overplotting, for different times, the pair correlation function $C(r, t)$ against the system length rescaled by $L(t)$. We have first checked that model (2.1) shows dynamical scaling with a scaling law $L(t) \sim t^{1/2}$ in the potential limit. Numerical evidence is shown in Fig. 2.26. In

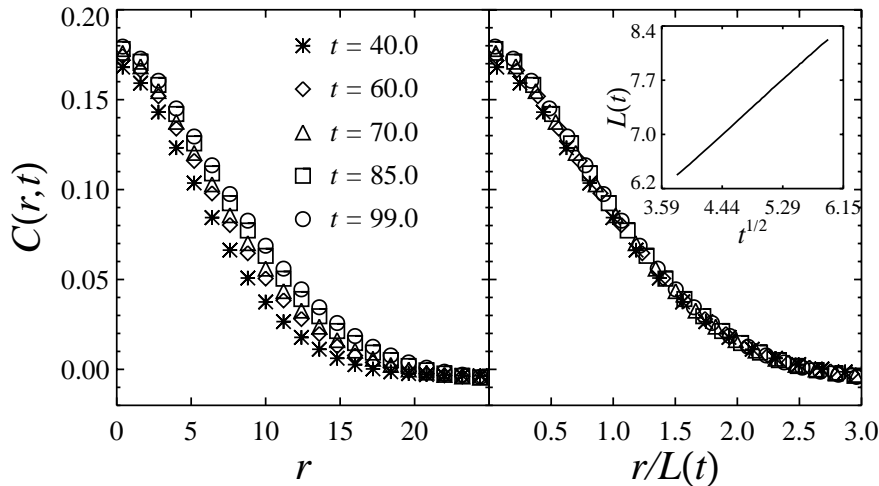


Figure 2.26: Equal-time correlation function versus (left) the nonscaled length and (right) scaled length for the potential case and different times in the interval $\Delta t = [40, 99]$. The inset shows the scaling law $L(t) t^{1/2}$. Other parameters: $\eta = 3.5$, $S = 256 \times 256$.

Fig. 2.27 the averaged correlation function before and after scaling the system length by the characteristic domain size is plotted in a nonpotential situation for $\delta = 0.01$. Clearly there is dynamical scaling. Therefore, nonpotential effects do not break down self-similarity in the case here studied. We also came to the same conclusion in section 2.4.2 for one-dimensional systems.

We have also observed the same results for other values of δ . However, when δ becomes large, finite size effects appear relatively soon so that the

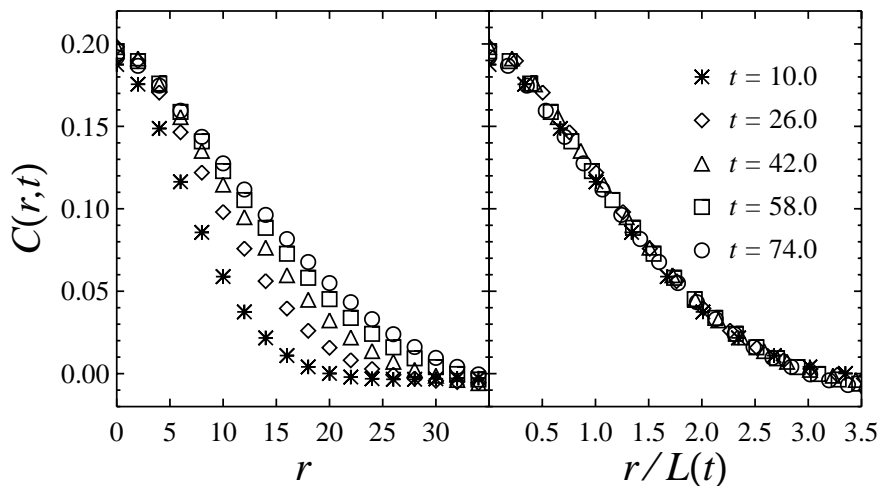


Figure 2.27: Equal-time correlation function versus (left) the nonscaled length and (right) scaled length for $\delta = 0.01$ and different times in the interval $\Delta t = [10, 74]$. Other parameters: $\eta = 3.5$, $S = 256 \times 256$.

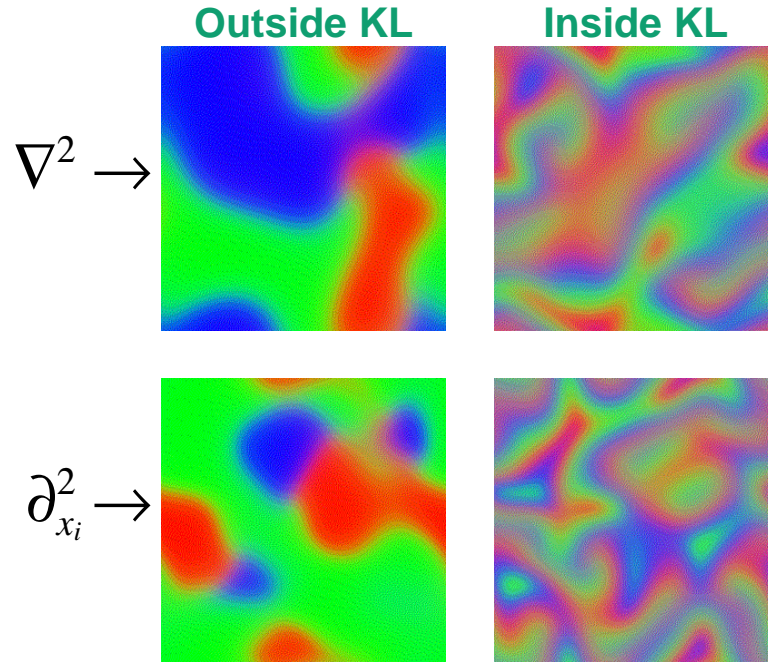


Figure 2.28: Snapshots corresponding to a numerical simulation in 2D of the BH model (2.1) with isotropic ($\mathcal{L}_j^{\text{ID}} = \nabla^2$) and anisotropic ($\mathcal{L}_j^{\text{AD}} = \partial_{x_j x_j}^2$) spatial derivatives. Cases out of and inside the KL instability region are presented. Parameter values are $\mu = 0.1$ and $\delta = 0.05$ (1.3) outside (inside) the KL regime.

range of time to be considered is rather small.

2.5.3 The Role of the Spatial Derivatives

We compare in this section the dynamical evolution corresponding to each of the isotropic and anisotropic spatial dependent terms presented in section 2.2, Eqs. (2.2) and (2.5) respectively. In particular, we study the effect of the different dynamics on the alternating period, also inside the KL instability region. It is important to realize that, above the KL instability, the period of alternation between the modes in a fixed point of space is the result of two combined phenomena: (1) the KL instability itself which manifests in the bulk of domains, and (2) the interface rotation around vertices.

We will show in the remaining of the section some results that follow, mainly, from a numerical integration of Eqs. (2.1) in 2D. It appears from the numerical simulations that the behavior beyond the KL instability point depends strongly on the type of spatial derivatives used as well on the magnitude of the parameter $\mu = \eta - 1$. We discuss first each type of derivatives separately.

Isotropic derivatives: Because of the isotropic nature of these terms, fronts move in the normal direction to each point, with a velocity given by the

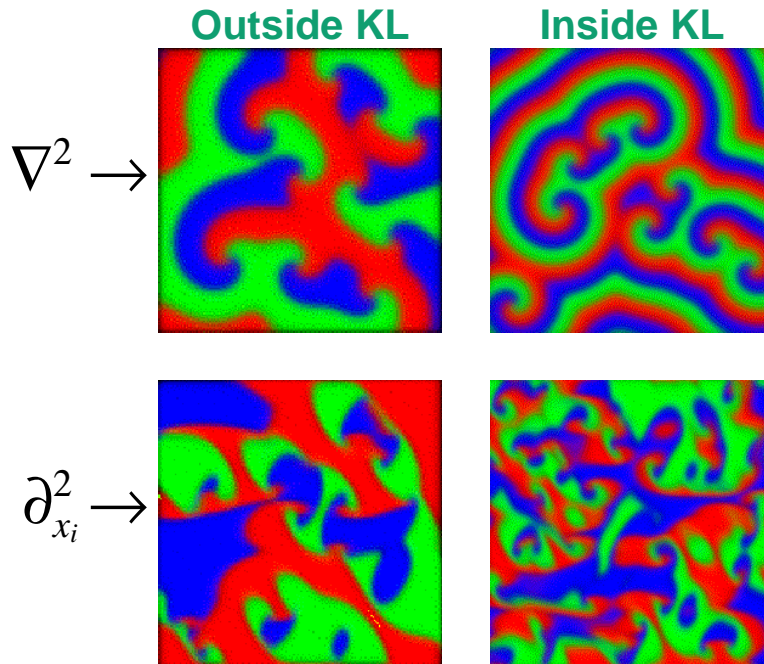


Figure 2.29: Snapshots corresponding to a numerical simulation in 2D of the BH model (2.1) with isotropic ($\mathcal{L}_j^{\text{ID}} = \nabla^2$) and anisotropic ($\mathcal{L}_j^{\text{AD}} = \partial_{x_j x_j}$) spatial derivatives. Cases out of and inside the KL instability region are presented. Parameter values are $\mu = 2.5$ and $\delta = 2$ (3.5) outside (inside) the KL regime.

eikonal equation (2.66). Closed domains have spherical symmetry and spiral structures are close to Archimedes' spirals.

For μ small, the bulk instability combined with the front motion is such that the intrinsic KL period stabilizes to a statistically constant value. This is to say: in a given point of space, we can see that the dominant amplitude changes due both to invasion from a rotating interface and a new amplitude growing inside the bulk. We give evidence of this combined mechanism in Fig. 2.28 where we have used the value $\mu = 0.1$ and we show representative configurations inside and outside the instability region.

For higher values of μ , the KL intrinsic period in the bulk is observed to increase with time. This is the same phenomenon that occurs in the zero-dimensional model without noise (see section 2.3.3). Therefore at long times the KL period is so large that we only see rotating interfaces around vertices, just like below the instability point. The two images of the upper row in Fig. 2.29 show domain configurations at long times for $\mu = 2.5$, below ($\delta = 2$) and beyond ($\delta = 3.5$) the KL instability point in the case of the isotropic terms. Apart from the typical size of the domains, it appears that there is no qualitative difference between them.

Anisotropic derivatives: Interface propagation no longer follows the normal direction at each point. Closed domains stretch or collapse along preferential

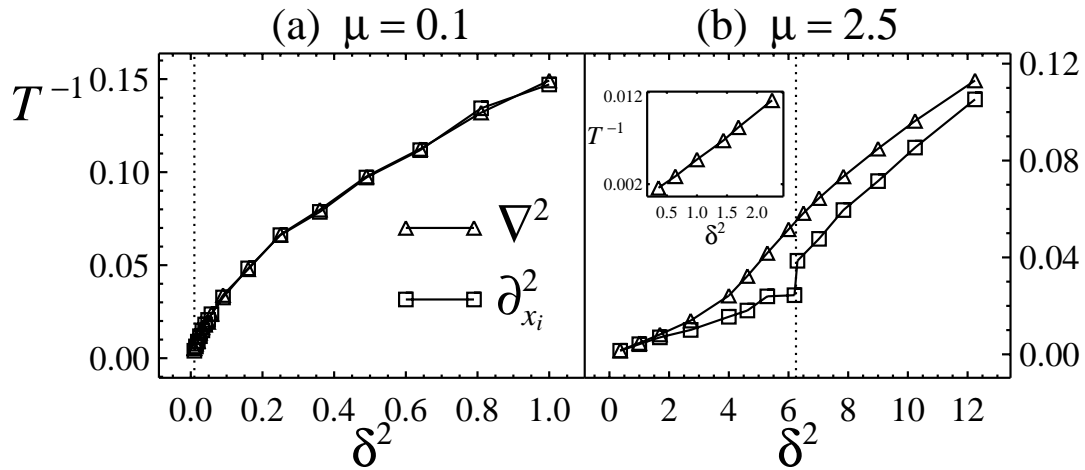


Figure 2.30: Inverse of the alternating mean period as a function of δ^2 for the 2D BH model with isotropic and anisotropic spatial-dependent terms. Each plot corresponds to a different value of the parameter μ . The KL instability takes place at the right of the vertical dotted lines.

directions so that they adopt an elliptic shape rather than a spherical one. Moreover the number of vertices is not constant for long times but they annihilate among them and also originate from the collision of interfaces. Two interfaces associated with the same vertex (and thus rotating in the same sense) may collide and generate new vertices.

Both for small and large μ , in the KL regime, we observe, in addition to the front motion, domains of one phase emerging in the bulk of other domains; this is seen at all times, indicating that, at variance with the isotropic derivative case, the period associated to the KL instability does not diverge with time. Evidence is given in Fig. 2.28 for $\mu = 0.1$ and Fig. 2.29 for $\mu = 2.5$. Both figures show results inside and outside the instability region.

In summary, for small μ , the morphology of domains inside the KL instability region turns out to be similar with both kinds of spatial-dependent terms. The alternating period is dominated by the KL instability and is similar with isotropic and anisotropic spatial derivatives. This shows up in the fact that the period computed in a single point of space does not depend essentially of the type of derivatives used, as shown in Fig. 2.30a. For large μ , on the other hand, the morphology is different for isotropic and anisotropic terms. For the isotropic ones, spiral rotation dominates the dynamics because of the divergence of the KL intrinsic period. For the anisotropic terms, both front motion and bulk instability are present at all times. In Fig. 2.30b it is seen that the period for the isotropic terms does not change abruptly on crossing the instability point. This result supports the fact that the intrinsic KL period is masked by that coming from rotating interfaces. Moreover, the theoretical relation $1/T \sim \delta^2$ is well-satisfied for small values of δ . On the other hand, the curve $T^{-1}(\delta^2)$ for anisotropic derivatives shows a jump at the instability point

$\delta = \mu$. This reflects the fact that, above the instability, the alternating period decreases by the appearance of the KL instability. Finally, as distinguished from regimes with small μ , the periods for isotropic and anisotropic spatial derivatives are different for intermediate and large values of δ , as seen in Fig. 2.30b.

2.6 Conclusions

We have studied interface dynamics and dynamical scaling in a nonpotential coarsening process. The model considered features three coupled amplitudes. It is related to models of competing population species and to a three-mode description of the phenomenon of Rayleigh-Bénard convection in a rotating cell.

In zero spatial dimensions, we find in a certain range of parameters a decomposition of the dynamics into relaxational plus a residual part. In this regime explicit expressions for the time variation of the amplitudes and the period of the orbits are given. We also show how noise can stabilize the mean period of the KL instability to a finite value. An analytical approach to the mean period as a function of the system parameters and noise intensity is reported in the limit of small noise intensities.

In one spatial dimension, the issues of domain growth and dynamical scaling are studied below the KL instability point, where the dynamics is still nonpotential and the system shows coarsening. A solitary kink moves at a constant velocity due to the nonpotential dynamics. In a multikink configuration, kinks move due to both domain wall interaction and nonpotential effects. In any case the dynamics is governed by kink motion. This motion is such that interfaces traveling in opposite directions annihilate with each other. The average domain size is observed to grow logarithmically with time for the shortest times but it becomes linear with time after a crossover. Logarithmic and linear behaviors are associated with dominant kink motion mechanisms which are domain wall interaction and nonpotential effects respectively. We have found that the scaling hypothesis still holds, as in the potential case, but with a different growth law that reflects the nonpotential dynamics of the system.

The two-dimensional version of this problem exhibits rather different dynamical behavior grossly dominated by vertices where three domain walls meet and which have no parallel in one-dimensional systems. The rotation of interfaces around vertices is driven by nonpotential effects and this inhibits coarsening for systems sufficiently large. The rotation angular velocity of the interfaces around an isolated vertex goes as $\omega \sim \delta^2$ to leading order in δ , the nonpotential parameter. In multivertex configurations, vertices interact with each other and diffuse through the system in a noncoarsening situation. Vertices of opposite sense of rotation annihilate with each other if located closer than a critical distance $d_c \sim \delta^{-1}$. As a consequence, coarsening takes place for

system sizes $S \lesssim \delta^{-1}$ (δ small). Vertex motion is influenced by the boundary conditions. For periodic boundary conditions, the number of vertices is even (half clockwise and half anticlockwise) and they only can annihilate by pairs of opposite sense of rotation. In addition, the motion is such that all vertices tend to move in the same direction. On the other hand, for null boundary conditions, there are no restrictions neither about the number nor the type of vertices. These may also disappear by collision against the edges of the system. Collective motions of vertices are not observed.

When only two amplitudes are excited in the transient dynamics, vertex formation is not possible and there is domain growth. In this situation, we checked that there is dynamical scaling, with a growth law different from that of the potential dynamics limit. Finally, we investigated the influence on the dynamics of the type of spatial dependent terms. For small values of the parameter $\mu = \eta - 1$, the morphology of domains inside the KL region turns out to be similar with isotropic and anisotropic spatial derivatives. The alternating period is dominated by the KL instability and is similar with both kinds of spatial-dependent terms. For large μ , on the contrary, the morphology of patterns as well as the alternating mean period are different for isotropic and anisotropic terms. While the KL intrinsic period diverges with time with isotropic derivatives, it saturates to a finite value in the anisotropic case.

Chapter 3

Parametrically Forced Complex Ginzburg-Landau Equation: Forcing at Three Times the Natural Frequency

Abstract. *The effect of a temporal modulation at three times the critical frequency on a Hopf bifurcation is studied in the framework of amplitude equations. The situation is described by a complex Ginzburg-Landau equation with an extra quadratic term, resulting from the strong coupling between the external field and unstable modes. On increasing the intensity of the forcing, the system goes from an oscillatory regime to an excitable one with three equivalent frequency locked states. In the first regime, topological defects are one-armed phase spirals, while in the second one they correspond to three-armed excitable amplitude spirals. Analytical results show that the transition between these two regimes occurs at a critical value of the forcing intensity. The transition between phase and amplitude spirals is confirmed by numerical analysis.*

3.1 Introduction

One of the main results that we have obtained in the previous chapter is the coarsening inhibition due to nonpotential effects in a two-dimensional system with three equivalent competing states. The system is at long times in a persistent dynamical state governed by rotating three-armed spirals, each arm corresponding to a domain wall separating two of the three stable states. The same generic dynamical phenomenon can be found in systems described by a single complex field with a broken phase symmetry. The symmetry breaking may lead to the appearance of several equivalent states. We study here the effect of a temporal modulation on a system near a Hopf bifurcation. This may be described by a complex Ginzburg-Landau equation (CGLE) with a parametric forcing that breaks the phase symmetry. We want to study the analogies between the spatio-temporal dynamics of the phase locked states and the competition dynamics of the roll states with three different orientations in the Busse-Heikes (BH) model. The study is within the more general

context of spatio-temporal dynamics in systems with broken symmetry. Several phenomena may occur on varying the intensity of the forcing term that breaks the phase symmetry. In particular, the transition between one-armed phase spirals and three-armed excitable amplitude spirals when the forcing intensity passes through a critical value is investigated.

In a general framework, the nucleation of spatio-temporal patterns is in many cases associated with continuous symmetry breakings, and these patterns are thus very sensitive to even small perturbations or external fields. Perturbations may be induced by imperfections of the system itself (e.g. impurities), of the geometrical set-up (e.g. the boundary conditions), of the control parameters, etc. External fields, on the other hand, may induce spatial or temporal modulations of the control or bifurcation parameters. In fact, spatially or temporally modulated systems are very common in nature, and the effect of external fields on these systems has been studied for a long time.

For example, the forcing of a large variety of nonlinear oscillators, from the pendulum to Van der Pol or Duffing oscillators, has led to detailed studies of the different temporal behaviors that were obtained. It has been shown that resonant couplings between the forcing and the oscillatory modes may lead to several types of complex dynamical behaviors, including quasi-periodicity, frequency lockings, devil's staircases, chaos and intermittency [120, 121]. In particular, physical systems that exhibit frequency locking include electronic circuits [122], Josephson junctions [123], chemical reactions [124], fields of fireflies [125], and forced cardiac systems [126]. The problem of frequency locking is also considered in reference [127], where a periodically forced Belousov-Zhabotinsky reaction-diffusion system is studied. Spiral patterns are observed in the absence of forcing. As the perturbation frequency varies, a sequence of resonance patterns is observed, each persisting over a range of perturbations frequencies (see Fig. 3.1).

In equilibrium systems, the importance of spatial modulations is known since a long time. For example, in the case of spatial modulations occurring in equilibrium crystals, such as spin or charge density waves, the constraint imposed by the periodic structure of the host lattice leads to the now commonly known commensurate-incommensurate phase transitions. The transition from the commensurate phase, where the wavelength of the modulated structure is a multiple of the lattice constant, to the incommensurate one occurs via the nucleation of domain walls separating domains which are commensurate with the host lattice [128, 129].

In nonequilibrium systems, the systematic study of the influence of external fields on pattern forming instabilities is more recent. It has been first devoted to instabilities leading to spatial patterns. For example, the Lowe-Gollub experiment [130] showed that, in the case of the electrohydrodynamic instability of liquid crystals, a spatial modulation of the bifurcation parameter may induce discommensurations, incommensurate wavelengths and domain walls. The similarities with analogous equilibrium phenomena rely

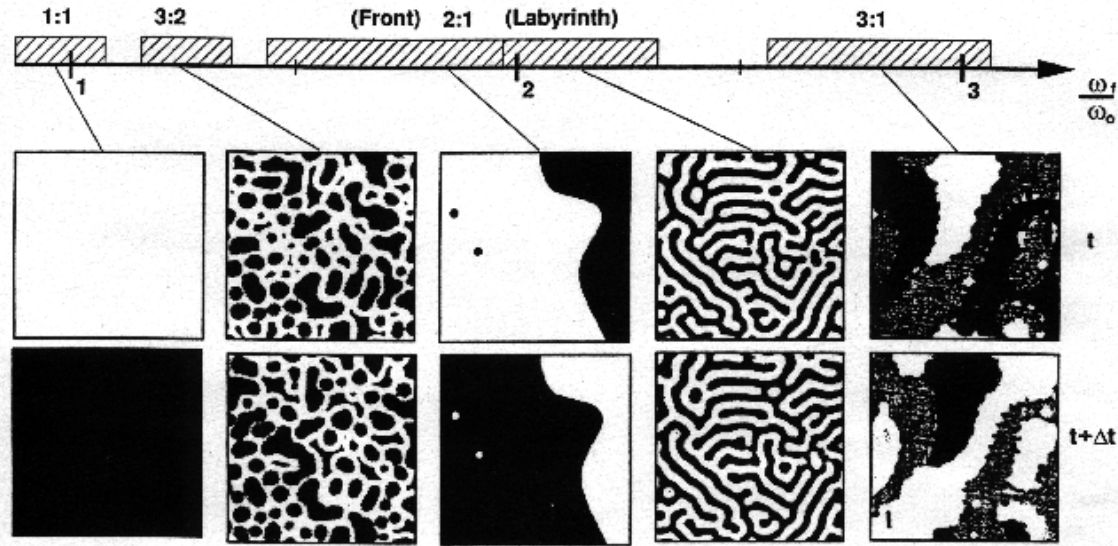


Figure 3.1: Frequency locked regimes observed in an experiment on a periodically perturbed ruthenium-catalyzed Belousov-Zhabotinsky reaction-diffusion system. The quantity ω_f/ω_0 stands for the ratio of the perturbation frequency ω_f to the natural frequency of the system ω_0 . Patterns are shown in pairs, one above the other, at times separated by $\Delta t = 1/\omega_f$, except for the 1 : 1 resonance where $\Delta t = 1/2\omega_f$. Striped boxes on the horizontal axis mark perturbation frequency ranges with the same frequency-locked ratio. Taken from [127].

on the fact that, close to this instability, the asymptotic dynamics is potential [131, 132].

In the case of Hopf bifurcations, however, original effects occur as a consequence of the nonpotential character of the dynamics. In particular, for wave bifurcations, unstable standing waves or two-dimensional wave patterns may be stabilized by pure spatial or temporal modulations of suitable wavelengths or frequencies [133, 134, 135, 136]. The case of pure temporal modulations of Hopf bifurcations in extended systems has been extensively studied by Coulet and Emilsson [137] through amplitude equations of the Ginzburg-Landau type. They considered periodic temporal modulations of frequency $\omega_e = (n/m)(\omega_0 - \nu)$, where n/m is an irreducible integer fraction, ω_0 is the critical frequency of the Hopf bifurcation, and ν is a small frequency shift. Such forcings break the continuous time translation down to discrete time translations, and the corresponding amplitude equations become, for the so-called strongly resonant cases ($n = 1, 2, 3, 4$) [138]:

$$\partial_t A = \mu A + (1 + i\alpha)\nabla^2 A - (1 + i\beta)A|A|^2 + \gamma_n \bar{A}^{n-1}. \quad (3.1)$$

Here \bar{A} stands for the complex conjugate of the field A . If the forcing intensity γ_n is sufficiently strong, this dynamics admits asymptotically stable uniform steady states, corresponding to frequency locked solutions. If $\gamma_n \gg \{\mu, \alpha, \beta\}$, the locked solutions behave as

$$R_0^{2(n-2)} \gamma_n^2 \approx R_0^4 \quad \Rightarrow \quad R_0 \approx \gamma_n^{1/(4-n)}. \quad (3.2)$$

Looking for a perturbed solution

$$A = R_0 e^{i\Phi_0} (1 + a_k e^{\omega_k t} e^{ikx}), \quad (3.3)$$

it yields the following growth rate:

$$\omega_k \propto -\gamma_n^{2/(4-n)} (2 \pm \sqrt{\Gamma}), \quad (3.4)$$

$$\Gamma \equiv 3 - 2n + (n - 1)^2 - (2n + 1)\beta^2. \quad (3.5)$$

For the strongly resonant cases $n = 1, 2, 3, 4$, we have $\text{Re}(\sqrt{\Gamma}) < 2$ so the frequency locked solutions are always stable in the large forcing limit, as it was intuitively expected since the forcing has a stabilizing effect.

There are n different frequency locked solutions, which only differ by a phase shift of $2\pi/n$. In this regime, the dynamics resembles some sort of excitability. The locked solutions may undergo various types of instabilities [137]. One of them is of phase type and occurs when $1 + \alpha\beta$ is sufficiently negative. In this case, competition between phase instability and forcing leads to the formation of stripes or hexagonal patterns, with their associated topological defects. If the forcing is decreased, these structures break down through spatio-temporal intermittency [137]. On the other hand, in the phase stable regime, frequency locked solutions may undergo a variety of bifurcations when forcing is decreased, leading to oscillation, quasi-periodicity or chaos.

The equivalence between the different frequency locked states makes possible the formation of stable inhomogeneous structures. These structures are composed of domains of the locked states separated by abrupt interfaces. Non-potential effects may induce interface motion and, in particular, the formation of n -armed spirals, each arm corresponding to an interface between two different frequency locked solutions.

These phenomena were studied in great detail by Coulet and Emilsson, for $n = 1$ and $n = 2$, in one- and two-dimensional systems [137]. For $n = 1$ they find excitable spirals in 2D which are very similar to observed chemical spiral waves. In the resonant case $n = 2$ Ising and Bloch walls may appear. The Bloch walls break the chiral symmetry as the order parameter can have two senses of rotation (in the complex plane to pass from one fixed point to the other). The chiral symmetry breaking for Bloch walls gives rise to the appearance of two-armed spirals centered around complex zeros. Unlike what happens in 1D, the late time dynamics in 2D may not be defect free which may inhibit coarsening. Starting from an initial condition which is a small perturbation of a locked state, several situations may occur depending on the value of the forcing amplitude γ_2 . For large values of γ_2 the locked solution is stable. On decreasing γ_2 a finite wavelength instability takes place and one can observe a number of patterns (see Fig. 3.2).

For $n = 3$, the existence of three-armed rotating spirals in two-dimensional systems is briefly mentioned in [137]. The aim of this chapter is to study this case in more detail, and especially the transition from phase spirals to

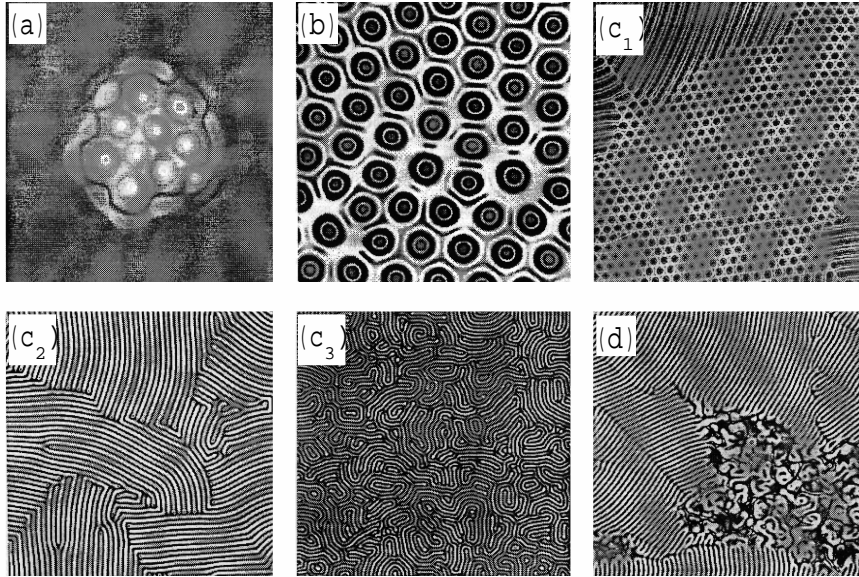


Figure 3.2: Several snapshots of the real part of the complex field A for different values of the forcing amplitude γ_2 . This decreases when going from (a) to (d). Description of the patterns: (a) isolated hexagons; (b) two penta-hepta pairs; (c₁) hexagon-stripe transition which leads to (c₂) a stripe pattern with defects that may eventually end up in (c₃) a labyrinthine structure; (d) intermittent destruction of pattern. Images taken from [137].

amplitude spirals as well as the analogies with the dynamics of systems with three competing real amplitudes which were studied in chapter 2. The study of the transition from phase to amplitude spirals confirms the robustness of the Ginzburg-Landau dynamics, which is recovered at low forcing, with all its complexity and its particular sensitivity to kinetic coefficients. Second, it presents original dynamical behavior in the excitable regime which shares generic properties with the spiral dynamics studied in chapter 2.

The chapter is organized as follows. The dynamical model and its uniform asymptotic solutions are presented in section 3.2. Section 3.3 is devoted to the description of the dynamics in terms of phase equations. The properties and possible development of front and spiral solutions are discussed in section 3.4. Numerical results for two-dimensional systems are presented in section 3.5 and conclusions are drawn in section 3.6.

3.2 Uniform Solutions

We consider an extended system undergoing a Hopf bifurcation, and submitted to a periodic temporal modulation of frequency $\omega_e = 3(\omega_0 - \nu)$. Sufficiently close to the bifurcation, its dynamics may be reduced to the following complex

Ginzburg-Landau equation, which is a particular case of Eq. (3.1):

$$\partial_t A = (\mu + i\nu)A + (1 + i\alpha)\nabla^2 A - (1 + i\beta)A|A|^2 + \gamma_3 \bar{A}^2, \quad (3.6)$$

where γ_3 is proportional to the external field intensity. The other parameters are standard [137, 138]. To simplify the notation we will call $\gamma \equiv \gamma_3$.

We look now for uniform solutions. By dropping the spatial derivative terms, the corresponding uniform equations are, in phase and amplitude variables ($A = R_0(t)e^{i\Phi_0(t)}$):

$$\dot{R}_0 = \mu R_0 - R_0^3 + \gamma R_0^2 \cos 3\Phi_0, \quad (3.7a)$$

$$\dot{\Phi}_0 = \nu - \beta R_0^2 - \gamma R_0 \sin 3\Phi_0. \quad (3.7b)$$

If we look for the stationary solutions (fixed points), Eqs. (3.7a–b) give

$$(1 + \beta^2)R_0^4 - (2\mu + 2\nu\beta + \gamma^2)R_0^2 + \mu^2 + \nu^2 = 0, \quad (3.8)$$

from where the amplitudes of the uniform solutions are given by:

$$R_{\pm}^2 = \frac{1}{2(1 + \beta^2)} [2\mu + 2\nu\beta + \gamma^2 \pm \sqrt{\gamma^4 + 4(\mu + \nu\beta)\gamma^2 - 4(\mu\beta - \nu)^2}]. \quad (3.9)$$

Such solutions exist provided that $\gamma^2 > \gamma_c^2$, with

$$\gamma_c^2 = 2[\sqrt{(\mu^2 + \nu^2)(1 + \beta^2)} - (\mu + \nu\beta)]. \quad (3.10)$$

In the rest of the chapter we will be considering the case of resonant forcing ($\nu = 0$), for which (3.10) becomes

$$\gamma_c^2 = 2\mu(\sqrt{1 + \beta^2} - 1). \quad (3.11)$$

Once the amplitude is determined by (3.9) the phase can be obtained from the stationary version of (3.7b):

$$\begin{aligned} \cos 3\Phi_0 &= \frac{R_0^2 - \mu}{\gamma R_0}, \\ \sin 3\Phi_0 &= \frac{-\beta R_0}{\gamma}. \end{aligned} \quad (3.12)$$

Each value of $R_0 = \{R_+, R_-\}$ gives rise to three solutions for the phase Φ_0 which only differ by a phase shift of $2\pi/3$. Hence, for $\gamma^2 > \gamma_c^2$ the system has six uniform solutions: $\{\Phi_1^u, \Phi_2^u, \Phi_3^u\}$ corresponding to R_- and $\{\Phi_1^e, \Phi_2^e, \Phi_3^e\}$ corresponding to R_+ . Looking for a perturbed solution in the form

$$\begin{aligned} A &= (R_0 + \delta R)e^{i(\Phi_0 + \delta\Phi)}, \\ \delta R &= \delta R_0 e^{ikx + \omega t}, \quad \delta\Phi = \delta\Phi_0 e^{ikx + \omega t}, \end{aligned} \quad (3.13)$$

we get the characteristic equation for perturbations of wave number k :

$$\omega^2 + 2\omega(2R_0^2 - \mu + k^2) + k^4(1 + \alpha^2) + 2k^2[2(1 + \alpha\beta)R_0^2 - \mu] + 3[(1 + \beta^2)R_0^4 - \mu^2] = 0. \quad (3.14)$$

An analysis of this equation for $k = 0$ shows that the Φ_i^u are always linearly unstable whereas the Φ_i^e are stable for $|\beta| < \sqrt{3}$. The three Φ_i^e solutions are called the frequency locked solutions. For $|\beta| > \sqrt{3}$ these become oscillatory unstable ($k = 0, \omega \neq 0$) in the range of forcing amplitudes $\gamma_c \lesssim \gamma' < \gamma < \gamma''$ with

$$\begin{aligned} \gamma' &= \sqrt{\gamma_c^2 + \mu f(\beta)}, \\ \gamma'' &= \sqrt{\mu(1 + \beta^2)/2}, \end{aligned} \quad (3.15)$$

$$f(\beta) = \frac{1}{2(3\beta^2 - 1)} [4\sqrt{1 + \beta^2}(1 - 3\beta^2) + 7\sqrt{3}\beta^3 - \beta^2 + 3\sqrt{3}\beta - 5]. \quad (3.16)$$

Here we have assumed (without loss of generality) that the γ 's are positive. In the range $\gamma_c < \gamma < \gamma'$ there is an instability at $k = 0, \omega = 0$. For $\gamma > \gamma''$ the homogeneous states R_+ are linearly stable. Notice that in the BH model there are also, in a certain range of parameters, three equivalent homogeneous stable states (referred to roll states; see section 2.3). Nevertheless, in the present case the states are all associated with the same field whereas in the BH model each state corresponds to a different amplitude.

In the case where the frequency locked solutions are stable, we can show that the system behaves as an excitable one. Effectively, let us construct the nullclines of the dynamics (3.1), which correspond to the system (3.7a–b) [see Fig. 3.3]. In both figures, it is easy to see that the states labeled u are unstable, while the states labeled e are stable for small perturbations. However,

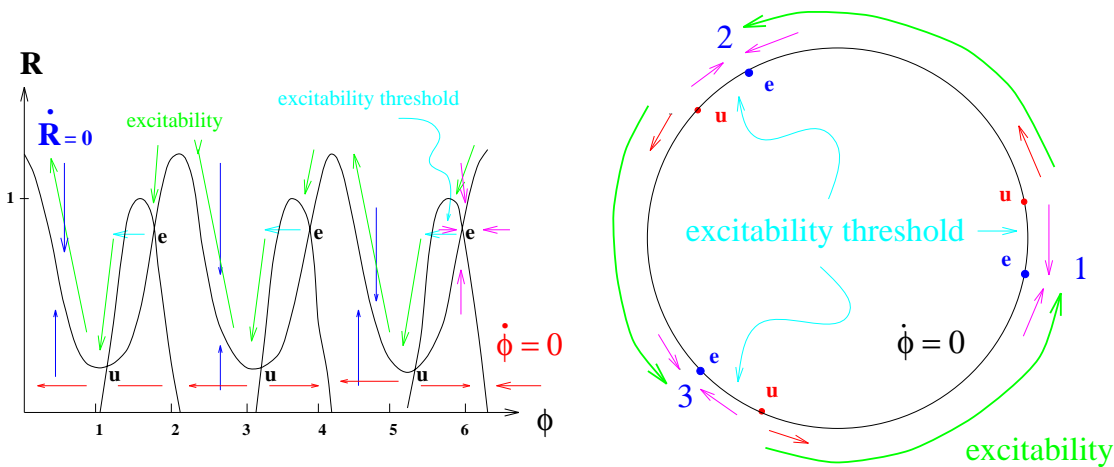


Figure 3.3: (Left) nullclines and fixed points of the forced Ginzburg-Landau equation in the (R, ϕ) plane in rectangular coordinates for $\gamma = \beta = 4\mu = 1$ and (right) in polar coordinates for $\gamma = \beta = 0.01, \mu = 0.25$. Note that for these parameters $R_+ \approx R_-$.

for perturbations larger than a well defined threshold, the latter are unstable and the system makes an excursion in the phase space, before reaching another, equivalent, steady state. It is a form of excitability. The excitability threshold can be explicitly computed in the limiting case $\beta, \gamma \ll \mu$. In this limit, and taking into account that $\gamma_c \simeq \beta\sqrt{\mu}$, the adiabatic elimination of the amplitude in (3.7b) leads to the phase equation:

$$\dot{\Phi}_0 = -\sqrt{\mu}(\gamma_c + \gamma \sin 3\Phi_0), \quad (3.17)$$

from where the excitable stable steady states are given by $\sin 3\Phi_i^e = -\gamma_c/\gamma$ and $\gamma \cos 3\Phi_i^e > 0$, and the three unstable steady states are given by $\sin 3\Phi_i^u = -\gamma_c/\gamma$ and $\gamma \cos 3\Phi_i^u < 0$, $i = 1, 2, 3$. In this case, the excitability threshold is thus given by:

$$\Delta\Phi = |\Phi_i^e - \Phi_i^u| \simeq \frac{\pi}{3} - \frac{2}{3} \frac{\gamma_c}{\gamma}. \quad (3.18)$$

For $\gamma^2 < \gamma_c^2$ there are no fixed points and asymptotic solutions correspond to temporal oscillations of the limit cycle type (oscillatory regime). For $\gamma = 0$ the limit cycle is a circle that becomes deformed for $0 < |\gamma| < \gamma_c$ (see Fig. 3.4). On increasing γ , the period of the oscillations increases and diverges for $\gamma^2 \rightarrow \gamma_c^2$. For $\gamma^2 > \gamma_c^2$ the system has six fixed points.

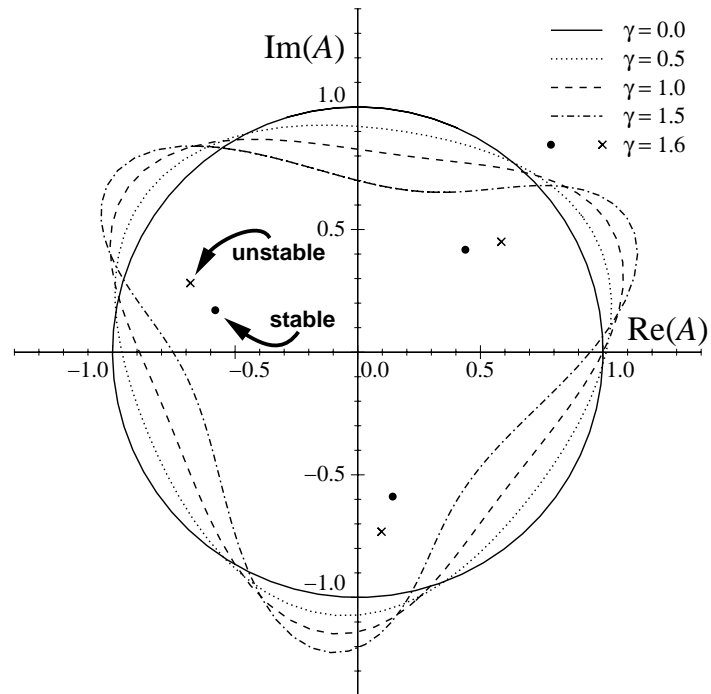


Figure 3.4: Uniform solutions of Eqs. (3.7a–b) for several values of the forcing parameter γ . System parameters are $\mu = 1$, $\beta = -2.0$ (so $\gamma_c = 1.57$). Note that for $\gamma < \gamma_c$ uniform solutions are of the limit cycle type whereas for $\gamma > \gamma_c$ they become fixed points.

3.3 Phase Approximation

In this section we present several phase equations, each one valid in a different region of parameters. These equations can be used to analyze the stability of the uniform patterns.

3.3.1 The Oscillatory Regime

In the oscillatory regime ($\gamma^2 < \gamma_c^2$), the phase dynamics may be obtained by perturbing the uniform solution $(R_0(t), \Phi_0(t))$, and writing $R = R_0(t) + \rho(\mathbf{r}, t)$, $\Phi = \Phi_0(t + \phi(\mathbf{r}, t))$. Following Hagan [139], the adiabatic elimination of the amplitude perturbations leads to the following phase dynamics:

$$\partial_t \phi = (1 + \alpha \bar{\beta}) \nabla^2 \phi + \kappa (\nabla \phi)^2 + \dots, \quad (3.19)$$

where T is the period of the oscillations, and

$$\bar{\beta} = \frac{\int_0^T dt \frac{2\beta R_0 + \gamma \sin 3\Phi_0}{2R_0 - \gamma \cos \Phi_0} \dot{\Phi}_0^2}{\int_0^T dt \dot{\Phi}_0^2}, \quad \kappa = \frac{\int_0^T dt \left(\frac{2\beta R_0 + \gamma \sin 3\Phi_0}{2R_0 - \gamma \cos \Phi_0} - \alpha \right) \dot{\Phi}_0^3}{\int_0^T dt \dot{\Phi}_0^2}. \quad (3.20)$$

For $\gamma \rightarrow 0$, one recovers the usual Burgers equation

$$\partial_t \bar{\phi} = (1 + \alpha \beta) \nabla^2 \bar{\phi} + (\alpha - \beta) (\nabla \bar{\phi})^2 + \dots, \quad (3.21)$$

with $\bar{\phi} = \beta \mu \phi$. Hence, in the regime where $1 + \alpha \bar{\beta} > 0$, stable (phase) spiral waves may be expected, with wavenumber proportional to κ , and thus depending on the characteristics of the oscillations [139, 140]. In this regime, the qualitative behavior and interaction between these topological defects should thus be almost insensitive to the forcing [141, 142, 143]. Furthermore, in the regime where $1 + \alpha \bar{\beta} < 0$, plane waves are phase unstable (Benjamin-Feir instability [144]), so that turbulence regimes may be expected [145]. In the oscillatory regime, the system presents thus qualitatively the same complexity and the same spatio-temporal behaviors than self-oscillating systems. Only quantitative aspects are affected by the forcing.

3.3.2 The Excitable Regime

In the excitable regime ($\gamma^2 > \gamma_c^2$) the phase dynamics can be obtained in the limit $\beta, \gamma \ll \mu$, $\beta \ll 1$, by eliminating adiabatically the amplitude of the field. Taking into account that, in this regime, $R^2 \simeq \mu$ and $\gamma_c \simeq |\beta| \sqrt{\mu}$, we are left with the following phase equation:

$$\partial_t \Phi = -\sqrt{\mu}(\gamma_c + \gamma \sin 3\Phi) + (1 + \alpha \beta) \nabla^2 \Phi - (\alpha - \beta) (\nabla \Phi)^2 + \frac{\alpha^2(1 + \beta^2)}{2\mu} \nabla^4 \Phi. \quad (3.22)$$

Besides the homogeneous solutions discussed in the previous section, this equation admits front solutions connecting stable states asymptotically at $x = \pm\infty$. In the case $\alpha = \beta = 0$ the phase equation is relaxational and the fronts connect two states with the same value of the potential and are, therefore, stationary. In the case $\alpha = \beta \neq 0$, the phase equation is still relaxational but now the steady states have different value of the potential and the front moves. Moreover, when $\alpha \neq \beta$ there is a purely nonpotential induced front motion. Eq. (3.22) will be used in the next section as the starting point to compute the velocity of the front solution.

In order to study pattern forming instabilities, we can use (3.22) in the limit of small Φ . Expanding the $\sin 3\Phi$ up to linear order in Φ , we are led to a damped Kuramoto-Sivashinsky phase equation [137]. It follows that frequency locked solutions are stable for $1 + \alpha\beta > 0$. If $1 + \alpha\beta < 0$, a pattern forming instability of the locked states would occur for [137]¹

$$\mu > 36\gamma^2 \frac{\alpha^4(1 + \beta^2)^3}{(1 + \alpha\beta)^4}. \quad (3.23)$$

Since, in this regime, $\gamma^2 > \gamma_c^2$, a necessary condition for this instability is thus

$$(1 + \alpha\beta)^4 > 72(\sqrt{1 + \beta^2} - 1)\alpha^4(1 + \beta^2)^3, \quad (3.24)$$

and this condition cannot be realized in the $\{1 + \alpha\beta < 0\}$ domain. Therefore, the frequency locked solutions are stable and pattern forming instabilities are ruled out within the phase approximation.

Note that in reference [146] the forced CGLE is studied for the resonant cases $n \geq 4$. Special emphasis is put in a front instability which may cause the decomposition of phase fronts with a difference of π between the phase of the uniform phase states into several fronts with a smaller shift phase. The transition occurs when the strength of the forcing is reduced below some critical value.

3.4 Fronts and Spirals

For $|\gamma| > \gamma_c$, the forced Ginzburg-Landau equation possesses three equivalent excitable steady states. The excitability mechanism described in section 3.2 provides a natural way of building fronts between these steady states. Despite the equivalence of the fixed points, such fronts are expected to move, as a result of the nonpotential character of the dynamics as described in 3.3.2.

3.4.1 One-dimensional systems

A one-dimensional front connecting two stable phase locked states may move due to nonpotential effects. This constitutes another example of front motion

¹This corrects the misprint of reference [137] in ϵ and k_0 after Eq. (28).

between dynamical equivalent states under a nonrelaxational dynamics. In section 1.3.3 we studied the motion of 1D Bloch fronts in the case of the CGLE with a 2ω -forcing (case $n = 2$). The 1D BH model, described in 2.4, provided another example of nonpotential front motion.

Consider a front solution of Eq. (3.22), e.g. $\Phi_{ij}(x - vt)$, joining the states i (at $x \rightarrow -\infty$) and j (at $x \rightarrow +\infty$), such that $\Phi_j^e > \Phi_i^e$. We look for a perturbed kink solution in the form

$$\Phi_{ij}(x - vt) = \Phi_{ij}^0(x - vt) + \varepsilon \Phi_{ij}^1(x - vt) + O(\varepsilon^2), \quad (3.25)$$

$$v = v^1 \varepsilon + O(\varepsilon^2), \quad (3.26)$$

where ε is a small parameter. If we assume that $\alpha \sim \beta \sim \varepsilon$ ($\Rightarrow \gamma_c \sim \varepsilon$), we have, to order $O(\varepsilon^0)$:

$$-\sqrt{\mu}\gamma \sin 3\Phi_{ij}^0 + \partial_{yy}\Phi_{ij}^0 = 0, \quad y \equiv x - vt, \quad (3.27)$$

and to order $O(\varepsilon^1)$:

$$\mathcal{L}\phi_{ij}^1 = \Psi, \quad (3.28)$$

$$\mathcal{L} = -3\sqrt{\mu}\gamma \cos 3\Phi_{ij}^0 \partial_y + \partial_{yy},$$

$$\Psi = -v^1 \partial_y \Phi_{ij}^0 + \sqrt{\mu}\gamma_c + (\alpha - \beta)(\partial_y \Phi_{ij}^0)^2.$$

The solvability condition for the linear equation (3.28) is $(\Psi, \partial_y \Phi_{ij}^0) = 0$, where (\cdot, \cdot) is a scalar product defined as $(f, g) = \int_{\mathbb{R}} dy f(y) \cdot g(y)$. From this solvability condition one can obtain the kink velocity to leading order as

$$v = \frac{2\pi\gamma_c\sqrt{\mu} + 3(\alpha - \beta) \int_{-\infty}^{+\infty} dy (\partial_y \Phi_{ij}^0)^3}{3 \int_{-\infty}^{+\infty} dy (\partial_y \Phi_{ij}^0)^2} + O(\varepsilon^2), \quad (3.29)$$

where we have used the fact that $\int_{-\infty}^{+\infty} dy \partial_y \Phi_{ij}^0 = \Phi_j^e - \Phi_i^e = \frac{2\pi}{3}$. Just like in preceding calculations for other systems [see Eqs. (1.62) and (2.62)], the front velocity turns out to be proportional to the nonpotential parameters in leading order. If we assume $\Phi_1^e < \Phi_2^e < \Phi_3^e$ we have that for $\alpha > \beta$ the fronts Φ_{12} , Φ_{23} and Φ_{31} move to the right, while the fronts Φ_{21} , Φ_{13} and Φ_{32} move to the left. Hence, any domain of one steady state, embedded in a domain of another one, either expands or shrinks, leaving the system in one steady state (domains of 2 embedded into 1, 3 into 2 and 1 into 3 shrink while domains of 1 into 2, 2 into 3 and 3 into 1 expand). However, a succession (from left to right) of domains with states in the order 1, 2, 3, 1, etc. moves as a whole to the right. When it is in the order 1, 3, 2, 1, etc., it moves as a whole to the left (see Fig. 3.5).

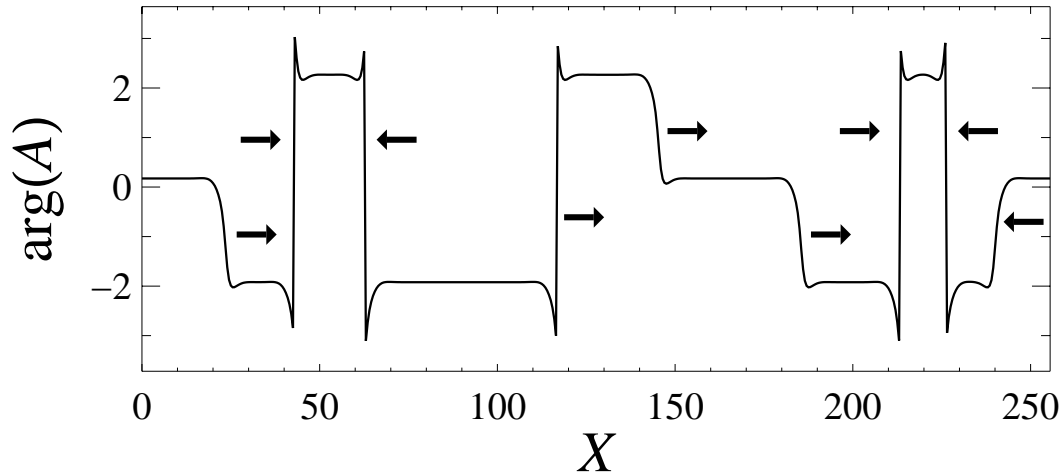


Figure 3.5: Plot of the phase field in the excitable regime in 1D. Note the existence of three homogeneous phase states. The arrows indicate the direction of motion of the several fronts. Parameter values are $\mu = 1$, $\alpha = 2$, $\beta = -0.2$, $\gamma = 0.5 > \gamma_c = 0.199$.

3.4.2 Two-dimensional systems

In two-dimensional systems, straight linear fronts have the same behavior as in one-dimensional systems. Furthermore, sets of two inclined fronts separating domains with different steady states also move away or annihilate, leaving the system in one steady state only (see Fig. 3.6).

New phenomena may arise when the three steady states coexist in the system. In this case, three fronts, which separate the respective domains, coalesce in one point (a vertex). The three fronts are expected to rotate around this point. The result is a rotating spiral whose angular velocity increases with the forcing amplitude. Spirals corresponding to sequences of states in the order $1 \rightarrow 2 \rightarrow 3$ or $1 \rightarrow 3 \rightarrow 2$ around the center have opposite senses of rotation. Isolated vertices remain immobile, but nonisolated ones have a dynamical evolution induced by mutual interactions, which may even lead to the annihilation of counter-rotating spirals. This dynamical behavior is illustrated by the results of the numerical analysis presented in the next section.

The analogies with the dynamics of the two-dimensional BH model described in section 2.5 are evident. In the case of the CGLE, the phase locked states are associated with a broken phase symmetry of a single complex order field. In the BH model, on the other hand, we deal with three dynamical states in competition, each associated with a different real amplitude. In two-dimensional systems, vertices may form when the three different types of domains meet at one point (note that it is not possible in one-dimensional systems [147, 148]). In both models, the nonpotential dynamics induces the rotation of interfaces around the vertices preventing the system from coarsening.

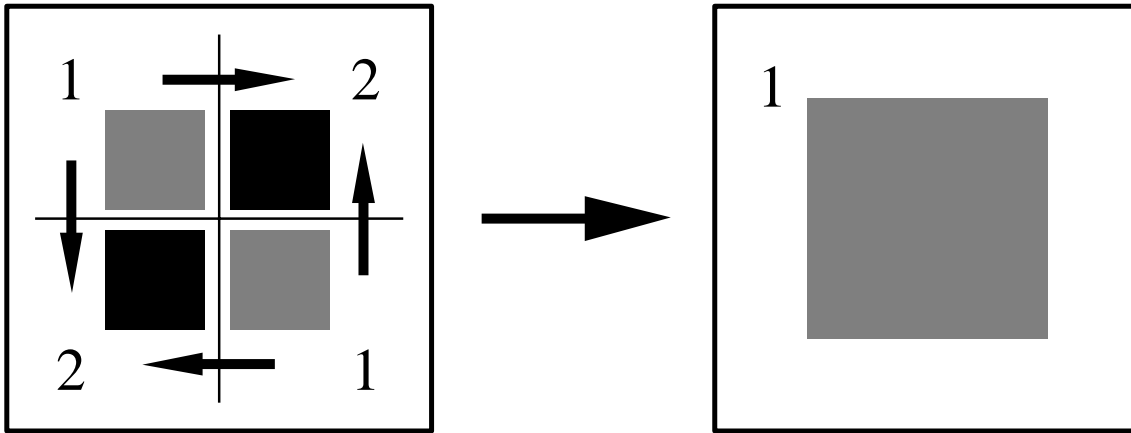


Figure 3.6: Example of motion of pairs of inclined fronts separating domains with equivalent steady states of the forced Ginzburg-Landau equation for $\gamma > \gamma_c$.

3.5 Numerical Results

In this section, we present numerical results in two spatial dimensions which illustrate the various dynamical behaviors described in the preceding sections. We have simulated the forced CGLE in two spatial dimensions by using a pseudospectral method with periodic boundary conditions. We discretized the system in a square mesh of 256×256 points. Cases within and beyond the validity of the phase approximation and above and below the line $1 + \alpha\beta = 0$ of the Benjamin-Feir (BF) instability were considered. In all the cases the parameter μ was taken fixed and equal to 1. We point out that although in the 1D CGLE without forcing regimes of phase and defect turbulence only appear above the BF line [149, 150] ($1 + \alpha\beta < 0$), defect turbulence regimes in 2D for $1 + \alpha\beta > 0$ are reported in [151]. Taking as starting point some of the cases treated in [151], we will study the structures observed when the forcing intensity is increased from $\gamma = 0$ to $\gamma > \gamma_c$. In table 3.1 we give the parameters chosen for each one of the cases studied.

μ	α	β	γ_c	Phase approx. valid?	$1 + \alpha\beta$	Regime ($\gamma = 0$)	Figure
1.0	2.0	-0.20	0.20	Yes	> 0	<i>Froz. stat.</i> (*)	3.7
1.0	5.5	-0.20	0.20	Yes	< 0	<i>Froz. stat.</i>	3.8
1.0	2.0	-0.76	0.72	No	< 0	<i>Ph. turb.</i> (*)	3.9
1.0	0.0	-1.80	1.45	No	> 0	<i>Def. turb.</i> (*)	3.10, 3.12
1.0	2.0	-1.00	0.91	No	< 0	<i>Def. turb.</i> (*)	3.11

Table 3.1: Parameters of the various cases discussed in section 3.5. Cases marked with (*) are studied in [151].

We start the discussion with cases for which the phase approximation applies ($\beta, \gamma \ll \mu$). Below the BF line ($1 + \alpha\beta > 0$) we took $\{\alpha = 2, \beta = -0.2; \gamma_c = 0.2\}$. This case corresponds to the *frozen states* regime when there is no forcing. In Fig. 3.7 we show the modulus and phase of the complex field A in the regimes of no forcing, oscillatory, $\gamma \simeq \gamma_c$ and excitable. As expected, spiral defects surrounded by shock lines occur in the no forcing regime [151]. When the strength of the forcing γ is increased but still being below the critical value γ_c (oscillatory regime), the phase dynamics does not change significantly. However, amplitude spirals appear in the modulus of the field. The split of the phase into three locked states is observed approximately at the predicted theoretical value of the forcing γ_c . For forcings slightly greater than γ_c , we observe annihilation of vertices until an homogeneous state is reached due to finite size effects. For larger forcings, the nonpotential dynamics is able to stop vertex annihilation and therefore to inhibit coarsening.

Above the BF line ($1 + \alpha\beta < 0$), we took $\alpha = 5.5$ and kept the rest of parameters as before. The most notorious difference with the previous case is the existence of asymptotic frozen states in the oscillatory regime and also close to the critical forcing γ_c (see Fig. 3.8). Below γ_c , we observe frozen targets while close to the transition the frozen patterns hold three locked phase states but without vertices. As expected, large enough forcings give rise to a time-dependent dynamics with three-armed spirals rotating around vertices.

Beyond the validity of the phase approximation, different phenomena may occur. In particular, pattern forming instabilities may take place for small and moderate forcings above the critical value γ_c . In the case above the BF line with parameters $\{\alpha = 1, \beta = -0.76; \gamma_c = 0.72\}$ (*phase turbulence* regime in the absence of external forcing), oscillating targets that coexist with vertices are observed close to the transition (see Fig. 3.9). In the modulus, pulses form at the center of the targets and move away, while the phase oscillates between $-\pi$ and π with a certain period. Still above the BF line we have considered a case of *defect turbulence* with parameters $\{\alpha = 2, \beta = -1; \gamma_c = 0.91\}$. In this case the no forcing dynamics is characterized by a great number of defects. The patterns observed on varying γ are qualitatively similar to those of the phase turbulence regime (see Fig. 3.11).

We also considered, beyond the regime of validity of the phase approximation, a case below the BF line. We took the set of parameters $\{\alpha = 0, \beta = -1.8; \gamma_c = 1.45\}$, which correspond to a *defect turbulence* regime at $\gamma = 0$. As $1 + \alpha\beta > 0$, well-developed spirals can be observed (see Fig. 3.10). The modulus of the field is characterized for $\gamma < \gamma_c$ by amplitude spirals that rotate around defects whereas the phase field shows a similar behaviour to the no forcing situation. On the other hand, since $|\beta| > \sqrt{3}$, and according to the discussion of section 3.2, there exists a range of forcing intensities for which the locked solutions are oscillatory unstable at zero wavenumber. This is seen in Fig. 3.12. This instability is observed after the annihilation of two counter-rotating defects. An oscillating target develops and its central part spreads

over the system as it oscillates, and eventually it disappears.

In all the cases studied, the phase becomes locked approximately at the value γ_c theoretically predicted for the forcing amplitude. When the phase approximation is valid, the locked phase states are seen to be stable but excitable spirals may be absent near the transition for system parameters such that $1 + \alpha\beta < 0$. When the phase approximation is not valid, instabilities of the homogeneous states for the phase may take place and give rise to complex patterns. It is important to emphasize that for $\gamma \gg \gamma_c$ the physics is essentially the same for all the regimes of parameters that we have explored, with interfaces rotating around vertices. This rotation, which is due to the underlying nonpotential dynamics, inhibits phase coarsening which would take place through vertex annihilation. The vertices are essentially pinned and the resulting pattern is nearly time periodic at relatively short time scales.

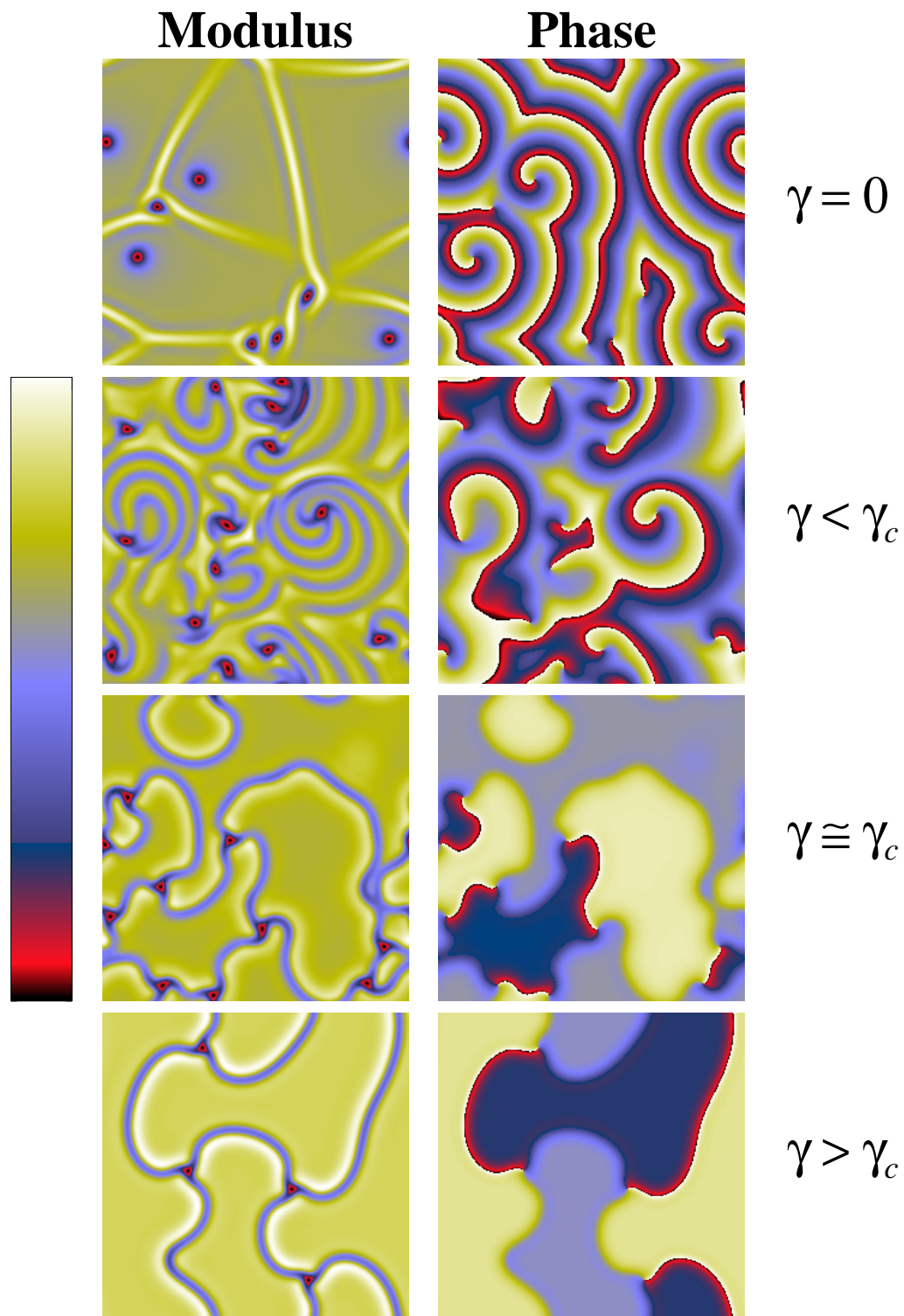


Figure 3.7: Modulus and phase of the complex field A in the cases $\gamma = 0$ (no forcing), $\gamma < \gamma_c$ (oscillatory), $\gamma \cong \gamma_c$ and $\gamma > \gamma_c$ (excitable). Parameter values are $\mu = 1$, $\alpha = 2$, $\beta = -0.2$ (so $\gamma_c \simeq 0.2$), and $\gamma = 0.1$ (0.25) for the oscillatory (excitable) case.

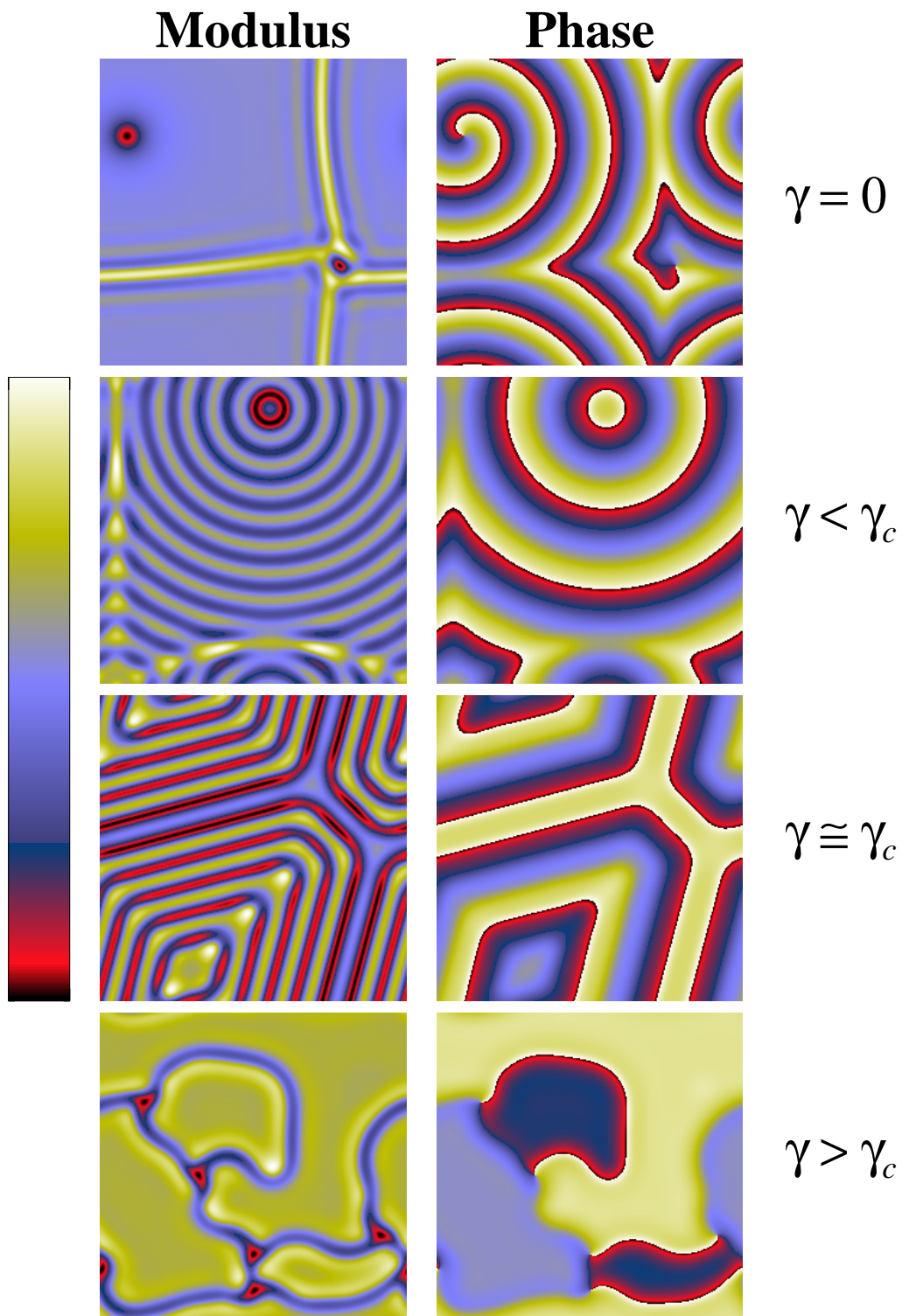


Figure 3.8: Same as in Fig. 3.7. Parameter values are $\mu = 1$, $\alpha = 5.5$, $\beta = -0.20$ (so $\gamma_c \simeq 0.2$), and $\gamma = 0.1$ (0.25) for the oscillatory (excitable) case.

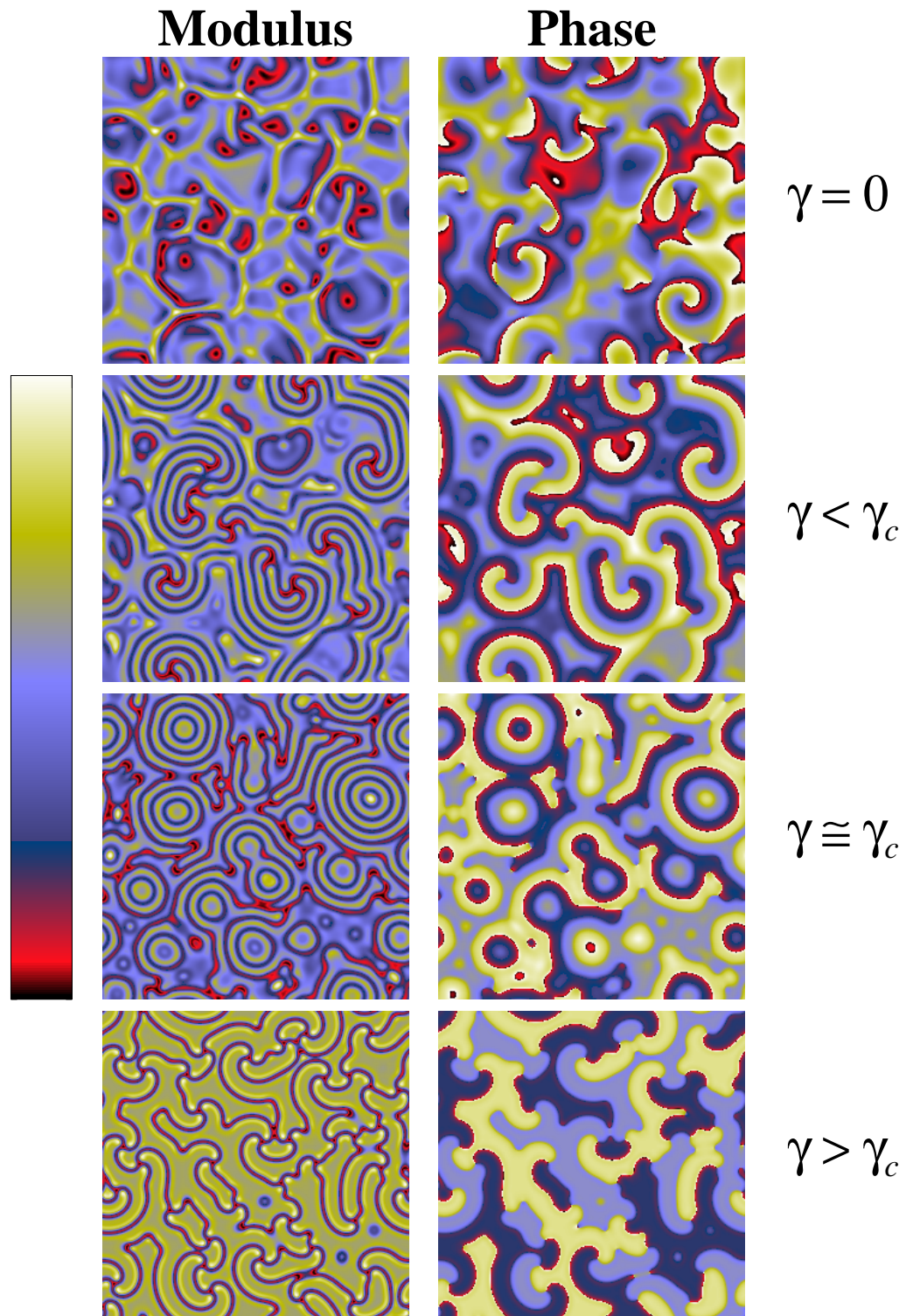


Figure 3.9: Same as in Fig. 3.7. Parameter values are $\mu = 1$, $\alpha = 2$, $\beta = -0.76$ (so $\gamma_c \simeq 0.72$), and $\gamma = 0.5$ (1.5) for the oscillatory (excitable) case.

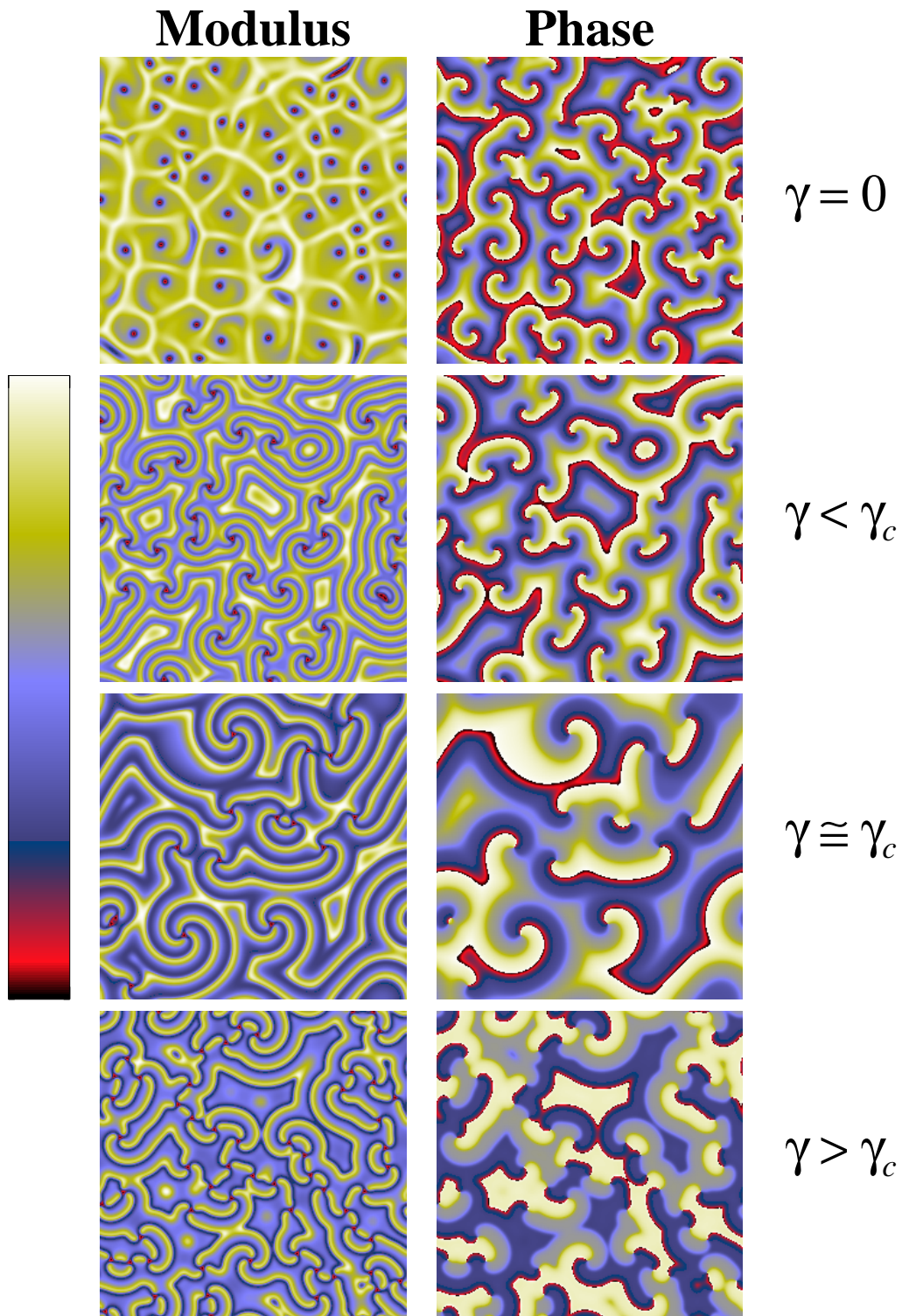


Figure 3.10: Same as in Fig. 3.7. Parameter values are $\mu = 1$, $\alpha = 0$, $\beta = -1.8$ (so $\gamma_c \simeq 1.45$), and $\gamma = 1$ (1.6) for the oscillatory (excitable) case.

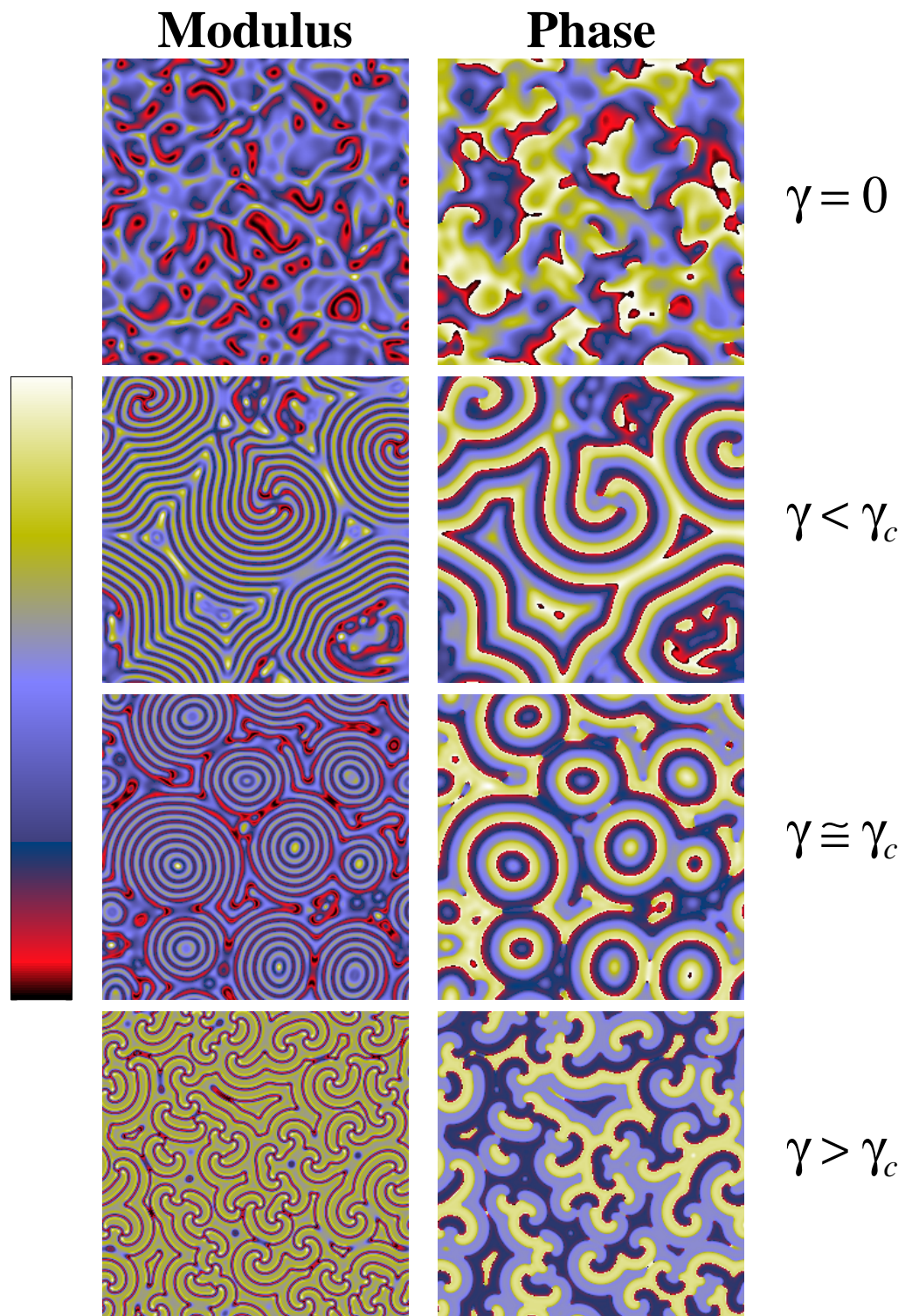


Figure 3.11: Same as in Fig. 3.7. Parameter values are $\mu = 1$, $\alpha = 2$, $\beta = -1$ (so $\gamma_c \simeq 0.91$), and $\gamma = 1$ (3) for the oscillatory (excitable) case.

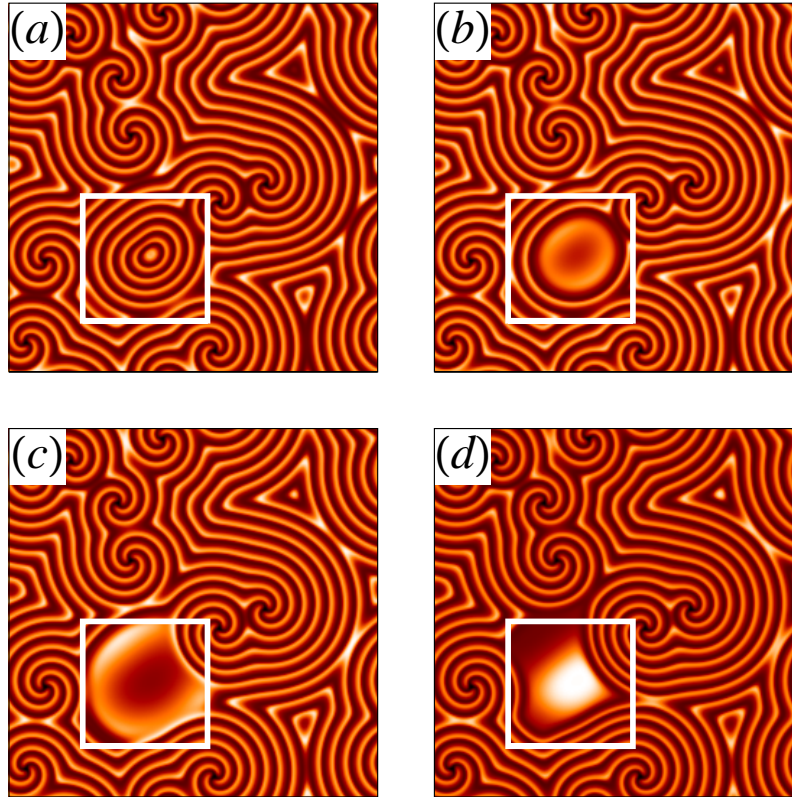


Figure 3.12: Snapshots of the modulus of the field in a regime of parameters where an oscillatory instability at zero wave number occurs. The square encloses an oscillating region. Time increases when going from (a) to (d).

3.6 Conclusions

In this chapter we have studied a special case of temporal forcing of nonlinear oscillators beyond a Hopf bifurcation. Temporal modulations with frequencies nearly equal to three times the critical one, may be strongly coupled with the unstable modes associated with the Hopf instability. It modifies the character of the bifurcation and the resulting spatio-temporal patterns.

For forcing amplitudes below a critical value, the system is in an oscillatory regime, where spatio-temporal behavior strongly depends on the parameters of the associated Ginzburg-Landau equation. In particular, topological defects correspond to one-armed phase spirals. For forcing amplitudes above the critical one, the system is in a phase locked regime with three equivalent steady states. In this regime there are a number of analogies with the patterns observed in rotating Rayleigh-Bénard convection. In this case the domains correspond to sets of parallel convection rolls with a certain orientation and the vertices to points at which the roll amplitudes take the same value. As in the case of the CGLE, the rotation of interfaces around vertices is due to nonpotential effects.

Like in the $n = 1$ and $n = 2$ cases of strongly resonant forcings, a form of excitability may also be observed. However, contrary to the $n = 1$ and $n = 2$ forcings, no pattern forming instability of frequency locked states occurs, in this case, in the regime where the phase approximation is valid. Due to the non-potential character of the dynamics, fronts between equivalent steady states move. The result is that, when the three equivalent steady states coexist in the system, three armed rotating spirals are generated around vertices where the fronts separating each domain meet. Hence, we predict a transition between one-armed phase spirals and three-armed excitable amplitude spirals, which occurs when the forcing amplitude passes through a critical value. This transition is confirmed by numerical analysis of the corresponding Ginzburg-Landau equation.

Chapter 4

Domain Growth, Localized Structures and Labyrinthine Patterns in Vectorial Kerr Resonators

Abstract. *We study domain growth in a nonlinear optical system useful to explore different scenarios that might occur in systems which do not relax to thermodynamic equilibrium. Domains correspond to equivalent states of different circular polarization of light. We describe three dynamical regimes: a coarsening regime in which dynamical scaling holds with a growth law dictated by curvature effects, a regime in which localized structures form, and a regime in which polarization domain walls are modulationally unstable and the system freezes in a labyrinthine pattern.*

4.1 Introduction: Domain Growth in Optical Systems

Driven nonlinear optical systems offer a wealth of opportunities for the study of pattern formation and other nonequilibrium processes in which the spatial coupling is caused by diffraction instead of diffusion. These systems are specially interesting because they naturally lead to the consideration of vectorial complex fields, being the vector character associated with the polarization of light, and also because they often support the formation of localized structures (LS's) [22, 67, 152] in the form of light spots which are being actively considered for applications in parallel optical processing. In addition, Hamiltonian or conservative dynamics are, generally speaking, essential ingredients in the dynamics of nonlinear optical systems. Only very recently domain growth has been considered in some of these systems and some growth laws obtained from numerical simulations have been reported [9, 22, 23, 24].

In reference [9] the problem of domain growth is studied for two optical systems that display optical bistability; in other words, there is coexistence of two homogeneous linearly stable states in a certain range of parameters.

The homogeneous solutions as a function of the input field are multivalued (s-shaped). In addition, these systems present a Turing type instability of the homogeneous solutions. The parameters are chosen to give a regime of bistability and in the weak dispersion limit (small cavity detunings). Under these conditions, the Turing instability is close to the limit points of the domains of multivalued homogeneous solutions. In addition, the band of unstable wavevectors includes $k = 0$ and is small (the critical wavevector of the Turing instability is close to zero). Starting from a random perturbation of a linearly unstable homogeneous state, modes with small wavenumber (including zero) are excited and interact during the transient dynamics. For these two models three stages of the space-time evolution are distinguished in reference [9]:

- (S1) Formation of a labyrinthine structure in the short time limit due to the exponential amplification of the unstable modes.
- (S2) The cavity field displays a few islands formed by one of the homogeneous steady states. Coarsening takes place with a growth law $L(t) \sim t^{1/3}$, similar to that of the Lifshitz-Slyozov-Wagner (LWS) theory [30] (see also sec. 1.4.1.c).
- (S3) The system ends up with a unique stationary stripe.

The first model is a Swift-Hohenberg equation type with real coefficients obtained from the Maxwell-Bloch equations for nascent hysteresis in the weakly dispersive regime [153]. This is a relaxational gradient equation which can be expressed in the form (see [9] for the details):

$$\partial_t \psi = -\frac{\delta \mathcal{F}}{\delta \psi}, \quad \mathcal{F} = \int \left[-V(\psi) + \frac{1}{2}(\nabla_{\perp}^2 \psi)^2 - (\nabla_{\perp} \psi)^2 \right], \quad (4.1)$$

$$V(\psi) = \left[\left(\frac{C - 3\psi_s^2}{6\Delta^2} \right) - \sqrt{3}\psi_s \frac{\psi}{3} - \frac{\psi^2}{4} \right] \psi^2, \quad (4.2)$$

where ψ has to do with the amplitude of the cavity field (ψ_s is the homogeneous state) and ∇_{\perp} is the gradient in the transverse plane. The key point is that the term $-(\nabla_{\perp} \psi)^2$, which has to do with “surface tension”, has a *negative* contribution. The authors of ref. [9] claim that it is the reason why the final state is a stripe rather than a disk. Notice that in the case of the Ginzburg-Landau functional (1.6), the contribution from the surface tension is positive.

The second system that produces bistability is the degenerate optical parametric oscillator (DOPO) in a ring cavity driven by an external injected signal E_0 at frequency 2ω . This field is converted into a field at frequency ω by a quadratic nonlinear medium ($\chi^{(2)}$ medium). This conversion process can be described by the following pair of coupled equations [154]:

$$\begin{aligned} \partial_t E_1 &= -(\gamma + i\Delta_1)E_1 + E_0 - E_2^2 + ia_1 \nabla_{\perp}^2 E_1, \\ \partial_t E_2 &= -(1 + i\Delta_2)E_2 + E_1 E_2^* + ia_2 \nabla_{\perp}^2 E_2, \end{aligned} \quad (4.3)$$

where

$E_{1,2}$: electric field envelopes at frequencies $\omega_1 = 2\omega$, $\omega_2 = \omega$.

Δ_j : cavity detuning of the field E_j .

γ : ratio of the photon lifetimes at frequency 2ω and ω .

$a_{1,2}$: diffraction coefficients (phase matching imposes $a_1/a_2 = 2$).

Eqs. (4.3) provide a clear example in which the diffusion (∇^2) is replaced by *diffraction operators* ($i\nabla^2$). Eqs. (4.3) admit two types of homogeneous solutions:

(HS1) Nolasing state:

$$|E_{s1}|^2 = \frac{E_0^2}{\gamma^2 + \Delta_1^2}, \quad E_{s2} = 0. \quad (4.4)$$

This is stable for $E_0 < \sqrt{(\gamma^2 + \Delta_1^2)(1 + \Delta_2^2)} = E_{\text{th}}$.

(HS2) Lasing state:

$$|E_{s1}|^2 = 1 + \Delta_2^2, \quad E_0^2 = |E_{s2}|^4 - 2(\Delta_1\Delta_2 - \gamma)|E_{s2}|^2 + |E_{\text{th}}|^2. \quad (4.5)$$

This is bistable if $\Delta_1\Delta_2 > \gamma$.

A situation of bistability in which both detuning parameters are negative is considered. Under this condition, the nolasing state undergoes a modulational instability at $E_0 = E_T = \sqrt{\gamma^2 + \Delta_1^2}$. Taking $\Delta_2 \ll 1$, the wavenumber of maximum growth rate $k_T = \sqrt{-\Delta_2/2}$ is close to zero. Starting from a random perturbation of the unstable homogeneous steady state, three stages of evolution take place. This is seen in Fig. 4.1. In the first stage $L(t) \sim \exp(t)$ whereas the asymptotic growth law is $L(t) \sim t^{1/3}$.

There exists another range of parameters in which domain growth takes place with a different growth law in the DOPO. When $\Delta_2 > 0$, the nolasing state becomes unstable for homogeneous perturbations ($k = 0$). The system evolves into any of two equivalent homogeneous lasing solutions that only differ in sign. The coarsening process corresponding to the dynamical evolution of the domains of these stable solutions is found to be self-similar with a growth law $L(t) \sim t^{1/2}$ [48].

Another optical system for which a growth law $t^{1/3}$ has been reported is studied in [23]. The authors consider an optical ring cavity with plane mirrors filled with a two-level medium and driven by a coherent plane-wave injected field. In the mean field limit, the dynamics of the single longitudinal mode can be described by the Maxwell-Bloch equations. The time-space evolution

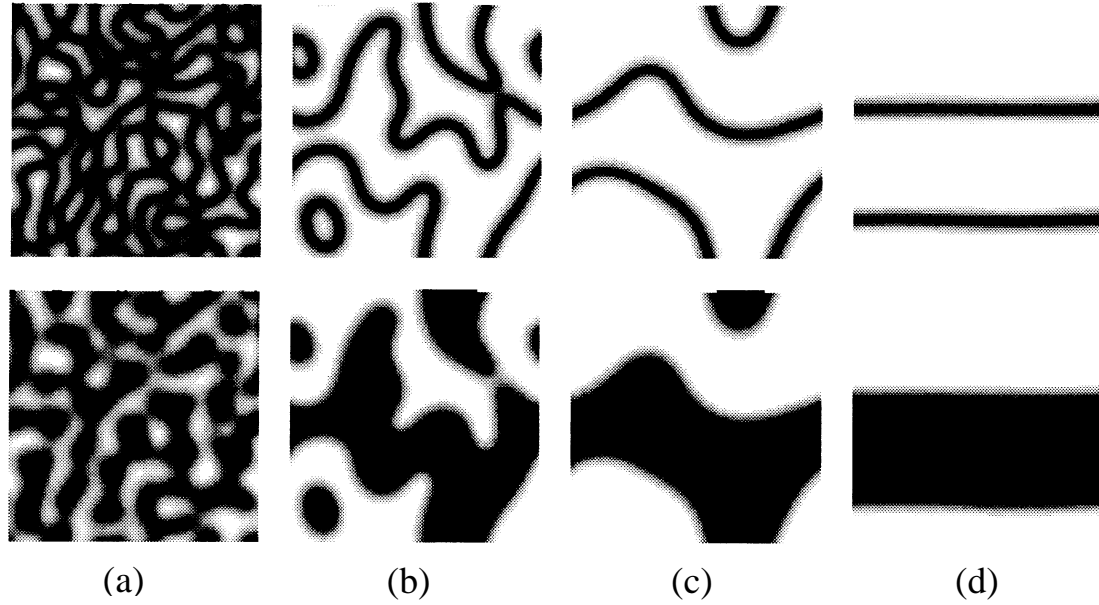


Figure 4.1: Time sequence showing three stages of domain growth in a DOPO. The figures in the upper (lower) row show the real part of the field E_2 (E_1). The initial condition is the unstable homogeneous steady state with small amplitude added. (a) Labyrinthine pattern; (b), (c) coarsening effect; (d) unique stationary stripe. High-field amplitude areas are plain white. Taken from [9].

of the slowly varying envelope of the cavity electric field is described by the simple partial differential equation [155, 156]:

$$\partial_t E = E_0 - (1 + i\theta)E - \frac{2C(1 - i\Delta)E}{1 + \Delta^2 + |E|^2} + i\nabla_{\perp}^2 E, \quad (4.6)$$

where

E : normalized slowly varying envelope of the electric field.

E_0 : real amplitude of the injected field.

∇_{\perp}^2 : transverse Laplacian.

θ, Δ : detunings.

C : population difference between the two levels normalized to the total population.

A linear stability analysis shows that there is bistability if $C > C_c$, where C_c is the real solution of $(C_c - 4)(1 + 2C_c) = 27\theta^2 C_c^2$. The homogeneous steady state solutions undergo a Turing instability, leading to the formation of stationary periodic patterns at $I_T^{\pm} = |E_T^{\pm}|^2 = [C - 1 \pm \sqrt{C(C - 4)}]/2$. Close to these bifurcation points there exists a band $[0, k_m]$ of unstable modes. On the other hand, the critical wavenumber k_T corresponding to the maximum gain

is $k_T = \sqrt{-\theta}$. Hence, spontaneous pattern forming instability requires $\theta < 0$ and $C > 4$ to have k_T real and I_T^\pm positive. As in the previous models (4.1) and (4.3), a situation such that the Turing bifurcation is close to the limit points of the bistability domain is considered. This is controlled by the detuning θ . The initial condition consists of a small random perturbation of the unstable homogeneous state, which is comprised between the two Turing bifurcation points. After an initial transient, domains of amplitudes corresponding to the lower and upper branches of the homogeneous steady states develop. For large sizes, the average domain size shows dominant behaviors in the sequence $L(t) \sim t^{1/3} \rightarrow t \rightarrow t^{1/3}$. The final state is a unique stationary localized stripe in the form of a kink in the transverse profile of the field cavity. Although the growth law of the LWS theory is recovered, there are no evident analogies with the present case.

We note that none of the optical examples described so far incorporates any conservation law. This raises the question of whether the important ingredient for a $t^{1/3}$ growth law is the specific form of the space-dependent terms or the existence of conservation laws.

The kinetics of domains has also been studied in vectorial intracavity second-harmonic generation [24]. The situation corresponds to two orthogonally polarized fundamental harmonic (FH) waves with equal mean frequencies that generate a second harmonic (SH) wave of either polarization in a high-finesse planar cavity with a quadratic nonlinear material. In contrast to the conventional scheme of an optical parametric oscillator, driving fields with two polarizations $E_{1,2}$ at the FH frequency are assumed. The space-time evolution equations for the emerging FH fields read:

$$\begin{aligned}\partial_t A_1 &= i\nabla_\perp^2 A_1 + (i\Delta_A - 1)A_1 + iA_2^* B - iE_1, \\ \partial_t A_2 &= i\nabla_\perp^2 A_2 + (i\Delta_A - 1)A_2 + iA_1^* B - iE_2, \\ \partial_t B &= \frac{1}{2}i\nabla_\perp^2 B + (i\Delta_B - \gamma)B + iA_1 A_2,\end{aligned}\tag{4.7}$$

where

$A_{1,2}$: cavity fields (at the FH frequency ω) of orthogonal polarizations.

B : idler (at the SH frequency 2ω) . It is required for quadratic interaction and corresponds to one of the two polarizations of the cavity fields.

$E_{1,2}$: driving fields (at the FH frequency ω) of orthogonal polarizations.

$\Delta_{A,B}$: detunings from the resonances scaled with the FH resonance width.

γ : ratio between the photon lifetimes.

For a symmetric input $E_1 = E_2 = E$ above a certain threshold there are two equivalent asymmetric ($A_1 \neq A_2$) homogeneous stationary solutions which are linearly stable. There is also a symmetric solution ($A_1 = A_2$) that is unstable.

In each of the two asymmetric solutions one of the polarization dominates. Domain walls between these two stable asymmetric solutions are then in fact polarization domain walls. In 1D, an isolated polarization front is at rest because of its symmetry with respect to an interchange of the two FH components. In 2D, however, a planar front is modulationally unstable. For spherical domains of large radius the modulational instability manifests itself in a radial expansion of the structure. The expansion velocity can be obtained by comparing the curvature of the circular structure with that of a developing modulational instability. The result is:

$$v_{\text{exp}} \simeq \frac{g(k_{\text{max}})}{k_{\text{max}}^2 R}, \quad (4.8)$$

where k_{max} is the wavevector at which the growth rate g of the modulational instability is maximum. Consequently, a circular domain of one polarization grows at the expense of the surrounding area with a velocity asymptotically approaching zero. For small radii or several interacting fronts, LS's may be formed because of the existence of oscillating tails in the front profiles (see section 1.3.4).

The examples discussed above show an interesting phenomenology for problems of domain growth in nonlinear optical systems. However, clear mechanisms for the growth laws have often not been identified, and some of these laws do not correspond unambiguously to an asymptotic regime. In addition, the question of dynamical scaling has, in general, not been addressed so far.

In the rest of the chapter we consider a Kerr medium as a clear example of a nonlinear optical system in which the issues of domain growth and dynamical scaling can be addressed and for which detailed clear results can be obtained. We show that after switching-on a pump field, domain walls are formed which separate regions with different polarization of light. The dynamical evolution of these polarization domain walls leads to three different regimes. For high pump values there is a coarsening regime for which we demonstrate dynamical scaling with a growth law $L(t) \sim t^{1/2}$. For lower pump values this process is contaminated by the emergence of LS's formed by the collapse of polarization domain walls to a stable bound structure. In a third regime the system evolves into a nearly frozen labyrinthine pattern caused by a transverse modulational instability of the polarization domain wall. These three qualitatively different regimes have been experimentally observed in another optical system [67] and considered in the realm of Swift-Hohenberg models [157].

The chapter is organized as follows. In section 4.2 we introduce the model and discuss the main features of the asymptotic homogeneous solutions. Interface dynamics is studied in section 4.3 for both one- and two-dimensional systems. Finally section 4.4 contains some conclusions.

4.2 Description of the Model and Asymptotic Steady States

Our calculations are based on a mean field model that describes the transverse spatio-temporal evolution of the two circularly polarized components of the electric field complex envelope, E_+ and E_- , in an optical cavity filled with an isotropic Kerr medium and pumped with a input field $E_{0\pm}$ (see Fig. 4.2) [25, 26]:

$$\partial_t E_{\pm}(\mathbf{r}, t) = -(1 + i\eta\theta)E_{\pm} + ia\nabla_{\perp}^2 E_{\pm} + E_{0\pm} + \frac{1}{4}i\eta(|E_{\pm}|^2 + \beta|E_{\mp}|^2)E_{\pm}, \quad (4.9)$$

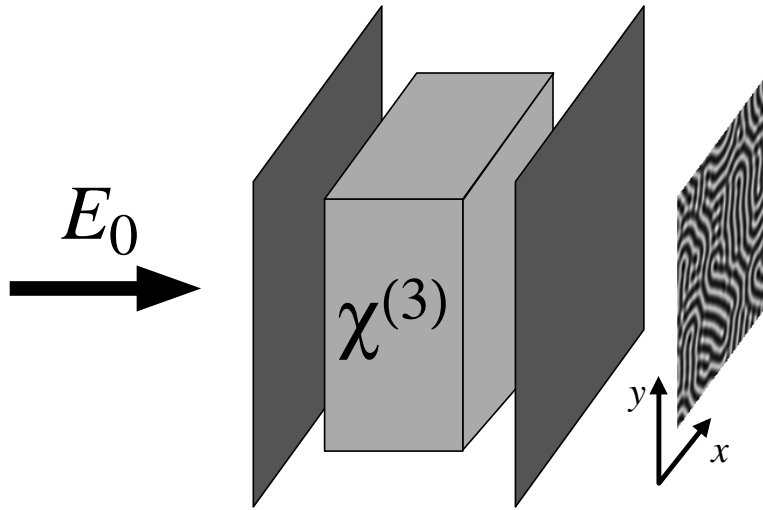


Figure 4.2: Configuration of the nonlinear cavity in a Fabry-Pérot geometry.

where $\eta = +1$ (-1) indicates self-focusing (self-defocusing), θ is the cavity detuning, a measures the relative strength of transverse diffraction, and ∇_{\perp}^2 is the transverse Laplacian. The parameter β is related to the components of the susceptibility tensor $\chi^{(3)}$. Except in section 4.3.1 we only consider the case $E_{0+} = E_{0-}$ which corresponds to a linearly polarized input field. In this case Eqs. (4.9) are symmetrical with respect to the interchange of the two fields E_{\pm} . We take $E_{0+} = E_{0-} \equiv E_0$ as a real quantity. This implies that the main axis of the polarization ellipse is in the X or Y direction. The relation of the circularly polarized components E_{\pm} with the Cartesian components $E_{x/y}$ is

$$E_{\pm} = \frac{1}{\sqrt{2}}(E_x \pm iE_y). \quad (4.10)$$

Therefore a linearly polarized state is characterized by $E_+ = E_-$, a circularly polarized one has $\{E_{\pm} = 0, E_{\mp} \neq 0\}$, and an elliptically polarized state is such that $E_+ \neq E_- \neq 0$.

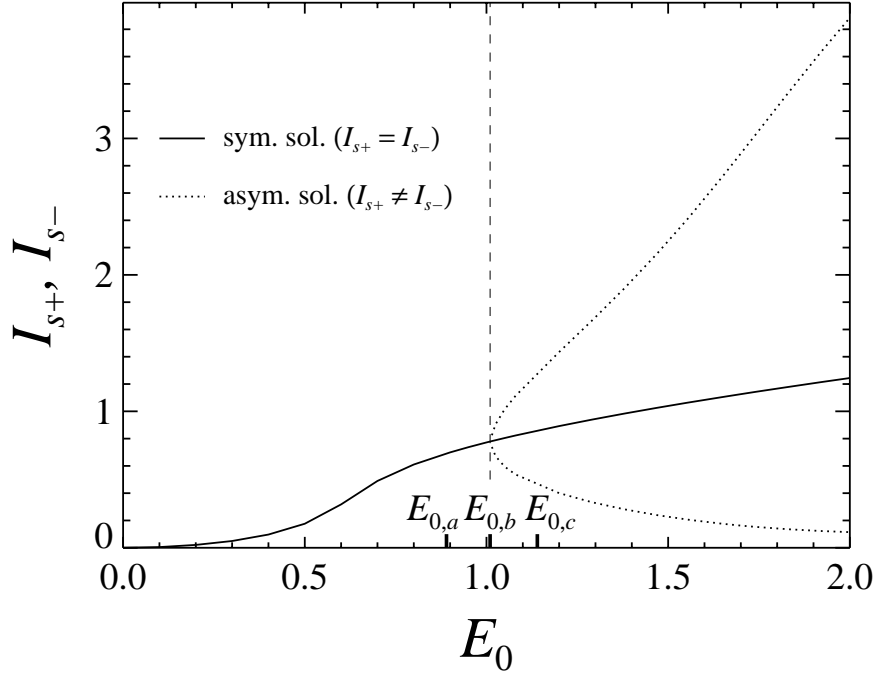


Figure 4.3: Steady state homogeneous solutions for system (4.9) as a function of the input field E_0 . The meaning of the values $E_{0,a} \simeq 0.89$, $E_{0,b} \simeq 1.01$ and $E_{0,c} \simeq 1.14$ is given in the text. Parameter values are $a = 1$, $\beta = 7$ and $\theta = 1$. These values are used in the remaining figures of this chapter.

Eqs. (4.9) are damped and driven coupled nonlinear Schrödinger equations which can be rewritten as

$$\partial_t E_{\pm} = -E_{\pm} - i \frac{\delta \mathcal{F}}{\delta E_{\pm}^*}, \quad (4.11)$$

where $\mathcal{F}[E_+, E_-]$ is a real functional given by

$$\begin{aligned} \mathcal{F}[E_+, E_-] = \int d\mathbf{r} \left\{ \eta \theta (|E_+|^2 + |E_-|^2) + a (|\nabla_{\perp} E_+|^2 + |\nabla_{\perp} E_-|^2) \right. \\ \left. - \frac{1}{4} \eta \left[\frac{1}{2} (|E_+|^4 + |E_-|^4) + \beta |E_+|^2 |E_-|^2 + 2E_0 (\text{Im}(E_+) + \text{Im}(E_-)) \right] \right\}. \end{aligned} \quad (4.12)$$

Therefore, except for the linear dissipative term, the dynamics can be written in Hamiltonian form. This corresponds to a rather different dynamics than the normal relaxational dynamics considered in systems that approach a state of thermodynamic equilibrium.

Eqs. (4.9) admit symmetric ($I_{s+} = I_{s-}$) and asymmetric ($I_{s+} \neq I_{s-}$) steady state homogeneous solutions, where $I_{\pm} = |E_{\pm}|^2$. The symmetric solution corresponds to linearly polarized output light, while the asymmetric one is elliptically polarized. In Fig. 4.3 we show the homogeneous solutions as a function of the input field E_0 .

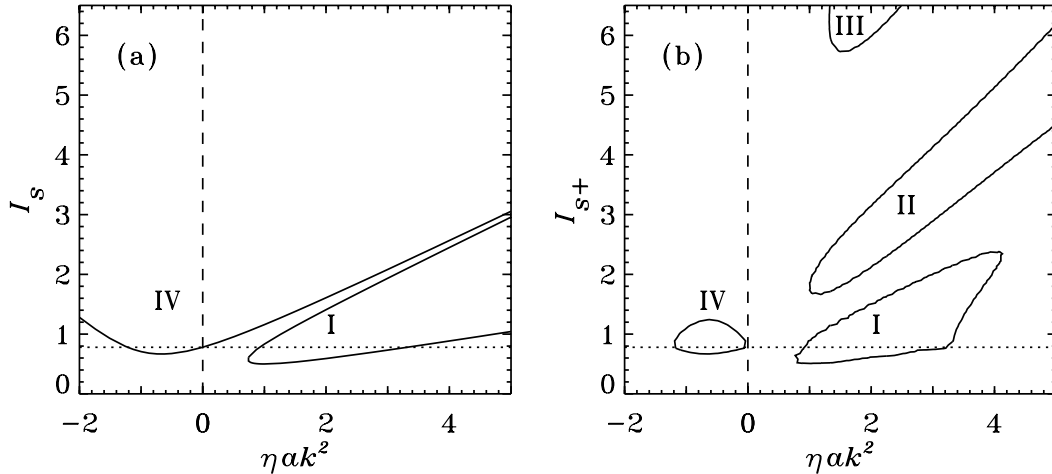


Figure 4.4: Marginal stability curves of the homogeneous solutions: (a) stability of the symmetric solution and (b) stability of the symmetric (up to the dotted line, which corresponds to $E_0 = E_{0,b}$) and asymmetric solutions. The vertical dashed line separates the cases self-focusing (right) and self-defocusing (left). Taken from [26].

The linear stability analysis of the homogeneous steady states can be performed along standard procedures. In Fig. 4.4 the marginal stability curves of the homogeneous solutions are shown. The homogeneous symmetric solution is linearly stable for $E_0 < E_{0,a}$, while the asymmetric solutions only exist for $E_{0,a} < E_{0,b} < E_0$ and they are linearly stable for $E_{0,b} < E_{0,c} < E_0$ in the self-defocusing case ($\eta = -1$) [158]. For the parameters we are considering ($a = 1$, $\theta = 1$, $\beta = 7$), $E_{0,a} \simeq 0.89$, $E_{0,b} \simeq 1.02$, $E_{0,c} \simeq 1.14$. Since we are interested in interfaces connecting stable homogeneous solutions, we only consider the self-defocusing case which supports *optical bistability* above a certain threshold for the input field $E_0 = E_{0,c}$. There are two equivalent homogeneous stable solutions for $E_{0,c} < E_0$, one in which $I_{s+} \gg I_{s-}$ and the other one, obtained by interchanging E_+ with E_- , in which $I_{s+} \ll I_{s-}$. These solutions are elliptically polarized, but very close to being circularly polarized, because one of the two circularly polarized components dominates. For simplicity we will call them the right and left circularly polarized solutions. If the pump field E_0 is switched-on from $E_0 = 0$ to a value $E_0 > E_{0,c}$, only the mode with zero wavenumber can initially grow from the initial condition $E_{\pm} = 0$. One then expects that either of the two equivalent homogeneous solutions will locally grow and that domains separated by polarization walls will emerge. This is indeed the process that we study. We note, however, that a solution with a stripe pattern orthogonally polarized to the pump exists for $E_0 > E_{0,a}$ [25, 26]. This pattern solution is the one obtained by continuity from the homogeneous symmetric solution through a Turing-like instability. We have numerically checked that such a solution remains stable for pump values $E_0 \gg E_{0,c}$, but it is not the solution approached by the physical process just described of switching-on the pump to a value $E_0 > E_{0,c}$.

4.3 Interface Dynamics

In this section we describe the main features of interface dynamics in one- and two-dimensional systems.

4.3.1 One-dimensional systems

Due to the symmetry of the equations with respect to the interchange of the two field components E_+ and E_- , a one-dimensional interface or kink is expected to be at rest. For elliptically polarized input light, however, the asymptotic solutions are no longer equally stable, so that a front connecting them will move. In Fig. 4.5 we plot the velocity of a kink as a function of the ellipticity χ of the input field. The situation is qualitatively similar to that in an equilibrium problem of a domain wall between two states with a nonzero “potential difference” (see section 1.3.1). Nevertheless the dynamics under study here does not have any potential or Lyapunov function.

We observe that the intensity profiles of the kinks do not approach monotonically the asymptotic value of the homogeneous state. Since the front profiles have oscillatory tails, the interaction between two walls can lead to repul-

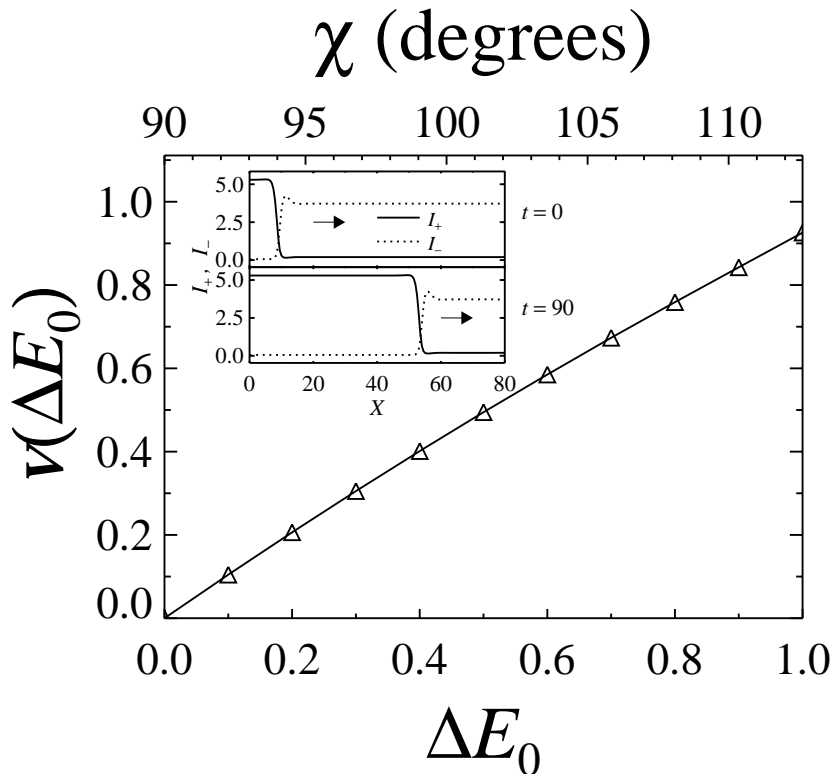


Figure 4.5: Velocity of an isolated kink in 1D as a function of the ellipticity χ of the input field $E_{0\pm}$. This is defined as $\chi \equiv 2 \tan^{-1}(E_{0+}/E_{0-})$. Input field values are $E_{0-} = 2.0$ and $E_{0+} = 2.0 + \Delta E_0$. The inset shows the kink profile (in intensities) at two different times.

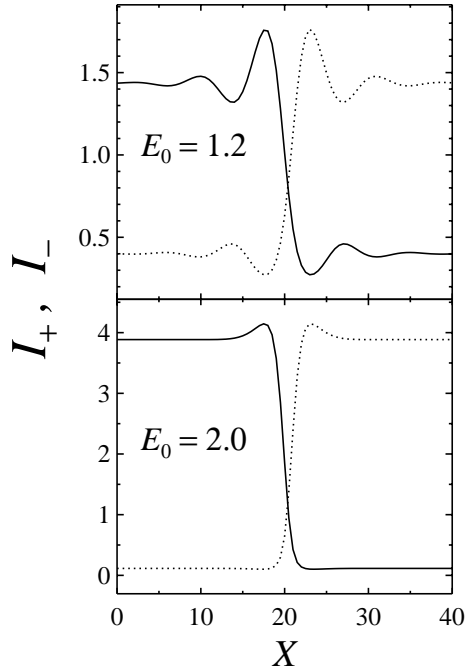


Figure 4.6: 1D intensity profiles of the polarization domain wall for two pump values: $E_0 = 1.2$, $E_0 = 2.0$.

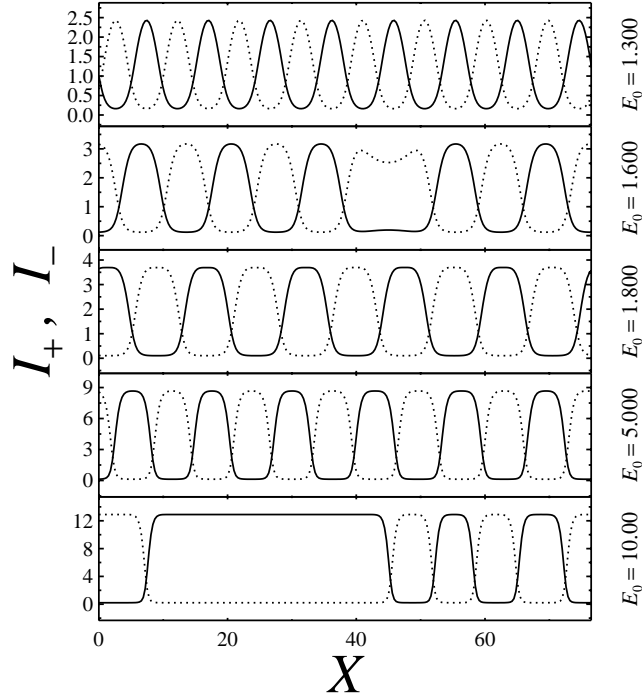


Figure 4.7: Snapshots of the intensities I_+ and I_- at long times in 1D for several values of the input pump E_0 . The boundary conditions are periodic and the initial condition corresponds to a random perturbation of the homogeneous state $E_{\pm} = 0$.

sive forces [38]. In Fig. 4.6 we show a kink profile for two different values of the input pump E_0 . The oscillatory tails are less important the larger is E_0 but the kinks are never monotonic for arbitrary large E_0 . Two kinks sufficiently separated tend to attract each other. However the oscillatory tails prevents them from getting closer than a certain distance. A localized structure forms. On the other hand, if the kinks are very close to each other, repulsive forces move them away until an equilibrium of forces is reached¹. Notice that this is different from what happens with monotonic kink profiles in other systems. They are only subjected to attractive forces so that two adjacent kinks (of opposite topological charge) might annihilate.

When several kinks are created in the transient dynamics, they interact with each other. Due to the oscillatory tails, coarsening is absent and a frozen pattern state is always dynamically reached. We show in Fig. 4.7 intensity field configurations at long times for several values of E_0 . In most cases, a periodic pattern forms; the associated wavenumber seems to depend on the random initial condition. On the other hand, frozen aperiodic patterns may arise. This is observed more frequently for large E_0 . It is known for other

¹A final homogeneous state is obtained when the pump is not linearly polarized ($E_{0+} \neq E_{0-}$). An isolated domain wall is then no longer stationary.

systems that oscillatory tails in the front profiles can stop coarsening in 1D and give rise to frozen structures [38]. This is a manifestation of spatial chaos.

4.3.2 Two-dimensional systems

We find in two dimensions three different dynamical regimes for $E_0 > E_{0,c}$, summarized in Fig. 4.8. For $E_0 > E_{0,2}$ domains grow and the system coarsens, for $E_{0,2} > E_0 > E_{0,1}$ stable LS's are formed, while for $E_{0,1} > E_0 > E_{0,c}$ a labyrinthine pattern emerges. These regimes are better understood by considering the evolution of an initial isolated polarization droplet: a circular domain of one of the solutions surrounded by the other solution. We find that the radius of the circular domain varies consistently with a curvature driven front motion. The normal front velocity v_n (eikonal equation) follows a law of the form

$$v_n(\mathbf{r}, t) = -\gamma(E_0)\kappa(\mathbf{r}, t), \quad (4.13)$$

where κ is the local curvature of the interface and $\gamma(E_0)$ is a coefficient that depends on the pump field amplitude. This interface dynamics is similar to that discussed in section 1.3.1. However, what in that case was explained in terms of surface tension effects, does not seem to apply to the present situation, where surface tension is not a proper concept for the diffractive spatial coupling considered in optical systems. For a circular domain we get $dR(t)/dt = -\gamma(E_0)/R(t)$. In Fig. 4.8 we show the function $\gamma(E_0)$ as obtained from the numerical solution of Eqs. (4.9) in a two-dimensional system for relatively large initial droplets. Notice that $\gamma(E_0)$ changes sign at $E_0 = E_{0,1}$, which indicates a change from droplet shrinkage to droplet growth.

In principle, it is possible, following the same technique used in [148], to work out the coefficient $\gamma(E_0)$ as a function of the planar front solutions. To leading order, we are left with a linear system $\mathcal{M}v = w$, where the matrix \mathcal{M} depends on the planar front solutions and on the system parameters. The condition for this linear system to be solvable is $(v_K^\dagger, w) = 0$, where $v_K^\dagger \in \ker(\mathcal{M}^\dagger)$ represent any vector of the nullspace of the matrix \mathcal{M}^\dagger . However, little analytical work can be done henceforth. The profiles of the planar fronts and the nullspace $\ker(\mathcal{M}^\dagger)$ must both be computed numerically. Then we could find the coefficient $\gamma(E_0)$ through the aforementioned solvability condition.

We first consider the regime of *domain coarsening* which occurs for $E_0 > E_{0,2}$. In this regime $\gamma(E_0) > 0$ and an isolated drop shrinks to zero radius. In the general dynamics starting from random initial conditions around $E_\pm = 0$, sharp domain walls are initially formed and they evolve reducing their curvature. The system approaches a final homogeneous state in which one of the two circularly polarized solutions fills the whole system (see Fig. 4.12). In order to characterize the coarsening process we have calculated the pair correlation function of I_+ and I_- , defined as

$$C_{I_\pm}(\mathbf{r}, t) = \langle I_\pm(\mathbf{x} + \mathbf{r}, t)I_\pm(\mathbf{x}, t) \rangle_{\text{i.c.}}. \quad (4.14)$$

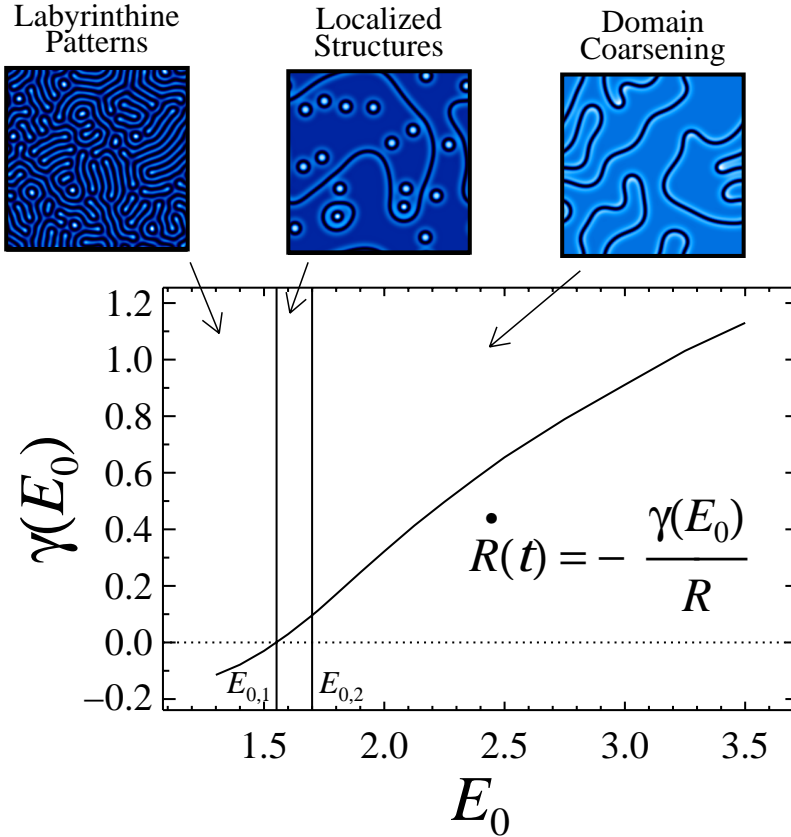


Figure 4.8: Coefficient $\gamma(E_0)$ as defined in the text. Snapshots of typical configurations for the total intensity $I = I_+ + I_-$ at late times are shown for each of the three dynamical regimes. The vertical lines identify the values of $E_{0,1} = 1.552$ and $E_{0,2} = 1.700$.

The average $\langle \dots \rangle$ is performed over a set of 100 different random initial conditions. Due to the symmetry of the problem $C_{I_+} = C_{I_-} \equiv C$. The mean size $L(t)$ of the domains is calculated as the distance at which $C(r, t)$ takes half its value at the origin, i.e., $C(L(t), t) = \frac{1}{2}C(0, t)$. As expected, we obtain a well-defined asymptotic growth law $L(t) \sim t^{1/2}$ that follows from domain wall motion curvature driven (see inset in Fig. 4.9). We have further obtained that the dynamics is self-similar, i.e., that there is dynamical scaling. This is seen in Fig. 4.9 where we plot the spherical averaged correlation function $C(r, t)$ before and after rescaling the spatial coordinate of the system with the characteristic domain size $L(t)$. We observe that curves for different times in the scaling regime collapse to the single scaling function after rescaling. These results coincide with those obtained for many thermodynamic systems with nonconserved order parameter [4, 32, 34, 69]. We note, however, that in our case the dynamics does not follow the minimization of any obvious free energy.

We next address the regime of formation of *localized structures* ($E_{0,2} > E_0 > E_{0,1}$). In this regime, as in the previous case, $\gamma(E_0) > 0$, and a large isolated droplet initially shrinks with a radius decreasing as $R(t) \sim t^{-1/2}$. How-

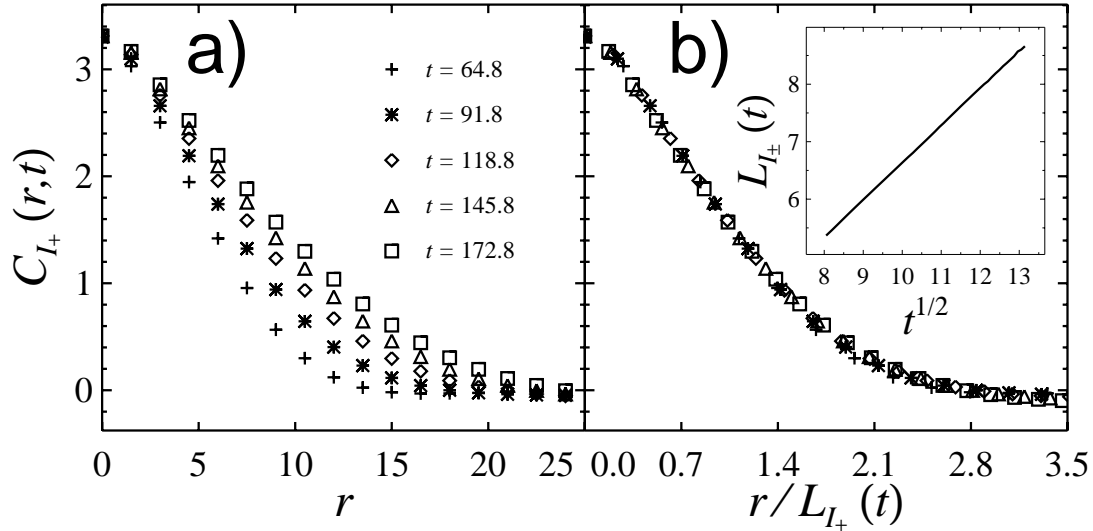


Figure 4.9: Spherical averaged pair correlation function for different times before and after rescaling the system length r by the characteristic domain size $L_{I_{\pm}}(t)$. The inset shows the growth law $L_{I_{\pm}}(t) \sim t^{1/2}$.

ever the shrinkage stops at a well-defined final value of the radius. Initial droplets with a smaller radius grow to this final stable radius. In the general dynamics following the switch-on of the pump, domain walls are initially formed. They first evolve reducing their length as in the coarsening regime. But while in that regime a closed loop disappears, here it collapses to a stable LS formed by a bound state of the domain wall. The final state is composed of stretched domain walls and LS's (see fig 4.13). What happens in our 2D situation is a competition between the 1D repulsive effect between fronts and

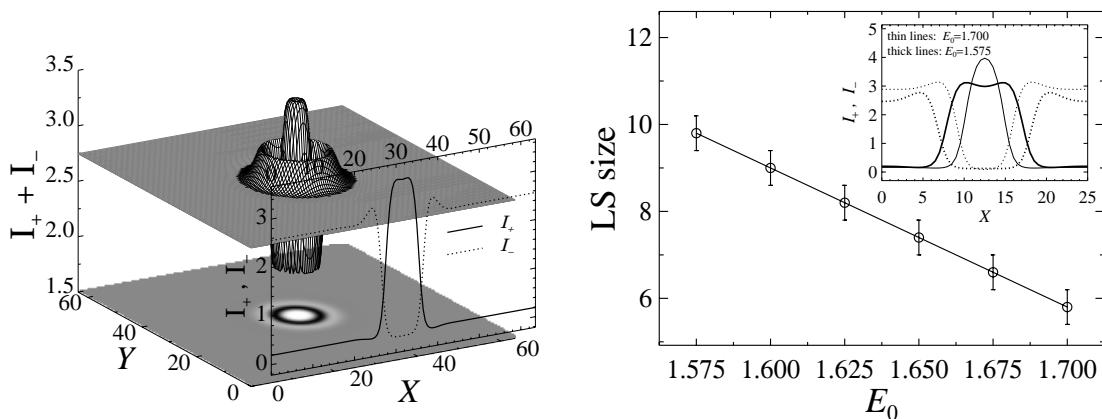


Figure 4.10: (left) Total field intensity of a LS and transverse profile of I_{+} and I_{-} along the center of the structure for a value $E_0 = 1.6$, and (right) diameter of a LS as a function of E_0 ; the inset shows the transverse profiles of I_{+} and I_{-} of two LS's at two different values of the pump.

the curvature effect that tends to reduce a droplet to zero radius. When the repulsive force is large enough, it might counterbalance the shrinkage process driven by curvature, and thus leads to the formation of a LS. This happens for $E_{0,1} < E_0 < E_{0,2}$. The mechanism is the one also discussed in [22]. Let us point out that while LS's appear only in a certain range of pump values in 2D, they are supported in 1D for any value of E_0 (we have explored values up to $E_0 = 10$) as explained in 4.3.1. These LS's can be seen as a hole of I_+ (I_-) in the background of a circularly + polarized (– polarized) state, together with a peak of I_- (I_+). Since the oscillatory tails are larger (in amplitude and range) as E_0 decreases, the size of the LS decreases with E_0 . We have found a perfect linear dependence of the diameter of the LS with E_0 . In Fig. 4.10 we show a plot of a LS together with its transverse profile, and the size of a LS as a function of E_0 . Notice that the intensity in the center of the LS is greater than in the surrounding background.

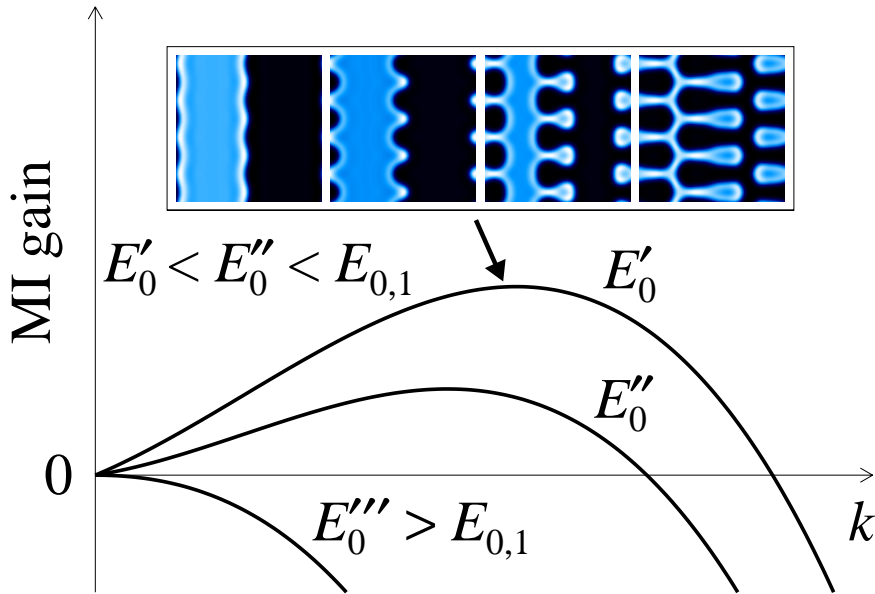


Figure 4.11: Diagram of the modulational instability gain for a planar front in $d = 2$. At $E_0 = E_{0,1}$ there is no range of unstable modes so that the planar front is stable against transversal perturbations. The images correspond to the development of a modulational instability for $E_0 = 1.4$.

We finally discuss the regime of *labyrinthine pattern* formation which occurs for $E_0 < E_{0,1}$: switching-on the pump produces a very dense pattern of domain walls that repel each other (see Fig. 4.14). In this regime $\gamma(E_0) < 0$, and an isolated droplet of arbitrary small size grows as $R(t) \sim t^{1/2}$. In an infinitely large system the droplet would grow without limit, but with periodic boundary conditions it grows until the interface surrounding the droplet interacts with itself. Repulsion of the interface leads eventually to a labyrinthine

pattern as shown in Fig. 4.14. An independent way of identifying the value $E_0 = E_{0,1}$, below which labyrinthine patterns emerge, is by means of a linear stability analysis in 2D of the 1D domain wall profile. We have numerically obtained that such a flat domain wall has a transverse modulational instability for values of the pump amplitude for which $\gamma(E_0) < 0$. We find a long wavelength instability in which arbitrary small wavenumbers become unstable for $E_0 < E_{0,1}$ (see Fig. 4.11). This is reminiscent of the situation described for vectorial second-harmonic generation [24]. In physical terms, both the droplet growth and the modulational instability indicate that the system prefers to have the longest possible domain walls, or equivalently the largest possible curvature. This leads to a nearly frozen state in which the oscillatory tails of the domain walls prevent their self-crossing and in which coarsening is suppressed. LS's might form, but their natural tendency to grow is stopped by surrounding walls.

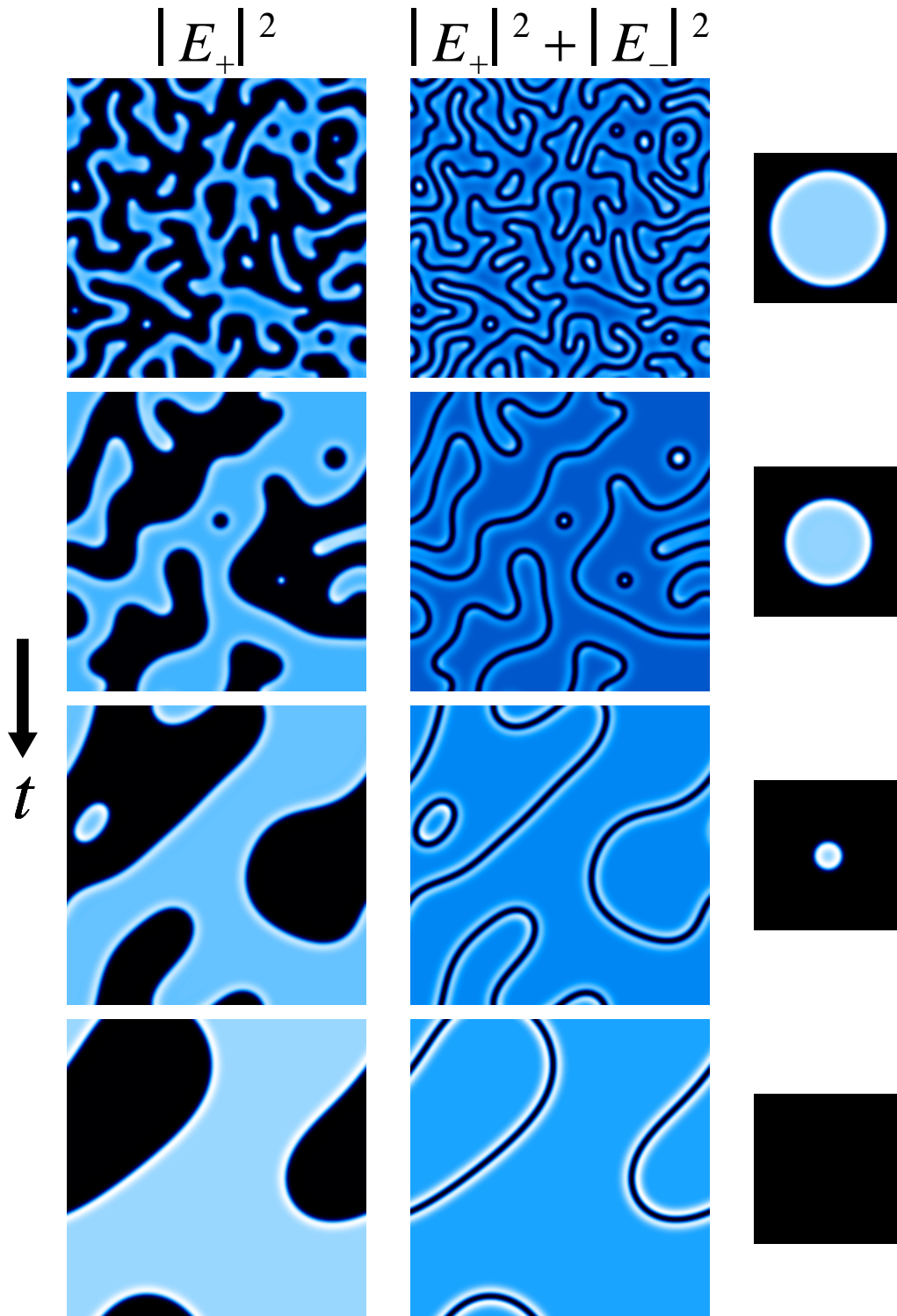


Figure 4.12: Snapshots corresponding to the time evolution of the intensities $|E_+|^2$ and $|E_+|^2 + |E_-|^2$ and evolution of an isolated spherical drop in the domain coarsening regime. Patterns at times $t = 30, 2400, 9000$ and 30000 . Drop images at times $t = 0, 2000, 4300$ and 5000 .

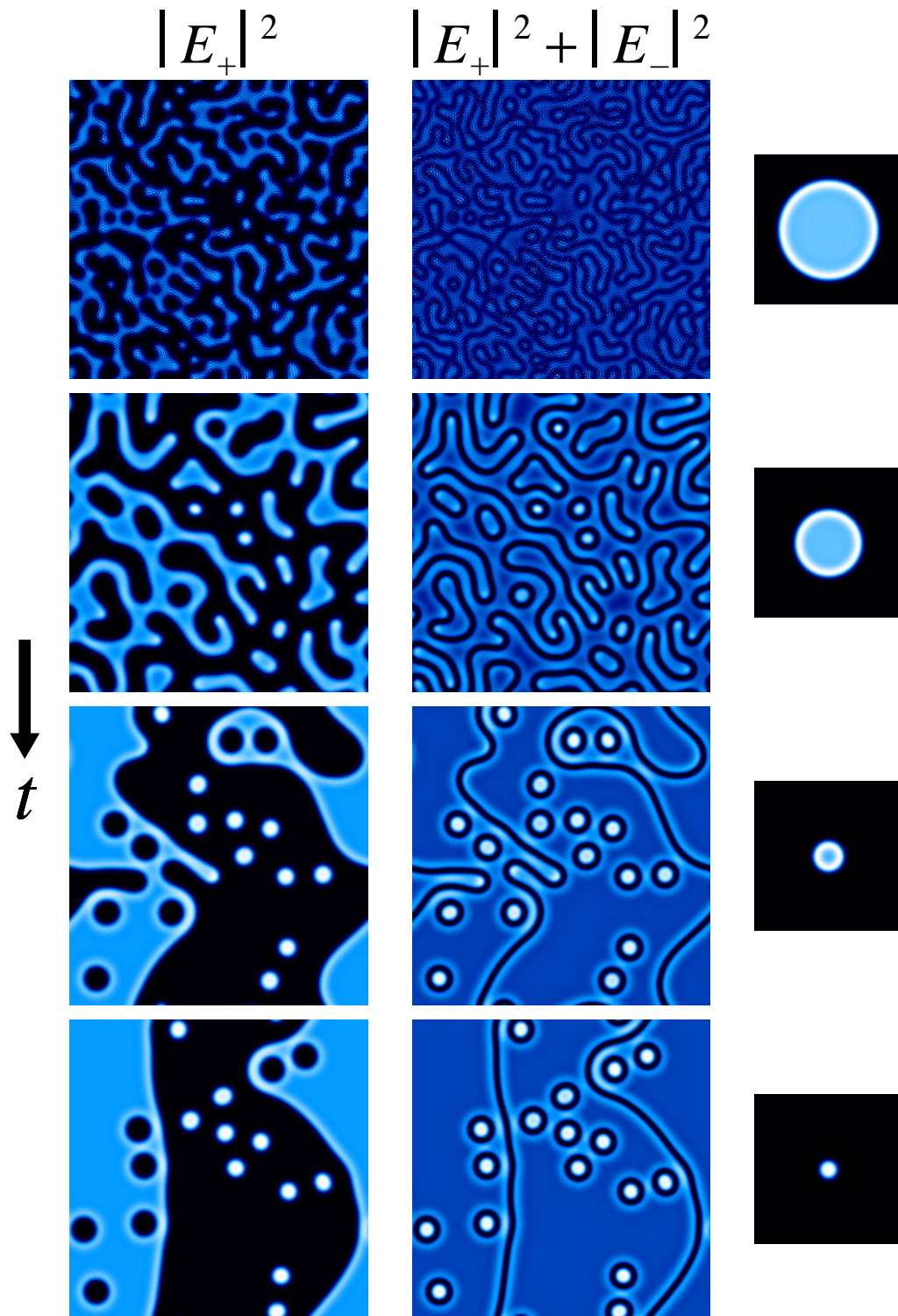


Figure 4.13: Same as in Fig. 4.12 in the regime of formation of LS. Patterns at times $t = 16, 200, 7700$ and 30000 . Drop images at times $t = 0, 4400, 7700$ and 11000 .

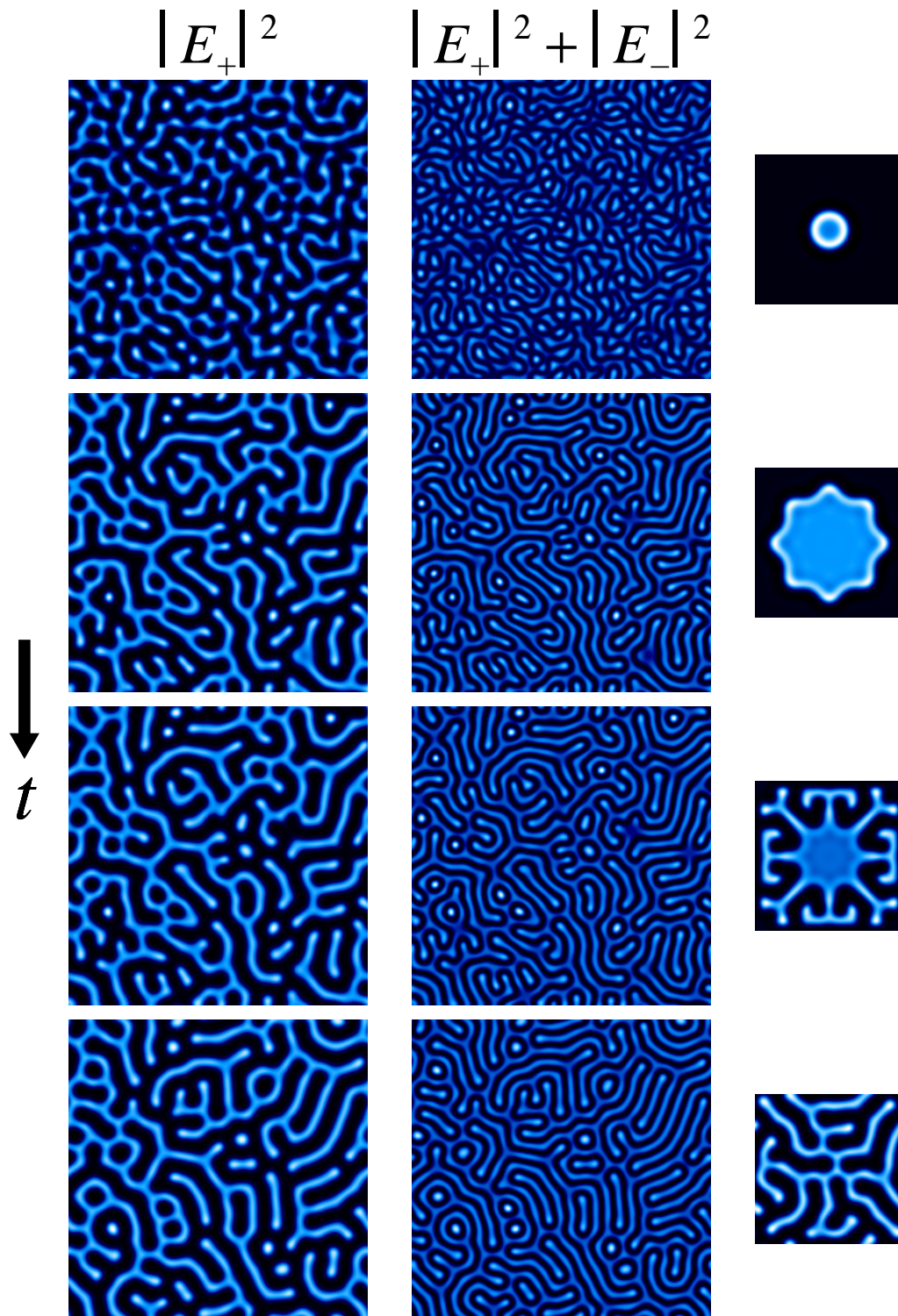


Figure 4.14: Same as in Fig. 4.12 in the regime of labyrinthine patterns. Patterns at times $t = 15, 40, 110$ and 3060 . Drop images at times $t = 0, 2200, 2600$ and 4900 .

4.4 Conclusions

In summary, a vectorial kerr resonator a situation in nonlinear optics in which many of the generic issues and possible scenarios of domain growth in non-thermodynamic systems occur. In spite of the nonrelaxational dynamics we have found a regime of self-similar evolution with a growth law characteristic of curvature driven motion. In other regimes, obtained just by changing the pump amplitude, domain growth is contaminated by the emergence of LS's or suppressed by an instability of the domain wall that leads to a nearly frozen labyrinthine pattern. Domain walls and LS's are here associated with the polarization vectorial degree of freedom of light.

Chapter 5

Conclusions

Throughout this work the role of nonpotential dynamics in problems of domain growth has been considered in several systems. In these examples the system has several equivalent homogeneous stable states which can be approached dynamically from an unstable initial state. Spatial domains of these states are formed in the transient dynamics. General conclusions that follow from the generic behavior of these systems are the following:

- ◆ New nonpotential mechanisms of domain wall motion lead to domain growth laws different from the ones observed in the potential limit.
- ◆ Despite the different growth laws, dynamical scaling still holds in nonpotential problems.
- ◆ In some cases there exist asymptotic statistically stationary states with persistent dynamics in which domain growth is inhibited. These states often originate in the nonpotential dynamics of topological defects. Such dynamics prevents their annihilation and subsequent disappearance from the system.
- ◆ Interactions among domain walls lead in some cases to stable localized structures that contaminate a final homogeneous state and mask the dominant growth law. This phenomenon can also occur in potential systems. In 1D this might stop coarsening. Spatial instabilities of domain walls can also lead to different forms of frozen nonhomogeneous states, such as labyrinthine patterns.

More specific conclusions on the dynamics of the different systems considered are the following:

1. *Busse-Heikes Model for Three Competing Amplitudes.*

- * In zero spatial dimensions (no spatial dependence) we find, in a certain range of parameters, a Lyapunov potential that allows us to split the

dynamics into a relaxational plus a residual part. We give explicit relations for the time variation of the amplitudes and the period of the orbits as a function of the energy. We show how noise can stabilize the mean period of the Küppers-Lortz instability to a finite value. By using the Lyapunov potential of the deterministic case, we deduce an approximate expression that yields the period as a function of the system parameters and noise intensity. The period increases logarithmically with decreasing noise intensity, a result confirmed by numerical simulations.

- * The one-dimensional version of the model constitutes a prototypical non-potential problem in which the issues of domain growth and dynamical scaling can be explored. Out of the Küppers-Lortz instability region, there are three stable states that coexist during the transient dynamics. There is domain coarsening with a growth law with two dominant behaviors, with a crossover between two well defined regimes. These are characterized by a logarithmic (potential limit) and linear (nonpotential limit) domain growth law respectively. Dynamical scaling holds throughout the two regimes.
- * The two-dimensional model exhibits rather different dynamical behavior grossly dominated by vertices where three domain walls meet and which have no parallel in one-dimensional systems. The system is at long times in a persistent dynamical state composed of three-armed rotating spirals, each arm corresponding to a domain wall that separates two of the three stable phases. The rotation angular velocity ω of one of such spiral structures goes as $\omega \sim \delta^2$ to leading order in δ , the nonpotential parameter. Vertices of opposite sense of rotation annihilate with each other if located closer than a critical distance $d_c \sim \delta^{-1}$. Vertex motion is strongly influenced by the type of boundary conditions. For periodic boundary conditions, the number of vertices is even (half clockwise and half anticlockwise) and they only annihilate by pairs of opposite sense of rotation. In addition, the motion is such that all vertices tend to move in the same direction. On the other hand, for null boundary conditions, there are no restrictions neither about the number nor the type of vertices. These may also disappear by collision against the edges of the system. Correlated motions of vertices are not observed.

Even being out of the Küppers-Lortz region, the nonpotential dynamics may inhibit coarsening for large enough systems. When only two amplitudes are excited in the transient dynamics, the formation of vertices is no longer possible and coarsening takes place independent of system size. This domain growth process is self-similar with a growth law different from that of the potential dynamics limit.

The dynamics is different for isotropic and anisotropic spatial derivatives. The most notable feature is that, in certain range of parameters, the intrinsic Küppers-Lortz period diverges with time with isotropic derivatives whereas it saturates to a constant value in the anisotropic

case. The alternating period in a fixed point of space is also different for both types of spatial-dependent terms.

2. *Forced Complex Ginzburg-Landau Equation.*

- * Systems with a broken phase symmetry, in an excitable regime, can display similar generic dynamical behavior than systems with competing fields. The Busse-Heikes model dynamics shows a number of analogies with the excitable dynamics of the Ginzburg-Landau Equation forced at three times the natural frequency.
- * On increasing the intensity of the forcing, the system goes from an oscillatory regime to an excitable one with three equivalent frequency locked states. In the first regime, topological defects are one-armed phase spirals, while in the second one they correspond to three-armed excitable amplitude spirals. Analytical results show that the transition between these two regimes occurs at a critical value of the forcing intensity. The transition between phase and amplitude spirals is confirmed by numerical analysis.

3. *Vectorial Kerr Resonators*

- * Self-similar dynamical evolution with a growth law characteristic of curvature driven motion in a nonlinear optical system with a nonrelaxational dynamics has been demonstrated. Domains correspond to different equivalent states of polarization of light.
- * In other regimes, obtained just by changing the intensity of the input field, domain growth is stopped by the emergence of localized structures or suppressed by an instability of the domain wall that leads to a nearly frozen labyrinthine pattern.

Appendix A

Analytical Approach of the Mean Energy for the Busse-Heikes Model in the Presence of Noise

In this appendix we give an analytical approach for the integral

$$\langle E \rangle = \frac{\int_0^\infty dx \int_0^\infty dy \int_0^\infty dz E(x, y, z) e^{-V(x, y, z; \mu)/\varepsilon}}{\int_0^\infty dx \int_0^\infty dy \int_0^\infty dz e^{-V(x, y, z; \mu)/\varepsilon}}, \quad (\text{A.1})$$

$$V(x, y, z; \mu) = -(x + y + z) + \frac{1}{2}(x^2 + y^2 + z^2) + (1 + \mu)(xy + xz + yz),$$

$$E(x, y, z) = \frac{xyz}{(x + y + z)^3},$$

in the limit $\varepsilon \rightarrow 0$. The change of variables $\{u = x, v = y, w = x + y + z\}$ transforms (A.1) into:

$$\begin{aligned} \langle E \rangle &= \frac{\int_0^\infty dw \int_0^w du \int_0^{w-u} dv \tilde{E}(u, v, w) e^{-\tilde{V}(u, v, w; \mu)/\varepsilon}}{\int_0^\infty dw \int_0^w du \int_0^{w-u} dv e^{-\tilde{V}(u, v, w; \mu)/\varepsilon}} \\ &= \frac{\int_0^\infty dw \int_0^w du \int_0^{w-u} dv w^{-3} uv(w - u - v) e^{\frac{1}{2\varepsilon}(w-1)^2 - \frac{\mu}{\varepsilon}[uv + (u+v)(w-u-v)]}}{\int_0^\infty dw \int_0^w du \int_0^{w-u} dv e^{\frac{1}{2\varepsilon}(w-1)^2 - \frac{\mu}{\varepsilon}[uv + (u+v)(w-u-v)]}} \end{aligned}$$

$$\stackrel{=}{\downarrow} \underset{[s=u/w, t=v/w]}{\int_0^\infty dw w^2 e^{-\frac{1}{2\varepsilon}(w-1)^2} \phi_1(w^2 \mu/\varepsilon)} \bigg/ \int_0^\infty dw w^2 e^{-\frac{1}{2\varepsilon}(w-1)^2} \phi_2(w^2 \mu/\varepsilon), \quad (\text{A.2})$$

with

$$\phi_1(a) = \int_0^1 ds \int_0^{1-s} dt st(1-s-t) e^{a(s^2+t^2+st-s-t)}, \quad (\text{A.3a})$$

$$\phi_2(a) = \int_0^1 ds \int_0^{1-s} dt e^{a(s^2+t^2+st-s-t)}. \quad (\text{A.3b})$$

For $a \rightarrow \infty$ we can perform a saddle-point type integration. The function

$$f(s, t) = s^2 + t^2 + st - s - t = -[st + (s+t)(1-s-t)] \quad (\text{A.4})$$

is $f(s, t) \geq 0$, $\forall (s, t) \in \Gamma = \{(s, t) \in \mathbb{R}^2 / 0 \leq s \leq 1, 0 \leq t \leq 1-s\}$. The maxima of $f(s, t)$ are reached whenever $f(s, t) = 0$ and this happens for $(s, t) = \{(0, 0), (1, 0), (0, 1)\}$. Therefore, we approximate the integrals by the contributions of these points only (see Fig. A.1):

$$\begin{aligned} \int_\Gamma ds dt f(s, t) e^{ag(s, t)} &\approx \int_{\Gamma_I} ds dt f(s, t) e^{ag(s, t)} + \int_{\Gamma_{II}} ds dt f(s, t) e^{ag(s, t)} \\ &= \int_0^\rho ds \int_0^\rho dt f(s, t) e^{ag(s, t)} + 2 \int_{1-\rho}^1 ds \int_0^{1-s} dt f(s, t) e^{ag(s, t)}, \end{aligned} \quad (\text{A.5})$$

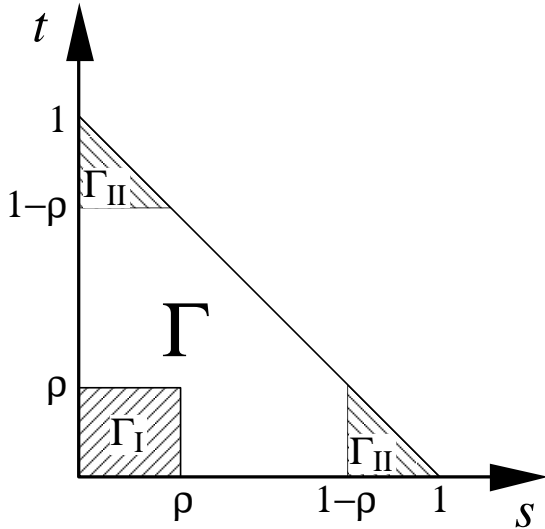


Figure A.1: Domain of integration of the integrals in Eqs. (A.3a–b). The regions Γ_I and Γ_{II} used in the saddle-point type integration are indicated.

where the factor 2 in the last integral on the rhs comes from the fact that $f(s, t) = f(t, s)$ and $g(s, t) = g(t, s)$. Now, in order to find the asymptotic behavior of the functions (A.3a–b), we linearize the function $f(s, t)$ in regions Γ_I and Γ_{II} of Fig. A.1.

Region Γ_I :

$$f(s, t) \approx -s - t. \quad (\text{A.6})$$

Region Γ_{II} : By defining the variable $\bar{s} = 1 - s$, we have that

$$f(s, t) = f(1 - \bar{s}, t) \approx -\bar{s}. \quad (\text{A.7})$$

Using the linearized expressions (A.6) and (A.7) we find the following asymptotic behaviors for $\phi_1(a)$ and $\phi_2(a)$:

$$\phi_1(a) \underset{a \rightarrow \infty}{\rightsquigarrow} \frac{3}{a^4}, \quad (\text{A.8a})$$

$$\phi_2(a) \underset{a \rightarrow \infty}{\rightsquigarrow} \frac{3}{a^2}. \quad (\text{A.8b})$$

We do now a quick saddle-point evaluation of the mean value of the energy (A.1). When $\varepsilon \rightarrow 0$ we have that

$$e^{-\frac{1}{2\varepsilon}(w-1)^2} \longrightarrow A \delta(w-1), \quad (\text{A.9})$$

so $w = O(1)$ gives the maximum contribution to the integral. For $w = O(1)$ it is $w^2 \mu / \varepsilon \rightarrow \infty$ and we can approximate:

$$\langle E \rangle \underset{\varepsilon \rightarrow 0}{\rightsquigarrow} \frac{\phi_1(\mu/\varepsilon)}{\phi_2(\mu/\varepsilon)} \underset{\varepsilon \rightarrow 0}{\rightsquigarrow} \frac{\frac{3}{(\mu/\varepsilon)^4}}{\frac{3}{(\mu/\varepsilon)^2}} = \left(\frac{\varepsilon}{\mu} \right)^2. \quad (\text{A.10})$$

Appendix B

Time Evolution of the Size of an Isolated Domain for the One-dimensional Busse-Heikes Model

In this appendix a derivation of Eq. (2.63) is given. This equation expresses the time evolution of the size of an isolated domain for the one-dimensional Busse-Heikes model .

We consider an isolated domain bounded by two domain walls associated with amplitudes A_1 and A_2 , while $A_3 = 0$ (see Fig. B.1). When the domain size is much greater than the interface width (“dilute-defect gas approximation”), a reasonable *ansatz* for this solution is

$$\begin{aligned} A_1(x, t) &= a(x - r(t)) + b(x - d + r(t)) + w_1(x, t), \\ A_2(x, t) &= b(x - r(t)) + a(x - d + r(t)) - 1 + w_2(x, t), \end{aligned} \tag{B.1}$$

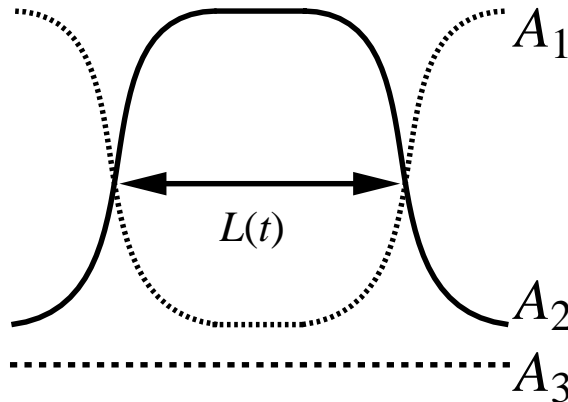


Figure B.1: Sketch of an isolated domain; $L(t)$ is the instantaneous domain size.

where $r(t)$ measures the displacement of the kinks, d is the initial domain size [so that the domain size at time t is $d - 2r(t)$], $\partial_t r$ and w_i ($i = 1, 2$) are assumed to be small corrections of order δ and $\partial_t w_i$ to be negligible with respect to w_i . To simplify notation, we use: $f \equiv f(x - r(t))$, $f_d \equiv f(x - d + r(t))$. The moving fronts a and b satisfy the boundary conditions $a(\infty) = b(-\infty) = 0$, $a(-\infty) = b(\infty) = 1$ and they are solutions of the system (2.53) (with one of the amplitudes equal to zero) so that the following equations hold:

$$\mathcal{M}_+(a, b) = \mathcal{M}_+(b_d, a_d) = \mathcal{M}_-(b, a) = \mathcal{M}_-(a_d, b_d) = 0, \quad (\text{B.2})$$

where the action of the operators $\mathcal{M}_\pm(\cdot, \cdot)$ is given by:

$$\mathcal{M}_\pm(f, g) = \partial_{xx} \pm v(\eta, \delta) \partial_x + f - f^3 - (\eta \pm \delta) f g^2. \quad (\text{B.3})$$

The parameter $v(\eta, \delta)$ is the front velocity as given by Eq. (2.62).

Introducing the ansatz (B.1) into (2.53) we obtain, to leading order, a linear system of equations for w_1 and w_2 :

$$\mathcal{L} \phi = \phi', \quad (\text{B.4})$$

$$\mathcal{L} = \begin{bmatrix} \partial_{xx} + 1 - 3(a + b_d)^2 - \eta(b + a_d - 1)^2 & -2\eta(a + b_d)(a_d + b - 1) \\ -2\eta(a + b_d)(a_d + b - 1) & \partial_{xx} + 1 - 3(a_d + b - 1)^2 - \eta(a + b_d)^2 \end{bmatrix},$$

$$\phi = \begin{bmatrix} w_1 \\ w_2 \end{bmatrix}, \quad \phi' = \begin{bmatrix} (\partial_x a + \partial_x b_d)v(\eta, \delta) + (\partial_x b_d - \partial_x a)\partial_t r + K_1\delta + K_2\eta + K_3 \\ (\partial_x b + \partial_x a_d)v(\eta, \delta) + (\partial_x a_d - \partial_x b)\partial_t r + K'_1\delta + K'_2\eta + K'_3 \end{bmatrix}.$$

where the functions $K_i(x, t)$ and $K'_i(x, t)$ ($i = 1, 2, 3$) are given by:

$$\begin{aligned} K_1 &= a(a_d - 1)^2 + 2b(a + b_d)(a_d - 1) + b_d(1 - 2a_d + b^2), \\ K_2 &= a(a_d - 1)^2 + 2(a_d - 1)(ab + a_d b_d + b b_d) + b_d(1 + b^2), \\ K_3 &= -2\partial_{xx} b_d + b_d(3a^2 + 3ab_d + 2b_d^2 - 2), \\ K'_1 &= -a(a + 2b_d)(a_d - 1) + b_d(b_d - 2ab - b b_d), \\ K'_2 &= a(a + 2b_d)(a_d - 1) + b_d(2ab + b b_d + 2a_d b_d - b_d), \\ K'_3 &= -2\partial_{xx} a_d + 3b^2(a_d - 1) + 3b(a_d - 1)^2 + 2a_d^3 - 3a_d^2 + a_d. \end{aligned}$$

The solvability condition for the existence of a solution $(w_1(x, t), w_2(x, t))$ for (B.4) reads

$$(\Psi^\dagger, \phi') = 0, \quad (\text{B.5})$$

where Ψ^\dagger belongs to the kernel of the auto-adjoint linear differential operator \mathcal{L} . We will show below that Ψ^\dagger is approximately given by $(\partial_x a, \partial_x b)^T$ (here T denotes the transposed vector), where $a = a(x - r(t))$ and $b = b(x - r(t))$ are the domain wall profiles around $x = r(t)$.

The first component of the vector $\mathcal{L}\Psi^\dagger$ is given by:

$$\begin{aligned}
(\mathcal{L}\Psi^\dagger)_1 &= \mathcal{L}_{11}\partial_x a + \mathcal{L}_{12}\partial_x b = \\
&\partial_{xxx}a + \partial_x a - 3(a + b_d)^2\partial_x a - \eta(a_d + b - 1)^2\partial_x a \\
&\quad - 2\eta(a + b_d)(a_d + b - 1)\partial_x b. \quad (\text{B.6})
\end{aligned}$$

As long as that the width of the interfaces is much smaller than the domain size (for all times t), we can make the following approximations: $ab_d \approx 0$, $aa_d \approx a$, $bb_d \approx b_d$. Moreover, this assumption implies that the product of the derivative with respect to x of an amplitude solution centered on $x = x_0$ multiplied by another amplitude shifted a length of order of the domain size, will be a function which will take values different from zero only in a small region around $x = x_0$. By using the approximations

$$\begin{aligned}
(a + b_d)^2\partial_x a &\approx a^2\partial_x a, \\
(a_d + b - 1)^2\partial_x a &\approx b^2\partial_x a, \\
(a + b_b)(a_d + b - 1)\partial_x b &\approx ab\partial_x b,
\end{aligned} \quad (\text{B.7})$$

we find:

$$(\mathcal{L}\Psi^\dagger)_1 = \partial_x [\partial_{xx}a + a - a^3 - \eta b^2 a]. \quad (\text{B.8})$$

Taking the derivative of (2.62) with respect to x we find that the right hand side of (B.8) is equal to zero when the amplitude solutions $a = a(x - r(t))$ and $b = b(x - r(t))$ are replaced by their form for $\delta = 0$. Hence, we conclude that $(\mathcal{L}\Psi^\dagger)_1 = O(\delta)$. Likewise, we can prove that $(\mathcal{L}\Psi^\dagger)_2 = O(\delta)$. Therefore, to lowest order in δ , $(\partial_x a, \partial_x b)^T$ belongs to the kernel of the operator \mathcal{L}^1 .

Now we can calculate the evolution of the domain size $L(t) = d - 2r(t)$ through the solvability condition (B.5). The result is:

$$\partial_t L \cong \pm 2v(\eta, \delta) + \frac{\int_{-\infty}^{\infty} dx (h_a \partial_x a + h_b \partial_x b)}{\int_{-\infty}^{\infty} dx [(\partial_x a)^2 + (\partial_x b)^2]}. \quad (\text{B.9})$$

where the functions h_a and h_b depend upon the amplitude solutions a and b and the non-potential parameter δ . The first term of the right hand side of (B.9) represents the rate of change of the domain size due to nonpotential effects which cause the kinks to move at a constant velocity $v(\eta, \delta)$. The second term is related to kink interaction. In the case $\eta = 3$ we can compute explicitly all the coefficients involved in (B.9) taking advantage of the analytical kink

¹As a matter of fact, the vector $(\partial_x a_d, \partial_x b_d)^T$ also belongs to the kernel of \mathcal{L} (to the lowest order in δ) as it can be proven analogously. It is straightforward to check that the solvability condition (B.5) leads to the same results with either of the two vectors.

profiles to lowest order in δ [Eq. (2.56)]. Making an expansion in powers of $e^{-\sqrt{2}L(t)}$, retaining only the leading terms, and provided that δ is a small parameter, we obtain:

$$\partial_t L = \pm \frac{\delta}{\sqrt{2}} - 24\sqrt{2} e^{-\sqrt{2}L(t)}, \quad (\text{B.10})$$

which is Eq. (2.63).

Appendix C

Eikonal Equation for the Busse-Heikes Model

In this appendix we give a proof of equation (2.66) which gives the normal velocity of an interface (*eikonal equation*) for the Busse-Heikes model in two spatial dimensions. The extension of the demonstration to higher dimensions is straightforward.

Since stable fronts are formed by two varying amplitudes, we only need to take into account two of the three equations of the model. Let us then consider a free front with two varying amplitudes $A_i(\mathbf{r}, t)$, $A_j(\mathbf{r}, t)$. The spatio-temporal dynamics of these fields is governed by the equations:

$$\partial_t A_i = \nabla^2 A_i + A_i - A_i^3 - (\eta + \delta) A_i A_j^2, \quad (\text{C.1a})$$

$$\partial_t A_j = \nabla^2 A_j + A_j - A_j^3 - (\eta - \delta) A_j A_i^2. \quad (\text{C.1b})$$

To track the motion of the front it is useful to make a change of coordinates to an orthogonal coordinate system (u, s) that moves with it. In the vicinity of the interface, the change of coordinates is defined by (see Fig. C.1):

$$\mathbf{r}(u, s, t) = \mathbf{R}(s, t) + u \hat{\mathbf{n}}(s, t), \quad (\text{C.2})$$

where $\mathbf{R}(s, t) = (X(s, t), Y(s, t))$ is the position vector of the points of the line front in the laboratory reference frame and $\mathbf{r}(u, s, t)$ is the position vector in the moving frame. The coordinate s is the arclength of the line front while u is the normal coordinate to the front. The vector $\hat{\mathbf{n}}(s, t) = Y_s \hat{\mathbf{x}} - X_s \hat{\mathbf{y}}$ is the unit normal vector to the curve, being $\hat{\mathbf{x}}$ and $\hat{\mathbf{y}}$ normal unitary vectors along the X and Y axis. The subscripts indicate partial derivatives. The Jacobian matrix of the transformation is given by:

$$M(u, s, t) \equiv \frac{\partial \mathbf{r}(u, s, t)}{\partial(u, s)} = \begin{bmatrix} Y_s & X_s + uY_{ss} \\ -X_s & Y_s - uX_{ss} \end{bmatrix}. \quad (\text{C.3})$$

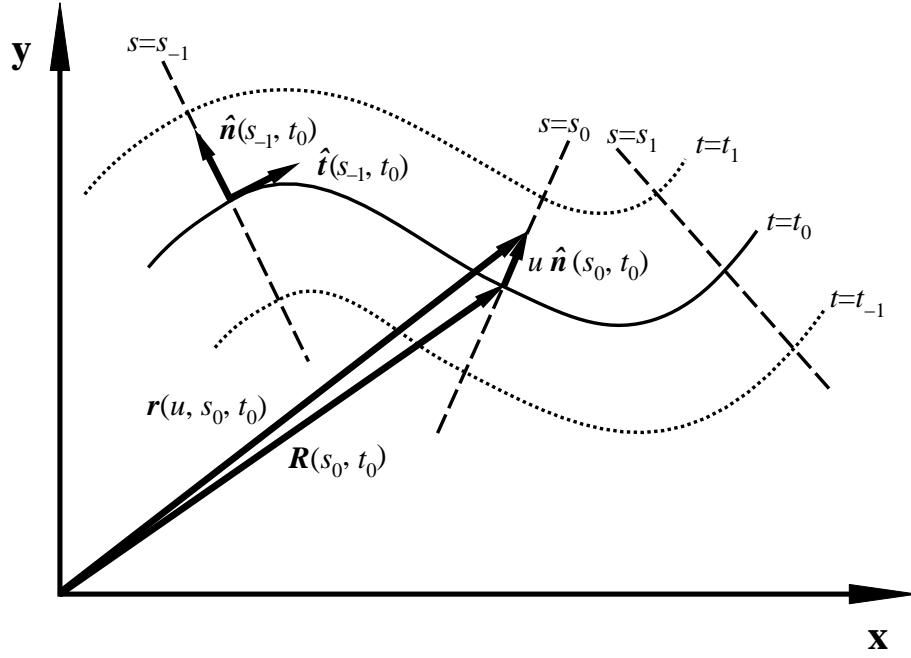


Figure C.1: Schematic of the change of coordinates defined by Eq. (C.2).

The matrix of the metric defined by the change of coordinates is now easily obtained:

$$G(u, s, t) \equiv M^\dagger M = \begin{bmatrix} 1 & 0 \\ 0 & (1 + u\kappa)^2 \end{bmatrix}. \quad (\text{C.4})$$

Here $\kappa(s, t)$ is the local curvature of the front line and we have used the identities:

$$\kappa(s, t) = X_s Y_{ss} - Y_s X_{ss} = \sqrt{X_{ss}^2 + Y_{ss}^2}, \quad (\text{C.5})$$

$$X_s^2 + Y_s^2 = 1. \quad (\text{C.6})$$

The Laplacian and the temporal derivative are transformed according to the relations:

$$\begin{aligned} \nabla_{u,s}^2 &= \frac{1}{G_{11}G_{22}} \left[\frac{\partial}{\partial u} \left(\sqrt{\frac{G_{22}}{G_{11}}} \frac{\partial}{\partial u} \right) + \frac{\partial}{\partial s} \left(\sqrt{\frac{G_{11}}{G_{22}}} \frac{\partial}{\partial s} \right) \right] \\ &= \frac{\kappa}{1 + u\kappa} \frac{\partial}{\partial u} + \frac{\partial^2}{\partial u^2} - \frac{u\kappa_s}{(1 + u\kappa)^3} \frac{\partial}{\partial s} + \frac{1}{(1 + u\kappa)^2} \frac{\partial^2}{\partial s^2}, \end{aligned} \quad (\text{C.7})$$

$$\frac{\partial}{\partial t} = -v_n \frac{\partial}{\partial u} - \frac{1}{1 + u\kappa} \mathbf{r}_t \cdot \hat{\mathbf{t}} \frac{\partial}{\partial s}, \quad (\text{C.8})$$

where $v_n = -\mathbf{r}_t \cdot \hat{\mathbf{n}}$ is the normal velocity and $\hat{\mathbf{t}} = X_s \hat{\mathbf{x}} + Y_s \hat{\mathbf{y}}$ is a unit vector tangent to the front line. If we assume that the curvature $\kappa(s, t)$ is a

smooth function of s and t , we can neglect the partial derivatives ∂_s and ∂_t as compared with ∂_u . With all this, the equations for the fields $A_i(u, s, t)$ and $A_j(u, s, t)$ in the new coordinate system are

$$\partial_{uu}A_i + \left(v_n + \frac{\kappa}{1 + u\kappa} \right) \partial_u A_i + 1 - A_i^3 - (\eta + \delta)A_i A_j^2 = 0, \quad (\text{C.9a})$$

$$\partial_{uu}A_j + \left(v_n + \frac{\kappa}{1 + u\kappa} \right) \partial_u A_j + 1 - A_j^3 - (\eta - \delta)A_j A_i^2 = 0, \quad (\text{C.9b})$$

or, equivalently,

$$\partial_{uu}A_i + v_p \partial_u A_i + 1 - A_i^3 - (\eta + \delta)A_i A_j^2 = - \left(v_n - v_p + \frac{\kappa}{1 + u\kappa} \right) \partial_u A_i, \quad (\text{C.10a})$$

$$\partial_{uu}A_j + v_p \partial_u A_j + 1 - A_j^3 - (\eta - \delta)A_j A_i^2 = - \left(v_n - v_p + \frac{\kappa}{1 + u\kappa} \right) \partial_u A_j, \quad (\text{C.10b})$$

where v_p is the planar front velocity. The curved front solution is of the form²:

$$A_i(u, s, t) = A_i^0(u) + \varepsilon A_i^1(u, s, t) + O(\varepsilon^2), \quad (\text{C.11a})$$

$$A_j(u, s, t) = A_j^0(u) + \varepsilon A_j^1(u, s, t) + O(\varepsilon^2). \quad (\text{C.11b})$$

Here $A_i^0(u)$ and $A_j^0(u)$ are the planar front solutions and ε is a small parameter. The planar fronts satisfy the equations:

$$\partial_{uu}A_i^0 + v_p \partial_u A_i^0 + 1 - (A_i^0)^3 - (\eta + \delta)A_i^0(A_j^0)^2 = 0, \quad (\text{C.12a})$$

$$\partial_{uu}A_j^0 + v_p \partial_u A_j^0 + 1 - (A_j^0)^3 - (\eta - \delta)A_j^0(A_i^0)^2 = 0. \quad (\text{C.12b})$$

By comparing Eqs. (C.10a–b) with (C.12a–b) it is clear that for weakly curved fronts, the quantity $v_n - v_p + \kappa/(1 + u\kappa)$ must be small. Now, by inserting (C.11a–b) into (C.10a–b) we arrived, to order $O(\varepsilon)$, at the next set of equations after absorbing the parameter ε in the definitions of A_i^1 and A_j^1 :

$$\begin{aligned} \partial_{uu}A_i^1 + v_p \partial_u A_i^1 + [1 - 3(A_i^0)^2 - (\eta + \delta)(A_j^0)^2] A_i^1 - 2(\eta + \delta)A_i^0 A_j^0 A_j^1 \\ = - \left(v_n - v_p + \frac{\kappa}{1 + u\kappa} \right) \partial_u A_i^0, \end{aligned} \quad (\text{C.13a})$$

$$\begin{aligned} -2(\eta - \delta)A_i^0 A_j^0 A_i^1 + \partial_{uu}A_j^1 + v_p \partial_u A_j^1 + [1 - 3(A_j^0)^2 - (\eta - \delta)(A_i^0)^2] A_j^1 \\ = - \left(v_n - v_p + \frac{\kappa}{1 + u\kappa} \right) \partial_u A_j^0. \end{aligned} \quad (\text{C.13b})$$

²Here we are assuming that a curved front solution can be expanded in terms of a small parameter ε .

We have assumed that the (small) quantity $v_n - v_p + \kappa/(1 + u\kappa)$ is of order ε . The previous set of equations can be cast into matrix form:

$$\mathcal{L}\alpha = \alpha', \quad (\text{C.14})$$

$$\mathcal{L} = \begin{bmatrix} M_{ij+} & -2(\eta + \delta)A_i^0 A_j^0 \\ -2(\eta - \delta)A_i^0 A_j^0 & M_{ji-} \end{bmatrix},$$

$$M_{ij\pm} \equiv \partial_{uu} + v_p \partial_u + 1 - 3(A_i^0)^2 - (\eta \pm \delta)(A_j^0)^2,$$

$$\alpha = \begin{bmatrix} A_i^1 \\ A_j^1 \end{bmatrix}, \quad \alpha' = - \left(v_n - v_p + \frac{\kappa}{1 + u\kappa} \right) \begin{bmatrix} \partial_u A_i^0 \\ \partial_u A_j^0 \end{bmatrix}.$$

Due to the translational invariance the operator \mathcal{L} is singular, that is, its nullspace is not empty. It is easy to see that

$$\mathcal{L}\phi = 0, \quad \phi = (\partial_u A_i^0, \partial_u A_j^0)^T \quad (\text{C.15})$$

Let ϕ^\dagger be a vector such that $\mathcal{L}^\dagger \phi^\dagger = 0$. The linear system (C.14) admits a solution (A_i^1, A_j^1) if and only if its right hand side is orthogonal to the nullspace of the linear operator \mathcal{L} , that is,

$$(\phi^\dagger, \alpha') = 0, \quad (\text{C.16})$$

$$\int_{-\infty}^{\infty} du \left(v_n - v_p + \frac{\kappa}{1 + u\kappa} \right) \phi \cdot \phi^\dagger = 0, \quad (\text{C.17})$$

$$v_n = v_p - \left[\frac{\int_{-\infty}^{\infty} du \phi \cdot \phi^\dagger (1 + u\kappa)^{-1}}{\int_{-\infty}^{\infty} du \phi \cdot \phi^\dagger} \right] \kappa. \quad (\text{C.18})$$

If W is the interface width and we assume that $\kappa \ll W^{-1}$ (this is equivalent to say that the size of the transformed region is much greater than the interface width), we can make the simplification:

$$\begin{aligned} \int_{-\infty}^{\infty} du \phi \cdot \phi^\dagger (1 + u\kappa)^{-1} &= \lim_{\xi_f \rightarrow \infty} \int_{-W/2}^{W/2} du \phi \cdot \phi^\dagger (1 + u\kappa)^{-1} \\ &\simeq \lim_{\xi_f \rightarrow \infty} \int_{-W/2}^{W/2} du \phi \cdot \phi^\dagger = \int_{-\infty}^{\infty} du \phi \cdot \phi^\dagger, \end{aligned} \quad (\text{C.19})$$

so (C.18) reduces to

$$v_n(s, t; \eta, \delta) = v_p(\eta, \delta) - \kappa(s, t), \quad (\text{C.20})$$

which is the desired result. Note that in the derivation of the previous equation no assumption about the size of δ has been made.

Appendix D

Computation of the Angular Velocity of a Vertex

D.1 Geometrical Approach

Let us consider a curve $\mathbf{R}(s, t) = (X(s, t), Y(s, t))$ in the (x, y) plane with a free end at zero arclength as illustrated in Fig. D.1. We call $\theta(s, t)$ the angle between the tangent direction to the curve and a fixed direction, say the x axis. The unit vectors tangent and normal to the curve at a point (s, t) are given by:

$$\hat{\mathbf{t}}(s, t) = \cos \theta \hat{\mathbf{x}} + \sin \theta \hat{\mathbf{y}}, \quad (\text{D.1})$$

$$\hat{\mathbf{n}}(s, t) = -\sin \theta \hat{\mathbf{x}} + \cos \theta \hat{\mathbf{y}}. \quad (\text{D.2})$$

Here $\hat{\mathbf{x}}$ and $\hat{\mathbf{y}}$ are unit vectors along X and Y axis. In an isotropic system, fronts move in the direction normal to each point. This is stated mathematically as:

$$\frac{d\mathbf{R}}{dt} = v_n \hat{\mathbf{n}}, \quad (\text{D.3})$$

where $v_n = v_n(s, t)$ is the normal front velocity. The normal propagation elongates or shortens the curve according to the sign of its curvature. As a result the arclength of the curve varies in time. Using (D.3) we have

$$\frac{d\mathbf{R}}{dt} = \left(\frac{\partial \mathbf{R}}{\partial s} \right)_t \frac{ds}{dt} + \left(\frac{\partial \mathbf{R}}{\partial t} \right)_s \Rightarrow \left(\frac{\partial \mathbf{R}}{\partial t} \right)_s = v_n \hat{\mathbf{n}} - \frac{ds}{dt} \hat{\mathbf{t}}, \quad (\text{D.4})$$

where we have used the identity $\hat{\mathbf{t}} = \partial \mathbf{R} / \partial s$ (note that this would not be true if the curve were not parametrized by the arclength). Taking the derivative of (D.1) with respect to time, we find

$$\frac{d\hat{\mathbf{t}}}{dt} = \frac{d\theta}{dt} \hat{\mathbf{n}}. \quad (\text{D.5})$$

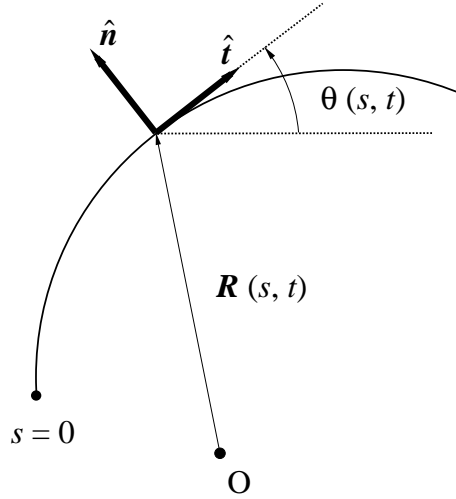


Figure D.1: Geometrical representation of a front $R(s, t)$ with a free end at arclength $s = 0$.

On the other hand:

$$\frac{d}{dt} \left(\frac{\partial \mathbf{R}}{\partial s} \right) = \frac{\partial^2 \mathbf{R}}{\partial s^2} \frac{ds}{dt} + \frac{\partial}{\partial t} \left(\frac{\partial \mathbf{R}}{\partial s} \right), \quad (\text{D.6})$$

$$\frac{\partial^2 \mathbf{R}}{\partial s^2} = \frac{\partial}{\partial s} \left(\frac{\partial \mathbf{R}}{\partial s} \right) = \frac{\partial \hat{\mathbf{t}}}{\partial s} = \underbrace{\frac{\partial \hat{\mathbf{t}}}{\partial \theta}}_{\hat{\mathbf{n}}} \underbrace{\frac{\partial \theta}{\partial s}}_{-\kappa} = -\kappa \hat{\mathbf{n}}, \quad (\text{D.7})$$

$$\frac{\partial}{\partial t} \left(\frac{\partial \mathbf{R}}{\partial s} \right) = \frac{\partial}{\partial s} \left(\frac{\partial \mathbf{R}}{\partial t} \right). \quad (\text{D.8})$$

Bringing (D.7) and (D.8) into (D.6) we arrive at

$$\frac{d\hat{\mathbf{t}}}{dt} = \frac{d}{dt} \left(\frac{\partial \mathbf{R}}{\partial s} \right) = \frac{\partial}{\partial s} \left(\frac{\partial \mathbf{R}}{\partial t} \right) - \kappa \frac{ds}{dt} \hat{\mathbf{n}}. \quad (\text{D.9})$$

It is easy to see that

$$\frac{\partial}{\partial s} \left(\frac{ds}{dt} \right) = \kappa v_n, \quad \frac{d\theta}{dt} = \frac{\partial v_n}{\partial s}. \quad (\text{D.10})$$

Now

$$\frac{d\theta}{dt} = \frac{\partial v_n}{\partial s} \Rightarrow \frac{\partial}{\partial s} \left(\frac{d\theta}{dt} \right) = \frac{\partial^2 v_n}{\partial s^2}, \quad (\text{D.11})$$

$$\frac{\partial}{\partial s} \left(\frac{\partial \theta}{\partial s} \frac{ds}{dt} + \frac{\partial \theta}{\partial t} \right) = \frac{\partial^2 v_n}{\partial s^2} \Rightarrow -\frac{\partial \kappa}{\partial s} \frac{ds}{dt} - \kappa \frac{\partial}{\partial s} \left(\frac{ds}{dt} \right) - \frac{\partial \kappa}{\partial t} = \frac{\partial^2 v_n}{\partial s^2}, \quad (\text{D.12})$$

and using (D.10) we find

$$\frac{\partial \kappa}{\partial t} = - \left(\kappa^2 + \frac{\partial^2}{\partial s^2} \right) v_n - \frac{\partial \kappa}{\partial s} \frac{ds}{dt}, \quad (\text{D.13})$$

where, according to (D.10)

$$\frac{ds}{dt} = \int_0^s ds' \kappa v_n + c_t, \quad c_t = \left(\frac{ds}{dt} \right)_{s=0}. \quad (\text{D.14})$$

The first term on the rhs of Eq. (D.14) represents the growth rate of the free end due to normal expansion whereas the second term, c_t , is the growth rate of the free end, or the tangential tip velocity. Eqs. (D.13) and (D.14) describe front dynamics in an isotropic system and they form the basis of the geometrical approach.

Now we apply the equation we have just obtained to a steady rotating spiral front line. In this case we have

$$\frac{\partial \kappa}{\partial t} = 0, \quad c_t = 0, \quad (\text{D.15})$$

so that Eq. (D.13) transforms into

$$0 = - \left(\kappa^2 + \frac{\partial^2}{\partial s^2} \right) v_n - \frac{\partial \kappa}{\partial s} \int_0^s ds' \kappa v_n. \quad (\text{D.16})$$

Integration of the previous equation between 0 and s yields (integrating the last term by parts)

$$\begin{aligned} 0 &= - \int_0^s ds' \kappa^2 v_n - \left. \frac{\partial v_n}{\partial s} \right|_0^s - \kappa \int_0^s ds' \kappa v_n + \int_0^s ds' \kappa^2 v_n \\ &\Rightarrow \frac{\partial v_n}{\partial s} + \kappa \int_0^s ds' \kappa v_n = \left(\frac{\partial v_n}{\partial s} \right)_{s=0} = \left. \frac{d\theta}{dt} \right|_{s=0} \equiv \omega, \end{aligned} \quad (\text{D.17})$$

where ω , the integration constant, is just the rotation angular velocity of the front line around the vertex point. The curvature has to satisfy the boundary conditions:

$$\lim_{s \rightarrow 0} \kappa(s) = \kappa_0, \quad \lim_{s \rightarrow \infty} \kappa(s) = 0. \quad (\text{D.18})$$

These conditions make (D.17) a nonlinear eigenvalue problem for the rotation rate. For the Busse-Heikes model the normal velocity is given by (2.66), so we have

$$\tilde{\kappa} \int_0^{\tilde{s}} ds' \tilde{\kappa} (1 - \beta \tilde{\kappa}) = \beta \frac{\partial \tilde{\kappa}}{\partial \tilde{s}} + \tilde{\omega}, \quad \beta = \kappa_0 / v_p, \quad (\text{D.19})$$

where $\tilde{\kappa} = \kappa / \kappa_0$, $\tilde{s} = s \kappa_0$ and $\tilde{\omega} = \omega / (v_p \kappa_0)$.

We can find ω either by solving (D.17) directly or by calculating inner and outer solutions for the curvature. We will follow the latter procedure.

◆ *Inner solution*

Near the vertex point we consider a solution for the curvature as a power series of the arclength \tilde{s}

$$\tilde{\kappa}(\tilde{s}) = \sum_{i=0}^{\infty} a_i \tilde{s}^i. \quad (\text{D.20})$$

Inserting Eq. (D.20) into (D.19) we find:

$$\tilde{\kappa}_{\text{inner}}(\tilde{s}) = 1 - \frac{\tilde{\omega}}{\beta} \tilde{s} + \frac{1}{2} \left(\frac{1}{\beta} - 1 \right) \tilde{s}^2 + O(\tilde{s}^3). \quad (\text{D.21})$$

◆ *Outer solution*

Since the curvature is a flat function of \tilde{s} for high values of \tilde{s} , we may neglect the term containing the derivative of the curvature on the rhs of (D.19). On the other hand, as $\tilde{\kappa} < 1$, we can assume that

$$\int_0^{\tilde{s}} ds' \tilde{\kappa}^2 \ll \int_0^{\tilde{s}} ds' \tilde{\kappa}. \quad (\text{D.22})$$

This can be seen by using the expression for the curvature of an Archimedes' spiral³. If we call ϕ the polar angle, the following asymptotic relations hold:

$$\int_0^{\phi_m} \tilde{\kappa}(\phi) \frac{\partial \tilde{s}}{\partial \phi} d\phi = \phi_m + O(\phi_m^{-1}), \quad (\text{D.23})$$

$$\int_0^{\phi_m} \tilde{\kappa}(\phi)^2 \frac{\partial \tilde{s}}{\partial \phi} d\phi = \frac{1}{2} \log(\phi_m) + O(\phi_m^{-2}). \quad (\text{D.24})$$

We also check the validity of (D.22) by means of numerical integration. With all these approximations, Eq. (D.19) reduces to:

$$\tilde{\kappa} \int_0^{\tilde{s}} ds' \tilde{\kappa} = \tilde{\omega}. \quad (\text{D.25})$$

The outer solution is found by solving (D.25):

$$\tilde{\kappa}_{\text{outer}}(\tilde{s}) = \left(\frac{\tilde{\omega}}{2\tilde{s}} \right)^{1/2}. \quad (\text{D.26})$$

³The polar equation for an archimedean spiral is $\rho = a\theta^{1/n}$. The particular case $n = 1$ corresponds to the Archimedes' spiral which is such that the distance between windings is constant.

By imposing the continuity of the inner and outer solutions and of their first derivative in a certain point $\tilde{s} = s_0$, we are led finally to

$$\left. \begin{aligned} \tilde{\kappa}_{\text{inner}}|_{\tilde{s}=s_0} &= \tilde{\kappa}_{\text{outer}}|_{\tilde{s}=s_0} \\ \frac{\partial \tilde{\kappa}_{\text{inner}}}{\partial \tilde{s}}|_{\tilde{s}=s_0} &= \frac{\partial \tilde{\kappa}_{\text{outer}}}{\partial \tilde{s}}|_{\tilde{s}=s_0} \end{aligned} \right\} \Rightarrow s_0 = \left(\frac{3\beta}{8}\right)^{1/2}, \quad \tilde{\omega} = \left(\frac{8\beta}{27}\right)^{1/2},$$

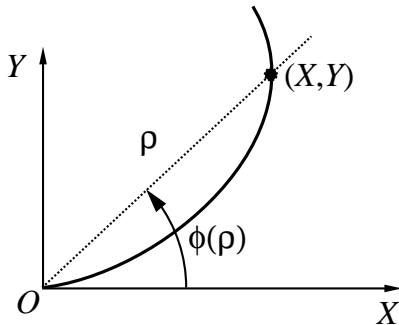
$$\omega = (8/27)^{1/2} v_p^{1/2} \kappa_0^{3/2}. \quad (\text{D.27})$$

Now, in order to find the relation $\omega = \Omega(v_p)$ one needs to know how the curvature at the origin κ_0 is related to the planar front velocity v_p . For an Archimedes' spiral, Eq. (D.13) evaluated at $s = 0$ gives $v_p = 3\kappa_0/2 \propto \kappa_0$. Hence (D.27) yields

$$\omega \propto v_p^2. \quad (\text{D.28})$$

D.2 Free Boundary Formulations

Other way to work out the rotation angular velocity is by considering the differential equation that gives the points of the rotating front line. The location of the front line of a rotating interface can be represented by



$$X(\rho) = \rho \cos(\phi(\rho) + \omega t), \quad (\text{D.29})$$

$$Y(\rho) = \rho \sin(\phi(\rho) + \omega t), \quad (\text{D.30})$$

where $(\rho, \phi(\rho))$ are the polar coordinates. The curvature and normal velocity are given by [159]:

$$\kappa = \frac{\psi'}{(1 + \psi^2)^{3/2}} + \frac{\psi}{\rho(1 + \psi^2)^{1/2}}, \quad (\text{D.31})$$

$$v_n = \frac{\omega \rho}{(1 + \psi^2)^{1/2}}, \quad (\text{D.32})$$

where $\psi(\rho) \equiv \rho \phi'(\rho)$. The eikonal equation (2.66) then becomes an ordinary differential equation for the function ψ :

$$\rho \psi'(\rho) = (1 + \psi^2)[v_p \rho(1 + \psi^2)^{1/2} - \omega \rho^2 - \psi]. \quad (\text{D.33})$$

When $\rho \rightarrow \infty$, we have that $\kappa \rightarrow 0$ and $v_n \rightarrow v_p$. Therefore, for large ρ we will have

$$v_p \approx \frac{\omega \rho}{(1 + \psi^2)^{1/2}} \Rightarrow \psi \sim \frac{\omega}{v_p} \rho \quad \text{as } \rho \rightarrow \infty, \quad (\text{D.34})$$

that is, the spiral is approximately archimedean far away from the tip. On the other hand, ψ must obey the boundary condition

$$\psi(0) = 0. \quad (\text{D.35})$$

Eqs. (D.33), (D.34) and (D.35) constitute an eigenvalue problem for ω . However, some information about this relation can be obtained at once by using the symmetry transformation $\{\psi \rightarrow \psi, \rho \rightarrow A\rho, \omega \rightarrow \omega/A^2, v_p \rightarrow v_p/A\}$ that leaves (D.33) invariant. Applying this transformation to $\omega = \Omega(v_p)$ with $A = v_p$ one gets

$$\omega \propto v_p^2. \quad (\text{D.36})$$

It is remarkably that the curvature at the origin does not appear explicitly in (D.36) while in expression (D.27) it does.

Bibliography

- [1] M. C. Cross and P. C. Hohenberg, *Rev. Mod. Phys.* **65**, 851 (1993).
- [2] P. S. Stevens, in *Patterns in Nature*, Penguin, London (1983).
- [3] J. M. García-Ruiz, E. Louis, P. Meakin, and L. M. Sander, in *Growth Patterns in Physical Sciences and Biology*, Plenum Press, New York (1983).
- [4] J. D. Gunton, M. San Miguel, and P. S. Sahni, in *Phase Transitions and Critical Phenomena*, edited by C. Domb and J. L. Lebowitz (Academic, New York, 1989), vol. 8, p. 269 (1983).
- [5] J. Langer, *Rev. Mod. Phys.* **52**, 1 (1980).
- [6] L. Sander, *Scientific American* **255**, 94 (1987); P. Meakin, in *Phase Transitions and Critical Phenomena*, C. Domb and J. L. Lebowitz eds., Academic Press, London, vol. 12, p. 336 (1988).
- [7] M. C. Cross and D. I. Meiron, *Phys. Rev. Lett.* **75**, 2152 (1995).
- [8] C. Josserand and S. Rica, *Phys. Rev. Lett.* **78**, 1215 (1997).
- [9] M. Tlidi, P. Mandel, and R. Lefever, *Phys. Rev. Lett.* **81**, 979 (1998).
- [10] S.-K. Chan, *J. Chem. Phys.* **67**, 5755 (1977).
- [11] P. Coulet, J. Lega, B. Houchmanzadeh, and J. Lajzerowicz, *Phys. Rev. Lett.* **65**, 1352 (1990).
- [12] S. Fauve and O. Thual, *Phys. Rev. Lett.* **64**, 282 (1990).
- [13] L. Kramer, *Z. Phys. B* **41**, 357 (1981); *Ibid.* **45**, 167 (1981).
- [14] W. van Saarloos and P. C. Hohenberg, *Physica D* **56**, 303 (1992).
- [15] Y. Pomeau, *Physica D* **51**, 546 (1991).
- [16] G. Küppers and D. Lortz, *J. Fluid. Mech.* **35**, 609 (1969).
- [17] M. C. Cross, D. Meiron, and Y. Tu, *Chaos* **4**, 607 (1994).

- [18] Y. Ponty, T. Passot, and P. L. Sulem, *Phys. Rev. Lett.* **79**, 71 (1997); *Phys. Rev. E* **56**, 4162 (1997).
- [19] A. J. Bray, *Adv. Phys.* **43**, 357 (1994).
- [20] P. Meakin, in *Fractals, scaling and growth far from equilibrium*, Cambridge University Press (1998); T. Vicsek, in *Fractal Growth Phenomena* (second edition), World Scientific (1992).
- [21] F. H. Busse and K. E. Heikes, *Science* **208**, 173 (1980).
- [22] G-L Oppo, A. J. Scroggie, and W. J. Firth, *Quantum Semiclass. Opt.* **1**, 133 (1999).
- [23] M. Tlidi and P. Mandel, *Europhys. Lett.* **44**, 449 (1998).
- [24] U. Peschel, D. Michaelis, C. Etrich, and F. Lederer, *Phys. Rev. E* **58**, R2745 (1998).
- [25] J. B. Geddes, J. V. Moloney, E. M. Wright, and W. J. Firth, *Opt. Commun.* **111**, 623 (1994).
- [26] M. Hoyuelos, P. Colet, M. San Miguel, and D. Walgraef, *Phys. Rev. E* **58**, 2992 (1998).
- [27] R. Montagne, A. Amengual, E. Hernández-García, and M. San Miguel, *Phys. Rev. E* **50**, 377 (1994).
- [28] W. van Saarloos, in *Three basic issues concerning interface dynamics in nonequilibrium pattern formation*, Proceedings of the IXth Summer School on Fundamental Problems in Statistical Mechanics (1998); W. van Saarloos, M. van Hecke, and R. Holyst, *Phys. Rev. E* **52**, 1773 (1995); W. van Saarloos, *Phys. Rev. A* **39**, 6367 (1989); W. van Saarloos, *Phys. Rev. A* **37**, 211 (1988); W. van Saarloos, *Phys. Rev. Lett.* **58**, 2751 (1987).
- [29] S. M. Allen and J. W. Cahn, *Acta metall* **27**, 1085 (1979).
- [30] I. M. Lifshitz and V. V. Slyozov, *J. Phys. Chem. Solids* **19**, 35 (1961); C. Z. Wagner, *Z. Electrochem.* **65**, 581 (1961).
- [31] M. San Miguel, A. Amengual, and E. Hernández-García, *Phase Transitions* **48**, 65 (1994).
- [32] K. Kaski *et al.*, *Phys. Rev. B* **31**, 3040 (1985).
- [33] M. Mondello and N. Goldenfeld, *Phys. Rev. A* **45**, 657 (1992).
- [34] H. Tutu, *Phys. Rev. E* **56**, 5036 (1997).
- [35] I. M. Lifshitz, *Sov. Phys. JETP* (1962).

- [36] M. San Miguel, M. Grant, and J. D. Gunton, *Phys. Rev. A* **31**, 1001 (1985).
- [37] K. R. Elder, J. Viñals, and M. Grant, *Phys. Rev. Lett.* **68**, 3024 (1992).
- [38] P. Couillet, C. Elphick, and D. Repaux, *Phys. Rev. Lett.* **58**, 431 (1987).
- [39] T. Ohta, *Physica D* **34**, 115 (1989).
- [40] D. Battogtokh, M. Hildebrand, K. Krischer, and A. S. Mikhailov, *Phys. Reports* **288**, 435 (1997).
- [41] H. Riecke, in *Pattern formation in continuous and coupled systems*, edited by M. Golubitsky, D. Luss and S. H. Strogatz (Springer, New York, 1993).
- [42] R. E. Goldstein, D. J. Muraki, and D. M. Petrich, *Phys. Rev. E* **53**, 3933 (1996).
- [43] R. J. Glauber, *J. Math. Phys.* **4**, 294 (1963).
- [44] K. Kawasaki, *Phys. Rev.* **145**, 224 (1966); *Ibid.* **148**, 375 (1966); *Ibid.* **150**, 285 (1966).
- [45] P. C. Hohenberg and B. I. Halperin, *Rev. Mod. Phys.* **49**, 435 (1977).
- [46] S. N. Majumdar and D. A. Huse, *Phys. Rev. E* **52**, 270 (1995).
- [47] R. Gallego, M. San Miguel, and R. Toral, to appear in *Phys. Rev. E*.
- [48] G-L Oppo, A. J. Scroggie, and W. J. Firth, *J. Opt. B* **1**, 133 (1999); Technical Digest of IQEC'98, p. 172–173 (1998).
- [49] F. de Pasquale, P. Tartaglia, and P. Tombesi, *Phys. Rev. A* **31**, 2447 (1985).
- [50] A. J. Bray, *J. Phys. A* **22**, L67 (1989).
- [51] T. M. Rodgers, K. R. Elder, and R. C. Desai, *Phys. Rev. B* **37**, 9638 (1988); R. Toral, A. Chakrabarti, and J. D. Gunton, *Phys. Rev. Lett.* **60**, 2311 (1988); R. Toral, A. Chakrabarti, and J. D. Gunton, *Phys. Rev. B* **39**, 4386 (1989); J. G. Amar, F. E. Sullivan, and R. D. Mountain, *Phys. Rev. B* **37**, 196 (1988).
- [52] Y. C. Chou and W. Goldberg, *Phys. Rev. A* **23**, 858 (1981); N. C. Wong and C. M. Knobler, *Phys. Rev. A* **24**, 3205 (1981); A. Craievich and J. M. Sánchez, *Phys. Rev. Lett.* **47**, 1308 (1981); S. Katano and M. Iizumi, *Phys. Rev. Lett.* **52**, 835 (1984); B. D. Gaulin, S. Spooner, and Y. Mori, *Phys. Rev. Lett.* **59**, 668 (1987).

- [53] R. Montagne, E. Hernández-García, and M. San Miguel, *Physica D* **96**, 47 (1996).
- [54] M. San Miguel and R. Toral, in *Stochastic Effects in Physical Systems, Instabilities and Nonequilibrium Structures VI*, Ed. E. Tirapegui and W. Zeller, Kluwer Academic, 1999.
- [55] R. Graham and T. Tél, *Phys. Rev. A* **42**, 4661 (1990).
- [56] R. Graham, in *Instabilities and Nonequilibrium Structures*, E. Tirapegui and D. Villarroel, eds. Reidel, Dordrecht (1993).
- [57] R. Graham, in *Instabilities and Nonequilibrium Structures III*, E. Tirapegui and W. Zeller, eds. Reidel, Dordrecht (1991).
- [58] R. Graham, in *25 years of Nonequilibrium Statistical Mechanics*, J. Brey, J. Marro, J. M. Rubi and M. San Miguel, eds. Springer Verlag (1995).
- [59] O. Descalzi and R. Graham, *Phys. Lett. A* **170**, 84 (1992).
- [60] O. Descalzi and R. Graham, *Z. Phys. B* **93**, 509 (1994).
- [61] J. S. Langer, in *Systems far from equilibrium*, Lecture Notes in Physics, vol. 132, eds. Springer Verlag (1980); J. S. Langer, in *Solids Far From Equilibrium*, edited by C. Godrèche (Cambridge University Press, 1992).
- [62] K. Kawasaki and T. Ohta, *Physica A* **116**, 573 (1982).
- [63] F. Barra, O. Descalzi, and E. Tirapegui, *Phys. Lett. A* **221**, 193 (1996).
- [64] T. Tél, R. Graham, and G. Hu, *Phys. Rev. A* **40**, 4065 (1989).
- [65] K. Staliunas and V. J. Sánchez-Morcillo, *Phys. Rev. A* **57**, 1454 (1998).
- [66] K. Staliunas and V. J. Sánchez-Morcillo, *Phys. Lett. A* **241**, 28 (1998).
- [67] V. B. Taranenko, K. Staliunas, and C. O. Weiss, *Phys. Rev. Lett.* **81**, 2236 (1998).
- [68] G. T. Dee and W. van Saarloos, *Phys. Rev. Lett.* **60**, 2641 (1988).
- [69] M. Mondello and N. Goldenfeld, *Phys. Rev. E* **47**, 2384 (1993).
- [70] M. San Miguel, in *Stochastic Methods and Models in the Dynamics of Phase Transitions*, editors: L. Pesquera and M. A. Rodríguez, Stochastic Processes Applied to Physics, p. 132–160, World Scientific, 1985.

- [71] G. F. Mazenko, O. T. Valls, and F. C. Zhang, *Phys. Rev. B* **32**, 5807 (1985); J. Viñals, M. Grant, M. San Miguel, J. D. Gunton, and E. T. Gawlinski, *Phys. Rev. Lett.* **54**, 1264 (1985); S. Kumar, J. Viñals, and J. D. Gunton, *Phys. Rev. B* **34**, 1908 (1986); C. Roland and M. Grant, *Phys. Rev. Lett.* **60**, 2657 (1988).
- [72] A. D. Rutenberg and A. D. Bray, *Phys. Rev. E* **50**, 1900 (1994).
- [73] T. Nagai and K. Kawasaki, *Physica A* **134**, 483 (1986).
- [74] D. A. Huse, *Phys. Rev. B* **34**, 7845 (1986); J. Amar, F. Sullivan, and R. Mountain, *Phys. Rev. B* **37**, 196 (1988); T. M. Rogers, K. R. Elder, and R. C. Desai, *Phys. Rev. B* **37**, 9638 (1988); R. Toral, A. Chakrabarti, and J. D. Gunton, *Phys. Rev. B* **39**, 4386 (1989); C. Roland, and M. Grant, *Phys. Rev. B* **39**, 11971 (1989).
- [75] A. J. Bray, *Phys. Rev. Lett.* **62**, 2841 (1989); *Phys. Rev. B* **41**, 6724 (1990).
- [76] I. M. Lifshitz and V. V. Slyozov, *J. Phys. Chem. Solids* **19**, 35 (1981); C. Wagner, *Z. Elektrochem* **65**, 581 (1961).
- [77] P. Martin, in *Potts Models and Related Problems in Statistical Mechanics*, Series on Advances in Statistical Mechanics, vol. 5, World Scientific (1991).
- [78] C. Sire and S. N. Majumdar, *Phys. Rev. Lett.* **74**, 4321 (1995).
- [79] G. S. Grest, D. J. Srolovitz, and M. P. Anderson, *Phys. Rev. B* **38**, 4752 (1988); M. P. Anderson, G. S. Grest, and D. J. Srolovitz, *Philos. Mag. B* **59**, 293 (1989); J. A. Glazier, M. P. Anderson, and G. S. Grest, *Philos. Mag. B* **62**, 615 (1990).
- [80] M. Lau, C. Dasgupta, and O. T. Valls, *Phys. Rev. B* **38**, 9024 (1988); J. Viñals and J. D. Gunton, *Phys. Rev. B* **33**, 7795 (1986); K. Kaski, J. Nieminen, and J. D. Gunton, *Phys. Rev. B* **31**, 2998 (1985).
- [81] C. Sire and S. N. Majumdar, *Phys. Rev. E* **52**, 244 (1995).
- [82] J. Viñals, E. Hernández-García, M. San Miguel, and R. Toral, *Phys. Rev. A* **44**, 1123 (1991).
- [83] Y. Pomeau and P. Manneville, *J. Phys. (Paris)* **40**, L609 (1979).
- [84] Y. Pomeau and P. Manneville, *Phys. Lett. A* **75**, 296 (1980).
- [85] E. Hernández-García, J. Viñals, R. Toral, and M. San Miguel, *Phys. Rev. Lett.* **70**, 3576 (1993).
- [86] K. R. Elder, J. Viñals, and M. Grant, *Phys. Rev. A* **46**, 7618 (1992).

- [87] P. C. Hohenberg and W. van Saarloos, *Phys. Rev. Lett.* **64**, 749 (1990); V. Hakim and Y. Pomeau, *Eur. J. Mech. B* **10**, 137 (1991).
- [88] C. Benkert and D. Z. Anderson, *Phys. Rev. A* **44**, 4633 (1991).
- [89] L. Frachebourg, P. L. Krapivsky, and E. Ben-Naim, *Phys. Rev. E* **54**, 6186 (1996).
- [90] R. Fisch, *Physica D* **45**, 19 (1990); *Ann. Prob.* **20**, 1528 (1992).
- [91] L. Frachebourg and P. L. Krapivsky, *J. Phys. A* **15**, L287 (1998).
- [92] M. Bramson, in *Convergence of Solutions of the Kolmogorov Equation to Traveling Waves*, Memoirs of the American Mathematical Society No. 285 (American Mathematical Society, 1983).
- [93] J. D. Murray, in *Mathematical Biology* (second edition), Springer (1993).
- [94] C. Kubstrup, H. Herrero, and C. Pérez-García, *Phys. Rev. E* **54**, 1560 (1996); H. Xi, J. D. Gunton, and J. Viñals, *Phys. Rev. E* **47**, R2987 (1993); M. Bestehorn, M. Fantz, R. Friedrich, H. Haken, and C. Pérez-García, *Z. Phys. B* **88**, 93 (1992).
- [95] H. S. Greenside and M. C. Cross, *Phys. Rev. A* **31**, 2492 (1985).
- [96] E. D. Siggia and A. Zippelius, *Phys. Rev. A* **24**, 1036 (1981).
- [97] M. C. Cross, *Phys. Rev. A* **29**, 391 (1984).
- [98] Y. Ponty, T. Passot, and P. L. Sulem, *Phys. Rev. Lett.* **79**, 71 (1997); H. Xi, J. D. Gunton, and A. Markish, *Physica A* **204**, 741 (1994).
- [99] J. Millán-Rodríguez, C. Pérez-García, M. Bestehorn, M. Fantz, and R. Friedrich, *Phys. Rev. A* **46**, 4729 (1992).
- [100] M. Neufeld and R. Friedrich, *Phys. Rev. E* **51**, 2033 (1995); J. Millán-Rodríguez, C. Pérez-García, M. Bestehorn, M. Neufeld, and R. Friedrich, *Chaos* **4**, 369 (1994).
- [101] L. A. Lugiato, M. Brambilla, and A. Gatti, Optical Pattern Formation, in *Advances in Atomic, Molecular and Optical Physics*, ed. by B. Bederson and H. Walther, Academic Press, to be published; *Nonlinear Optical Structures, Patterns, Chaos*, edited by L. A. Lugiato, special issue of *Chaos, Solitons and Fractals*, **4**, 1251 (1994).
- [102] E. Oguz, A. Chakrabarti, R. Toral, and J. D. Gunton, *Phys. Rev. B* **42**, 704 (1990).
- [103] D. S. Fisher and D. A. Huse, *Phys. Rev. B* **38**, 373 (1988).

- [104] N. Mason, A. N. Pargellis, and B. Yurke, *Phys. Rev. Lett.* **70**, 190 (1993); H. Orihara and Y. Ishibashi, *J. Phys. Soc. Japan* **55**, 2159 (1986); T. Nagaya, T. Orihara, and Y. Ishibashi, *ibid.* **56**, 1898 (1987); *Ibid.* **59**, 377 (1990).
- [105] T. Ohta, D. Jasnow, and K. Kawasaki, *Phys. Rev. Lett.* **49**, 1223 (1982).
- [106] A. J. Bray and K. Humayun, *Phys. Rev. E* **48**, 1609 (1993).
- [107] Y. Hu, R. E. Ecke, and G. Ahlers, *Phys. Rev. E* **55**, 6928 (1997).
- [108] Y. Hu, R. E. Ecke, and G. Ahlers, *Phys. Rev. Lett.* **74**, 5040 (1995).
- [109] R. E. Ecke *et. al.*, *Science* **269**, 1704 (1995).
- [110] Y. Tu and M. C. Cross, *Phys. Rev. Lett.* **69**, 2515 (1992).
- [111] M. Neufeld, R. Friedrich, and H. Haken, *Z. Phys. B* **92**, 243 (1993).
- [112] R. M. May and W. J. Leonard, *SIAM J. Appl. Math.* **29**, 243 (1975).
- [113] G. Szabó, M. A. Santos, and J. F. F. Mendes, cond-mat/9907333 (1999).
- [114] A. C. Newell and J. A. Whitehead, *J. Fluid Mech.* **38**, 279 (1969); L. A. Segel, *ibid.* **38**, 203 (1969).
- [115] G. H. Gunaratne, Q. Ouyang, and H. L. Swinney, *Phys. Rev. E* **50**, 2802 (1994).
- [116] R. Graham, *Phys. Rev. Lett.* **76**, 2185 (1996).
- [117] A. M. Soward, *Physica D* **14**, 227 (1985).
- [118] B. A. Malomed, A. A. Nepomnyashchy, and M. I. Tribelsky, *Phys. Rev. A* **42**, 7244 (1990).
- [119] Y. Elskens and H. L. Frisch, *Phys. Rev. A* **31**, 3812 (1985).
- [120] J. Guckenheimer and P. Holmes, in *Nonlinear Oscillations, Dynamical Systems and Bifurcations of Vector Fields*, Springer-Verlag, New York (1983).
- [121] H. Bai-Lin, in *Chaos*, World Scientific, Singapore (1983).
- [122] L. Pivka, A. L. Zheleznyak, and L. O. Chua, *Int. J. of Bif. and Chaos* **4**, 1743 (1994); M. Itoh, H. Murakami, and L. O. Chua, *ibid.* **4**, 1721 (1994).
- [123] T. Bohr, P. Bak, and M. H. Jensen, *Phys. Rev. A* **30**, 1970 (1984).
- [124] V. Petrov, Q. Ouyang, and H. L. Swinney, *Nature* **388**, 655 (1997).

- [125] J. Buck and E. Buck, *Sci. Am.* **234**, 74 (1976); R. E. Mirollo and S. H. Strogatz, *SIAM J. Appl. Math.* **50**, 1645 (1990).
- [126] M. R. Guevara and L. Glass, *J. Math. Biology* **14**, 1 (1982); L. Glass, *Physics Today* **49**, 40 (1996); A. M. Kunysz, A. Shrier, and L. Glass, *Am. J. Physiol.* **273** (*Cell Physiol.* **42**), 331 (1997).
- [127] A. L. Lin, V. Petrov, and H. L. Swinney, Proceedings of IMA Workshop on Pattern Formation and Nonlocal Effects, U Minn (1998).
- [128] P. Bak and J. von Boehm, *Phys. Rev. B* **21**, 5297 (1980).
- [129] L. N. Bulaevskii and D. I. Khomskii, *Sov. Phys. JETP* **47**, 971 (1978).
- [130] M. Lowe and J. P. Gollub, *Phys. Rev. A* **31**, 3893 (1985).
- [131] T. C. Lubensky and K. Ingersent, in *Patterns, Defects and Microstructures in Nonequilibrium Systems*, NATO ASI Series E121, D. Walgraef ed., Martinus Nijhoff, p. 48 Dordrecht (1987).
- [132] P. Couillet, *Phys. Rev. Lett.* **56**, 724 (1986).
- [133] H. Riecke, J. D. Crawford, and E. Knobloch, *Phys. Rev. Lett.* **61**, 1942 (1988).
- [134] D. Walgraef, *Europhys. Lett.* **7**, 485 (1988).
- [135] I. Rehberg, S. Rasenat, J. Fineberg, M. de la Torre Juárez, and V. Steinberg, *Phys. Rev. Lett.* **61**, 2449 (1988).
- [136] P. Couillet and D. Walgraef, *Europhys. Lett.* **10**, 525 (1989).
- [137] P. Couillet and K. Emilsson, *Physica D* **61**, 119 (1992).
- [138] D. Walgraef, in *Spatio-Temporal Pattern Formation*, Springer-Verlag, New York (1996).
- [139] P. S. Hagan, *SIAM J. Appl. Math.* **42**, 762 (1976).
- [140] T. Yamada and Y. Kuramoto, *Prog. Theor. Phys.* **55**, 2035 (1976).
- [141] S. Rica and E. Tirapegui, *Physica D* **48**, 396 (1991).
- [142] L. Kramer, I. Aranson, and A. Weber, *Physica D* **53**, 376 (1991).
- [143] L. M. Pismen and A. A. Nepomnyashchy, *Physica D* **54**, 183 (1992).
- [144] T. B. Benjamin and J. Feir, *J. Fluid Mech.* **27**, 417 (1967); A. Newell, *Lect. Appl. Math.* **15**, 157 (1974).
- [145] P. Couillet, L. Gil, and J. Lega, *Phys. Rev. Lett.* **62**, 1619 (1989).

- [146] C. Elphick, A. Hagberg, and E. Meron, *Phys. Rev. Lett.* **80**, 5007 (1998).
- [147] R. Gallego, M. San Miguel, and R. Toral, *Physica A* **257**, 207 (1998).
- [148] R. Gallego, M. San Miguel, and R. Toral, *Phys. Rev. E* **58**, 3125 (1998).
- [149] B. Shraiman *et al.*, *Physica D* **57**, 241 (1992); H. Chaté, *Nonlinearity* **7**, 185 (1994); H. Chaté, in *Spatiotemporal Patterns in Nonequilibrium Complex Systems*, vol. XXI of *Santa Fe Institute in the Sciences of Complexity*, edited by P. Cladis and P. Palffy-Muhoray (Addison-Wesley, New York, 1995), p. 5–49.
- [150] R. Montagne, Ph.D. Thesis, Universitat de les Illes Balears (1996).
- [151] H. Chaté and P. Manneville, *Physica A* **224**, 348 (1996).
- [152] M. Tlidi, P. Mandel, and R. Lefever, *Phys. Rev. Lett.* **73**, 640 (1994); W. Firth and A.J. Scroggie, *Phys. Rev. Lett.* **76**, 1623 (1996); C. Etrich, U. Peschel, and F. Lederer, *Phys. Rev. Lett.* **79**, 2454 (1997); M. Brambilla *et al.*, *Phys. Rev. Lett.* **79**, 2042 (1997); K. Staliunas and J. V. Sánchez-Morcillo, *Phys. Rev. A* **57**, 1454 (1998).
- [153] P. Mandel, M. Georgiou, and T. Erneux, *Phys. Rev. A* **47**, 4277 (1993).
- [154] G-L Oppo, M. Brambilla, and L. A. Lugiato, *Phys. Rev. A* **49**, 2028 (1994).
- [155] L. A. Lugiato and C. Oldano, *Phys. Rev. A* **37**, 3896 (1988).
- [156] W. Firth and A. J. Scroggie, *Europhys. Lett.* **26**, 521 (1994).
- [157] K. Ouchi and H. Fujisaka, *Phys. Rev. E* **54**, R3895 (1996).
- [158] M. Hoyuelos and H. O. Martín, *Phys. Rev. E* **48**, 3309 (1993).
- [159] J. P. Keener, *SIAM J. Appl. Math.* **46**, 1039 (1986).

Curriculum Vitae

Datos personales

APELLIDOS: Gallego Amez
NOMBRE: Rafael
SEXO: Varón
D.N.I.: 10.864.835 A
FECHA DE NACIMIENTO: 27/11/68
DIRECCION PARTICULAR: C/ Pasaje Dante, 18, 1B
CIUDAD: Palma de Mallorca
CODIGO POSTAL: 07007
TELEFONO: 971 249479/971 172536
E-MAIL: rafa@imedea.uib.es

Formación académica

- ❖ **Licenciado en Ciencias Físicas (Especialidad Fundamental)**
Facultad de Ciencias (Universidad de Cantabria). 1989–1993.
- ❖ **V Máster en Energía Nuclear**
Centro de Investigaciones Energéticas, Medioambientales y Tecnológicas,
y Universidad Autónoma de Madrid (CIEMAT-UAM). Enero–Diciembre
1994.
- ❖ **Suficiencia investigadora**
Universitat de les Illes Balears. Diciembre 1998.

Experiencia profesional

- ❖ **CIEMAT** 2/95–12/95
Investigador del Instituto de Tecnología Nuclear
- ❖ **ENUSA (Empresa Nacional del Uranio, SA)** 9/94–12/94
Proyecto fin del V Máster en Energía Nuclear

Idiomas (R=regular, B=bien, C=correctamente)

<u>IDIOMA</u>	<u>HABLA</u>	<u>LEE</u>	<u>ESCRIBE</u>
Espanol	C	C	C
Inglés	C	C	C

Publicaciones

- ⟨1⟩ R. Gallego, M. C. Vicente, y J. J. Serna, “*Simulación del experimento de irradiación IFA-513 con un código de comportamiento termomecánico de barra combustible*”, Revista de la SNE (Noviembre 1995).
- ⟨2⟩ R. Gallego, M. San Miguel, y R. Toral, “*Domain growth in a multivariable nonpotential system*”, Physica A **257**, 207 (1998).
- ⟨3⟩ R. Gallego, M. San Miguel, y R. Toral, “*Fronts, domain growth and dynamical scaling in a $d=1$ nonpotential system*”, Phys. Rev. E **58**, 3125 (1998).
- ⟨4⟩ R. Gallego, M. San Miguel, y R. Toral, “*Domain growth and coarsening inhibition in a nonpotential system*”, Comp. Phys. Comm. **121**, 324 (1999).
- ⟨5⟩ R. Gallego, M. San Miguel, y R. Toral, “*Self-similar domain growth, localized structures and labyrinthine patterns in vectorial kerr resonators*”, por aparecer en Phys. Rev. E.
- ⟨6⟩ R. Gallego, D. Walgraef, M. San Miguel, y R. Toral, “*Numerical and analytical study of the 3ω parametrically forced complex Ginzburg-Landau equation*”, enviado a publicar.
- ⟨7⟩ R. Toral, M. San Miguel, y R. Gallego, “*Period stabilization of the Küppers-Lortz instability in the Busse-Heikes model*”, enviado a publicar.
- ⟨8⟩ R. Gallego, M. San Miguel, y R. Toral, “*Domain growth and spiral formation for three competing states*”, enviado a publicar.

Presentaciones y Congresos

⟨1⟩ **XXI Reunión Anual de la Sociedad Nuclear Española**

TITULO: *Simulación del experimento de irradiación IFA-513 con un código de comportamiento termomecánico de barra combustible.*

TIPO DE PARTICIPACION: Exposición oral

LUGAR DE CELEBRACION: Reus (Tarragona)

AnO: 1995

⟨2⟩ **Miniworkshop on Pattern Formation and Spatio-Temporal Chaos**

TITULO: *Fronts, domain growth and dynamical scaling in a $d=1$ nonpotential system*

TIPO DE PARTICIPACION: Exposición oral

LUGAR DE CELEBRACION: Trieste (Italia)

AnO: 1997

⟨3⟩ Física Estadística'97

TITULO: *Mode competition and domain growth in a nonvariational system: the Küppers-Lortz instability*

TIPO DE PARTICIPACION: Póster

LUGAR DE CELEBRACION: Getafe (Madrid)

AnO: 1997

⟨4⟩ V Latin American Workshop on Nonlinear Phenomena

TITULO: *Mode competition and domain growth in a nonvariational system: the Küppers-Lortz instability*

TIPO DE PARTICIPACION: Póster

LUGAR DE CELEBRACION: Canela (Brasil)

AnO: 1997

⟨5⟩ Patterns, Nonlinear Dynamics and Stochastic Behaviour in Spatially Extended, Complex Systems

TITULO: *Mode competition and domain growth in a nonvariational system: the Küppers-Lortz instability*

TIPO DE PARTICIPACION: Póster

LUGAR DE CELEBRACION: Budapest (Hungría)

AnO: 1997

⟨6⟩ STATPHYS 20, XX IUPAP International Conference on Statistical Physics

TITULO: *Domain growth and coarsening inhibition in a nonpotential system*

TIPO DE PARTICIPACION: Póster

LUGAR DE CELEBRACION: París (Francia)

AnO: 1998

⟨7⟩ 1998 Conference on Computational Physics

TITULO: *Domain growth and coarsening inhibition in a nonpotential system*

TIPO DE PARTICIPACION: Póster

LUGAR DE CELEBRACION: Granada (España)

AnO: 1998

⟨8⟩ Computer-Aided Analysis of Dynamical Structures and Defects

TITULO: *Spiral formation and domain growth in nonpotential systems*

TIPO DE PARTICIPACION: Exposición oral

LUGAR DE CELEBRACION: Dresden (Alemania)

AnO: 1999

⟨9⟩ **Control of Complex Behaviour in Optical Systems and Applications**

TITULO: *Patterns, dynamical scaling and localized structures in vectorial kerr resonators*

TIPO DE PARTICIPACION: Exposición oral

LUGAR DE CELEBRACION: Münster (Alemania)

AnO: 1999

Conferencias

⟨1⟩ **Pattern Formation, Interfacial Dynamics and Crystal Growth**

3-7 Junio 1996, Toledo (España).

⟨2⟩ **Nonlinear Oscillations, Waves and Patterns**

28 Julio-9 Agosto 1996, Cork (Irlanda).

⟨3⟩ **Dinámicas no Lineales de Autoorganización Espaciotemporal**

10-12 Febrero 1998, Barcelona (España).

Otros méritos

❖ **Becas, ayudas y premios recibidos:**

- Premio fin de carrera al mejor expediente académico.
- Becario del V Máster en Energía Nuclear durante el año 1994.
- Becario del CIEMAT durante el año 1995.
- Becario de Plan de Formación del Personal Investigador del Ministerio de Educación y Cultura (DGICYT) en las convocatorias de 1996, 1997 y 1998.

❖ **Estancia en centros extranjeros:**

- Supercomputer Computations Research Institute, Tallahassee (Florida-USA). Mayo-Junio 1998.

❖ **Experiencia con sistemas informáticos**

- Conocimientos de FORTRAN, C, IDL y JavaScript.
- Sistemas operativos usados: UNIX, MSDOS, VMS, entre otros.
- Ordenadores usados: estaciones de trabajo HP-UX9000, Cray Y-MP, IRIX64, Vax 9000, Digital, entre otros.

Index

- Allen-Cahn law, 12, 25, 40
- Busse-Heikes model, 46
 - spatial-dependent terms, 46, 82
 - with noise, 58
- coarsening inhibition, 90, 98, 100, 101, 119
- complex Ginzburg-Landau equation, 8, 30
 - parametrically forced, 18
- complex Ginzburg-Landau equation
 - parametrically forced, 92
- correlation function, 36, 38, 39, 41, 68, 120
- critical radius, 13, 75
- defects, *see* topological defects
- degenerate optical parametric oscillator, 110
- domain growth, 23–36
 - 1D Busse-Heikes model, 69
 - 2D Busse-Heikes model, 79
 - nonlinear optical systems, 109–114, 120
- dynamical scaling, 36–42
 - 1D Busse-Heikes model, 72
 - 2D Busse-Heikes model, 79
 - kerr resonator, 121
- eikonal equation, 12, 75, 120
- excitability, 94, 96
- excitable dynamics, 95
- frequency locking, 88, 89, 93
- Hamiltonian dynamics, 30, 53, 56, 109
- Hopf bifurcation, 18, 91
- interface velocity, 11, 12, 16, 20, 25, 40, 64, 75, 97, 118, 120
- Ising and Bloch walls, 19, 90
- Ising model, 23, 27, 33, 39, 71
- Küppers-Lortz instability, 44
- kerr resonator, 36, 115
- kink, 11, 21, 62, 118
- labyrinthine pattern, 22, 110, 123
- Lifshitz-Slyozov-Wagner theory, 26, 110, 113
- localized structure, 21, 31, 114, 121
- Lotka-Volterra models, 32, 49
- Lyapunov functional, 5
 - q -state Potts models, 27
 - Busse-Heikes model, 48, 51
 - model A dynamics, 6
 - Swift-Hohenberg equation, 28, 110
- Maxwell-Bloch equations, 111
- model A dynamics, 6, 8, 24–25, 37, 71
- model B dynamics, 7, 25–26
- nonlinear Schrödinger equation, 30
- nonpotential front motion, 20, 63, 75, 97
- nonpotential system, 8
- OJK theory, 40
- optical bistability, 36, 109, 111, 112, 117

- orthogonality condition, 8, 15, 51, 60
- oscillatory dynamics, 95
- oscillatory tails, 20, 118, 123, 124
- period, 55, 56, 59, 61, 77
- phase approximation, 95
- phase dynamics, 95
- Porod's Law, 38
- potential system, 5
- Potts models, 26
- Rayleigh-Bénard convection, 35
- scaling function, 37, 72, 121
- second-harmonic generation, 113, 124
- spiral dynamics
 - BH model, 75
 - forced CGLE, 95, 98
- spiral pattern, 34
- structure factor, 36, 39, 69
- surface tension, 12, 110, 120
- Swift-Hohenberg equation
 - nonpotential, 34
 - potential, 27, 110
- symmetry breaking, 88
- TDGL equation, *see* model A dynamics
- topological defects, 36, 38, 95
- vertex, 27, 73, 75, 98
 - annihilation, 77